



**HAL**  
open science

# Development of microsystems for the controlled formation of cell aggregates by dielectrophoresis

Jonathan Cottet

► **To cite this version:**

Jonathan Cottet. Development of microsystems for the controlled formation of cell aggregates by dielectrophoresis. Other. Université de Lyon, 2018. English. NNT: 2018LYSEC033 . tel-02168176

**HAL Id: tel-02168176**

**<https://theses.hal.science/tel-02168176v1>**

Submitted on 28 Jun 2019

**HAL** is a multi-disciplinary open access archive for the deposit and dissemination of scientific research documents, whether they are published or not. The documents may come from teaching and research institutions in France or abroad, or from public or private research centers.

L'archive ouverte pluridisciplinaire **HAL**, est destinée au dépôt et à la diffusion de documents scientifiques de niveau recherche, publiés ou non, émanant des établissements d'enseignement et de recherche français ou étrangers, des laboratoires publics ou privés.



ÉCOLE  
**CENTRALE** LYON

N°d'ordre NNT : 2018LYSEC033

**THESE de DOCTORAT DE L'UNIVERSITE DE LYON  
opérée au sein de l'ÉCOLE CENTRALE DE LYON**

**Ecole Doctorale N° 160  
Electronique, Electrotechnique et Automatique**

**Spécialité de doctorat** : Ingénierie pour le vivant

Soutenue publiquement le 29/11/2018, par :  
**Jonathan COTTET**

---

Development of microsystems for the  
controlled formation of cell aggregates by  
dielectrophoresis

---

**Devant le jury composé de :**

Van den Berg, Albert	Full Professor, Université de Twente	Rapporteur
Français, Olivier	Professeur des Universités, ESIEE	Rapporteur
Gué, Anne-Marie	Directrice de Recherche au CNRS, LAAS	Présidente du jury
Ramos Reyes, Antonio	Professor, Université de Séville	Examineur
Buret, François	Professeur des Universités, Ecole Centrale de Lyon	Directeur de thèse
Renaud, Philippe	Professeur ordinaire, Ecole Polytechnique Fédérale de Lausanne	Co-directeur de thèse
Frénéa-Robin, Marie	Maitre de conférences HDR, Université Claude Bernard Lyon 1	Co-directrice de thèse

Laboratoire de recherche : Laboratoire Ampère CNRS UMR 5005



To my family



## Acknowledgments

This PhD thesis is the result of a collaboration between two laboratories: the Biomicrosystems, Bioelectrochemistry and Bioelectromagnetism team of the Ampère laboratory (UMR CNRS 5005) and the Laboratory of Microsystems 4 (LMIS4) at Ecole Polytechnique Fédérale de Lausanne (EPFL).

I would like to thank Albert Van den Berg and Olivier Français for accepting the task of being reviewers of my PhD thesis as well as Anne-Marie Gué for being president of the jury and Antonio Ramos and Carlotta Guiducci for being external examiners.

I am deeply thankful to my PhD directors for their constant support: Philippe Renaud for hosting me in his laboratory during the entire duration of the PhD, providing me access to the facilities and particularly the cleanroom environment, for his time and feedback; François Buret for being my “official” director and providing me help when I needed it, especially during the last month with the feedback on the manuscript; Marie Frénéa-Robin for proposing me the subject, helping to submit it to ENS Rennes for funding and her constant availability and feedback, as well as the long videoconference we had during the 3 years: without her my PhD would have been much more difficult and less successful. I can’t thank my directors enough for this opportunity to perform the PhD thesis between France and Switzerland.

I am thankful to ENS Rennes for the opportunity they gave me to perform a PhD on a subject of my choosing. A special thanks to Bernard Multon, one of my mentors for all the constant support he provided me as a student and as a colleague. I don’t forget the help provided by Jean Meunier and Alexis Martin in the earlier development of the first version of MyDEP in Matlab: thank you guys!

I thank the PALSE program and LABEX iMUST for funding part of my time in Switzerland as well as the Doctoral School ED EEA for funding my participation to the conference Biosensors 2018.

I would like to thank all my collaborators and colleagues in both laboratories:

In Lyon:

I would like to thank Riccardo Scorretti for coordinating the project DYNAMO on electroporation where I had the opportunity to be involved, Olivier Fabregue for the work of transferring MyDEP from Matlab to Java and considerably improving the software in our fructuous collaboration, Charles Berger for implementing the database in MyDEP. I also would like to thank Edith Bergeroux and Marie-Christine Havgoudoukian for all the administrative support. I am grateful to the teaching team of “Automatique et traitement du signal” where I taught for 3 years especially the director of the doctoral school Gérard Scorletti, Catherine Musy-Bassot and Emmanuel Boutleux who coordinated the teaching team as well as my teaching colleagues Laurent Bako, Anton Korniienko, Hassan Omram, Xavier Bombois. I also want to thank all my colleagues from the team, Naoufel Haddour, Julien Marchalot and Laurent Krähenbühl for the valuable discussions. I am also thankful to my former office-mates David Royet, Agathe Paitier, and Arthur Perodou for all the discussions we had when I was in Lyon.

In Lausanne

I would like to thank my office-mate Harald for the great discussions we had during then whole PhD and the support he provided me, my semester students Alexandre Kehren and Soufian Lasli who performed most of the experimental work in this thesis, Clarisse Vaillier for the help with the development of the fabrication and alignment method and together with Margaux Duchamp for the assistance in the cell culture. I am grateful to Robert Meissner and Filiz Yesilköy for introducing me to the fields of impedance and dilectrophoresis respectively as well as to Marjan Shaker for the experimental support on impedance spectroscopy at the beginning.

I am also thankful to the secretaries of the laboratory Sylvie Clavel and Christine Vuichoud for making my life easy and the administrative assistance, and the secretaries of the EDMi doctoral School Marie Halm and Lucie Auberson who helped with my affiliation with the Doctoral School during my stay at EPFL.

I am thankful to Arnaud Bertsch for the critical discussions and feedback on my work.

I am thankful to all the LMIS4 team members, past and present, Shady Gawad, Sebastien Jiguet, Marc Heuschkel, Camille Raillon, Yufei Ren, Mojtaba Taghipoor, David Bonzon, David Forchelet, Guillaume Petit-Pierre, Stefano Varricchio, Ludovic Serex, Benoit Desbiolles, Thomas Braschler, Joan Teixidor, Clémentine Lipp, Fatemeh Navaee, Jiande Zhou, Nicolas Maïno, Amélie Bédurier, Patrick Bursch, Elodie Dahan, Roberta Calmo, Martina Genta, Silvia Demuru and those I may have forgotten to mention but who contributed, in one way or another to this thesis.

I thank all my former professors who trained my mind and critical thinking during my education, my PhD is in a way the final stone of my academic studies.

I am also deeply thankful to my friends and to my family for being there all the time. I will never be thankful enough to my parents and my sister for all the sacrifices they made to offer me an education and to make me the man I am today.

Lastly, I would like to dedicate this thesis to those who will read it! You are one of the reasons why I wrote it!





# Table of Content

Acknowledgments .....	5
List of Figures .....	15
List of Tables .....	29
Abbreviations .....	31
Introduction .....	33
Chapter 1     State of the art .....	37
1.1 From single cell to cell aggregates .....	38
1.2 Different fields of application of 3D aggregates and need of an intermediary model.....	40
1.2.1 In-vitro therapeutic screening.....	40
1.2.2 Electroporation .....	40
1.2.3 Understanding the dielectric properties of naturally formed aggregates .....	43
1.3 Type of cell aggregates: terminology .....	44
1.4 Creation methods of 3D aggregates .....	45
1.4.1 Contact methods .....	46
1.4.1.1 Micromolding .....	46
1.4.1.2 Liquid overlay .....	46
1.4.1.3 Hanging drop culture method .....	46
1.4.1.4 Rotary cell culture system: .....	46
1.4.1.5 Pellet culture system .....	47
1.4.1.6 Bioprinting .....	47
1.4.1.7 Conclusion on the contact methods.....	48
1.4.2 Non-Contact methods.....	48
1.4.2.1 Magnetic levitation method .....	49
1.4.2.2 Acoustophoresis.....	49
1.4.2.3 Optical trapping .....	50
1.4.2.4 Dielectrophoresis .....	51

1.5	Dielectrophoresis trapping design .....	52
1.5.1	For single cells .....	52
1.5.1.1	With pDEP.....	52
1.5.1.2	With nDEP .....	54
1.5.2	From individual cells to cell aggregates .....	60
1.5.2.1	DEP and physical confinement .....	60
1.5.2.2	Use of Octopole electrodes .....	61
1.5.2.3	Array of quadrupole electrodes .....	62
1.5.2.4	Using transistor.....	64
1.5.3	Conclusion on the trapping design for cell and aggregates. ....	65
1.5.4	DEP and cell culture.....	66
1.5.5	Conclusions on all the trapping designs .....	66
1.6	Requirement for controlled cell aggregate.....	67
Chapter 2	Dielectrophoresis theory and modeling with MyDEP .....	69
2.1	Dielectrophoresis historical overview .....	70
2.1.1	Polarization and dispersion mechanism .....	71
2.2	Dielectrophoresis theory.....	73
2.2.1	DEP basics.....	73
2.2.2	Conventional dielectrophoresis .....	74
2.2.3	Physical explanation of dielectrophoresis.....	74
2.2.4	Electrorotation.....	75
2.2.5	Travelling-Wave Dielectrophoresis (TWD).....	77
2.2.6	Dielectrophoresis Field-Flow Fractionation (DEP-FFF).....	77
2.2.7	Electrodeless and insulating dielectrophoresis (iDEP).....	77
2.3	Cell modeling and MyDEP.....	78
2.3.1	Cell models .....	78
2.3.2	Cell suspension.....	80
2.3.3	Aggregate modeling.....	81

2.4	Software for dielectric modeling .....	82
2.4.1	Existing tools .....	82
2.4.2	MyDEP software .....	83
2.5	Features, different types of analysis and database .....	84
2.5.1	Database .....	84
2.5.2	CM factor .....	85
2.5.3	Parameter sweep .....	86
2.5.4	Cell separation .....	87
2.5.5	Conductivity and permittivity of cell and suspension .....	88
2.5.6	Crossover frequencies .....	90
2.5.7	Graph export .....	91
2.6	Conclusions .....	91
Chapter 3	Trapping design and simulations .....	93
3.1	DEP Trapping .....	94
3.1.1	Physics behind the trapping: .....	94
3.1.1.1	The DEP force .....	94
3.1.1.2	The hydrodynamic viscous drag force .....	94
3.1.1.3	The gravitational force and buoyancy force .....	95
3.1.1.4	The electrothermal forces .....	95
3.1.1.5	Brownian motion .....	95
3.1.1.6	Particle-particle interaction .....	96
3.1.1.7	Conclusion on the forces .....	96
3.1.2	Effects of electric field on cells .....	96
3.1.2.1	Current-Induced Heating .....	96
3.1.2.2	Direct Electric-Field Interactions (transmembrane voltage) .....	96
3.1.3	Trapping parameters .....	97
3.1.4	Trapping design .....	99
3.2	Finite element simulations .....	102

3.2.1	COMSOL Multiphysics simulations .....	102
3.2.2	Trapping simulation and test design.....	102
3.2.2.1	Flow simulations .....	102
3.2.2.2	Electric field and dielectrophoresis simulations .....	103
3.2.3	All results .....	105
3.2.4	Limits of the 2D simulations .....	107
3.2.5	3D simulations .....	108
3.3	Conclusion .....	108
Chapter 4	Chip fabrication .....	109
4.1	Introduction.....	110
4.2	Methods.....	113
4.2.1	Fabrication .....	113
4.2.1.1	Process flow.....	113
4.2.1.2	Mold fabrication .....	115
4.2.1.3	PDMS molding in PMMA sarcophagus .....	116
4.2.2	Alignment .....	117
4.2.2.1	Alignment with mask Aligner .....	117
4.2.2.2	Results and discussion .....	118
4.3	Conclusion .....	120
Chapter 5	Experimental trapping results .....	121
5.1	Introduction.....	122
5.2	Materials and Methods.....	122
5.2.1	Beads preparation .....	122
5.2.2	Cell culture and preparation.....	122
5.2.3	BSA preparation .....	123
5.2.4	Experimental setup .....	123
5.3	Experimental testing of the test design .....	124
5.3.1	Initial assessment of the cell viability .....	126
5.4	Discussion on the test design.....	127

5.5	Design and setup improvement .....	127
5.5.1	Design improvements .....	127
5.5.1.1	Design .....	127
5.5.1.2	Fluidic simulations .....	128
5.5.1.3	Electric field and dielectrophoresis simulations .....	129
5.5.2	Setup Improvements.....	133
5.5.3	Experiments and trapping with a fully automated setup.....	133
5.6	Conclusion .....	135
Chapter 6	Design proposition for impedance sensing of single cells and cell aggregates .....	137
6.1	Introduction.....	138
6.2	Simulations .....	142
6.2.1	Simulated designs.....	142
6.2.2	Simulation specifications .....	143
6.2.3	Simulation results .....	144
6.2.3.1	Influence of <i>del</i> .....	144
6.2.3.2	Influence of <i>wel</i> .....	145
6.2.3.3	Influence of <i>b</i> .....	146
6.2.4	Proposed design for testing .....	147
6.2.5	Vertical and longitudinal position sensitivity.....	149
6.3	Laboratory experiments .....	151
6.3.1	Fabrication .....	151
6.3.2	Experimental setup .....	151
6.4	Results and discussion.....	152
6.5	Combining DEP Trapping with impedance measurement .....	156
6.6	Conclusions.....	158
Chapter 7	Conclusion and Outlook .....	160
7.1	Conclusion .....	161
7.2	Outlook.....	162

7.2.1 Theory and MyDEP .....	162
7.2.2 Simulations .....	163
7.2.3 Fabrication .....	164
7.2.4 Impedance.....	164
7.2.5 Design and experiments.....	164
7.2.6 Applications.....	165
Appendix A Dielectrophoresis theory and modeling with MyDEP .....	167
Appendix B Trapping design and simulations.....	191
Appendix C Chip fabrication .....	195
Appendix D Design proposition for impedance sensing of single cells and cell aggregates .....	205
Bibliography .....	213
List of publications.....	236

## List of Figures

Figure 1:1 Principle of application of electroporation in the biomedical field. A) General reversible electroporation principle. B) Electrochemotherapy. C) Electrogenetherapy. D) Irreversible electroporation. Figures adapted from (Calvet and Mir 2016). .....	42
Figure 1:2 Bioprinting techniques. A) Schematic of laser-based bioprinting. B) Schematic of extrusion-based bioprinting. C) Schematic of (Left) thermal and (Right) piezoelectric-based inkjet bioprinting. All schematics are adapted from (Dababneh and Ozbolat 2014). .....	48
Figure 1:3 Principle of magnetic cell levitation. A) Cells are put in contact with magnetic nanoparticles and incubated. The remaining particle are later washed away. B) After the application of an external magnetic field with a magnet, cells are levitating. C) After 12h, characteristic structures are formed. Illustrations adapted from (Souza, et al. 2010).....	49
Figure 1:4 3D acoustic tweezers illustrations. A) Configuration of the planar acoustic wave generators with interdigitated electrodes B) Numerical simulation illustrating the acoustic trap. Both illustrations are adapted from (Guo, et al. 2016). .....	50
Figure 1:5 A) Principle of optical tweezers. Adapted from (Lenshof and Laurell 2010). B) Schematic diagram of the optical trapping apparatus used by Akselrod et al. to create 3D construct. Adapted from (Akselrod, et al. 2006). .....	51
Figure 1:6 A) Schematic of grid-electrode geometry. The particle is trapped at the intersection between the two electrodes. Adapted from Voldman (Voldman 2006) B) Protoplast being moved from one position to another Adapted from Suehiro and Pethig (Suehiro and Pethig 1998).....	52
Figure 1:7 A) Example of the concentric ring levitor with a particle in levitation and B) the related feedback control. ....	53
Figure 1:8 A) Schematic of the point-and-lid geometry, adapted from (Voldman 2006) B) Endothelial cells patterned using one version of this geometry from (Gray, et al. 2004a) C) Fibroblasts patterned using a different version of the geometry and embedded in a hydrogel matrix from (Gray, et al. 2004a). .....	54



Figure 1:9 A) Schematic of the ring-dot geometry from (Voldman 2006). B) and C) are two images showing addressable removal of green-labeled human HL-60 in an array from (Voldman 2006). ..... 54

Figure 1:10 A) Principle of interdigitated castellated electrodes capture of cell by DEP. Adapted from (Pesch 2018). B) Capture of viable yeasts at the electrode edges by pDEP and of non-viable yeast in triangular aggregates by nDEP. Adapted from (Markx, et al. 1994). ..... 55

Figure 1:11 A) Schematic of the insulating post principle from (Voldman 2006). B) Cells are injected from the right to the left and, since the nDEP is larger on viable yeast cells (green) than dead yeast cells, they are retained farther from posts. Adapted from (Lapizco-Encinas, et al. 2004). ..... 56

Figure 1:12 A) Schematic of the quadrupole electrodes from (Voldman 2006) and B) Mouse fibroblast trapping from (Fuhr, et al. 1994). ..... 56

Figure 1:13 3D quadrupoles made of A) Electroplated gold on a SU-8 mold from (Voldman, et al. 2002) and B) Metal coated SU-8 structures from (Kilchenmann, et al. 2016). ..... 57

Figure 1:14 A) Schematic of octupole electrodes, Adapted from (Voldman 2006) B) Jurkat cell trapped in the structure, adapted from (Reichle, et al. 1999). 58

Figure 1:15 A) Schematic of the strip electrode configuration, adapted from (Voldman 2007). B) nDEP used to deflect yeast cells in PBS from (Seger-Sauli, et al. 2005). ..... 58

Figure 1:16 A) Schematic from the nDEP microwell, adapted from (Voldman 2006) B) HL60 cells trapped on nDEP electrode array, scalebar 200  $\mu\text{m}$  from (Mittal, et al. 2007). ..... 59

Figure 1:17 A) Schematic of the transistor-based structure B) zoom on particles trapped in potential cages. Both pictures are adapted from (Manaresi, et al. 2002) ..... 59

Figure 1:18 A) Schematic of a side and top view of the design. B) Phase contrast image of groups of four bovine pulmonary arterial endothelial cells in a specifically-designed pattern. This image is overlaid with the corresponding nuclear stain (blue), adapted from (Gray, et al. 2008). ..... 60

Figure 1:19 A) Top and B) Side view of the principle of the trapping with cavities presented by Ibrahim et al. Figures adapted from (Ibrahim, et al. 2012) .....	61
Figure 1:20 A) Picture of the electrode layout composed of two funnels (F1, F2) , three field cages (C1–C3) and one resistance sensor (S). B) Phase applied on two voltage configurations of the electrodes C) Yeast cell proliferation in the nDEP cage. All figures are adapted from (Jaeger, et al. 2008). .....	62
Figure 1:21 A) (a) to (d) fabrication of the quadrupole array with the bond-detach lithography. B) Formation of HEK-293 cell aggregates by nDEP. A) Cell aggregates formed in a $\sigma m = 50 \text{ mS/m}$ medium B) reconstruction of the z-stack images. All figures are adapted from (Menad, et al. 2015).....	63
Figure 1:22 Experiment steps for the creation of aggregates with the DEP array technology. Adapted from (Medoro, et al. 2003). .....	65
Figure 2:1 Frequency dependence of biological tissues. Adapted from (Meissner 2013). Original figure from (Schwan 1994). .....	72
Figure 2:2 Principle of A) pDEP and B) nDEP. $\mathbf{E}$ represents the electric field (in green), $\mathbf{m}$ the dipolar moment and $\mathbf{F}_a$ and $\mathbf{F}_b$ the Coulomb force ( $\mathbf{F}=\mathbf{qE}$ ) on each barycenter of the charges (red and blue circles) on each side of the particle.....	75
Figure 2:3 Illustration of the different spherical and ellipsoidal cell and particle models implemented in the interface. All the models “homogeneous sphere”, “single-shell”, “two-shell” and “three-shell” are illustrated with an example. The implemented “four-shell” model is not illustrated here. ....	78
Figure 2:4 Main menu of the “IMPEDANCE ANALYSIS mini” program. Adapted from (Irimajiri, et al. 1991) .....	82
Figure 2:5 Overview of the database explorer (Search) from MyDEP. A click on the desired element from the literature shows the values associated in the interface. ....	85
Figure 2:6 Example of $\text{Re}[\text{CM}(f)]$ and $\text{Im}[\text{CM}(f)]$ for viable and non-viable yeast cells suspended in a low conductivity medium ( $\sigma m = 7.8 \text{ mS/}$ , $\epsilon m = 78$ ). Data from (Talary, et al. 1996). The black line represents the baseline at 0. ....	86

Figure 2:7 Example of the evolution of  $\text{Re}[\text{CM}(f)]$  and  $\text{Im}[\text{CM}(f)]$  with a logarithmic sweep on ten values of  $\sigma_m$  from 1 mS/m to 1.6 S/m for a Jurkat cell. Data from (14). The black line represents the baseline at 0. .... 87

Figure 2:8 Example of the different  $\text{Re}[\text{CM}(f)]$  for a HEK cell (Zimmermann, et al. 2008) and a MCF-7 cell (Henslee, et al. 2011) in a medium with  $\sigma_m = 50$  mS/m. The crossover frequencies are respectively 169 kHz and 65kHz. These two cell populations can be separated based on their electrical properties at 100 kHz (vertical blue line). .... 88

Figure 2:9  $\epsilon_{eq}$ ,  $\epsilon_m$  and  $\epsilon_{mix}$  corresponding to respectively the equivalent relative permittivity of a HEK cell, the relative permittivity of the suspension medium and the equivalent relative permittivity of the suspension of HEK cells at a volume fraction  $\phi=0.3$  (implemented using the Hanai methodology).  $\sigma_m = 0.156$  S/m ..... 89

Figure 2:10  $\sigma_{eq}$ ,  $\sigma_m$  and  $\sigma_{mix}$  corresponding to respectively the equivalent electrical conductivity of a HEK cell, the electrical conductivity of the suspension medium and the equivalent electrical conductivity of the suspension of HEK cells at a volume fraction  $\phi=0.3$  (implemented using the Hanai methodology).  $\sigma_m = 0.156$  S/m ..... 89

Figure 2:11  $|\epsilon_{eq} * |/\epsilon_0$ ,  $|\epsilon_m * |/\epsilon_0$  and  $|\epsilon_{mix} * |/\epsilon_0$  corresponding to respectively the modulus of the equivalent complex relative permittivity of a HEK cell, the modulus of the complex relative permittivity of the medium and the modulus of the equivalent complex relative permittivity of the HEK cells in suspension in the medium at a volume fraction  $\phi=0.3$  (implemented using the Hanai methodology).  $\sigma_m = 0.156$  S/m ..... 90

Figure 2:12 Evolution of the crossover frequencies for a Jurkat cell for 50 conductivities logarithmically spaced between 1 mS/m and 0.5 S/m. .... 91

Figure 3:1 Real part of the Clausius-Mossotti factor for polystyrene beads in two media  $\sigma_m = 1.5$  S/m (blue dash dotted line) and  $\sigma_m = 0.156$  S/m (red line). The transition from nDEP to pDEP is represented by the black dotted line. At 10 kHz, polystyrene beads experience nDEP with the maximum amplitude in both media. Graph generated using MyDEP software (Cottet, et al. 2019a).. 98

Figure 3:2 Real part of the Clausius-Mossotti factor for a HEK cell in two media with  $\sigma m = 1.5$  S/m (blue dash dotted line) and  $\sigma m = 0.156$  S/m (red line). The transition from nDEP to pDEP is represented by the black dotted line. At 10 kHz, HEK cells experience nDEP with the maximum amplitude in both media. Graph generated using MyDEP software (Cottet, et al. 2019a)..... 99

Figure 3:3 Trapping design composed of 8 electrodes arranged in circle (dark gray rectangles). The fluidic inlet and outlet are respectively located at electrodes 1 and 5. All electrodes are separated from the trapping chamber by a 50  $\mu\text{m}$  recess. Scalebar 50  $\mu\text{m}$ ..... 100

Figure 3:4 Design principle of liquid electrodes located on the same side of a microchannel A) Coplanar electrodes located on dead-end side chambers are equivalent to B) 3D electrodes located in the sidewall of the central channel. C) Top view of the simplified representation of the liquid electrodes. A) B) and C are adapted from (Demierre 2008). D) Top and E) side view of the liquid electrodes located on both sides of the microchannel. D) and E) are adapted from (Shaker, et al. 2014)..... 101

Figure 3:5 A) COMSOL Multiphysics 2D simulation of the fluid velocity profile along the x axis, in  $\mu\text{m/s}$ , in the chip with an inlet velocity of 500  $\mu\text{m/s}$ . B) Flow velocity profile along y at the inlet (in blue), at  $x = -150$   $\mu\text{m}$  (in red) and in the center of the trapping chamber (in green)..... 103

Figure 3:6 A) 2D simulation of the electric potential in the chip. B) Evolution of  $|E|$  along the x axis. C) 2D simulation of the trapping position of a cell using 3 electrodes (4, 5 and 6) supplied with  $V=10$   $V_p$  at 10 kHz. The surface represents  $\partial E^2 \partial x$ . The white dot indicates the trapping position of a HEK cell (diameter 15  $\mu\text{m}$ ). D) Evolution of the DEP and drag forces along the AA' cut. The resulting force is represented with the black dashed line and the red dashed vertical line indicates the position where the resulting force is equal to zero. The gray dot with the arrow indicates the direction of the force on the particle. E) Side and Top F) 3D representations of the amplitudes of the DEP (in blue) and drag (in green) forces along the x axis in the chip. The white/red dashed line in F) indicates where the x component of two forces are equal in the

trapping chamber. The electrode numbers are indicated. A logarithmic scale is used for both representations.....	105
Figure 3:7 Evolution of the DEP and drag forces along the y axis at A) $x=0$ and B) $x=x_{\text{trap}}=24 \mu\text{m}$ . The resulting force is represented with the black dotted line and the red dotted line indicates the positions where the resulting force is equal to zero. The gray dot with the arrow indicates the direction of the force on the particle. C) Side and D) Top 3D representations of the amplitudes of the DEP (in blue) and drag (in green) forces along the y axis in the chip. The white/red dashed line in D) indicates where the x component of two forces are equal (from Figure 3:6 F) and the black cross the final position of the particle. The electrode numbers are indicated. A logarithmic scale is used for both representations. ....	106
Figure 4:1 Process flow for the PDMS mold fabrication (A to F), PDMS molding (G and H) and alignment with the glass chip (I). ....	115
Figure 4:2 Scanning Electron Microscope (SEM) images of A) a Si mold and B) a SOI mold. For sake of clarity, the oxide layer is artificially colored in blue. Scalebar $10 \mu\text{m}$ . ....	116
Figure 4:3 A) Exploded view of the sarcophagus for PDMS molding. B) Cross section of the sarcophagus during PDMS pouring. C) Cross section of the sarcophagus in curing position. ....	117
Figure 4:4 A) MJB4 mask aligner used in the alignment procedure and eyepiece view (insert). B) Scheme (cut view) and picture of the PDMS and chip before contact and C) after plasma bonding. ....	118
Figure 4:5 A) Fabricated chip with the PDMS slab bonded on the glass chip patterned with electrodes. B) Zoom in the DEP focusing region of the chip with an optical microscope. The channel was filled with a blue dye to make sure there was no leak. Scalebar $50 \mu\text{m}$ . C) Trapping design fabricated Scalebar $50 \mu\text{m}$ . ....	120
Figure 5:1 Experimental setup used for the trapping. A) PCB platform mounted on an inverted microscope (Leica) used to supply the chip with the centering and trapping voltages. B) Schematic representation of the system controlling	

by a computer with LabVIEW<sup>TM</sup> all the different instruments: the uEye camera for visualization, the pressure controller and two arbitrary function generators. DEP centering electrodes are used to center particles laterally and to provide a vertical lift. The grey areas corresponding to our impedance sensing unit are presented in the following chapter. .... 124

Figure 5:2 Illustration of the trapping of 8  $\mu\text{m}$  diameter polystyrene beads with 3 different configurations of the electrodes. Channel height 50  $\mu\text{m}$ , inlet and outlet width 50  $\mu\text{m}$ ,  $V = 22.5 V_p$  at  $f_{DEP} = 10 \text{ kHz}$ ,  $\sigma m = 0.156 \text{ S/m}$  and  $Q = 1 \mu\text{L/h}$ ..... 124

Figure 5:3 Evolution of the position of 8  $\mu\text{m}$  diameter polystyrene beads with the number of beads in the trapping chamber with 3 electrodes. The solution flows in the chip from left to right.  $V = 17.3 V_p$ ,  $f_{DEP} = 10 \text{ kHz}$ ,  $\sigma m = 0.156 \text{ S/m}$  and  $Q = 1 \mu\text{L/h}$ ..... 125

Figure 5:4: For configuration 3(a) Left: Simulated evolution of the position of a polystyrene bead with the diameter. Center: Experimental evolution of the position of the cluster with the increase of the number of beads.  $V = 17.3 V_p$ ,  $f_{DEP} = 10 \text{ kHz}$ ,  $\sigma m = 0.156 \text{ S/m}$  and  $Q = 1 \mu\text{L/h}$ . Right: Sketch of the design with the axis origin and the scale in  $\mu\text{m}$ . .... 125

Figure 5:5 Example of HEK cell aggregation under flow conditions using 3 electrodes. The time stamps are in the mm:ss format. Scalebar 50  $\mu\text{m}$ . A) Chip with only fluid inside. B) Cells reaching the trapping zone are stopped when the DEP force compensates the drag force. C) and D) The aggregate increased in size as more cells were reaching the trapping zone with 5 cells (C) and 8 cells and 1 arriving (D). Channel height 50  $\mu\text{m}$ , Inlet and Outlet width 50  $\mu\text{m}$ ,  $V = 22.5 V_p$  at  $f_{DEP} = 10 \text{ kHz}$ ,  $\sigma m = 0.156 \text{ S/m}$  and  $P_{in} = 2 \text{ mbar}$ . .... 126

Figure 5:6 Evolution of an HEK aggregate for different number of trapped cells with a 3-electrode configuration.  $V = 22.5 V_p$  at  $f_{DEP} = 10 \text{ kHz}$ ,  $\sigma m = 0.156 \text{ S/m}$ . The solution flows in the chip from left to right..... 127

Figure 5:7 Improved trapping design composed of 4 electrodes (dark gray rectangles) with 1 inlet/3 outlets located at electrodes 1 and 2/3/4 respectively

(Scalebar 50  $\mu\text{m}$ ). The trapping chamber is colored in yellow. Scalebar 100  $\mu\text{m}$ .

..... 128

Figure 5:8 A) COMSOL Multiphysics 2D simulation of the fluid velocity profile, in  $\mu\text{m/s}$ , in the improved chip design with an inlet velocity of 500  $\mu\text{m/s}$ . B) Flow velocity profile along  $y$  at the inlet (in blue), at  $x = -400 \mu\text{m}$  (in red), in the center of the trapping chamber at  $x = 0$  (in green) and after the trapping chamber at  $x = 400 \mu\text{m}$  (in black). ..... 129

Figure 5:9 A) 2D simulation of the electric potential in the chip. B) Evolution of  $|\mathbf{E}|$  along the  $x$  axis. C) 2D simulation of the trapping position of a cell using 3 electrodes supplied with  $V=10 V_p$  at 10 kHz. The surface represents  $\partial\mathbf{E}^2\partial x$ . The white dot indicates the trapping position,  $x_{trap}$ , of a HEK cell (diameter 15  $\mu\text{m}$ ). D) Evolution of the DEP and drag forces along the BB' cut. The resulting force is represented with the black dashed line and the red dashed vertical lines indicate the position where the resulting force is equal to zero. The gray dot with the arrow indicates the direction of the resulting force on the particle and the red dashed line between zones 1 and 2 the trapping position. E) Side and Top F) 3D representations of the amplitudes of the DEP (in blue) and drag (in green) forces along the  $y$  axis in the chip. The white/red dashed line in F) indicates where the  $x$  component of the two forces are equal in the trapping chamber. The electrode numbers are indicated. A logarithmic scale is used for both representations. .... 131

Figure 5:10 Evolution of the DEP and drag forces along the  $y$  axis at A)  $x=0$  and B)  $x=x_{trap}=17 \mu\text{m}$ . The resulting force is represented with the black dotted line and the red dotted line indicates the positions where the resulting force is equal to zero. The gray dot with the arrow indicates the direction of the force on the particle. C) Side and D) Top 3D representations of the amplitudes of the DEP (in blue) and drag (in green) forces along the  $y$  axis in the chip. The white/red dashed line in D) indicates where the  $x$  components of the two forces are equal (from Figure 5:9 F) and the white cross the final position of the particle. The electrode numbers are indicated. A logarithmic scale is used for both representations. .... 132

Figure 5:11 Experimental setup used for the trapping with the improved trapping design. A) PCB platform mounted on an inverted microscope (Leica) used to supply the chip with the centering and trapping voltages. A manual switch enables to activate a 4th electrode (number 1 in Figure 5:7) for compacting the aggregate. B) Schematic representation of the system with a computer controlling with LabVIEW<sup>TM</sup> all the different instruments as presented in Figure 5:1. The grey areas corresponding to our impedance sensing unit are presented in the following chapter. .... 133

Figure 5:12 Example of HEK cell aggregation in flow using the 3 electrodes on the right. The time stamps are in the mm:ss format. Scalebar 100  $\mu\text{m}$ . A) Chip with only fluid inside. B) Arrival of the first cell in the trapping chamber. C) 10 cells are trapped under flow conditions, forming a line, while more cells arrive (4 then 3 cells arriving). D) DEP voltage and inlet pressure are reduced to  $V_f$  and  $P_f$  to prevent more cells to reach the 21 cells located in the trapping zone. E) The 4<sup>th</sup> electrode (located on the left) is activated leading to the centering of the cell aggregate. The DEP force is also increased back to  $V_{trap}$  to compact the aggregate. F) After 5 min, the aggregate is more compact. G) The DEP force is cancelled and the inlet pressure increased to  $P_{release}$  to help the formed aggregate to leave the trapping chamber. H) No cell separation is observed in a narrower meander (width 40  $\mu\text{m}$ ) located after the trapping chamber. Channel height 50  $\mu\text{m}$ ,  $V_{trap} = 15 V_p$  for the trapping and the compacting and  $V_f = 5 V_p$  when the flow is reduced (both at  $f = 10 \text{ kHz}$ ),  $\sigma_m = 0.156 \text{ S/m}$ ,  $P_{trap} = 2 \text{ mbar}$ ,  $P_f = 1 \text{ mbar}$  and  $P_{release} = 2 \text{ mbar}$ . .... 134

Figure 6:1 A a) Principle of differential impedance sensing with coplanar electrodes with b) the corresponding differential impedance signal. B a) Electrical equivalent circuit with b) the corresponding SPICE simulated complex impedance for a 10  $\mu\text{m}$  diameter cell. All schematics are adapted from (Gawad, et al. 2001). .... 139

Figure 6:2 Principle of the facing electrode design. Adapted from (Cheung, et al. 2005). .... 140



Figure 6:3 Comparison between two electrode layouts. A) Conventional layout composed of the 3 electrodes. B) Improved design proposed by Clausen. Adapted from (Clausen, et al. 2014). ..... 141

Figure 6:4 Top view and 3D view of A) the conventional design and B) the conceptual design.  $lel = 50 \mu m$ ,  $h = 50 \mu m$  and  $w = 50 \mu m$  are kept constant.  $a$ ,  $b$ ,  $d$ ,  $del$  and  $wel$  are the parameters to optimize. Electrodes are represented in blue. .... 143

Figure 6:5 Simulation of the evolution of the current variation with the inter-electrode distance  $d_{el}$  due to an  $8 \mu m$  diameter polystyrene bead located at  $x = 0 \mu m$ ,  $y = 0 \mu m$  and  $z = h/2 = 25 \mu m$  for  $w = wel = 50 \mu m$ . ..... 145

Figure 6:6 Simulation of the current variation due to an  $8 \mu m$  diameter polystyrene bead located at  $x = 0 \mu m$ ,  $y = 0 \mu m$ ,  $z = h/2 = 25 \mu m$ . Evolution with  $wel$  for (a)  $del = d = 50 \mu m$  and (b)  $del = 150 \mu m$  with  $a = 50 \mu m$ ,  $b = 0 \mu m$ ,  $d = 50 \mu m$ . Evolution with  $b$  for (c)  $del = 50 \mu m$  for  $wel = 90 \mu m$ ,  $a = 5 \mu m$ ,  $d = del - 2 * (a + b) = 40 - 2b$  and (d)  $del = 150 \mu m$  for  $w = 50 \mu m$ ,  $wel = 140 \mu m$ ,  $d = 50 \mu m$ ,  $a = (d - ddel)/2 - b = 50 - b$ . Fitted curves are displayed in red. 146

Figure 6:7 Simulation of the current variation due to an  $8 \mu m$  diameter polystyrene bead located at ( $y = 0 \mu m$ ,  $z = h/2 = 25 \mu m$ ). Evolution with the  $x$  position in the microchannel for the 4 designs: Short Optimized (SO), Short Conventional (SC), Long Optimized (LO) and Long Conventional (LC). The red cross indicates the point ( $x=0$ ,  $y=0$ ) on each design. .... 148

Figure 6:8 Simulation of the current variation due to an  $8 \mu m$  diameter polystyrene bead for the 4 designs. Evolution with (a) the  $y$  position in the microchannel (located at  $x = 0 \mu m$ ,  $z = h/2 = 25 \mu m$ ) and with (b) the  $z$  position in the microchannel (located at  $x = 0 \mu m$ ,  $y = 0 \mu m$ ). The red vertical dotted line represents the position of the particle in the center ( $x = 0 \mu m$ ,  $y = 0 \mu m$  and  $z = 25 \mu m$ )..... 149

Figure 6:9 Simulation of the current variation due to an  $8 \mu m$  diameter polystyrene bead. Evolution with the  $x$  position in the microchannel (located at  $y = 0 \mu m$ ) at different heights for the 4 designs: (A) SC (B) SO (C) LC (D) LO. Electrode positions (in black) are indicated under each graph..... 150

Figure 6:10 Photographs of the different designs (a) SC (b) SO (c) LC (d) LO. Scalebar 50 $\mu\text{m}$ . Ti/Pt Electrodes are visible as black stripes.....	151
Figure 6:11 Schematic representation of the system with a photograph of the chip showing 3 designs. Scalebar 100 $\mu\text{m}$ .....	152
Figure 6:12 Experimental data showing the evolution with time of the average current variation for each design with $\pm 2$ times the standard deviation ( $n \geq 8$ ) due to an 8 $\mu\text{m}$ diameter polystyrene bead in the microchannel for the 4 designs. Measurements were performed for the 4 designs at a flow rate of 10 $\mu\text{l/h}$ (particle speed in the order of 1000 $\mu\text{m/s}$ ).....	153
Figure 6:13 Full chip fabricated version with the DEP centering electrodes A) with and B) without the auxiliary outlets) and two LO designs located before and after the improved trapping chamber. Scalebar 100 $\mu\text{m}$ .....	156
Figure 6:14 Schematic representation of the experimental setup with a computer controlling with LabVIEW™ all the different instruments: the uEye camera for visualization, the pressure controller, and HF2LI and HF2TA from Zurich Instruments and two arbitrary function generators. DEP centering electrodes are used to center particles laterally and to provide a vertical lift.....	157
Figure 6:15 Snapshots of live HEK cells trapping with the improved trapping design without auxiliary outlets and detection with the LO design at (a) $t = 40.4$ s (b) $t = 57$ s (c) $t = 63$ s and (d) $t = 91$ s. $V_{\text{trap}} = 22.5 V_p$ at $f_{\text{DEP}} = 10$ kHz for the trapping and centering, $V_{\text{IS}} = 0.8 V_p$ at $f_{\text{IS}} = 500$ kHz for the impedance sensing with the LO design, no centering voltage was applied, $\sigma m = 0.156$ S/m and $P = 2$ mbar. ....	158
Figure 7:1 Proposal for creating composite aggregates. Scalebar 100 $\mu\text{m}$ . ....	166
Figure 7:2 Design proposal of a chip combining cell centering, cell trapping and impedance sensing. Scalebar 100 $\mu\text{m}$ . ....	166
Figure S B:1 COMSOL Multiphysics location to change the equation used for dielectrophoresis to implement the single-shell model with $C_{\text{cm}}$ and $G_{\text{cm}}$ ...	192
Figure S B:2 Graphs for all the tested trapping configurations.....	194

Figure S C:1 A) Custom-made steel chuck with magnets for positioning. B) Positioning of the glass chip at the center of the custom-made chuck. C) Positioning on the opposite corner of the chip of the two magnets. D) Positioning of the PDMS slab on the glass mask. E) Retrieval of the bonded chip with tweezers. F) Chip filled with blue ink: no leakage is visible. ....	202
Figure S D:1 Mesh used for the optimization simulations in this study, presented on the conceptual design.....	207
Figure S D:2 Mesh convergence study for a Long Conventional (LC) design with an 8 $\mu\text{m}$ diameter polystyrene bead located at $x = 0 \mu\text{m}$ , $y = 0 \mu\text{m}$ , and $z = h/2 = 25 \mu\text{m}$ . Evolution of the current between the two electrodes with the maximum size of the elements (ES) using a Swept Mesh on all the design. .	208
Figure S D:3 Mesh convergence study for a Long Conventional (LC) design with an 8 $\mu\text{m}$ diameter polystyrene bead located at $x = 0 \mu\text{m}$ , $y = 0 \mu\text{m}$ , and $z = h/2 = 25 \mu\text{m}$ . Evolution of the current between the two electrodes with the maximum size of the free tetrahedral elements (ES) (the central part of the design is meshed with the swept mesh with 2 $\mu\text{m}$ as the Maximum Element Size).....	208
Figure S D:4 Evolution of the current with time for a SO design. (A) and (C) Raw data after acquisition (B) and (D) Processed signal after application of a moving average filter and a Savitzky-Golay filter and normalization of the value. Peaks are detected and marked with the red dots. ....	209
Figure S D:5 Figure S D:6 Current density line plot in the plane $x = 0$ for the four designs (A) SC (B) SO (C) LC (D) LO .....	210
Figure S D:7 Evolution of the current variation with the longitudinal misalignment for (A) the SO and (B) LO designs. ....	211
Figure S D:8 Simulation of the current variation due to a 30 $\mu\text{m}$ diameter polystyrene bead with the LO design. Evolution with the x position in the microchannel (located at $y = 0 \mu\text{m}$ ) at 3 different heights ( $z = 16 \mu\text{m}$ , $z = 25 \mu\text{m}$ and $z = 34 \mu\text{m}$ ). Electrode positions (in black) are indicated under the graph.....	212





## List of Tables

Table 1 Trapping result for each configuration of the electrodes tested in simulation. The trapping position is indicated with a number corresponding to the center of the particle of by a cross if the particle is not trapped. ....	104
Table 2 Geometrical parameters used for each design, optimized parameters values are in bold. (*) indicates that the value was chosen but not optimized. ....	147
Table 3 Comparison of the simulated influence of the different diameters of polystyrene beads (located at $x = 0 \mu\text{m}$ , $y = 0 \mu\text{m}$ , and $z = h/2 = 25 \mu\text{m}$ ) on the current variation for a Long Optimized (LO) design for two different electrical conductivities of the medium ( $\sigma_m = 1.6 \text{ S/m}$ and $\sigma_m = 0.16 \text{ S/m}$ ). ....	155



## Abbreviations

BSA	Bovine Serum Albumin
CAD	Computer-Aided Design
DEP	Dielectrophoresis
DEP-FFF	Dielectrophoresis Field-Flow Fractionation
DFC	Dielectric Field Cage
DMEM	Dulbecco's Modified Eagle Medium
DNA	Deoxyribonucleic Acid
ECT	Electrochemotherapy
EGT	Electrogenetherapy
EHD	Electrohydrodynamics
EIFC	Electrical Impedance Flow Cytometry
EP	Electroporation
FBS	Fetal Bovine Serum
FEM	Finite Element Method
HEK	Human Embryonic Kidney
IBE	Ion Beam Etching
iDEP	Insulating Dielectrophoresis
IRE	Irreversible Electroporation
IS	Impedance Spectroscopy
ITO	Indium Tin Oxide
LOC	Lab On Chip



PBS	Phosphate-Buffered Saline
PCB	Printed Circuit Board
PDMS	Polydimethylsiloxane
PEG	Polyethylene Glycol
PFOTS	Trichloro(1H,1H,2H,2H-perfluorooctyl)silane
PMMA	Poly(methyl methacrylate)
POC	Point Of Care
PS	Penicillin Streptomycin
RBC	Red Blood Cell
RNA	Ribonucleic Acid
ROT	Electrorotation
SAW	Surface Acoustic Wave
SEM	Scanning Electron Microscope
Si	Silicon
SNR	Signal to Noise Ratio
SOI	Silicon-On-Insulator
TSA	Top Side Alignment
TWD	Travelling-Wave Dielectrophoresis
WEC	Wedge Error Compensation
$\mu$ TAS	Micro Total Analysis System

# Introduction

Our today life is governed by the use of electromagnetic fields for various applications such as communication, transport, cooking, etc. Yet the impact of electromagnetic fields on the human body is still an important field of research. Due to the complex structure of human beings, mathematical models are still in development to better understand the impact of electromagnetic fields on living matter. Involuntary exposition to an intense electric field might lead to detrimental consequences but using an electric field in a controlled way can be beneficial in, for example, the biomedical field with applications for diagnostics as well as for cancer treatment. However, this implies to understand the interaction between electromagnetic fields and the living which requires to first know the field values at the cellular and tissue level while they are generated at the macroscopic scale and second to know the dielectric properties of cells and how they are modified in tissues and then in organs and inversely.

Nowadays the emergence of the field of microfluidics, the handling of small amounts of liquids in fluid channels in the order of the  $\mu\text{m}$ , has opened new ways to study the dielectric properties of cells with the development of different strategies using electric field to characterize cells such as electrorotation and impedance spectroscopy. In electrorotation, a rotating electric field leads cells to rotate at different speeds and directions of rotation. In impedance spectroscopy, the electric current flowing between two electrodes is modified by cells located in-between and this modification is frequency dependent. Both the rotation and impedance spectra can be analyzed to characterize single cells and retrieve their dielectric properties since the obtained signals depend on those properties. For example, at low frequency, the cell membrane behaves as an

insulator with a capacitive effect which no longer exists as the frequency increases and the interior of the cell becomes accessible to the electric current.

For most applications, analyses of isolated cells are no longer sufficient and more complex structures such as 3D multicellular constructs shall be created and characterized. However, those analyses are more difficult to perform when the analyzed objects become multicellular. The properties of the individual cells are often unknown and the variability in size and composition of the analyzed multicellular construct might limit the characterization and its applicability to further formulate theoretical models. Multicellular constructs offer new ways to get quantitative modeling of biological systems as they enable to take cell-cell contacts and interactions into account. The underlying question is then to understand how to relate the dielectric properties of single cells and cell aggregates.

The first step is to be able to reproducibly create such 3D cell aggregates of controlled size and properties before characterization. Such technique is today still missing. In this thesis, we propose to use the electric field to construct those 3D cell aggregates based on the dielectric properties of single cells and their suspension medium, a technique called dielectrophoresis, abbreviated DEP. Negative DEP offers the possibility to selectively trap cells and confine them far from the electric field maxima. Combining DEP with flow conditions, we propose a geometry of a microfluidic chip based on an arrangement of microelectrodes to create cell aggregates of controlled size. The addition of impedance sensors in the chip before and after the “trapping chamber” (where aggregation takes place) would allow to characterize the properties of both single cells and created cell aggregates.

### **Thesis layout**

The objective of this thesis is to design a microfluidic device for the controlled formation of cell aggregates using dielectrophoresis under flow conditions. The manuscript is structured as follows:

## Introduction

Chapter 1 presents the need for 3D cell aggregates of controlled properties. An overview of 3D cell aggregates formation methods and the trapping designs with dielectrophoresis is presented. Lastly, the requirements to build a platform to create controlled-3D cell aggregates under flow conditions is presented.

Chapter 2 presents an overview of the theories behind dielectrophoresis and dielectric modeling of single cell and cell aggregates. MyDEP, our computational tool for dielectric modeling of particles and cells, is presented.

Chapter 3 presents important parameters in DEP trapping of particles and cells. The physics of the trapping is discussed as well as the effects of electric fields on cells. A microfluidic chip geometry is proposed and COMSOL Multiphysics simulations are used to predict the position of the trapped particles.

Chapter 4 describes the reproducible method we developed for the chip fabrication, involving  $\mu\text{m}$  precision alignment of PDMS microchannels with coplanar electrodes using a conventional mask aligner.

Chapter 5 presents the experimental trapping results obtained for particles and cells. An improved version of the trapping design is proposed as well as a setup automation.

Chapter 6 describes a comprehensive analysis of the geometrical parameters influencing the sensitivity of a coplanar electrode layout for electrical impedance flow cytometry. Two improved designs for impedance sensing are proposed.

Chapter 7 reports the conclusions obtained from the trapping experiments and proposes an outlook of this thesis.



# Chapter 1 State of the art

This chapter presents how biology moved from single cells analysis to multicellular constructs experiments and the need for 3D cell aggregates of controlled properties. An overview of 3D cell aggregates formation methods and of existing trapping designs based on dielectrophoresis is presented. Lastly, the requirements to build a platform to create controlled-3D cell aggregates under flow conditions is presented.

## 1.1 From single cell to cell aggregates

Cells were first observed and named by Robert Hooke in 1665 (Hooke 1665). Using a microscope lens, he was able to distinguish the cellular structure of plants in a section of cork. Since then cells have been intensively studied and are still considered as the basic unit of life. Cells have been grown in bulk but, even though it can provide good statistics on the cell population response, the risk of observing an “average cell”, not representative of either subpopulation, exists (Levsky and Singer 2003). Even though cells may have the same morphology and genes, they are heterogeneous in their response (Altschuler and Wu 2010). To overcome those limitations, scientists developed some analysis methods and tools to study single cells. Fluorescence Activated Cell Sorting (FACS), which enables to sort cells based on fluorescent labelling, is widely recognized as the gold standard technique for single cell analysis.

Single cell analysis offers the possibility to see cell-to-cell variations within a cell population. It offers the possibility to study rare cells or events as well as precious samples (Narayanamurthy, et al. 2017). Protein levels and gene expressions for each cell can be studied to reduce the biological noise (Wang and Bodovitz 2010). They have been used in various fields such as disease studies, drug discoveries and development (Heath, et al. 2016), stem cell differentiation (Llorens-Bobadilla, et al. 2015), cancer (Gorges, et al. 2016), embryos and adults physiological functions. Thanks to those studies, many discoveries have been made. Properties such as cell size and shape can be related to the physiological state. More generally cells assays are often providing meaningful responses with a higher throughput than costly animal testing and without ethical considerations. Animal experiments are also limited and can lead to high failure rates in clinical trials since they do not predict well all the parameters for humans such as liver toxicity (Sivaraman, et al. 2005). Single-cell analysis has also been used for example to prove that human embryonic stem cells have heterogeneous genetic expression (Zhong, et al. 2008). However, studying single cells on their own does not allow to understand how cells influence each other in terms of mechanical and biochemical signaling.

2D cell structures allow cells to be in contact with neighboring cells. Cell culture techniques are usually easy to handle, maintain reproducibility in cell growth and consistency over passages (Butler 2004). They often provide significant advantages in drug discoveries such as reducing time and cost for screening. Cell observation are also possible with a conventional microscope with one focal plane. Cells cultivated with conventional culture techniques such as monolayers might, however, lose their phenotypic properties (Benya and Shaffer 1982). Furthermore, 2D cell culture conditions are very different from the native environment of cells where they are exposed to specific 3D features with specific mechanical and dynamics properties of the extracellular matrix (ECM) (Tan, et al. 2003), signaling molecules and cell-cell interactions. The value of 2D cell culture is also limited to predict clinical response as the conditions form a limited model of the in-vivo microenvironment (Marx and Sandig 2006).

Cells are moreover often in contact with a substrate that may differ dramatically from their original environment. Nowadays scientists are trying to understand how cell-cell interactions and tissue structure might influence cell response. Cellular models should now mimic the functions of living tissues hence the 3D structures are overseen to bring a better modeling than 2D ones. They proved their abilities to restore cell phenotypes (Benya and Shaffer 1982) and cells present more resistance to external molecules like cytotoxic agents (Torisawa, et al. 2005). 3D models are more fitted to get quantitative modeling of biological systems (Pampaloni, et al. 2007). For the case of tumors, 3D cell constructs help to mimic in vivo-like conditions and similar drug sensitivity patterns can be observed (Torisawa, et al. 2005).

Performing single cell analysis up to the creation of 3D organoids was enabled by the use of microfluidics, the handling of small amounts of liquids in fluid channels in the order of the  $\mu\text{m}$ . At this scale, cells can be handled individually and moved in the device directly with the fluid or in combination with a vast majority of forces. The use of miniaturization and more specifically microfluidics allowed to increase the throughput by parallelizing analysis and to reduce the



quantity of reagents and the cost associated as well as human error via automation.

However, 3D cell cultures are more complex to operate, and the generated 3D structures require more expensive methods to be observed and characterized such as confocal microscopy and Z-stack images.

The created 3D models proved their usefulness in a variety of applications.

## **1.2 Different fields of application of 3D aggregates and need of an intermediary model**

### **1.2.1 In-vitro therapeutic screening**

3D aggregates are regarded as a more representative model than 2D cell cultures on which to perform in vitro drug screening (Zanoni, et al. 2016). Furthermore, spheroids present characteristics that are often found in tumor such as nutrient and oxygen gradient, extracellular matrix and cell interconnections (Santini, et al. 2000). Multicellular heterospheroids have been used by Nakamura et al. (Nakamura, et al. 1999) to understand the formation and growth of cancer masses. Spheroids, however, do not have any vascularization.

### **1.2.2 Electroporation**

Electroporation (EP) is the name used to describe the increase of the permeability of a cell membrane following the application of a certain number of short and intense electric pulses as presented in Figure 1:1 A) (Calvet and Mir 2016). In 1968, Sale and Hamilton used an electric field to lyse red blood cells and protoplasts and proved that the electric field could enable the release of big molecules by the cells (Sale and Hamilton 1968). The insertion of DNA molecules in mouse lymphoma cells was performed 15 years later by Neumann and collaborators (Neumann, et al. 1982). Today electroporating cells is a technique routinely used in laboratories for transfecting cells (Sambrook and Russell 2006). Three variations of electroporation in the biomedical field are usually distinguished:

- Electrochemotherapy or ECT corresponds to the application of electroporation in combination with the injection of a cytotoxic drug (bleomycin and cisplatin (Breton and Mir 2012, Escoffre and Rols 2012)) which is poorly membrane-permeant as presented in Figure 1:1 B). Both drugs create DNA lesions (both single-strand and double-strand DNA breaks for bleomycin and formation of inter and intra DNA crosslinks for cisplatin) that lead to cell death upon cell divisions. Only the cells located in the volume exposed to electroporation which are in division, hence mostly the cancer cells, are killed by this method. By injecting the drug directly into the tumor before application of the EP, ECT allows to reduce the drug dose compared to classical chemotherapy protocols.
- Electrogenetherapy or EGT corresponds to the transfer of DNA into the cells via an electroporation delivery. In this two steps process, the cells are first permeabilized with short and intense electric pulses and second the DNA molecules are driven electrophoretically into the cell with long and low-voltage electric pulses as presented in Figure 1:1 C). The transmembrane transport mechanism is still debated (Cervia and Yuan 2018).
- Irreversible electroporation or IRE corresponds to excessive electroporation (too many, too intense or too long pulses) that triggers cell death as presented in Figure 1:1 D). This technique is, however, not selective, both tumor and normal cells being affected.

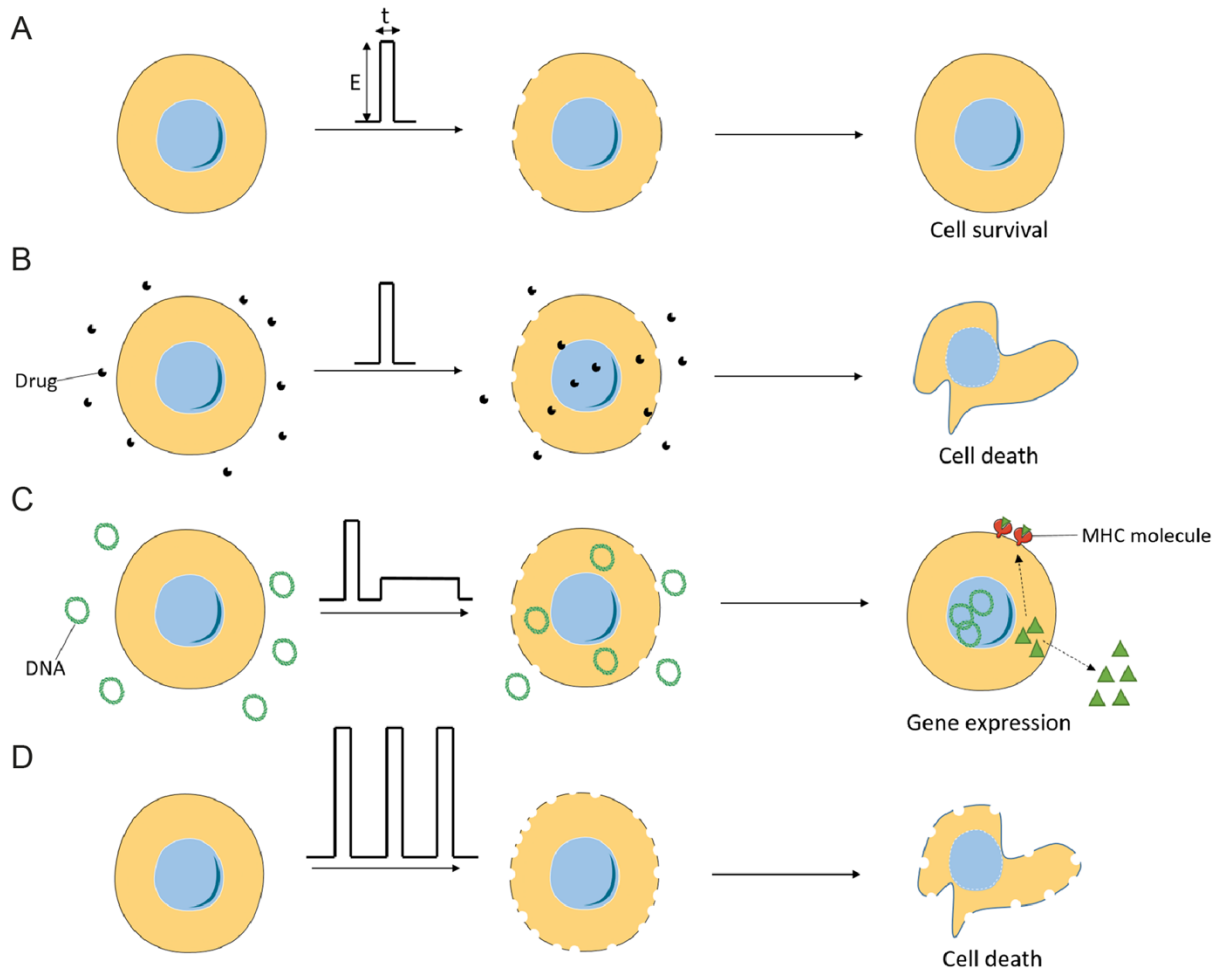


Figure 1:1 Principle of application of electroporation in the biomedical field. A) General reversible electroporation principle. B) Electrochemotherapy. C) Electrogenotherapy. D) Irreversible electroporation. Figures adapted from (Calvet and Mir 2016).

In both electrochemotherapy and electrogenotherapy, cells should survive the electroporation process. This means that the electroporation parameters should be carefully chosen in order to avoid excessive electroporation. In the body, the environment of each tumor is different, and the electroporation parameters (e.g. pulse duration and intensity, number of pulses, etc) should be chosen according to the tumor size, the degree of vascularization, fibrosis, and necrosis, otherwise the treatment might result in suboptimal transfer of the material (gene, drug) in the cell (Marty, et al. 2006, Mir, et al. 2006). The tissue heterogeneity, in particular the proximity of blood vessels, will affect the distribution of the electric field and reduce its amplitude (Golberg, et al. 2015).

More recently Brown et al (Brown, et al. 2018) have developed a device combining electroporation and electrical impedance spectroscopy. Between each

pulse, the tissue is analyzed, and the electroporation parameters are modified accordingly thanks to a feedback-controlled loop. Electrorotation has also been used to monitor the dielectric properties of spheroid during permeabilization (Trainito, et al. 2016).

Microfluidic devices have been proven to be more efficient for electroporation than the bulk-electroporation (Fox, et al. 2006, Valero, et al. 2008).

The success rate of gene transfer via electrogenetherapy is highly dependent on the type of tissue. For example, muscle tissue (Dona, et al. 2003) is more easily transfected than tumors (Rols, et al. 1998). Chopinet et al. (Chopinet, et al. 2012) proposed to use a specific type of cell aggregates called multicellular tumor spheroids to study the electrotransfer of DNA molecules. Originally proposed by Sutherland (Sutherland 1988), a spheroid can make a good model to reproduce the tumor structure in vitro compared to cell suspensions. They have been used in the study and optimization of many gene transfection techniques (Gil-Cardeza, et al. 2010, Lobjois, et al. 2009, Madsen, et al. 2006, Mellor, et al. 2006). Their preparation is based on the hanging drop method. Even when EGT is optimized on cell culture, its efficiency is reduced on 3D (Chopinet, et al. 2012). Thus, 3D aggregates might be an interesting model to understand and to improve ECT and EGT.

### **1.2.3 Understanding the dielectric properties of naturally formed aggregates**

Biological cells are commonly observed individually or as part of a suspension. In both cases the properties of the single cell play a crucial role in the observed dielectric properties. Cells, especially adherent cells, often do not stay separated in the suspension but tend to form more compact structures like aggregates. The aggregate properties such as its size, shape and compactness can vary depending on the original properties of the suspension. Often seen as a side product, such aggregates can be used to understand how the properties of a cell assembly differ from those of single cells. Cells aggregates can help to understand the dielectric properties modification in processes such as mitosis, cell contacting as well as cell connection by gap junctions.

In the case of mitosis, a mother cell dividing two daughter cells, cells are in direct contact joined by a narrow neck (Asami, et al. 1998, Asami, et al. 1999, Asami, et al. 2000). Similarly, gap junctions serving as passageways for ions and small molecules between cytoplasms of contiguous cells, may influence the low frequency dispersion observed in liver (Gersing 1998) and heart (Schaefer, et al. 2002).

Another example of such modifications of cell properties is the significant change in the dielectric dispersion of human blood when erythrocytes form a disk-like shape stack called “rouleau formation” as found by Irimajiri (Irimajiri, et al. 1996). Raicu et al. have shown that the organization of the liver cells into hepatic plates can be approximated by cells tightly packed into an aggregate (Raicu, et al. 1998). Most attempts to simulate the dielectric properties of cell assemblies are unconvincing due to the difficulty to model the hierarchical organization of biological tissues in all its complexity. The development of experimental approaches enabling to relate the properties of single cells to that of controlled cell assemblies is therefore of great interest.

### **1.3 Type of cell aggregates: terminology**

Depending on the literature found, different terms can be used to designate a structure composed of cells such as cell cluster, cell aggregate, spheroid, mammosphere, micromass, organoid or microfabricated tissues. They can be grown directly by cell-cell contact, on a 3D scaffold material (Moroni, et al. 2008) or embedded in gels (Slaughter, et al. 2009).

Among the possible terms, aggregates and clusters are more generic terms, not only related to cells. Clusters is often seen as a temporary structure while aggregates are more permanent structures.

Mammosphere was used by Dontu et al. (Dontu, et al. 2003) to name spherical colonies of human mammary epithelial cells cultivated on non-adherent surfaces in the presence of growth factors.

Micromass refers to a cell aggregate of chondroncytic cells (Greco, et al. 2011).

Spheroid are aggregates of non-substrate-adherent cells that mutually adhere to each other forming a sphere-like shape (Fennema, et al. 2013). Multicellular tumor spheroids or tumorspheres were first described by Sutherland by culturing cancer cell lines under non-adherent conditions (Sutherland, et al. 1971).

Embryoid body are 3D aggregates of pluripotent stem cells that are undergoing the initial developmental specification.

Organoids corresponds to an assembly of stem cells or adult cells that organize to mimic human physiology and diseases in vitro. A definition of an organoid was proposed by Lancaster et al. (Lancaster and Knoblich 2014) as:

“A collection of organ-specific cell types that develops from stem cells or organ progenitors and self-organizes through cell sorting and spatially restricted lineage commitment in a manner similar to in vivo.”

An organoid, as the name states, implies that the formed structure should resemble an organ. To fit such requirement, they proposed three conditions:

- “Should be composed of multiple organ specific cell types,
- Be capable of recapitulating some specific function of the organ (eg. excretion, filtration, neural activity and contraction)
- Grouped together and spatially organized similar to an organ”.

Microfabricated tissues are spatial arrangements of tissue components with similar tissue architectures and functions (Rivron, et al. 2009).

As stated by Sebastian et al. (Sebastian, et al. 2006), understanding the response to signals between different cell types is of paramount importance and is limited by our ability to generate those 3D structures with different cell types.

## 1.4 Creation methods of 3D aggregates

Several techniques have been developed to create 3D multicellular structures. They can be divided in two categories: contact and non-contact (Rodriguez-Devora, et al. 2011). Contact methods usually rely on the direct contact with a

surface. In the case of non-contact methods, cells can be moved with an additional force.

#### **1.4.1 Contact methods**

##### ***1.4.1.1 Micromolding***

Micromolding methods use molds, generally fabricated through either soft photolithography or rapid prototyping, where cells are seeded (Güven, et al. 2015). Using non-adhesive molds such as agarose based, cells self-assemble into 3D constructs with high cell density (Napolitano, et al. 2007a, Napolitano, et al. 2007b). The viability of such aggregates can be up to several weeks.

##### ***1.4.1.2 Liquid overlay***

In this technique, a cell suspension is seeded in agarose-covered dishes (Carlsson and Yuhas 1984). Cells are let with medium for several days before inspection. Then, if the cells aggregated as sphere, spherical aggregates are sorted for the experiments. This solution is suited for mass production of aggregates but offers little control of the size of the aggregates.

##### ***1.4.1.3 Hanging drop culture method***

In this method, cells in pipetted droplets are concentrated by gravity at the liquid-air interface when the plate is inverted (Kelm, et al. 2003). They form aggregates and, after 1 day, spheroids are composed of the original cells pipetted in the droplet. This technique can be easily parallelized in 96 and 384-well plates (Hsiao, et al. 2012, Tung, et al. 2011) which are commercially available.

##### ***1.4.1.4 Rotary cell culture system:***

This technique was originally developed at NASA to study cell tissues in microgravity (Ingram, et al. 1997). The system is based on clinorotation, the nullification of the gravity force by slow rotation of the system about one or two axes. A single cell suspension is placed in a rotating chamber. As cells aggregate are formed, the rotating speed is gradually increased to avoid sedimentation.

#### ***1.4.1.5 Pellet culture system***

In this method, cells are placed in an Eppendorf tube and centrifugated to form one pellet spheroid per tube (Johnstone, et al. 1998).

#### ***1.4.1.6 Bioprinting***

Bioprinting is defined as “the use of computer-aided transfer processes for patterning and assembling living and non-living materials with a prescribed 2D or 3D organization in order to produce bio-engineered structures serving in regenerative medicine, pharmacokinetic and basic cell biology studies” (Guillemot, et al. 2010). It corresponds to the biomedical application of additive manufacturing where living cells and biomaterials are simultaneously “written” layer by layer to fabricate structures mimicking living tissues (Dababneh and Ozbolat 2014). The printing systems can be divided in three categories: laser-, extrusion and inkjet-based printing systems as presented in Figure 1:2.

Bioprinting has been used to deposit cells and also cell aggregates on a surface or in contact with a 3D matrix and will further aggregate and self-organize in a final tissue construct (Mironov, et al. 2003).



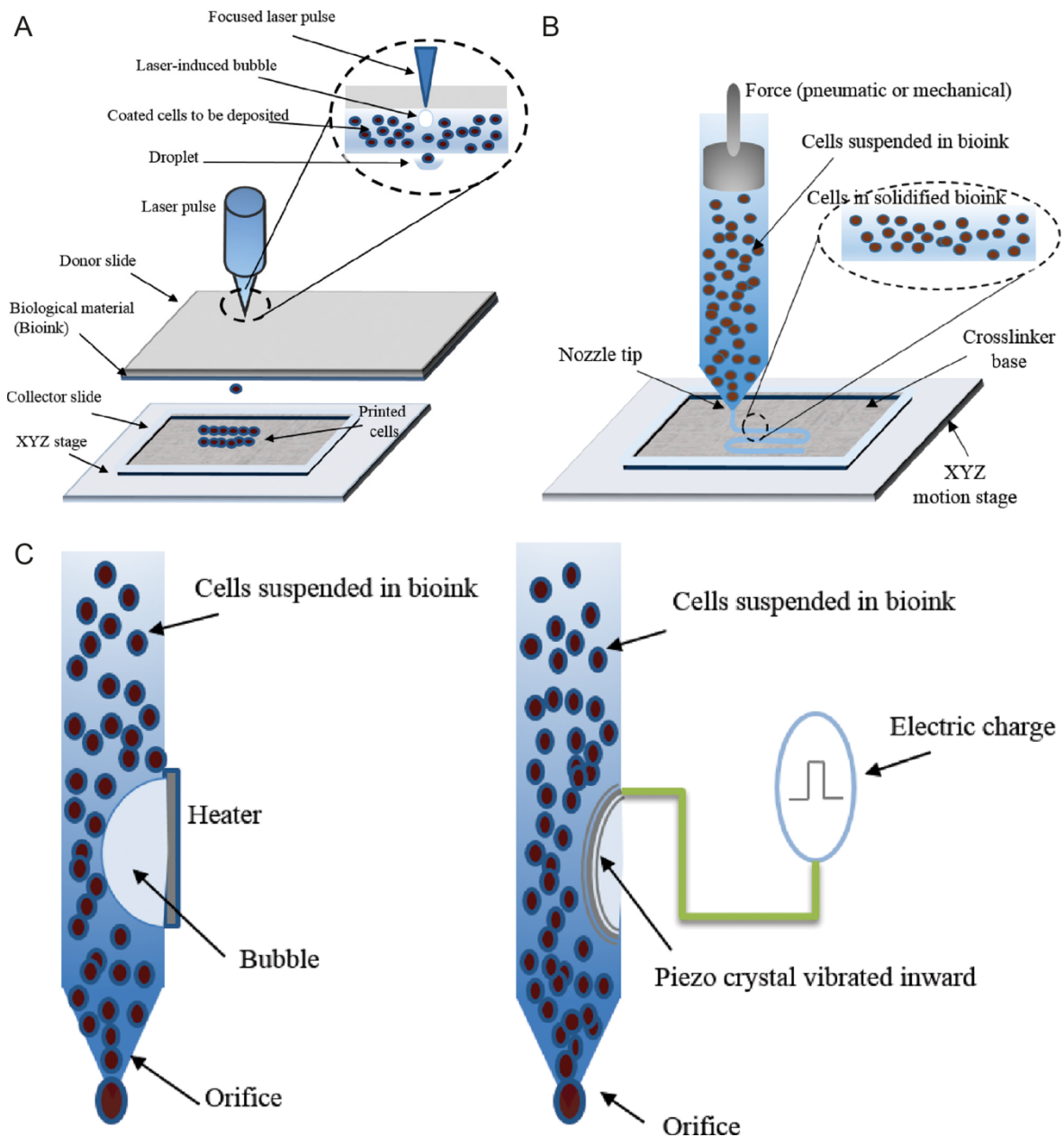


Figure 1:2 Bioprinting techniques. A) Schematic of laser-based bioprinting. B) Schematic of extrusion-based bioprinting. C) Schematic of (Left) thermal and (Right) piezoelectric-based inkjet bioprinting. All schematics are adapted from (Dababneh and Ozbolat 2014).

#### 1.4.1.7 Conclusion on the contact methods

With all the described methods the properties of this formed aggregate are, however, not fully controlled and depend on the initial volume of liquid and cells dispensed in the drop.

#### 1.4.2 Non-Contact methods

More recently the non-contact methods have become increasingly popular since the force used can offer more control on the formation of the cell aggregates.

Such methods are relying on magnetophoresis, acoustophoresis, optical trapping and dielectrophoresis.

#### 1.4.2.1 *Magnetic levitation method*

Magnetic levitation requires the cellular uptake of magnetic nanoparticles to confer cells magnetic responsiveness (Haisler, et al. 2013). Then cells can be further concentrated and levitated with an external magnetic field to form 3D cell aggregates (Souza, et al. 2010). This method requires the use of a label (magnetic nanoparticles) to operate.

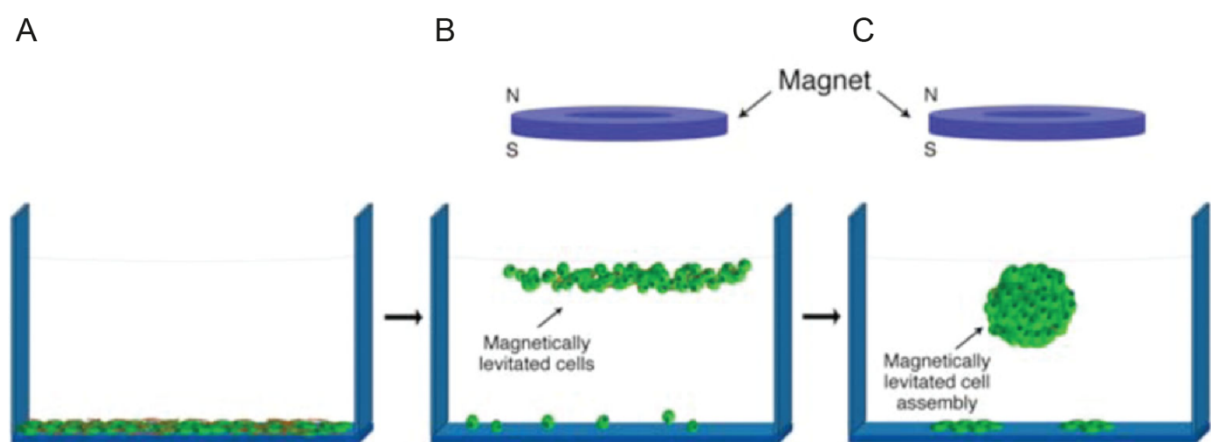


Figure 1:3 Principle of magnetic cell levitation. A) Cells are put in contact with magnetic nanoparticles and incubated. The remaining particles are later washed away. B) After the application of an external magnetic field with a magnet, cells are levitating. C) After 12h, characteristic structures are formed. Illustrations adapted from (Souza, et al. 2010).

#### 1.4.2.2 *Acoustophoresis*

Acoustic tweezers are using surface acoustic waves (SAW) generated by interdigitated electrodes to manipulate particles as illustrated in Figure 1:4. When the acoustic field is activated, particles are pushed from the antinode to the static node where they can be positioned and, shall several particles be located in the area, aggregate. The vertical position of the particle can be tuned by adjusting the input acoustic power (Guo, et al. 2016) as well as the position of the node by adjusting the relative phase angle between each interdigitated electrode. This method is label-free.

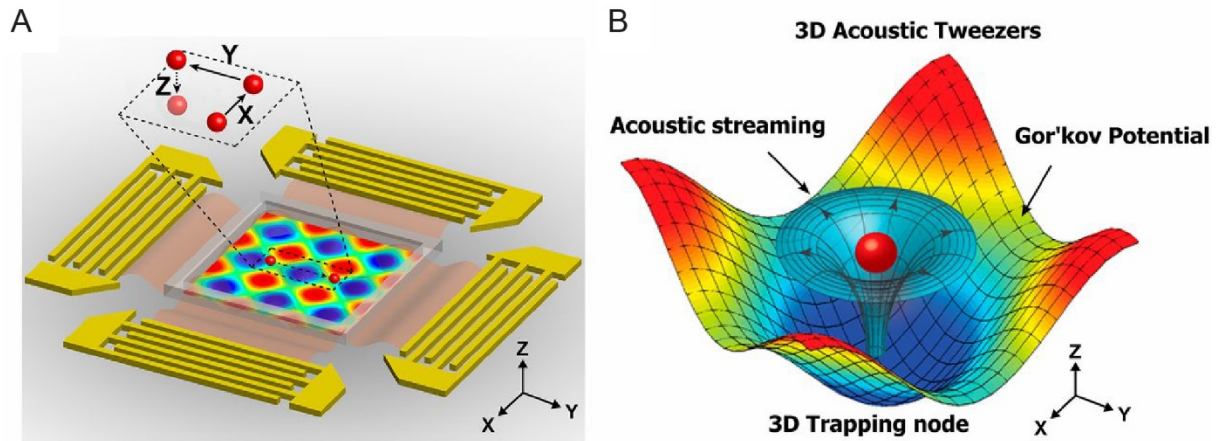


Figure 1:4 3D acoustic tweezers illustrations. A) Configuration of the planar acoustic wave generators with interdigitated electrodes B) Numerical simulation illustrating the acoustic trap. Both illustrations are adapted from (Guo, et al. 2016).

### 1.4.2.3 Optical trapping

Optical tweezers are based on the use of a difference in refractive index between a particle (or a cell) and the suspension medium (Nieminen, et al. 2007). By applying a focused laser beam with a high numerical aperture, the cell is attracted towards the focused beam (Ferrari, et al. 2005). As illustrated in Figure 1:5 an uncentered particle will be moved to the centre of the beam since a more intense momentum is transferred through the center (Lenshof and Laurell 2010). It can, therefore, be moved by displacing the beam slowly. The first stable optical trap was reported by Ashkin (Ashkin, et al. 1986) and was later used to move cells (Ashkin, et al. 1987). However, the use of a focused laser beam with high energy density might induce some damage to biological cells leading to “opticcution” (death by light) (Suehiro and Pethig 1998). The equipment used to operate the optical tweezer is also complex and with limited portability. Also called laser-guided direct writing (LGDW), this technique has been used to assemble different cell types into 3D structures with single-cell control (Akselrod, et al. 2006). This method is label-free.

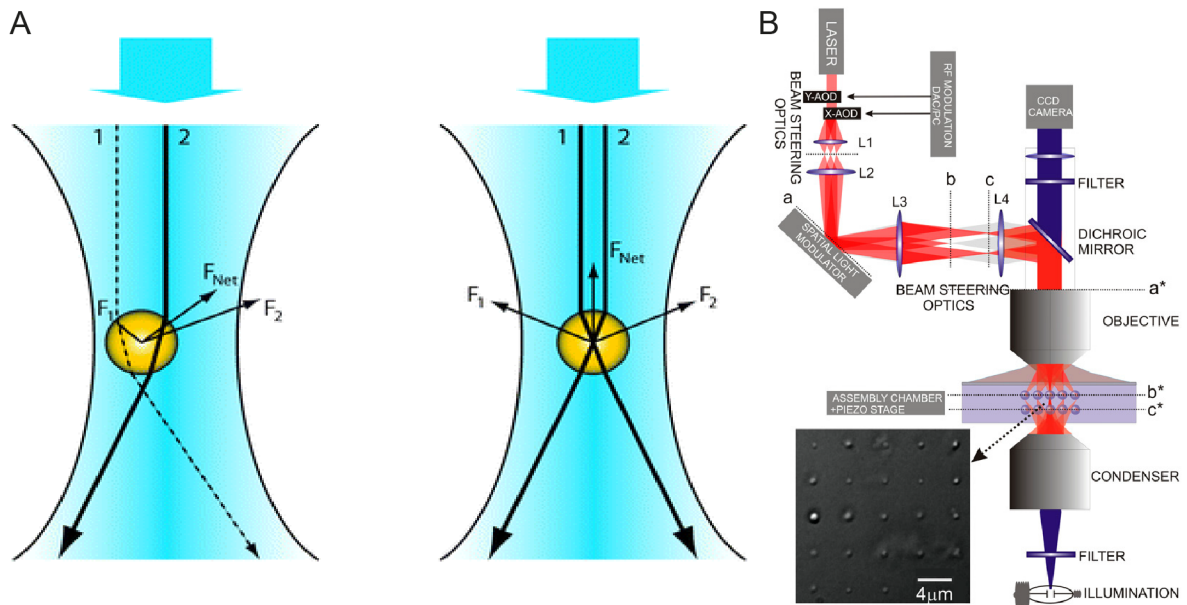


Figure 1:5 A) Principle of optical tweezers. Adapted from (Lenschhof and Laurell 2010). B) Schematic diagram of the optical trapping apparatus used by Akselrod et al. to create 3D construct. Adapted from (Akselrod, et al. 2006).

#### 1.4.2.4 Dielectrophoresis

Electric field-based methods present many advantages due to their label-free nature. They can be used both to form cell assemblies and to characterize them using dielectrophoresis and electrical impedance spectroscopy, respectively. The physical and dielectric parameters of the cells can be used to move them. Originally observed with particles by Pohl (Pohl 1951), dielectrophoresis is commonly used to separate various cells as they present different dielectric properties (Fiedler, et al. 1998, Gascoyne, et al. 1992). Depending on the dielectric properties of the cells and the suspending medium, cells can be directed towards areas of maximum field intensity (which is called positive dielectrophoresis or pDEP) or repelled in the area of low electric field intensity (which is referred to as negative dielectrophoresis or nDEP). More details on dielectrophoresis will be given in Chapter 2.

The following section is dedicated to an extensive review of the dielectrophoresis trapping designs.

## 1.5 Dielectrophoresis trapping design

Since the trapping force is proportional to  $\nabla E^2$ , the geometry of the electrodes has a high impact on the trapping of a particle. Many electrode configurations are presented in the literature, and pDEP and nDEP are demonstrated in various studies for both single cells and cell aggregates. Most of the configurations start with an initial solution of cells injected in the chip before applying any voltage, thus working between static conditions without fluid flow for the trapping. The following section is a summary of the literature.

### 1.5.1 For single cells

#### 1.5.1.1 With pDEP

##### 1.5.1.1.1 Grid-electrode geometry

This design, first presented by Suehiro and Pethig in 1998 (Suehiro and Pethig 1998), uses parallel sets of electrodes, located on the bottom and top of the chip, which are individually addressable. Those facing electrodes are perpendicular to each other. Bottom and top electrodes are made of gold and indium tin oxide (ITO), respectively. A local field maximum is created at the grid intersection when a pair of bottom and top electrodes are connected with an AC signal. The cell is attracted by this maximum by pDEP as shown in Figure 1:6.

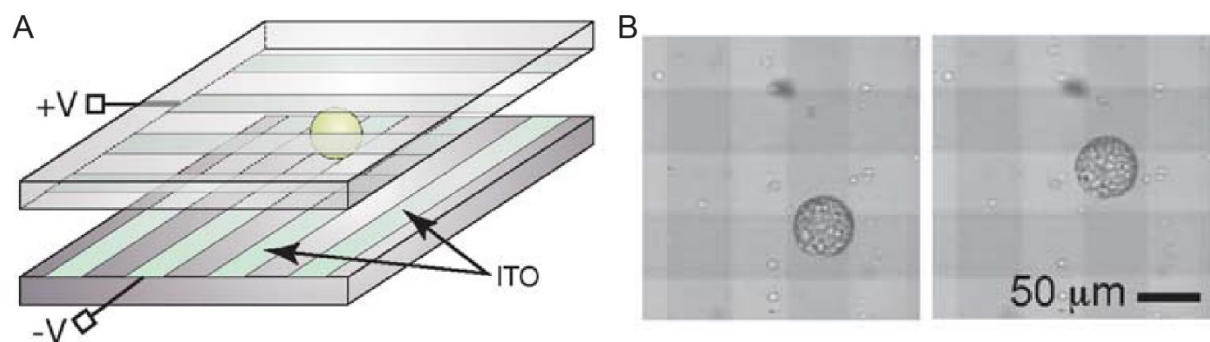


Figure 1:6 A) Schematic of grid-electrode geometry. The particle is trapped at the intersection between the two electrodes. Adapted from Voldman (Voldman 2006) B) Protoplast being moved from one position to another Adapted from Suehiro and Pethig (Suehiro and Pethig 1998).

## 1.5.1.1.2 Concentric ring levitator and feedback

Another example is a concentric ring levitator developed by Qian (Qian, et al. 2002) that uses feedback-controlled pDEP to actually trap particles away from the electrodes. The voltage is tuned to balance the gravitational force as presented in Figure 1:7.

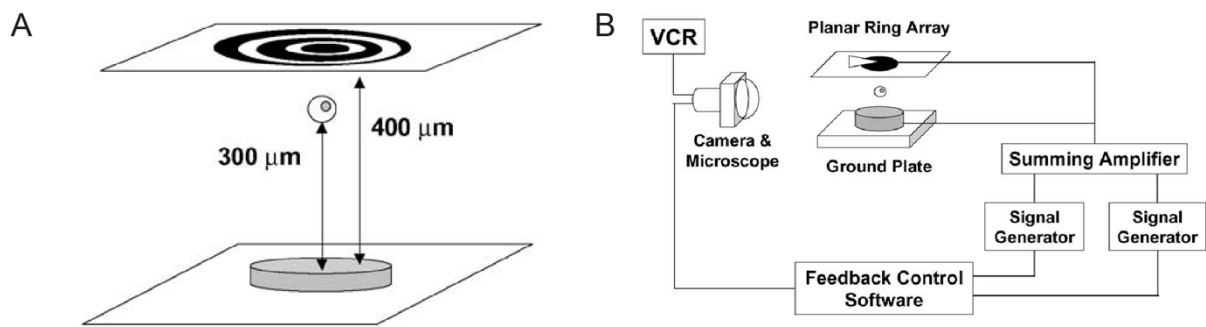


Figure 1:7 A) Example of the concentric ring levitator with a particle in levitation and B) the related feedback control.

## 1.5.1.1.3 Points-and-lid geometry

Using pDEP was also used to attract particles directly on the bottom plate by Gray from the Voldman group. Based on conducting points in the bottom plate and a top conducting lid, particles can be patterned at specific locations on the leads. Depending on their size, the points at the bottom can trap from single cells Figure 1:8 B to larger group of cells Figure 1:8 C (Gray, et al. 2004b). As presented by Albrecht (Albrecht, et al. 2006), this technique can be also performed in a photopolymerizable hydrogel such as polyethylene glycol (PEG) which allows entrapment of the multicellular structures which can be further stacked together.

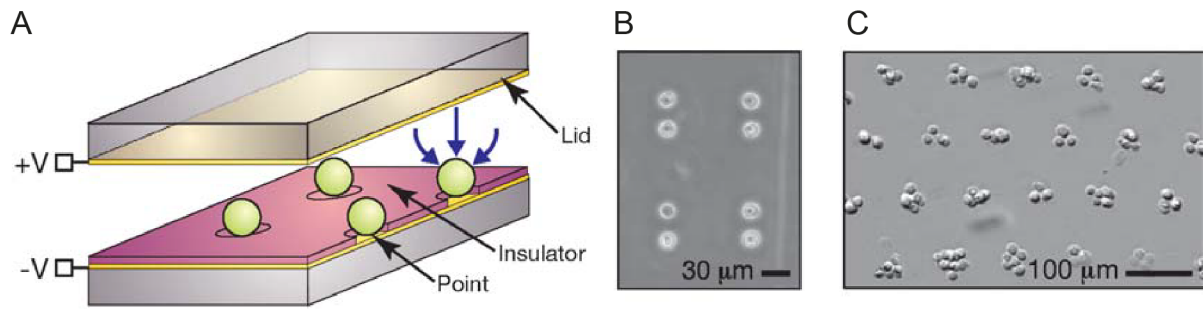


Figure 1:8 A) Schematic of the point-and-lid geometry, adapted from (Voldman 2006) B) Endothelial cells patterned using one version of this geometry from (Gray, et al. 2004a) C) Fibroblasts patterned using a different version of the geometry and embedded in a hydrogel matrix from (Gray, et al. 2004a).

#### 1.5.1.1.4 Ring-dot geometry

The ring-dot geometry is based on a similar principle as the points-and-lid geometry but this time the second electrode is no longer on the top lid but surrounds the dot (Taff and Voldman 2005). This configuration uses two metal layers on the bottom plate separated by an insulator as presented in Figure 1:9. Cells are attracted by the dot which corresponds to a field maximum. This configuration can be used in an array as shown in Figure 1:9 B and C).

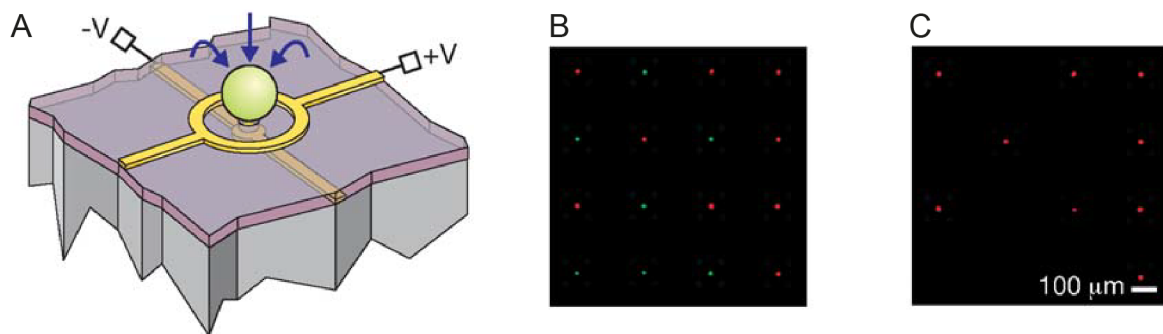


Figure 1:9 A) Schematic of the ring-dot geometry from (Voldman 2006). B) and C) are two images showing addressable removal of green-labeled human HL-60 in an array from (Voldman 2006).

### 1.5.1.2 With nDEP

#### 1.5.1.2.1 Interdigitated electrodes (low cell concentration)

The interdigitated electrode structure is composed of two electrodes patterned on a surface. Cells can be attracted by pDEP on the electrode edges or repelled by nDEP between the electrodes. If the patterned electrodes are castellated

electrodes, as presented in Figure 1:10, the nDEP trapping zone takes a triangular shape.

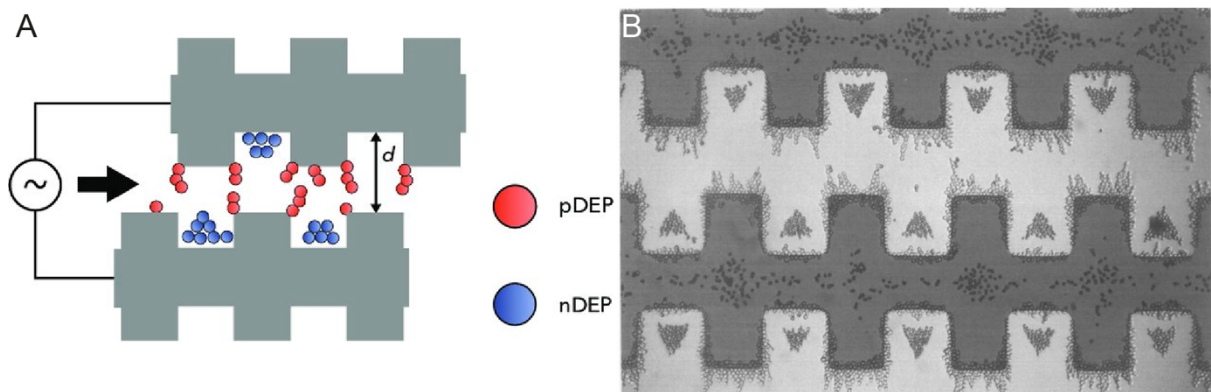


Figure 1:10 A) Principle of interdigitated castellated electrodes capture of cell by DEP. Adapted from (Pesch 2018). B) Capture of viable yeasts at the electrode edges by pDEP and of non-viable yeast in triangular aggregates by nDEP. Adapted from (Markx, et al. 1994).

More generally for interdigitated electrodes, reducing the height of the chamber will reduce the cell patterning time as presented by (Albrecht, et al. 2004).

#### 1.5.1.2.2 Insulating-post geometry

This design uses two electrodes separated by an array of insulating posts which are creating field inhomogeneity and, therefore, dielectrophoresis as presented in Figure 1:11 A). The fabrication of this design is easier since it does not require conducting materials inside the channels and the electrodes can be added later. This design is also working under flow conditions as shown in Figure 1:11 B). However, this design requires high voltages to operate.



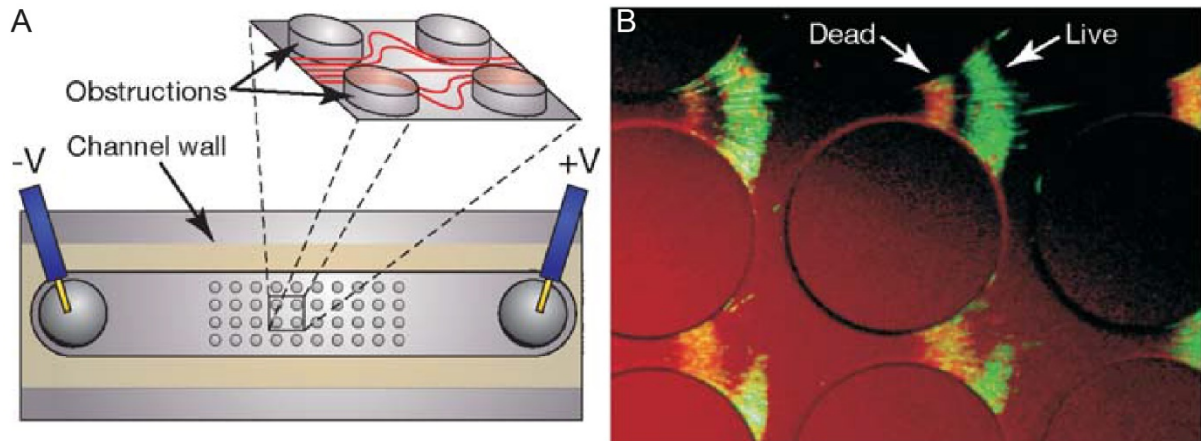


Figure 1:11 A) Schematic of the insulating post principle from (Voldman 2006). B) Cells are injected from the right to the left and, since the nDEP is larger on viable yeast cells (green) than dead yeast cells, they are retained farther from posts. Adapted from (Lapizco-Encinas, et al. 2004).

### 1.5.1.2.3 Quadrupole electrodes

Quadrupole electrodes are composed of four electrodes arranged in a circle and supplied with alternating voltage polarities in order to obtain a field minimum at the center of the inter electrode space as presented in Figure 1:12 A). This design was initially developed by the Fuhr group (Fuhr, et al. 1992, Fuhr, et al. 1994). Cells located between the electrodes are centered in the design. Depending on the applied voltage, cells are concentrated on the bottom of the surface or are levitating above. This technique was also used to create small aggregates of cortical neurons from rat fetuses by Heida (Heida, et al. 2001).

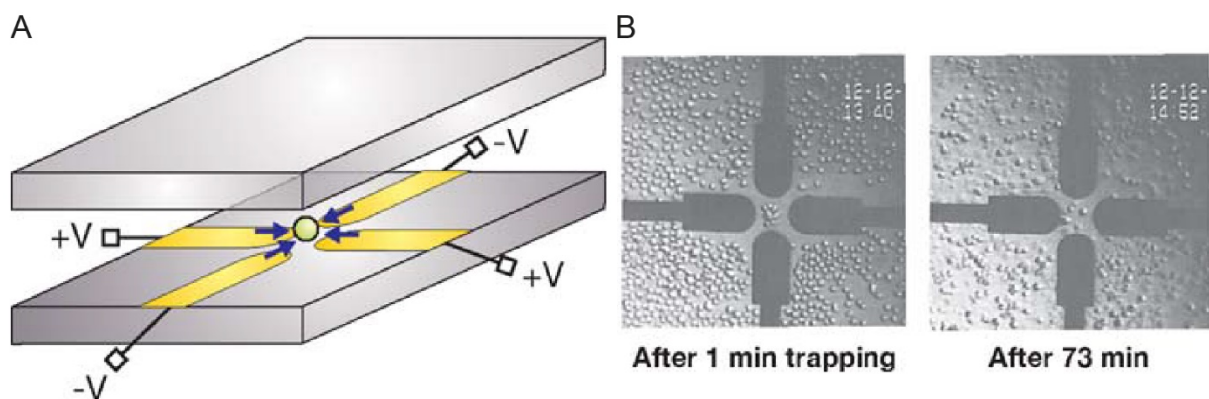


Figure 1:12 A) Schematic of the quadrupole electrodes from (Voldman 2006) and B) Mouse fibroblast trapping from (Fuhr, et al. 1994).

The trapping capability of this design can be improved by extending the electrodes in the third dimension. Thick electrodes can be made of electroplated

gold, as proposed by the Voldman group (Voldman, et al. 2002), or of metal coated SU-8, as demonstrated recently in the Guiducci group (Kilchenmann, et al. 2016). This will result in a higher DEP force but with a more complex fabrication process.

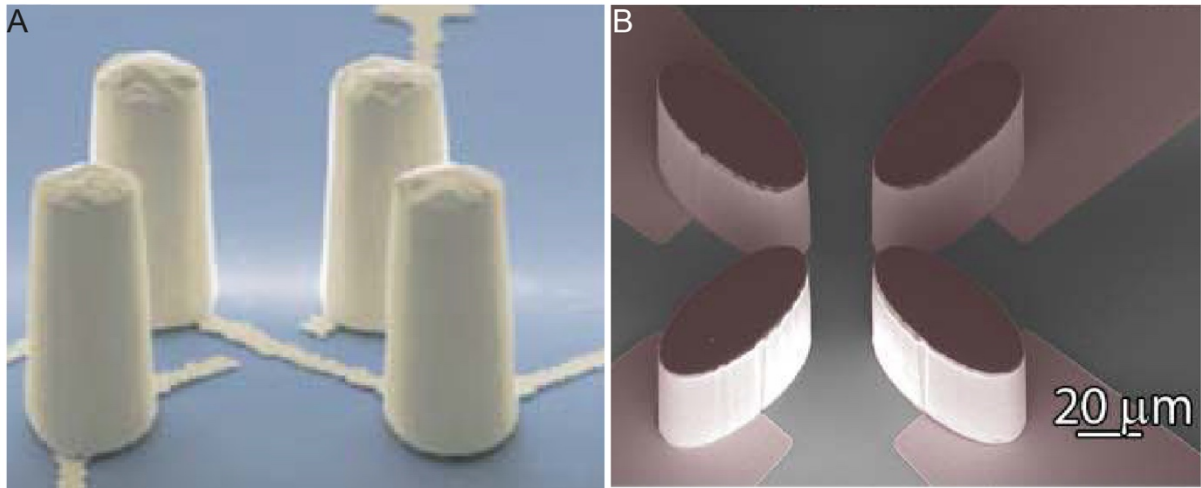


Figure 1:13 3D quadrupoles made of A) Electroplated gold on a SU-8 mold from (Voldman, et al. 2002) and B) Metal coated SU-8 structures from (Kilchenmann, et al. 2016).

#### 1.5.1.2.4 Octopole electrodes

The octopole electrodes provide another way to increase the trapping strength. This configuration, developed by the Fuhr group (Reichle, et al. 1999), is composed of two quadrupoles located on the top and bottom of the chip as presented in Figure 1:14 A). Despite an easier fabrication process than the extruded quadrupole, the alignment between both electrode sets can be challenging. Cells can be trapped with this design and electrorotation experiment can be performed.

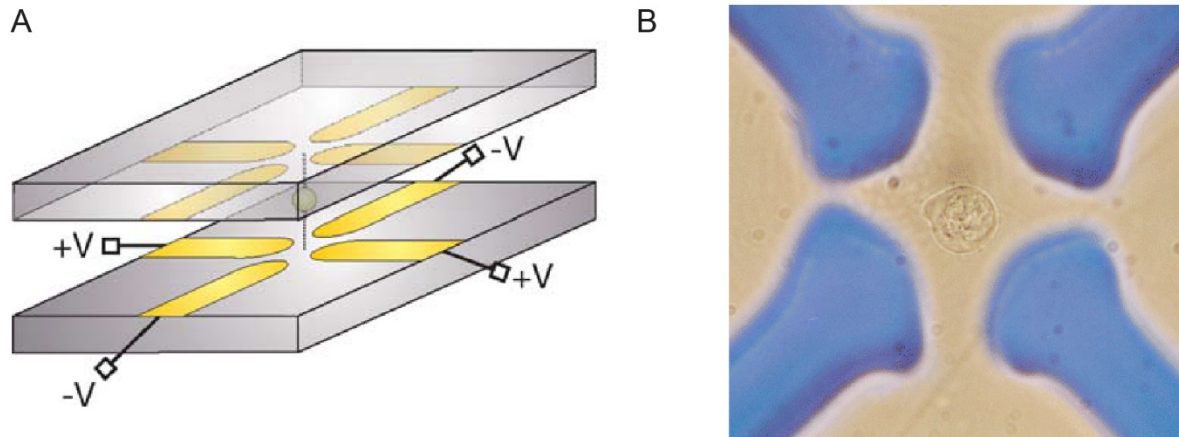


Figure 1:14 A) Schematic of octupole electrodes, Adapted from (Voldman 2006) B) Jurkat cell trapped in the structure, adapted from (Reichle, et al. 1999).

#### 1.5.1.2.5 Strip Electrodes

The strip electrodes, which are also facing electrodes, create a non-uniform electric field aiming to stop the incoming particles. In this dynamic configuration, the nDEP force counterbalances the drag force. It was first introduced by Fiedler from the Fuhr group (Fiedler, et al. 1998). Those electrodes can also be used to deflect cells as shown in Figure 1:15.

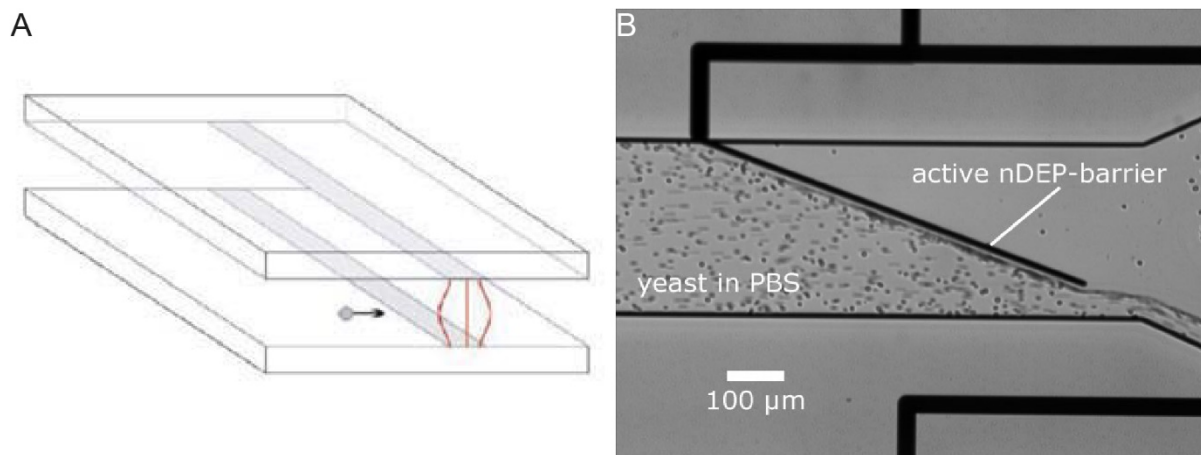


Figure 1:15 A) Schematic of the strip electrode configuration, adapted from (Voldman 2007). B) nDEP used to deflect yeast cells in PBS from (Seger-Sauli, et al. 2005).

#### 1.5.1.2.6 nDEP microwell

In this design, an interdigitated electrodes geometry is modified to include square areas at the center of which the field will be minimum, as presented in Figure 1:16. This concept has been developed for specifically trapping single

cells in order to pattern them, but it offers room for the cell to proliferate afterwards.

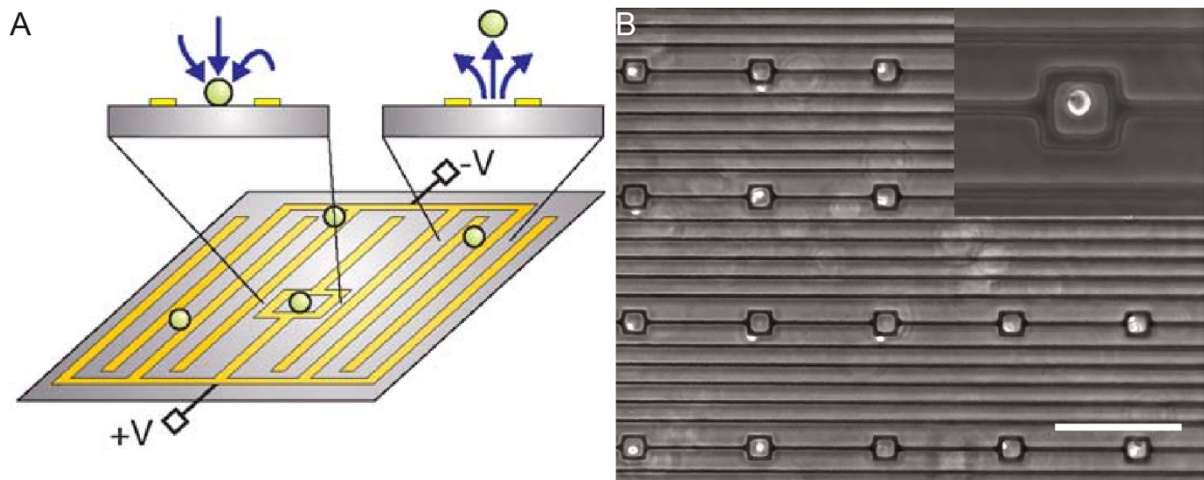


Figure 1:16 A) Schematic from the nDEP microwell, adapted from (Voldman 2006) B) HL60 cells trapped on nDEP electrode array, scalebar 200  $\mu\text{m}$  from (Mittal, et al. 2007).

#### 1.5.1.2.7 Transistor-based structures

Another approach, developed by an Italian team from Bologna, uses an array of electrodes addressable individually with a transistor and a top conductive lid as presented in Figure 1:17 A) and B). Potential cages are created where cells can be trapped and later moved. Initially presented by Medoro (Medoro 2000), this technology is currently commercialized by Silicon Biosystems.

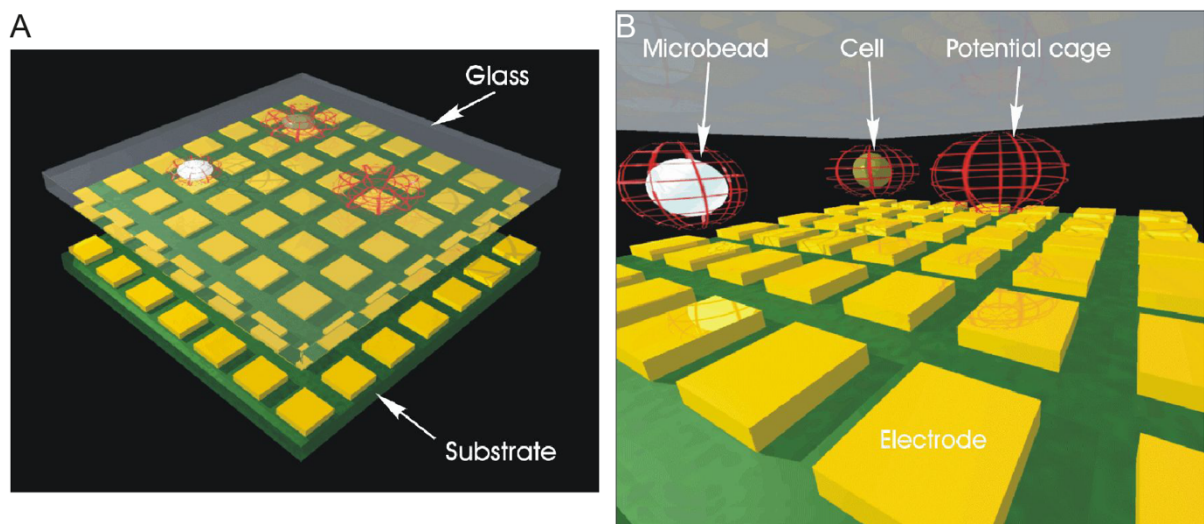


Figure 1:17 A) Schematic of the transistor-based structure B) zoom on particles trapped in potential cages. Both pictures are adapted from (Manaresi, et al. 2002)

### 1.5.2 From individual cells to cell aggregates

Most of the previous structures have been designed to trap either individual cells or an uncontrolled number of cells. Some designs intentionally aim at trapping several cells together to study their interactions using either pDEP or nDEP.

#### 1.5.2.1 DEP and physical confinement

In order to control the number of cells in contact and to understand how those cells contact each other, Gray et al. (Gray, et al. 2008) proposed a design where the structure is based on the points-and-lid geometry with the addition of a patterned layer of agarose with wells as presented in Figure 1:18 A). Once trapped in the well thanks to the electric field, cells can adhere to the surface and spread as presented in Figure 1:18 B).

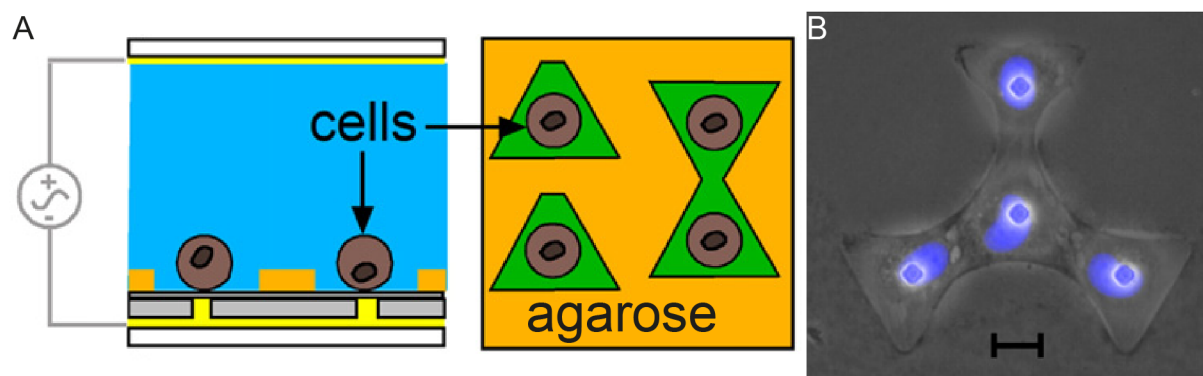


Figure 1:18 A) Schematic of a side and top view of the design. B) Phase contrast image of groups of four bovine pulmonary arterial endothelial cells in a specifically-designed pattern. This image is overlaid with the corresponding nuclear stain (blue), adapted from (Gray, et al. 2008).

This physical confinement in a microcavity was also demonstrated using nDEP by Ibrahim and coworkers (Ibrahim, et al. 2012), who proposed to use a quadrupole configuration of the electrodes with an opening in the insulating SU-8 layer and a back contact electrode in the center, as illustrated in Figure 1:19. Under nDEP conditions, cells are moved to the center of the quadrupole where the cavity is located.

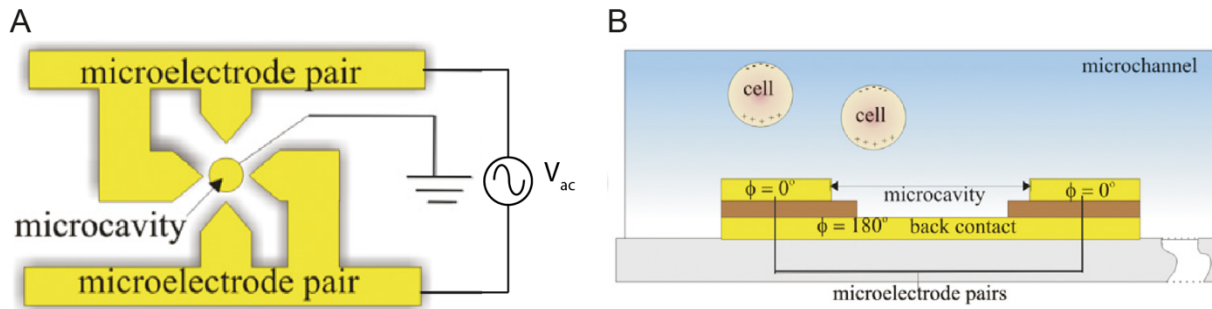


Figure 1:19 A) Top and B) Side view of the principle of the trapping with cavities presented by Ibrahim et al. Figures adapted from (Ibrahim, et al. 2012)

### 1.5.2.2 Use of Octopole electrodes

The octupole electrodes geometry has also been used to trap a single yeast cell and to let it proliferate under the AC field by Jaeger (Jaeger, et al. 2008) as illustrated in Figure 1:20 C). The size limit of the cell aggregate is roughly the height of the microchannel, in this case 40  $\mu\text{m}$ . The dielectric field cage (DFC) microchips (Perkin Elmer, Hamburg, Germany) presented in Figure 1:20 A) were used. They reported successful cell culture over several hours while suspending cells by nDEP in cell culture medium. They, however, reported that cell growth speed might be lower at non-physiological temperature (lower than 15°C and higher than 37.5°C).

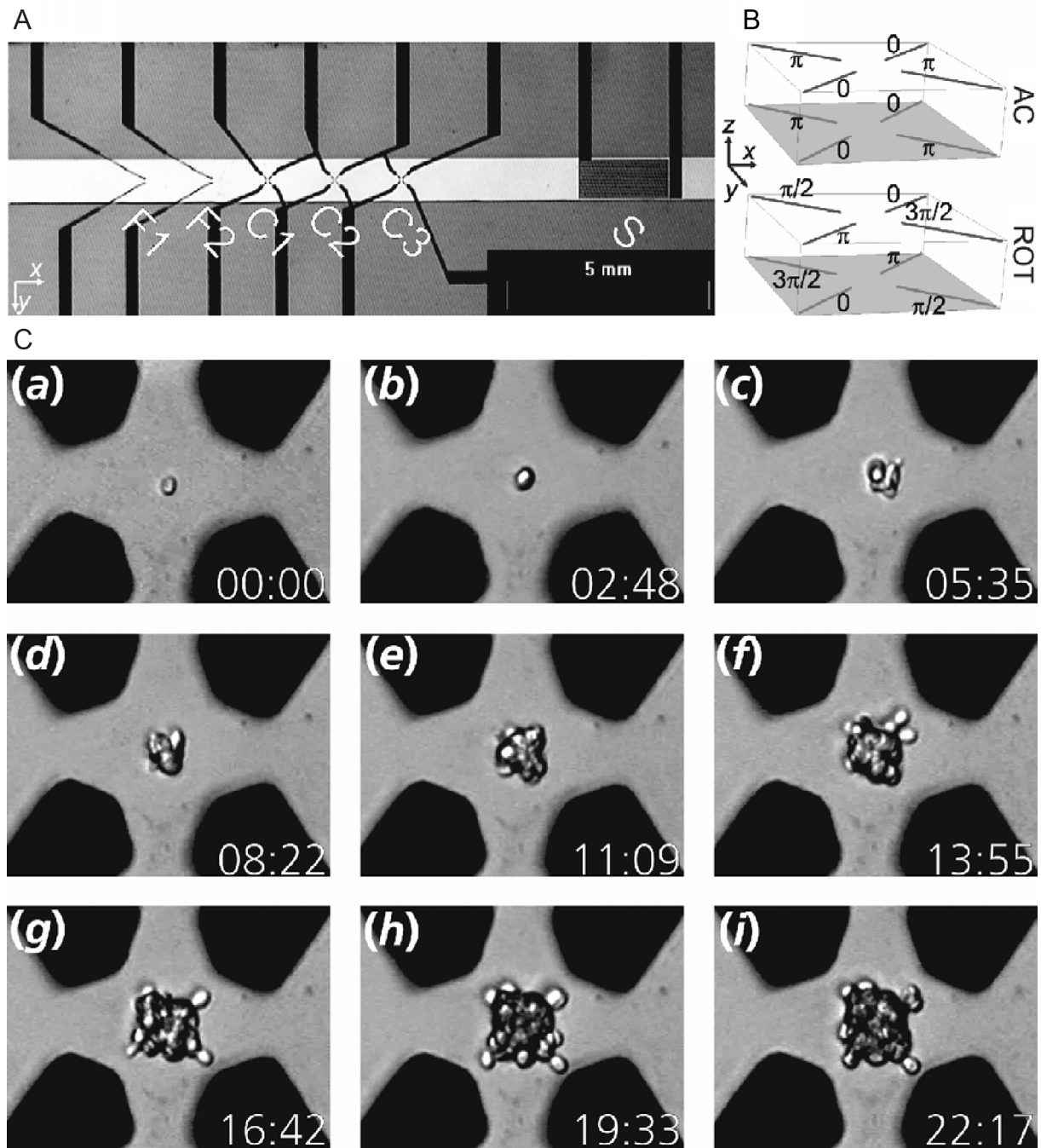


Figure 1:20 A) Picture of the electrode layout composed of two funnels (F1, F2) , three field cages (C1–C3) and one resistance sensor (S). B) Phase applied on two voltage configurations of the electrodes C) Yeast cell proliferation in the nDEP cage. All figures are adapted from (Jaeger, et al. 2008).

### 1.5.2.3 Array of quadrupole electrodes

Quadrupole electrodes can be used to fabricate aggregates, but parallelization requires a tedious multistep fabrication process with two metal layers as shown by Frénéa et al. (Frénéa, et al. 2003). Menad (Menad, et al. 2014) proposed a simpler fabrication process based on bond-detach lithography to form selective

openings in a thin PDMS layer, used as an insulator for the electric field, enabling the conversion of a bipolar castellated ITO electrode array into a quadripolar electrodes one as presented in Figure 1:21. This structure was used to create aggregates of HEK cells of controlled size (Menad, et al. 2015) which proved to be permanent and viable after 10 to 15 minutes of electric field exposure.

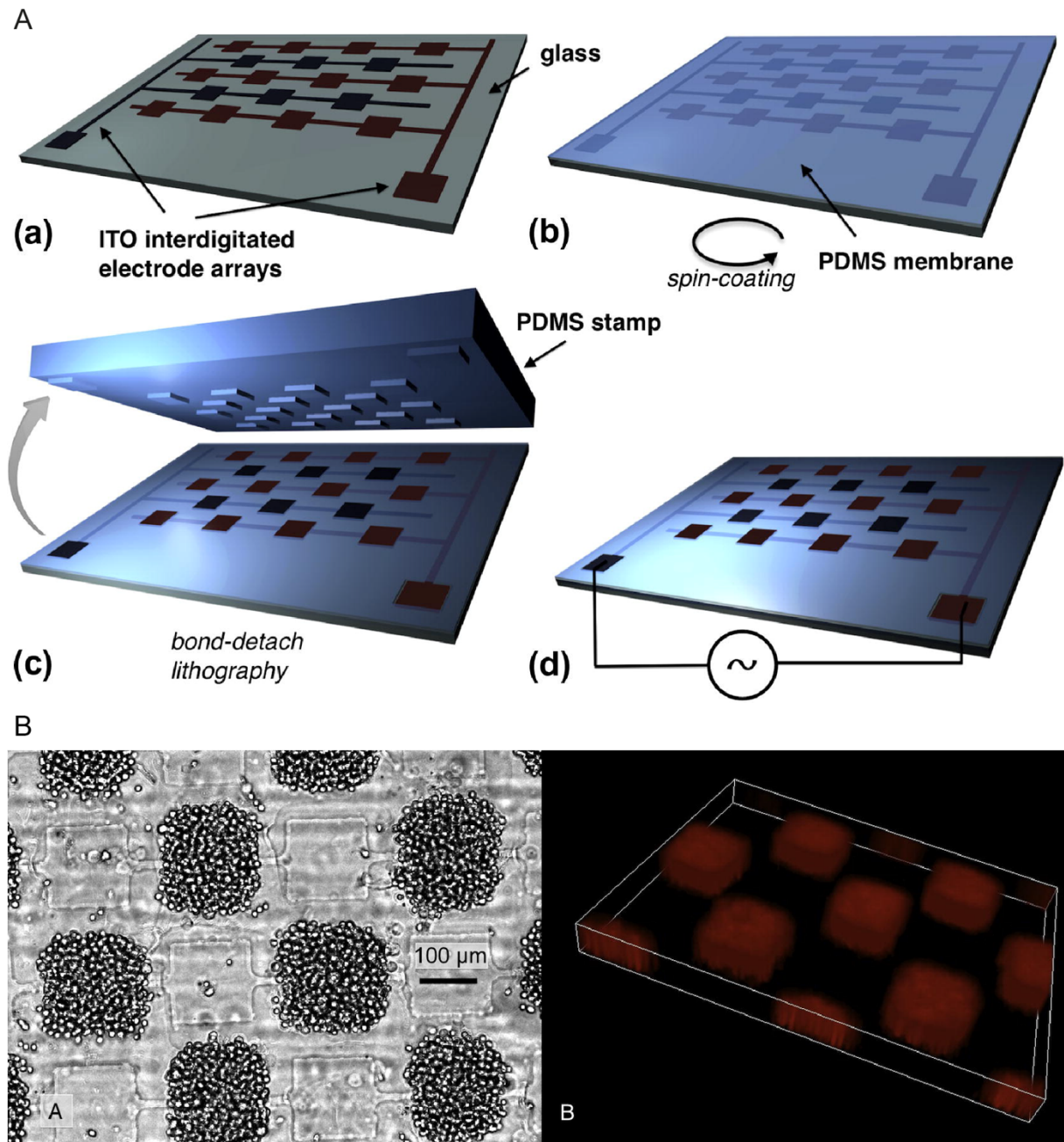


Figure 1:21 A) (a) to (d) fabrication of the quadripole array with the bond-detach lithography. B) Formation of HEK-293 cell aggregates by nDEP. A) Cell aggregates formed in a  $\sigma_m = 50 \text{ mS/m}$  medium B) reconstruction of the z-stack images. All figures are adapted from (Menad, et al. 2015).



#### ***1.5.2.4 Using transistor***

Using PCB technologies Medoro et al (Medoro, et al. 2003) used their transistor array to create aggregates first with beads and then with yeast cells. The different steps are presented in Figure 1:22. The suspension is first injected in the chip and then, as presented in Figure 1:22 b), the device is powered on and cells are trapped in nDEP cages. The particle located in the different nDEP cages can be contacted together by merging the nDEP cages to form larger aggregates. Interestingly, the authors of the paper suggested to use impedance measurement rather than visual control to investigate the position of cells and the size of cells and clusters.

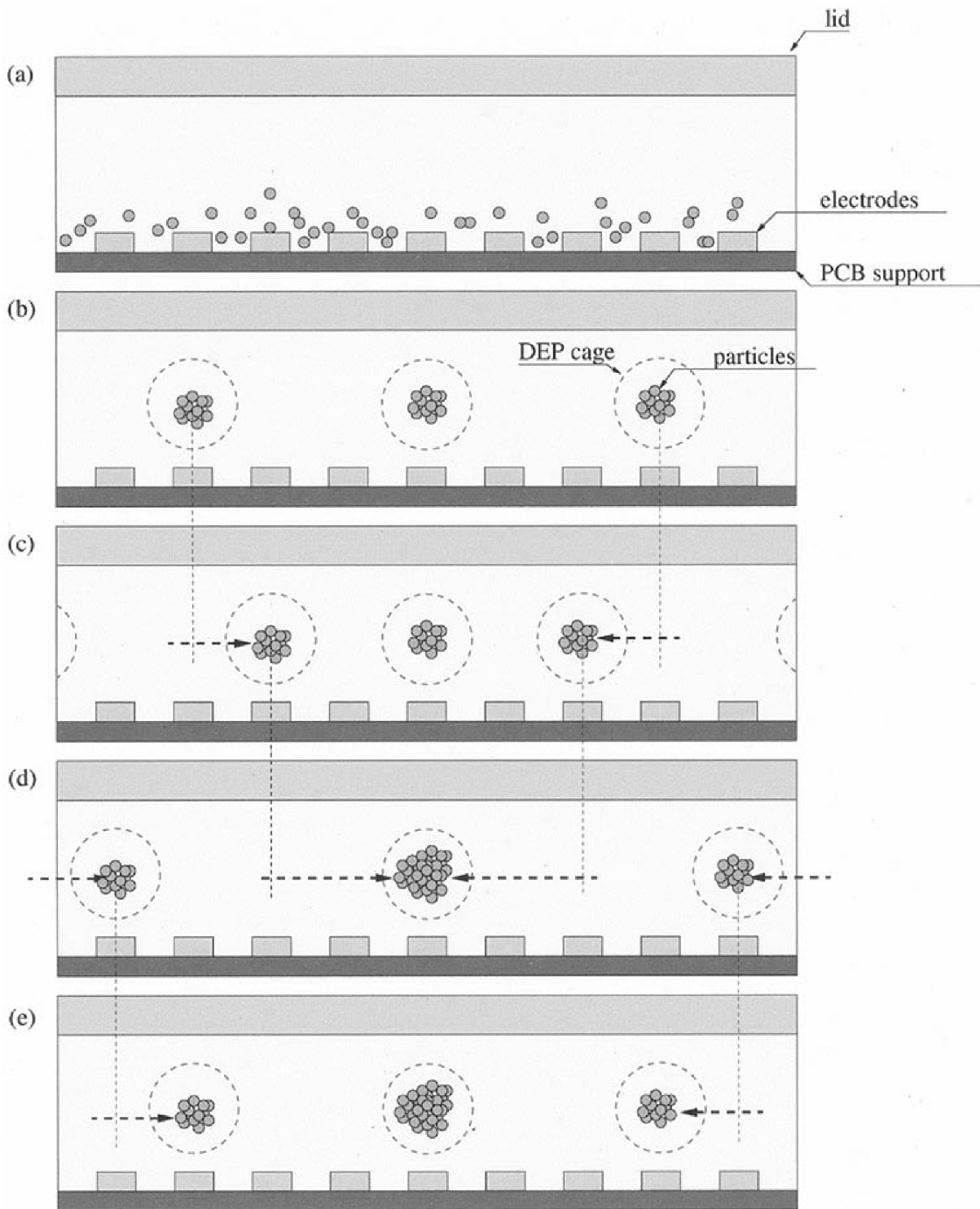


Figure 1:22 Experiment steps for the creation of aggregates with the DEP array technology. Adapted from (Medoro, et al. 2003).

### 1.5.3 Conclusion on the trapping design for cell and aggregates.

As presented many designs are available for trapping with pDEP and nDEP from specifically the single cell to the cell aggregates. nDEP designs offer the advantage of trapping cells far from the electrodes, hence limiting the impact

of the electric induced effects on cells (current induced heating, increase in transmembrane potential leading to electroporation) which will be described in Chapter 3.

#### **1.5.4 DEP and cell culture**

Few studies have been done on the impact on the electric field on cell culture. Puttawamy (Puttaswamy, et al. 2010) showed that using a modified medium with a lower conductivity and corrected osmolarity might reduce the damage on the cells caused by DEP, in this case human liver cell line HepG2 patterning with nDEP. This effects of the electric field on cells will be discussed in Chapter 3. Replacing the low conductivity medium by the native culture medium DMEM after patterning helped to enhance the viability. A similar conclusion was drawn by Sebastian (Sebastian, et al. 2007) for pDEP by using castellated electrodes to create aggregates of Jurkat cells in between 10 to 15 minutes. He also noticed that the prolonged exposure of the cells to the electric field increased the adhesion between them. Layered temporary aggregates made of AC3 stromal cells and Jurkat T lymphocytes were successfully constructed with the same castellated electrodes and pDEP (Sebastian, et al. 2006). The cell aggregates created by Menad using nDEP proved to be viable thanks to a Calcein AM assay. Calcein is a compound that permeates living cells and stain the cytoplasm of living cells in green. They were also cultivable in DMEM in a poly-L-Lysine treated microchip and presented pseudopodia, membrane protrusions showing that cells adhered to the substrate and were alive.

#### **1.5.5 Conclusions on all the trapping designs**

For all the presented design, controlling the number of cells contained in the aggregate is a limiting factor. It can be performed but at the expense of unretrievable cells in microcavities, or of a complex and expensive transistor array. The size and composition of the aggregates are often controlled by the cell initial position in the chip, which limits reproducibility.

## 1.6 Requirement for controlled cell aggregate

None of the existing designs and operation modes has proven efficient for creating aggregates controlled in size up to the one cell precision using DEP under flow conditions, relatively inexpensively. To achieve this goal, the created microchip should meet the following requirements:

- The cells should arrive with the liquid and be captured in a precise position while the flow is maintained during the arrival of the different cells.
- The trap should be activated from the beginning and accept new cells to join the cells already present.
- The size of the trapping area should be adapted to the size of the envisioned aggregate.
- The created device should offer the possibility to create aggregates made of different cells in a controlled way.
- The stability of the trap should be robust to flow variations.
- The fabrication process should be relatively simple.
- The applied voltage should be compatible with cell handling.
- The temperature in the chamber should be compatible with cells.
- The device should integrate a sensor to characterize single cell and cell aggregates.

This thesis is dedicated to the development and testing of a microsystem matching these requirements.

The following chapter presents an overview of theory behind dielectrophoresis and dielectric modeling of single cell and cell aggregates.



# Chapter 2 Dielectrophoresis theory and modeling with MyDEP

This chapter presents an overview of theory behind dielectrophoresis and dielectric modeling of single cells and cell aggregates as well as MyDEP, our computational tool for dielectric modeling of particles and cells. The content of the chapter is partially published in the article (Cottet, et al. 2019a):

Cottet, J., Fabregue, O., Berger, C., Buret, F., Renaud, P. & Frénéa-Robin, M. MyDEP: A New Computational Tool for Dielectric Modeling of Particles and Cells. *Biophysical Journal* 116, 12-18, doi:10.1016/j.bpj.2018.11.021 (2019).

## 2.1 Dielectrophoresis historical overview

The term “Dielectrophoresis”, abbreviated DEP, was first introduced by Pohl in 1951 (Pohl 1951) to describe the motion of dielectric particles due to interaction with a non-uniform electric field. It comes from the Greek “phorein” and means that the particle is “carried as a result of its dielectric properties” (Pethig 2010). One of the effects was the polarization of the particle, effect already observed by Thales of Miletus 600 B.C. when a rubbed amber piece was able to attract light objects like straws. The mathematical treatment of dielectrophoresis was possible, thanks to Maxwell’s theories. The phenomenon had also been previously observed in 1923 by Hatschek and Thorne (Hatschek and Thorne 1923) and in 1924 Stattford patented the use of what was in fact DEP. At the same time, Hatfield used dielectrophoresis to treat tin ores as a separation method for cassiterite and quartz (Hatfield 1924). Pohl was interested in the industrial application of DEP to remove carbon-black filler from polyvinyl chloride samples.

It was only in 1966 that Pohl and Hawk applied DEP to biological cells for the characterisation and separation of live and dead yeast cells as explained by Pohl in his seminal book *Dielectrophoresis : the behavior of neutral matter in nonuniform electric fields* (Pohl 1978). Using a “point and plane” configuration, they observed that live cells were attracted towards the electrodes using a 30  $V_{RMS}$  signal at 2.55 MHz and the dead cells remained in solution, actively repelled from the electrodes. Until the end of the 1980s, electrodes were machined or made of pins and rods and the arrangement of the electrodes was the limiting factor for DEP separation.

Thanks to the use of microfabrication techniques commonly used in the semiconductor industry, electrodes could be made smaller and as a consequence, large electric field could be generated with lower voltages. The pattern of the 2D electrodes could be tuned as desired, and small features, in the micrometer range, could be fabricated.

In the early 1990's, several new methods could be developed such as traveling-wave dielectrophoresis (TWD) in 1991 (Fuhr, et al. 1991), dielectrophoresis field-flow fractionation (DEP-FFF) in 1997 (Huang, et al. 1997, Markx, et al. 1997) and electrodeless dielectrophoresis in 1990 (Washizu 1990).

To overcome the limitation of 2D electrode designs, the third dimension was explored either virtually by using 2D electrodes at the top and the bottom of the microchannel (Li and Kaler 2004) or physically by electroplating electrodes (Voldman, et al. 2002, Wang, et al. 2007), carbonizing (Martinez-Duarte, et al. 2011) or metal-coating SU-8 pillars. More recently Henslee et al. (Henslee, et al. 2011) proposed to use “fluid electrodes”, isolated and capacitively coupled with the main channel.

More historical details on dielectrophoresis can be found in the review by Pethig (Pethig 2010) and Hughes (Hughes 2016).

The following section will be dedicated to the physical explanation of the different phenomena previously presented.

### **2.1.1 Polarization and dispersion mechanism**

Polarization corresponds to the process of charge redistribution in an electric field. When a dielectric, electrically neutral, is exposed to an electric field, the positive and negative bound charges move and their centers of charge as well. This process is referred to as induced polarization. Since both the particles and their suspending medium are dielectrics, they contain charges and get polarized when submitted to an external electric field.

Observation of biomaterials at different frequencies, also called dielectric spectroscopy, has led to the observation of three relaxation mechanisms, also called dispersions, by Swan in 1957 (Schwan 1957) as presented in Figure 2:1:

- A very-low frequencies, from the mHz to the kHz, the  $\alpha$ -dispersion is observed. It corresponds to the counter-ion effects near the membrane surface (Grimnes and Martinsen 2014). Since the cytoplasm and extracellular medium are both ionic media, free charges from the medium



come to counter balance the charges of the cytoplasm. The mechanism is responsible for the ionic environment around the cell and the surface conductivity.

- From 1 kHz to 100 MHz, the  $\beta$ -dispersion can be observed. It corresponds to the relaxation of cell membranes.
- From 0.1 to 100 GHz, the  $\gamma$ -dispersion is observed. It corresponds to dipolar relaxation of water molecules.

If charges are induced at the interface between different materials, then an interfacial polarization appears called the Maxwell-Wagner polarization.

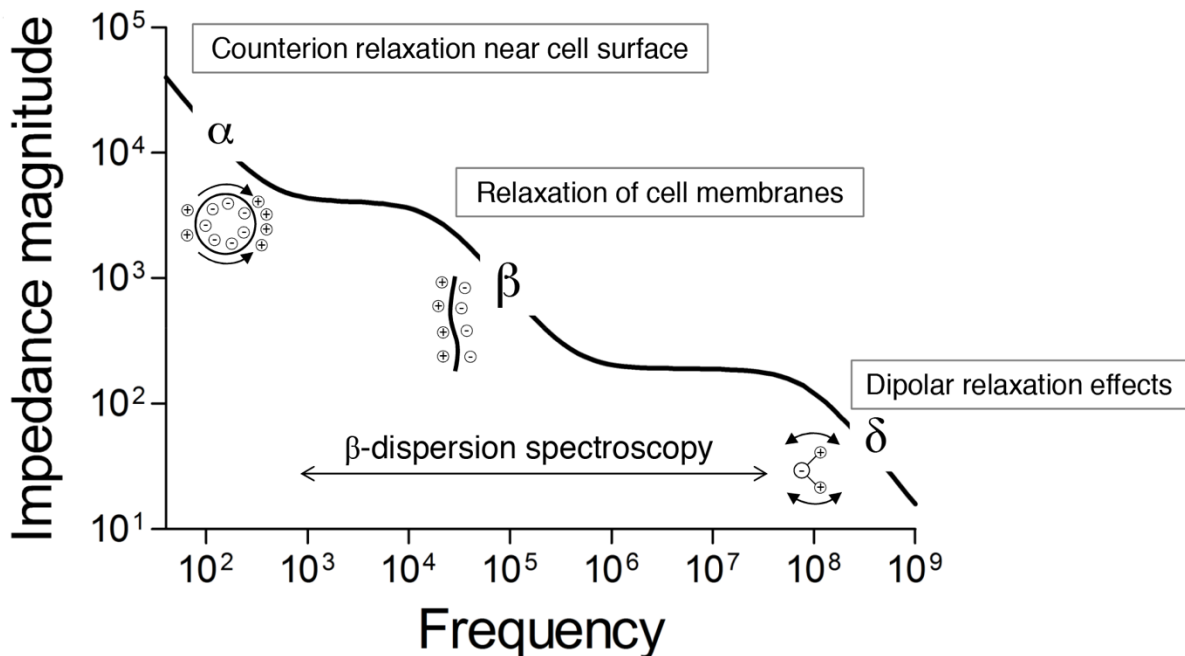


Figure 2:1 Frequency dependence of biological tissues. Adapted from (Meissner 2013).  
Original figure from (Schwan 1994).

Each particle and cells have a different complex permittivity, frequency dependent, which is its signature. Dielectrophoresis mostly investigates the  $\beta$ -dispersion.

In dielectrophoresis, two mechanisms are involved in the polarization: the displacement of free charges by conduction and the perturbation of bound charges (dielectric displacement). Particles are, hence modeled as lossy

dielectrics containing both a conductivity and permittivity as presented in equation (4). At low frequency, the polarization is due to conduction since the ions have time to move at the interface. However, at high frequency, ions no more have time to migrate and the polarization is mostly linked to permittivity hence the polarization of bound charges (Gagnon 2011).

## 2.2 Dielectrophoresis theory

### 2.2.1 DEP basics

As presented previously, DEP corresponds to the displacement of dielectric particles subjected to a non-uniform electric field. Depending on the frequency of the applied field and on the dielectric properties of the particle and its immersion medium, different polarization mechanisms come into play, the main mechanisms being related to the formation of an electric double layer at the particle/liquid interface and to charge accumulation at interfaces between media of different electrical properties (Maxwell-Wagner interfacial polarization effect) (Pethig 2017). The force resulting from the interaction between the induced dipole moment  $\mathbf{m}$  and the field gradient is expressed by:

$$\mathbf{F}_{\text{DEP}} = -\nabla U_{El} = (\mathbf{m} \cdot \nabla) \mathbf{E} \quad (1)$$

where  $U_{El}$  refers to the electric potential energy and  $\mathbf{E}$  to the electric field.

For a spherical particle of radius  $r_{ext}$ , the induced dipolar moment is given by:

$$\mathbf{m} = 4\pi\epsilon_m\epsilon_0 CM(f)r_{ext}^3 \mathbf{E} \quad (2)$$

where  $CM(f)$  is the Clausius-Mossotti factor:

$$CM(f) = \frac{\epsilon_p^* - \epsilon_m^*}{\epsilon_p^* + 2\epsilon_m^*} \quad (3)$$

$\epsilon_p^*$  and  $\epsilon_m^*$  refer to the complex permittivities of particle and medium, which depend on their respective electrical conductivities and relative permittivities and on the field angular frequency  $\omega$ :

$$\epsilon_i^* = \epsilon_i\epsilon_0 - j\frac{\sigma_i}{\omega} \quad (4)$$

where  $\varepsilon_i$  is the relative permittivity,  $\varepsilon_0$  the vacuum permittivity,  $\sigma_i$  the electrical conductivity and  $\omega = 2\pi f$  with  $f$  the frequency.

Development of equation (1) leads to the expression of the generalized time-averaged DEP force (Hughes 2002):

$$\mathbf{F}_{\text{DEP}} = 2\pi\varepsilon_m\varepsilon_0r_{ext}^3(Re[CM(f)]\nabla E_{RMS}^2 + Im[CM(f)](E_x^2\nabla\phi_x + E_y^2\nabla\phi_y + E_z^2\nabla\phi_z)) \quad (5)$$

where  $\phi_x$ ,  $\phi_y$  and  $\phi_z$  are the phase shifts of the field components in the Cartesian coordinates.

### 2.2.2 Conventional dielectrophoresis

If the electric field applied is stationary, equation (5) simplifies to:

$$\mathbf{F}_{\text{cDEP}} = 2\pi\varepsilon_m\varepsilon_0r_{ext}^3Re[CM(f)]\nabla E_{RMS}^2 \quad (6)$$

This phenomenon is sometimes referred to as “conventional dielectrophoresis”, abbreviated cDEP. The force depends on the gradient of the squared electric field intensity and exists only in the presence of a non-uniform electric field. It is proportional to the volume of the particle, as well as to the real part of the Clausius-Mossotti factor,  $Re[CM(f)]$ . This term, reflecting the polarizability contrast between the particle and its immersion medium, also determines the direction of the force:

- When the particle is more polarizable than its immersion medium ( $Re[CM(f)] > 0$ ), the force acts in the gradient direction and, therefore, drives the particle towards areas of maximum field intensity. This corresponds to *positive dielectrophoresis* (pDEP).
- On the contrary, when the particle is less polarizable than its immersion medium ( $Re[CM(f)] < 0$ ), the force moves the particle against the gradient, towards the regions of minimum field intensity, which is referred to as *negative dielectrophoresis* (nDEP).

### 2.2.3 Physical explanation of dielectrophoresis

Dielectrophoresis can also be explained more graphically.

In pDEP the particle is more polarizable than the medium and more charges will be moved inside the particle than in the medium. The particle becomes polarized since the barycenters of the positive and negative charges are no more the same and the particle can be considered as a dipole with a dipolar moment  $\mathbf{m}$ . In an inhomogeneous electric field, the forces on each side of the particle will be unbalanced and the particle will move towards the high electric field areas as illustrated in Figure 2:2 A).

In nDEP, the particle is less polarizable than the medium and more charges will move around the particle than inside. The created dipole has an opposite orientation compared to pDEP and the particle will move towards the low electric field regions as illustrated in Figure 2:2 B).

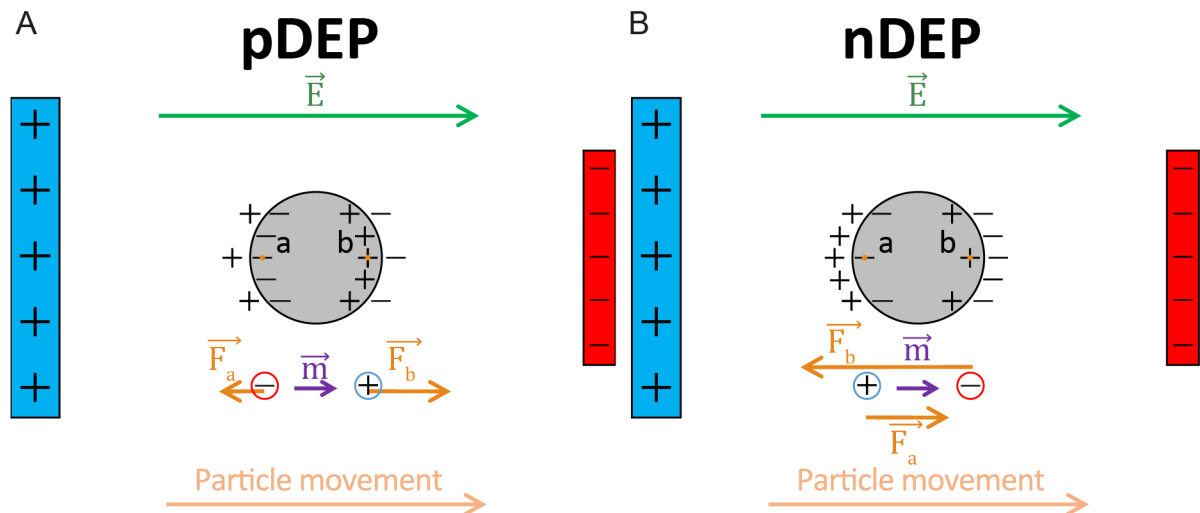


Figure 2:2 Principle of A) pDEP and B) nDEP.  $\mathbf{E}$  represents the electric field (in green),  $\mathbf{m}$  the dipolar moment and  $\mathbf{F}_a$  and  $\mathbf{F}_b$  the Coulomb force ( $\mathbf{F}=\mathbf{qE}$ ) on each barycenter of the charges (red and blue circles) on each side of the particle.

Depending on the frequency, the charges involved are the free charges (ions) at low frequency (conduction) and the bound charges at high frequency (dielectric polarization).

#### 2.2.4 Electrorotation

While conventional dielectrophoresis is based on the use of stationary electric fields, electrorotation, abbreviated ROT, induces a rotary motion on a polarizable particle exposed to a rotating field. This technique was developed in

the 1980s by Arnold and Zimmermann (Arnold and Zimmermann 1988), who proposed to use a four-pole electrode structure to generate the field by applying 90° phase-shifted signals between two adjacent electrodes.

When a polarizable particle is suspended in a rotating electric field, a dipole forms and should rotate synchronously with the field. In practice, when the angular frequency of the field is sufficiently high, the dipolar relaxation time is too long to allow this synchronism. The temporal shift (or phase delay) between the dipole and the field results in a torque exerted on the particle, of expression:

$$\langle \mathbf{\Gamma}_{\text{ROT}} \rangle = \mathbf{m} \times \mathbf{E} = -4\pi r_{ext}^3 \epsilon_m \epsilon_0 \text{Im}[CM(f)] E^2 \mathbf{e}_z \quad (7)$$

where  $\mathbf{e}_z$  represents the unit vector normal to the electrode plane and  $CM(f)$  the Clausius-Mossotti factor (cf. (3)).

As the particle rotates, it experiences a resistive viscous torque from the surrounding fluid of expression (Lei, et al. 2006)

$$\mathbf{\Gamma}_\eta = -8\pi\eta r_{ext}^3 \Omega_0(f) \mathbf{e}_z \quad (8)$$

Where  $\eta$  is the dynamic viscosity of the medium and  $\Omega_0(f)$  is the constant angular velocity of the particle.

At the equilibrium between induced torque and viscous drag, the rotation rate for a spherical particle is given by:

$$\Omega_0(f) = -\frac{\epsilon_0 \epsilon_m}{2\eta} \text{Im}[CM(f)] E^2 \quad (9)$$

where  $\eta$  represents the medium viscosity.

The minus sign indicates that the particle rotates against the field direction for  $\text{Im}[CM(f)] > 0$ . Otherwise the direction of rotation is with the field. Curve fitting procedures may be used to obtain the dielectric parameters of a cell, by minimizing the deviation between the experimental ROT spectrum (plot of the rotation rate with respect to the field frequency) and the theoretical spectrum predicted by the appropriate multi-shell model.

### 2.2.5 Travelling-Wave Dielectrophoresis (TWD)

The Travelling-Wave Dielectrophoresis force, abbreviated TWD, acts on a particle subjected to a travelling electric field. It is related to the phase non-uniformity of the electric field and arises from the interaction of the travelling field with the phase-lagging component of the induced dipole moment. Such a field can be produced by planar electrodes arranged in rows and driven by a polyphase AC voltage. TWD is, therefore, an analogue of ROT, equation (5) remains the same, but with electrodes arranged in line, rather than in a circle. The resulting translational force propels the particle along the electrodes, with or against the field direction, depending on whether  $Im[CM(f)]$  is negative or positive, respectively. In practice, cDEP and TWD effects can be observed simultaneously: while the particle translates, it is either pushed above the electrodes (nDEP) or attracted onto them (pDEP), depending on the sign of  $Re[CM(f)]$  (Jones 2003).

### 2.2.6 Dielectrophoresis Field-Flow Fractionation (DEP-FFF)

The principle of Dielectrophoresis Field-Flow Fractionation, abbreviated DEP-FFF, is to use a liquid containing cells and electrodes that will repel the cells with nDEP. Cells, typically injected at the bottom of the microchannel, will be repelled from the bottom of the chamber and, depending on the magnitude of the DEP force they experience, will levitate at a certain height. The speed of each particle type will be different and can be used to separate them.

### 2.2.7 Electrodeless and insulating dielectrophoresis (iDEP)

The principle of “electrodeless” dielectrophoresis is to use insulating obstacles in the flow, either obstructions or beads, to create field non-uniformities instead of the electrode layout. The approach was nicknamed insulating dielectrophoresis, abbreviated iDEP, by Cummings (Cummings and Singh 2003) and used as a high-throughput separation method. In this approach, very high voltages are commonly used with highly conductive medium which can lead to significant Joule heating.

## 2.3 Cell modeling and MyDEP

Most particles, and especially biological cells, are not homogeneous. It is therefore mandatory to model the different layers that constitute them (cell membrane and cytoplasm in particular). Calculating the Clausius-Mossotti factor requires to successively calculate the equivalent permittivities of the inner layers to obtain a homogeneous equivalent particle. In this thesis, a computational tool, MyDEP (Cottet, et al. 2018), was developed to simulate cell dielectrophoretic behavior alone and in a suspension.

### 2.3.1 Cell models

The different models implemented in MyDEP are: “homogeneous particle”, “single-shell”, “two-shell”, “three-shell” and “four-shell” are presented in Figure 2:3.

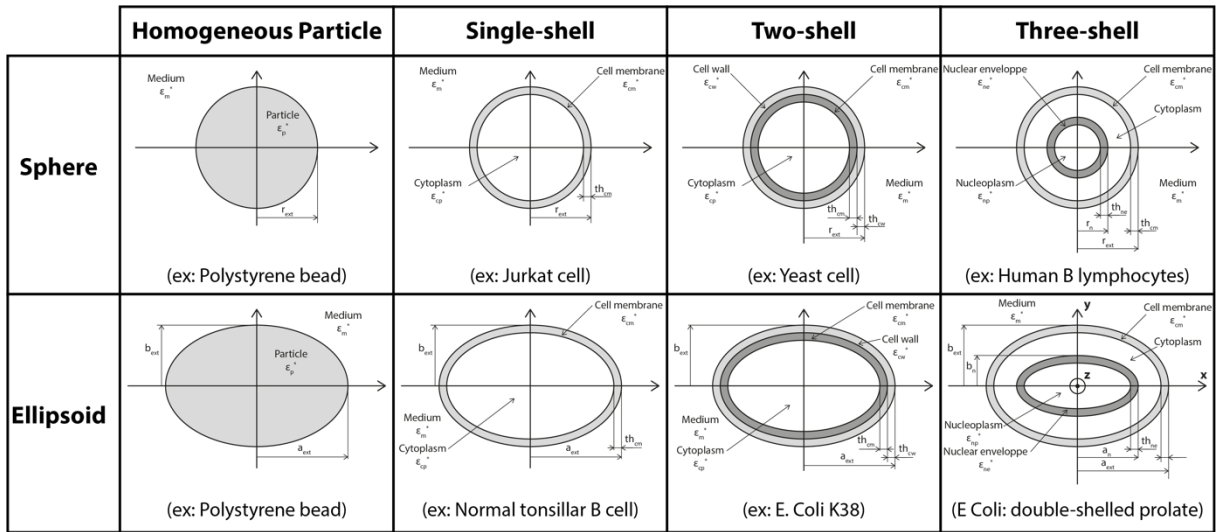


Figure 2:3 Illustration of the different spherical and ellipsoidal cell and particle models implemented in the interface. All the models “homogeneous sphere”, “single-shell”, “two-shell” and “three-shell” are illustrated with an example. The implemented “four-shell” model is not illustrated here.

For a cell modeled with a “single-shell” model composed of a cytoplasm surrounded by a cell membrane, the equivalent complex permittivity (Gascoyne, et al. 1995) is:

$$\epsilon_{eq}^* = \epsilon_{cm}^* \frac{\left(\frac{r_{ext}}{r_{ext} - th_{cm}}\right)^3 + 2 \left(\frac{\epsilon_{cp}^* - \epsilon_{cm}^*}{\epsilon_{cp}^* + 2\epsilon_{cm}^*}\right)}{\left(\frac{r_{ext}}{r_{ext} - th_{cm}}\right)^3 - \left(\frac{\epsilon_{cp}^* - \epsilon_{cm}^*}{\epsilon_{cp}^* + 2\epsilon_{cm}^*}\right)} \quad (10)$$

where  $th_{cm}$  is the thickness of the cell membrane,  $\epsilon_{cm}^*$  and  $\epsilon_{cp}^*$  are respectively the complex permittivities of the cell membrane and the cytoplasm. As for a cell  $th_{cm} \ll r_{ext}$ , this formula can be approximated as (Gascoyne, et al. 1995):

$$\epsilon_{eq}^* = \frac{r_{ext} C_{cm}^* \epsilon_{cp}^*}{r_{ext} C_{cm}^* + \epsilon_{cp}^*} \quad (11)$$

With

$$C_{cm}^* = C_{cm} - j \frac{G_{cm}}{\omega} \quad (12)$$

where  $C_{cm} = \epsilon_{cm}/th_{cm}$  and  $G_{cm} = \sigma_{cm}/th_{cm}$  are the membrane specific capacitance and conductance respectively. The full development can be found in paragraph A.3 in Appendix A.

A similar principle for the calculation of  $\epsilon_{eq}^*$  for layered particles can be applied for the “two-shell”, “three-shell” and “four-shell” model. The related formulas are presented in paragraph A.1 in Appendix A.

Particles and cells are not always spherical and can be elongated along one axis. In this case modeling the particle reaction to the electric field should consider its geometry and orientation. For a homogenous ellipsoidal particle randomly oriented, equation (6) becomes:

$$F_{DEP} = 2\pi a_{ext} b_{ext} c_{ext} \epsilon_m \text{Re}[CM(f)] \nabla E^2 \quad (13)$$

Where the Clausius-Mossotti factor is the average of the Clausius-Mossotti factor in each axis:

$$CM(f) = \frac{CM_x(f) + CM_y(f) + CM_z(f)}{3} \quad (14)$$

And



$$CM_\alpha = \frac{1}{3} \frac{\epsilon_p^* - \epsilon_m^*}{\epsilon_m^* + (\epsilon_p^* - \epsilon_m^*)A_{0\alpha}} \quad (15)$$

With

$$A_{0\alpha} = \frac{abc}{2} \int_0^\infty \frac{ds}{(s + \alpha^2) \sqrt{(s + a^2) * (s + b^2) * (s + c^2)}} \quad (16)$$

$A_{0\alpha}$  is the depolarization factor along the  $\alpha$  axis (x, y or z) and a, b and c are the semi-axis along the x-, y- and z axis respectively.

In his article, Kakutani (Kakutani, et al. 1993) proposed the formula that should be used for an multi-shelled ellipsoids depending on the geometry and the orientation. The related formulas are presented in paragraph A.2 in Appendix A.

### 2.3.2 Cell suspension

In the presence of particles, the effective permittivity of the suspension  $\epsilon_{mix}^*$  depends on the volume fraction  $\phi$  occupied by the particles. It is given by the Maxwell-Garnett mixing equation if the volume fraction  $\phi < 0.1$ :

$$\frac{\epsilon_{mix}^* - \epsilon_m^*}{\epsilon_{mix}^* + 2\epsilon_m^*} = \phi \frac{\epsilon_p^* - \epsilon_m^*}{\epsilon_p^* + 2\epsilon_m^*} \quad (17)$$

which is equivalent, according to (Sihvola and Kong 1988), to the direct formulation:

$$\epsilon_{mix}^* = \epsilon_m^* \left( 1 + 3\phi \frac{\frac{\epsilon_p^* - \epsilon_m^*}{\epsilon_p^* + 2\epsilon_m^*}}{1 - \phi \frac{\epsilon_p^* - \epsilon_m^*}{\epsilon_p^* + 2\epsilon_m^*}} \right) \quad (18)$$

or by the Hanai equation (Hanai 1960), theoretically up to  $\phi < 0.8$  (Hanai 1968, Hanai, et al. 1982):

$$\left( \frac{\epsilon_{mix}^* - \epsilon_p^*}{\epsilon_m^* - \epsilon_p^*} \right) \left( \frac{\epsilon_m^*}{\epsilon_p^*} \right)^{1/3} = 1 - \phi \quad (19)$$

Unfortunately, there is no direct expression for the calculation of  $\epsilon_{mix}^*$  and the value can therefore be obtained either by solving the cubic equation or by

numerical integration with the difference equation of the Hanai equation. The later has been implemented in MyDEP, with the possibility to choose the number of increments. The methodology can be found in (Hanai, et al. 1979, Irimajiri, et al. 1991) and is described in paragraph A.4 in Appendix A.

### 2.3.3 Aggregate modeling

Often biological cells tend to form aggregates of various shapes. While computing the complex permittivity of a cell suspension is relatively feasible, calculating the complex permittivity of touching particles is however not straightforward. Most of the time an aggregate is modeled as an equivalent elementary particle with a specific shape (commonly a sphere or an ellipsoid) and similar electrical properties (Raicu and Feldman 2015). This model has been successfully used by Raicu et al. (Raicu, et al. 1998) to approximate the organization of the liver cells into hepatic plates. They also showed (Raicu and Feldman 2015) that in the specific case of spherical aggregates no differences in the analytical model is seen between a suspension of spherical aggregates and particles individually dispersed. However, if the aggregate is composed of polarized cells interacting electrically with each other or physically connected it is difficult to obtain an analytical model.

Numerical modeling can be used to calculate the electrical potential distribution inside the aggregate and can provide a more accurate solution to obtain the effective complex permittivity of the aggregate.

The equation (19) derived by Hanai for concentrated suspension assumed only far field interactions and therefore is not normally suited for aggregate modeling. However, this equation has qualitatively explained the changed observed during rouleaux formation of erythrocytes aggregates (Irimajiri, et al. 1996). The mitosis phenomenon has also been simulated by Asami (Asami, et al. 1998) as well as the gap junctions in liver (Gersing 1998) and heart (Schaefer, et al. 2002). However, modeling cells in close proximity or in contact through a narrow neck or gap junctions is difficult to perform and requires a lot of computing power.

## 2.4 Software for dielectric modeling

Before performing experiments in the lab with DEP, it is useful to predict the particle and cell responses to the electric field. This requires knowledge of particles or cells properties, which can be obtained from the literature, and implementation of equations related to the particle model.

### 2.4.1 Existing tools

In 1991, Irimajiri and al. (Irimajiri, et al. 1991) published a software for dielectric modeling of particles in suspension called “IMPEDANCE ANALYSIS mini”, programmed in BASIC and presented in Figure 2:4. This program allowed to choose the number of layers for spherical and ellipsoidal models and to calculate the relative permittivity and electrical conductivities. Unfortunately, this program is not available anymore.

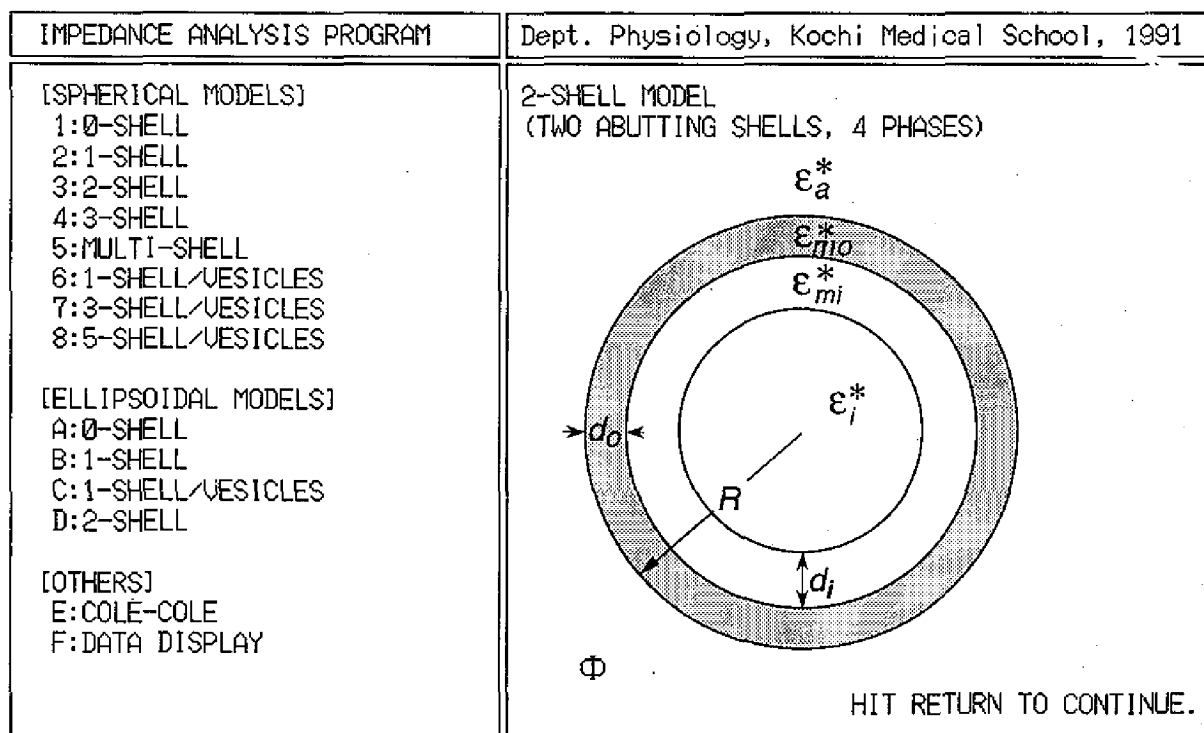


Figure 2:4 Main menu of the “IMPEDANCE ANALYSIS mini” program. Adapted from (Irimajiri, et al. 1991)

Dielectric modeling of particles behavior is often done in MATLAB (Hughes 2002, Pethig 2017) and some authors have proposed MATLAB based programs that are available (Erdem, et al. 2017). Those programs are, however, limited

in terms of functionalities implemented, platform dependent and may lack stability through the different releases of MATLAB and require an access to MATLAB. For those reasons a multiplatform, executable and user-friendly program is needed. This software is intended to be used by both the dielectrophoresis community and for teaching activities. It does not require any prior knowledge of the dielectrophoresis equations.

### 2.4.2 MyDEP software

MyDEP software is a computational software, programmed in Java, aiming to study dielectrophoretic behavior of particles and cells in a suspended medium that was developed in this thesis in collaboration with Olivier Fabregue. More precisely the software can calculate and display the Clausius-Mossotti factor (real and imaginary parts) used in DEP for different conditions (medium, frequency range, particle model). It can also calculate the equivalent permittivities and conductivities of particles alone and in suspension in a medium thanks to the Maxwell-Garnett and Hanai equations. Graphs representing crossover frequencies versus electrical conductivity of the medium are also available.

MyDEP software is written in Java<sup>1</sup> using the swing API and is freely available as a standalone .jar file for Windows, Mac or Linux at <http://doi.org/10.5281/zenodo.1321928>. The installation of Java (also known as the Java Runtime Environment or JRE) is required (<https://java.com/en/download>).

A static website, hosted on GitHub Pages, <https://mydepsoftware.github.io>, was built using Jekyll. This website is composed of different sections:

- “Getting started with MyDEP”: A full manual on how to use MyDEP and the different functions

---

<sup>1</sup> The Java programming was done by Olivier Fabregue.

- “A bit of theory”: Basics of dielectrophoresis and electrorotation
- “Citing MyDEP”: How to cite the software
- “Acknowledgments”: Institutional support for the project
- “Contacts”: Page explaining how to contact the authors

## **2.5 Features, different types of analysis and database**

### **2.5.1 Database**

MyDEP allows the user to specify the electrical as well as the geometrical parameters of the investigated particle. No prior knowledge of the equations behind is required to use the software, which makes it interesting for users non-familiar with DEP. A database compiling information from the literature is provided to help the user to start with already existing data. The user can also enrich the database with new information. A local database is embedded within the application using the SQL database engine SQLite. The Java Database Connectivity (JDBC) API was used to interact with SQLite. The provided database contains for each set of data the name of the model, the authors, the title of the article, the journal where it was published, the year of publication as well as the DOI or URL to help the users to identify where the model they are using is coming from. An example of the database explorer is displayed in Figure 2:5.

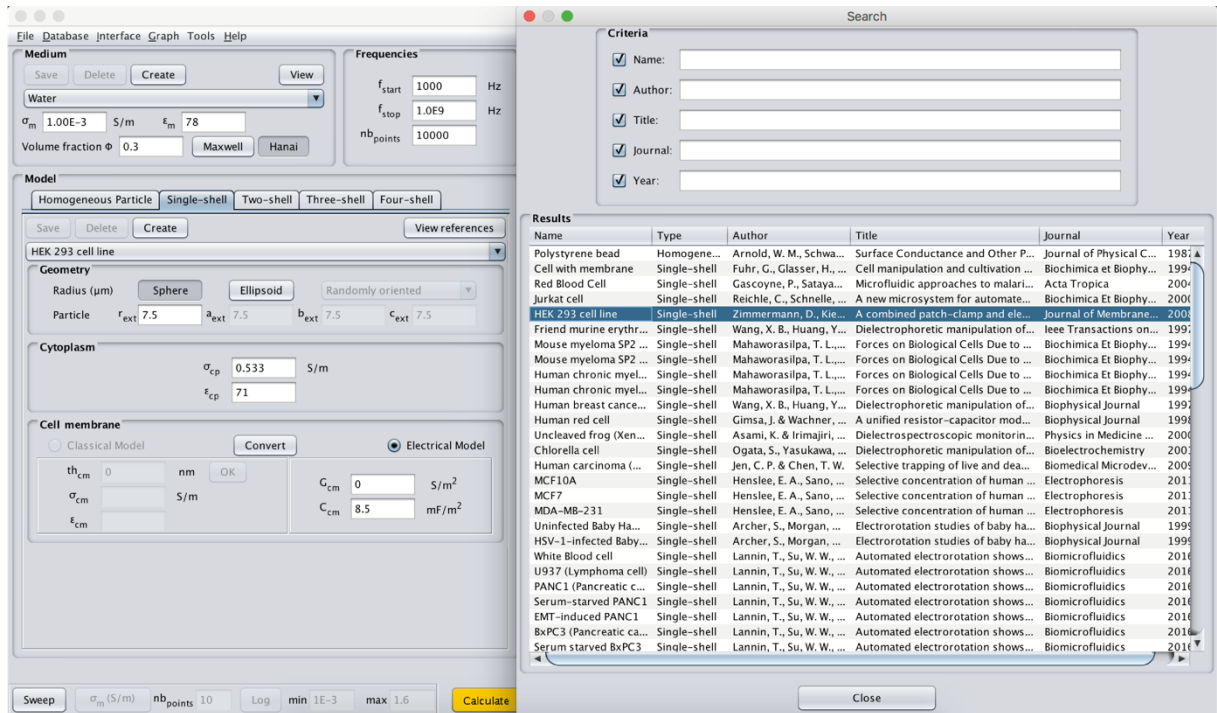


Figure 2:5 Overview of the database explorer (Search) from MyDEP. A click on the desired element from the literature shows the values associated in the interface.

### 2.5.2 CM factor

MyDEP allows the user to display different graphs linked to the dielectric properties of particles and cells. Real and imaginary parts of the Clausius-Mossotti factor can be displayed in the interface. Users can get values about the displayed curves in the “Results” panel. In particular the values of the crossover frequencies, corresponding to the frequencies at which  $Re[CM(f)] = 0$ , are directly accessible as well as the frequencies of the minimum and maximum of  $Im[CM(f)]$ . This graph can be used to determine the direction of the DEP force. As shown in Figure 2:6, viable and non-viable yeast cells will have a different behavior for the same medium conductivity,  $\sigma_m = 7.8 \text{ mS/m}$ . The DEP force which is proportional to  $Re[CM(f)]$  is always higher in magnitude for the viable yeast cells.

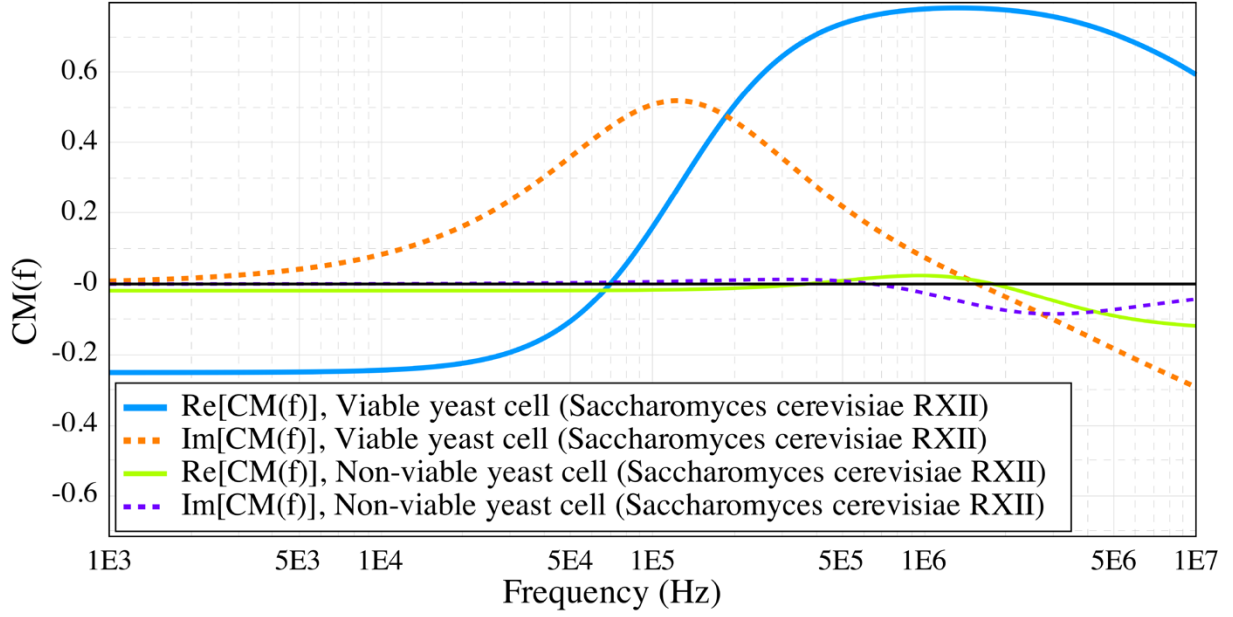


Figure 2:6 Example of  $\text{Re}[CM(f)]$  and  $\text{Im}[CM(f)]$  for viable and non-viable yeast cells suspended in a low conductivity medium ( $\sigma_m = 7.8 \text{ mS/}$ ,  $\epsilon_m = 78$ ). Data from (Talary, et al. 1996). The black line represents the baseline at 0.

### 2.5.3 Parameter sweep

All the parameters of the medium and of the different models can be swept linearly or logarithmically between two values. Figure 2:7 illustrates the graph generated by a logarithmic sweep on ten values of  $\sigma_m$  for Jurkat cells (Reichle, et al. 2000). The more the electrical conductivity increases, the lower the initial values of the  $\text{Re}[CM(f)]$  and the shorter the frequency range where Jurkat cells experience pDEP. As  $\sigma_m$  increases, the frequencies of the maximum and minimum of  $\text{Im}[CM(f)]$  are shifted to higher values up to the point where  $\text{Im}[CM(f)]$  keeps a positive value.

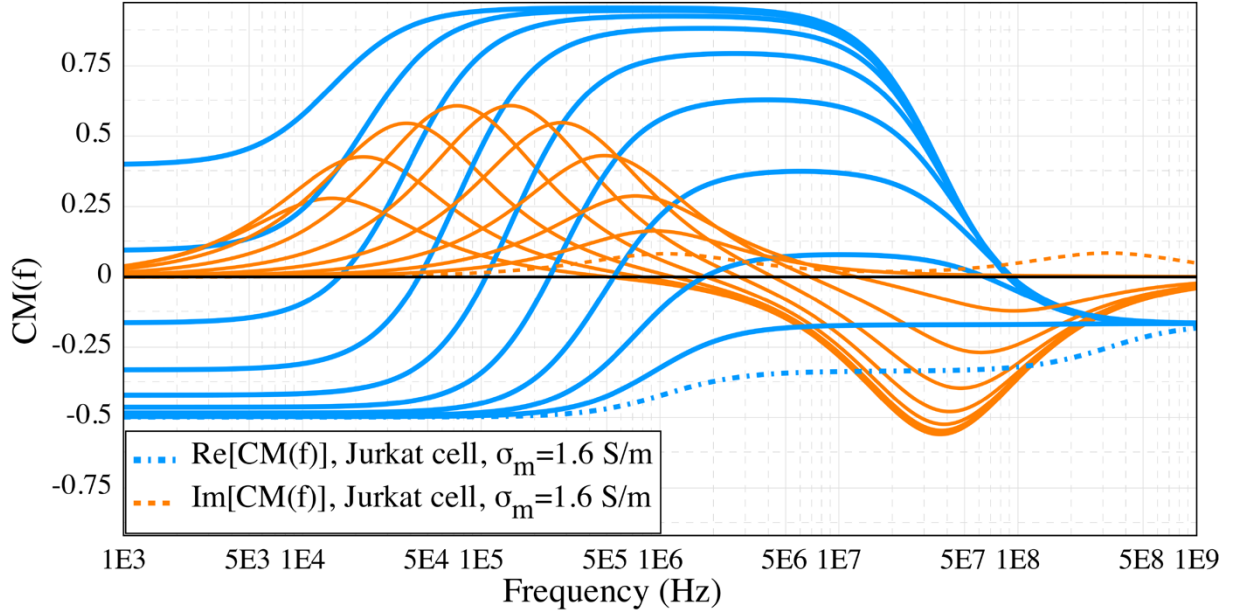


Figure 2:7 Example of the evolution of  $\text{Re}[\text{CM}(f)]$  and  $\text{Im}[\text{CM}(f)]$  with a logarithmic sweep on ten values of  $\sigma_m$  from 1 mS/m to 1.6 S/m for a Jurkat cell. Data from (14). The black line represents the baseline at 0.

#### 2.5.4 Cell separation

Depending on their dielectric properties, different cell types can be separated. Figure 2:8 illustrates that HEK cells (Zimmermann, et al. 2008) and MCF7 cells (Henslee, et al. 2011) have different responses to the electric field with the frequency. The crossover frequency, transition from the nDEP regime to the pDEP regime, are respectively 169 kHz and 65 kHz for the HEK and MCF7 cells in the specified medium. These two cell populations can be separated based on their electrical properties between these frequencies. In particular at 100 kHz (vertical blue line in Figure 2:8) HEK cells experience nDEP contrary to MCF7 cells, which experience pDEP.



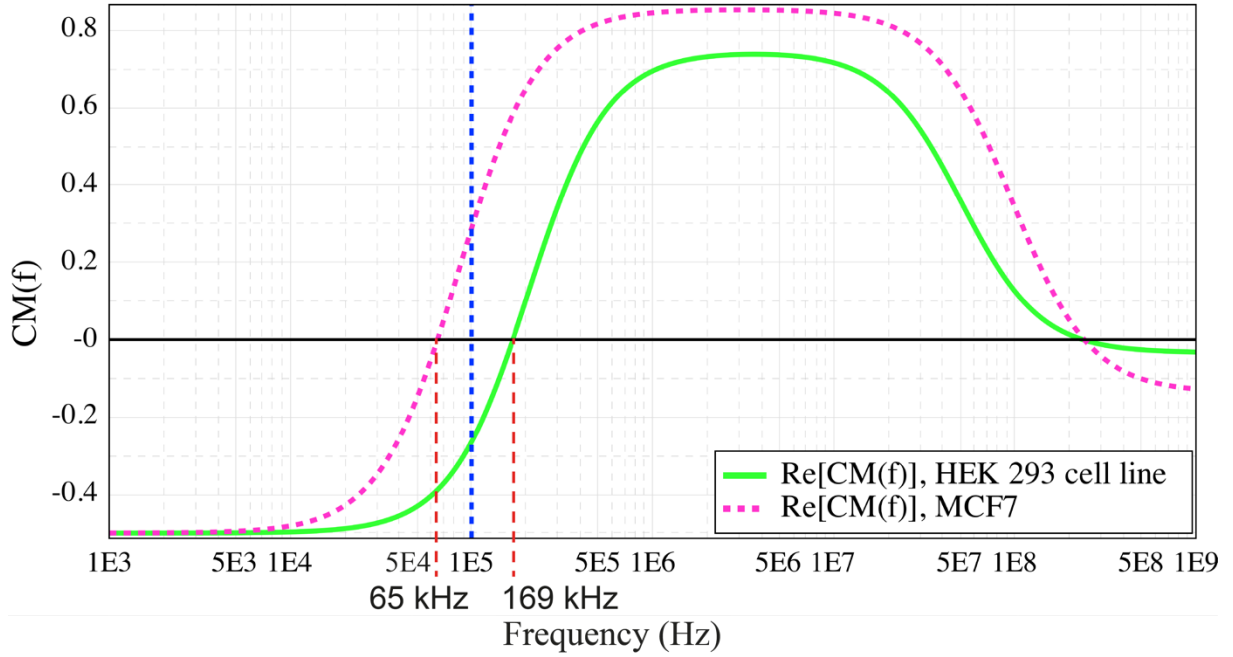


Figure 2:8 Example of the different  $\text{Re}[CM(f)]$  for a HEK cell (Zimmermann, et al. 2008) and a MCF-7 cell (Henslee, et al. 2011) in a medium with  $\sigma_m = 50$  mS/m. The crossover frequencies are respectively 169 kHz and 65kHz. These two cell populations can be separated based on their electrical properties at 100 kHz (vertical blue line).

### 2.5.5 Conductivity and permittivity of cell and suspension

Figure 2:9, Figure 2:10 and Figure 2:11 illustrate how cells and medium properties influence the properties of the suspension. In each of those figures the orange dotted line corresponds to the properties of the medium alone and the blue solid line to the homogenized properties of a HEK cell. The green dashed line corresponds to the properties of the suspension at a specific volume fraction,  $\phi = 0.3$  for those figures.

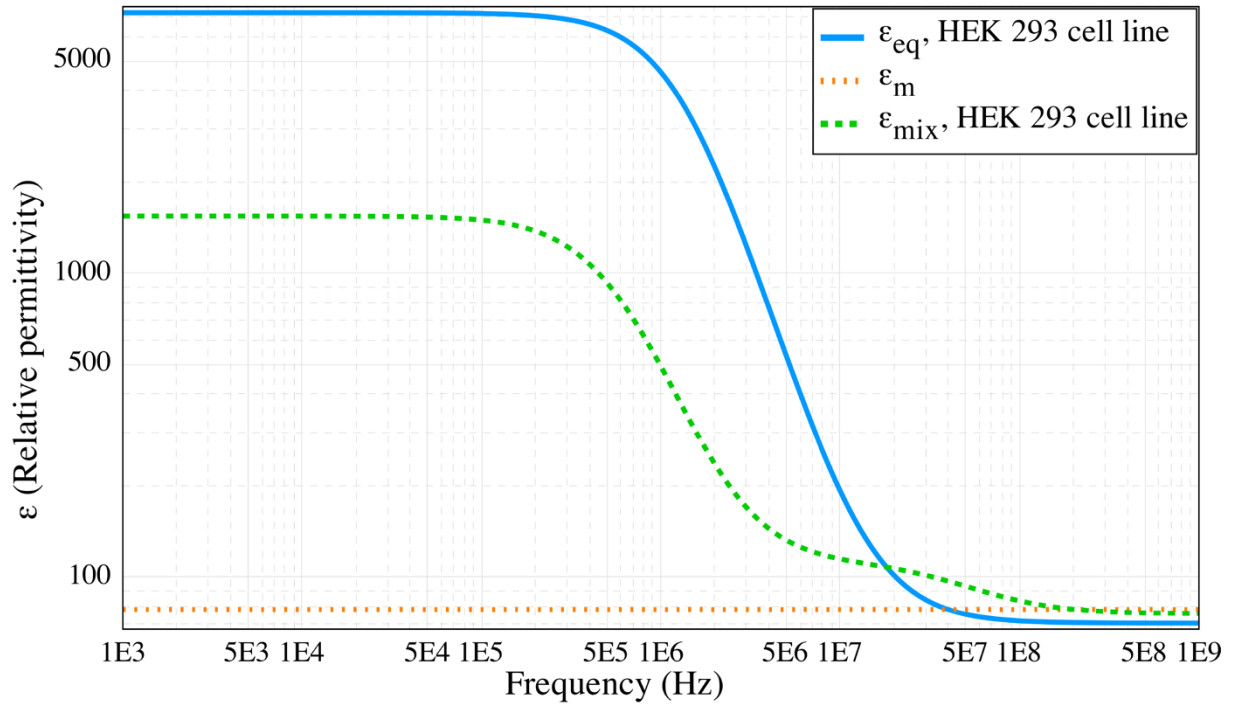


Figure 2:9  $\epsilon_{eq}$ ,  $\epsilon_m$  and  $\epsilon_{mix}$  corresponding to respectively the equivalent relative permittivity of a HEK cell, the relative permittivity of the suspension medium and the equivalent relative permittivity of the suspension of HEK cells at a volume fraction  $\phi=0.3$  (implemented using the Hanai methodology).  $\sigma_m = 0.156$  S/m

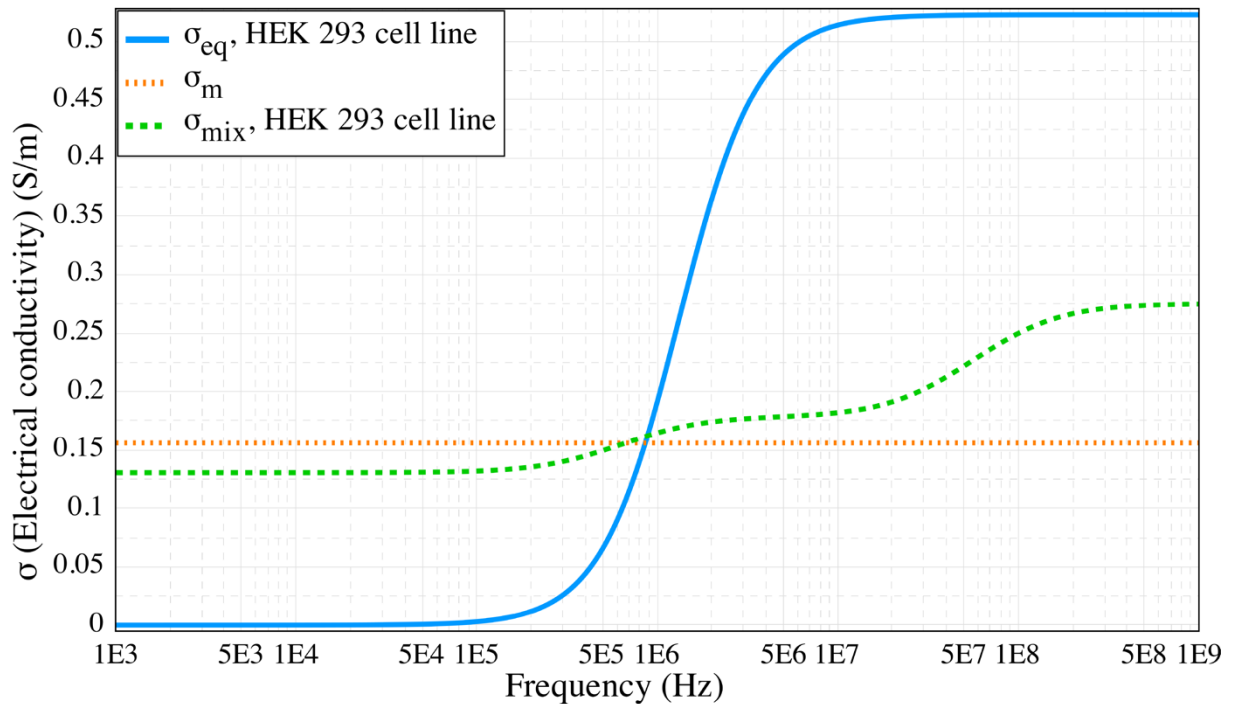


Figure 2:10  $\sigma_{eq}$ ,  $\sigma_m$  and  $\sigma_{mix}$  corresponding to respectively the equivalent electrical conductivity of a HEK cell, the electrical conductivity of the suspension medium and the equivalent electrical conductivity of the suspension of HEK cells at a volume fraction  $\phi=0.3$  (implemented using the Hanai methodology).  $\sigma_m = 0.156$  S/m

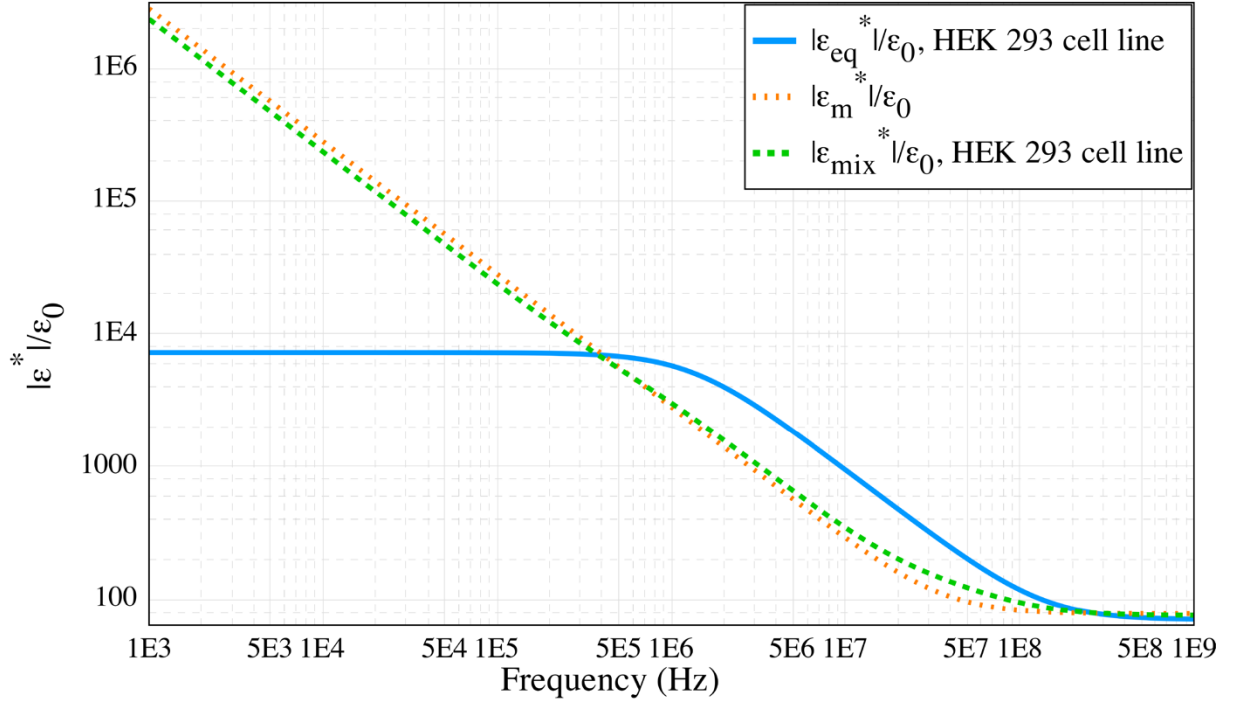


Figure 2:11  $|\varepsilon_{eq}^*|/\varepsilon_0$ ,  $|\varepsilon_m^*|/\varepsilon_0$  and  $|\varepsilon_{mix}^*|/\varepsilon_0$  corresponding to respectively the modulus of the equivalent complex relative permittivity of a HEK cell, the modulus of the complex relative permittivity of the medium and the modulus of the equivalent complex relative permittivity of the HEK cells in suspension in the medium at a volume fraction  $\phi=0.3$  (implemented using the Hanai methodology).  $\sigma_m = 0.156$  S/m

### 2.5.6 Crossover frequencies

Crossover frequencies correspond to the frequencies at which  $Re[CM(f)] = 0$ . It corresponds to the transition from a nDEP regime to a pDEP regime and vice versa. For each electrical conductivity of the medium  $\sigma_m$ , this value might differ. Figure 2:12 illustrates the evolution of the crossover frequencies with  $\sigma_m$  for Jurkat cell. In this figure, the lower crossover, in blue, corresponds to the transition from nDEP to pDEP and the upper crossover frequency, in orange, to the transition from pDEP to nDEP. At approximately  $\sigma_m = 0.392$  S/m, there is only one crossover frequency point which means that, at a higher conductivity, cells only experience nDEP.

Crossover frequencies are commonly used as a discriminatory factor between different cell types.

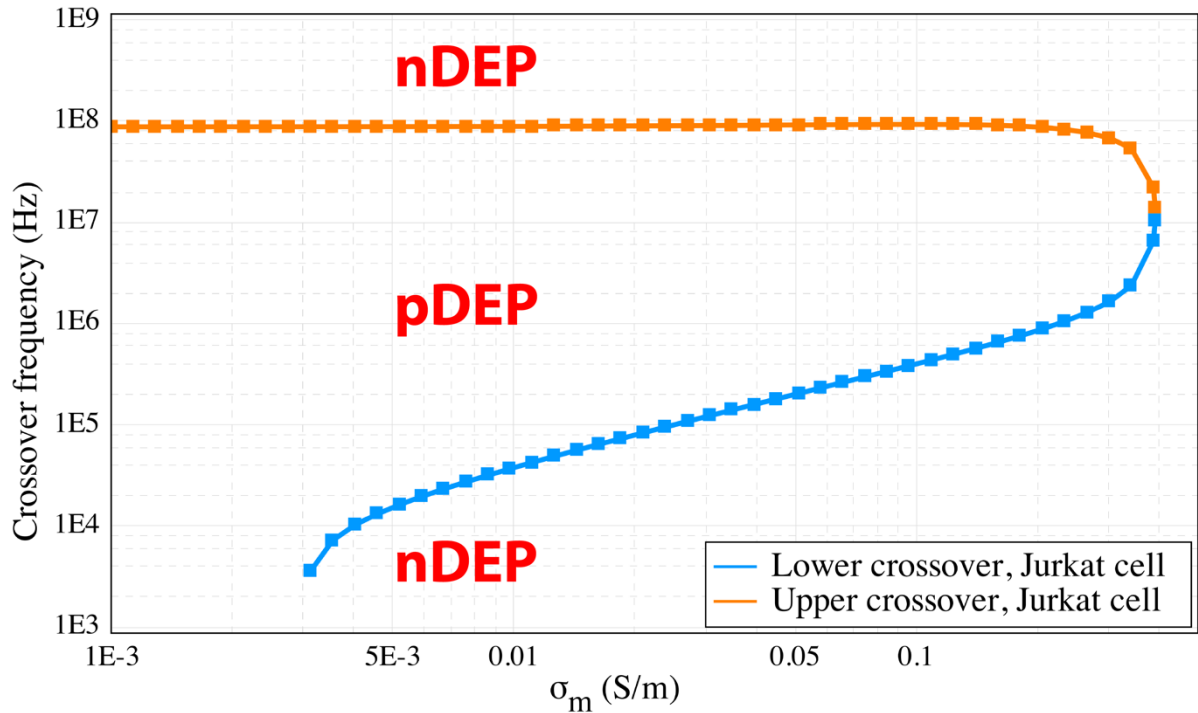


Figure 2:12 Evolution of the crossover frequencies for a Jurkat cell for 50 conductivities logarithmically spaced between 1 mS/m and 0.5 S/m.

### 2.5.7 Graph export

All the graph generated in MyDEP are fully editable. The font style and size, the color, the legend content, the curve style and size can all be adjusted directly in the interface. The export menu enables the user to directly generate the displayed graph as an image file with the possibility to tune the size and resolution as well as the file format. A CSV file can be generated if additional data processing is required and not already available in the MyDEP software.

## 2.6 Conclusions

MyDEP offers a new software alternative aimed at both DEP specialists and beginners. The software, delivered with a database compiling data from the literature, which can be updated automatically, aims at centralizing the electrical properties published in the literature and making them accessible easily to generate graphs. MyDEP also offers the possibility to import the user's own data points to compare them to different cell models. Future developments of MyDEP will be towards parameters extraction from the user's own dataset and to impedance calculation.

## Dielectrophoresis theory and modeling with MyDEP

MyDEP will be used in the next chapter to predict the behavior of different kind of particles and cells at different electrical conductivities.

# Chapter 3 Trapping design and simulations

This chapter presents the important parameters in DEP trapping for particles and cells. The physics of the trapping is discussed as well as the effect of electric field on cells. COMSOL Multiphysics simulations are used to predict the position of the trapped particles. The content of the chapter is partially published in the article (Cottet, et al. 2019b):

Cottet, J., Kehren, A., Lasli, S., van Lintel, H., Buret, F., Frénéa-Robin, M. & Renaud, P. Dielectrophoresis-assisted creation of cell aggregates under flow conditions using planar electrodes. *Electrophoresis* 40, 1498-1509, doi:10.1002/elps.201800435 (2019).

## 3.1 DEP Trapping

### 3.1.1 Physics behind the trapping:

In order to trap particles and cells with dielectrophoresis in a microchannel, the physics of trapping should be properly understood. For a particle to be trapped, the net force applied to this particle should be zero. The trapping position is stable if the force field brings the particle back to this trapping position after small disturbances.

The forces which may be involved in the trapping are:

- The DEP force
- The hydrodynamic viscous drag force
- The gravitational and buoyancy force
- The electrothermal forces
- Brownian motion
- Particle-particle interaction

#### 3.1.1.1 The DEP force

The force exerted by the non-uniform electric field on spherical particle has been previously described in Chapter 2:

$$\mathbf{F}_{\text{cDEP}} = 2\pi\epsilon_m\epsilon_0r_{ext}^3\text{Re}[CM(f)]\nabla E_{RMS}^2 \quad (20)$$

The expression of the force is valid if the field inhomogeneity can be considered as constant across the particle.

For ellipsoidal particles, the expression of the force is given in Chapter 2 and Appendix A.

#### 3.1.1.2 The hydrodynamic viscous drag force

For a particle immersed in a moving liquid, the fluid will exert a force, called hydrodynamic viscous drag force, on the non-moving particle that will affect its velocity (Morgan and Green 2003). The fluid motion will cause this force to pull the particle along. If the particle is at the fluid velocity, no force is applied on the particle. In microsystems, because of the small Reynolds number, the flow

can be considered as laminar. This regime is called creeping flow or also Stokes flow.

The expression of the drag force on a spherical particle is:

$$\mathbf{F}_{Drag} = 6\pi r_{ext}\eta\mathbf{v} \quad (21)$$

with  $\eta$  the dynamic viscosity of the medium and  $\mathbf{v}$  the fluid velocity relative to the particle.

The constant term in front of  $\mathbf{v}$  is called the friction factor and depends on the particle geometry (Berg 1993, Morgan and Green 2003).  $6\pi r_{ext}\eta$  corresponds to the friction factor of a sphere.

### ***3.1.1.3 The gravitational force and buoyancy force***

The expression of the net force between the gravitational and buoyancy force on a particle is:

$$\mathbf{F}_{grav} = \frac{4}{3}\pi r_{ext}^3(\rho_p - \rho_m)\mathbf{g} \quad (22)$$

where  $\rho_p$  and  $\rho_m$  refer to the densities of the particle and the medium respectively, and  $\mathbf{g}$  is the gravitational acceleration constant. Cells and beads are usually denser than the medium and will tend to sediment.

### ***3.1.1.4 The electrothermal forces***

Since the voltage applied on the electrodes will create a power dissipation, a thermal gradient will arise in the solution which will in turn generate gradients of electrical conductivity and permittivity. Those phenomena are described by the field of electrohydrodynamics (EHD) (Castellanos 1998).

### ***3.1.1.5 Brownian motion***

The Brownian motion, the indeterministic movement of particle in a medium, is due to the thermal energy of a system caused by the collisions between vibrating molecules of a solution and larger particles. Brownian motion can usually be neglected for particle bigger than 1  $\mu\text{m}$  (Morgan and Green 2003).



### ***3.1.1.6 Particle-particle interaction***

Particles polarized by the electric field will behave as dipoles and hence might interact together due to their induced dipolar moment which may lead to the formation of aggregates or the so called “pearl chain” as described by Jones (Jones 1995).

### ***3.1.1.7 Conclusion on the forces***

For a particle in the tens of  $\mu\text{m}$ , the most important forces to consider are the DEP force and the hydrodynamic forces.

## **3.1.2 Effects of electric field on cells**

During dielectrophoretic trapping, cells are exposed to strong electric fields that may affect the physiology of cells. The main effects on cells are mostly due to current-induced heating and direct interactions with the field (Voldman 2007).

### ***3.1.2.1 Current-Induced Heating***

The use of electric fields in an electrically conductive medium will cause power dissipation per fluid unit volume due to Joule effect equal to (Ramos, et al. 1998):

$$P = \sigma_m E^2 \quad (23)$$

For interdigitated castellated electrodes, the incremental rise of temperature can be estimated as:

$$\Delta T \approx \frac{\sigma_m V_{rms}^2}{k} \quad (24)$$

With  $k$  the thermal conductivity of the medium.

While very-high temperature might lead to cell death, smaller temperature increase also have a physiological effect on cells (Weaver, et al. 1999). A common rule of thumb is to try to limit those temperature variations under  $1^\circ\text{C}$  for mammalian cells (Voldman 2006).

### ***3.1.2.2 Direct Electric-Field Interactions (transmembrane voltage)***

Electric field can also have an effect on cell membranes (Tsong 1992). The additional transmembrane voltage added by the electric field, usually in the

order on tens of mV, can affect the ions gated channels (Catterall 1995). An approximation of the imposed transmembrane voltage is (Foster and Schwan 1989):

$$|V_{tm}| = \frac{1.5|E|r_{ext}}{\sqrt{1 + (\omega\tau)^2}} \quad (25)$$

With the time constant  $\tau$

$$\tau = \frac{r_{ext}C_{cm} \left( \frac{1}{\sigma_{cp}} + \frac{1}{2\sigma_m} \right)}{1 + r_{ext}G_{cm} \left( \frac{1}{\sigma_{cp}} + \frac{1}{2\sigma_m} \right)} \quad (26)$$

Where  $C_{cm}$  and  $G_{cm}$  are the membrane specific capacitance and conductance respectively, as presented in Chapter 2.

At low frequencies,  $|V_{tm}|$  can be approximated to  $1.5|E|r_{ext}$  and decreases above the characteristic frequency  $\tau^{-1}$  which is in the order of the MHz for mammalian cells.

### 3.1.3 Trapping parameters

The choice of a given electrode configuration (size, shape, location relative to the microchannel, etc) is obviously a critical determinant of trapping efficiency. Then, for a given configuration, 4 parameters can be adjusted:

- The electrical conductivity of the medium  $\sigma_m$
- The trapping frequency of the electric field  $f_{DEP}$
- The voltage applied on the electrode  $V$
- The flow speed  $v$  (and flow rate  $Q$ )

For both polystyrene beads and HEK cells, trapping with nDEP with the lowest possible voltage requires the real part of the Clausius-Mossotti to be around - 0.5 (maximum negative achievable amplitude for a spherical particle). This can be performed in highly conductive medium (Fuhr, et al. 1994, Glasser and Fuhr 1998) but might lead to Joule heating and electrothermal flow motion (Puttaswamy, et al. 2010). Working with a lower electrical conductivity will reduce the Joule heating while keeping the same dielectrophoretic response at

low frequencies. Polystyrene beads and HEK cells dielectrophoretic behavior were predicted in PBS ( $\sigma_m = 1.5 \text{ S/m}$ ) and 10X PBS ( $\sigma_m = 0.156 \text{ S/m}$ ) as presented in Figure 3:1 and Figure 3:2. The parameters used are  $\{\sigma_p = 7\text{E} - 6 \text{ S/m}$  and  $\epsilon_p = 2.56\}$  for polystyrene beads (Arnold, et al. 1987) and  $\{r_{ext} = 7.5 \text{ }\mu\text{m}, \sigma_{cp} = 0.533 \text{ S/m}, \epsilon_{cp} = 71, G_{cm} = 0 \text{ S/m}^2$  and  $C_{cm} = 8.5 \text{ mF/m}^2\}$  for HEK cells (Zimmermann, et al. 2008).

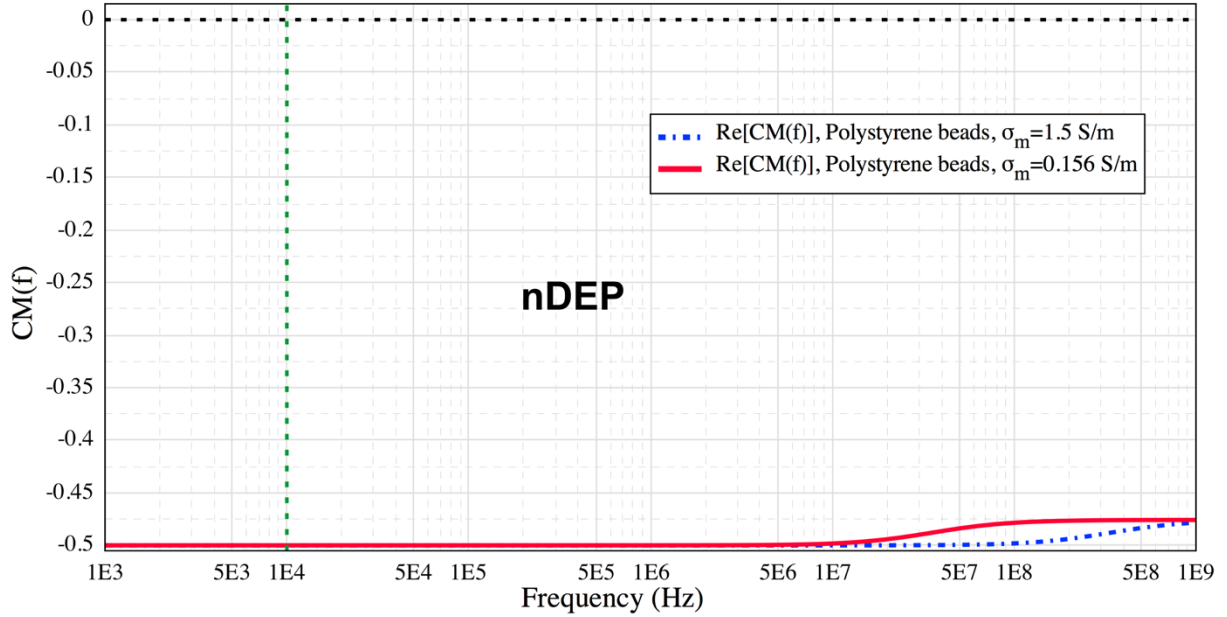


Figure 3:1 Real part of the Clausius-Mossotti factor for polystyrene beads in two media  $\sigma_m = 1.5 \text{ S/m}$  (blue dash dotted line) and  $\sigma_m = 0.156 \text{ S/m}$  (red line). The transition from nDEP to pDEP is represented by the black dotted line. At 10 kHz, polystyrene beads experience nDEP with the maximum amplitude in both media. Graph generated using MyDEP software (Cottet, et al. 2019a).

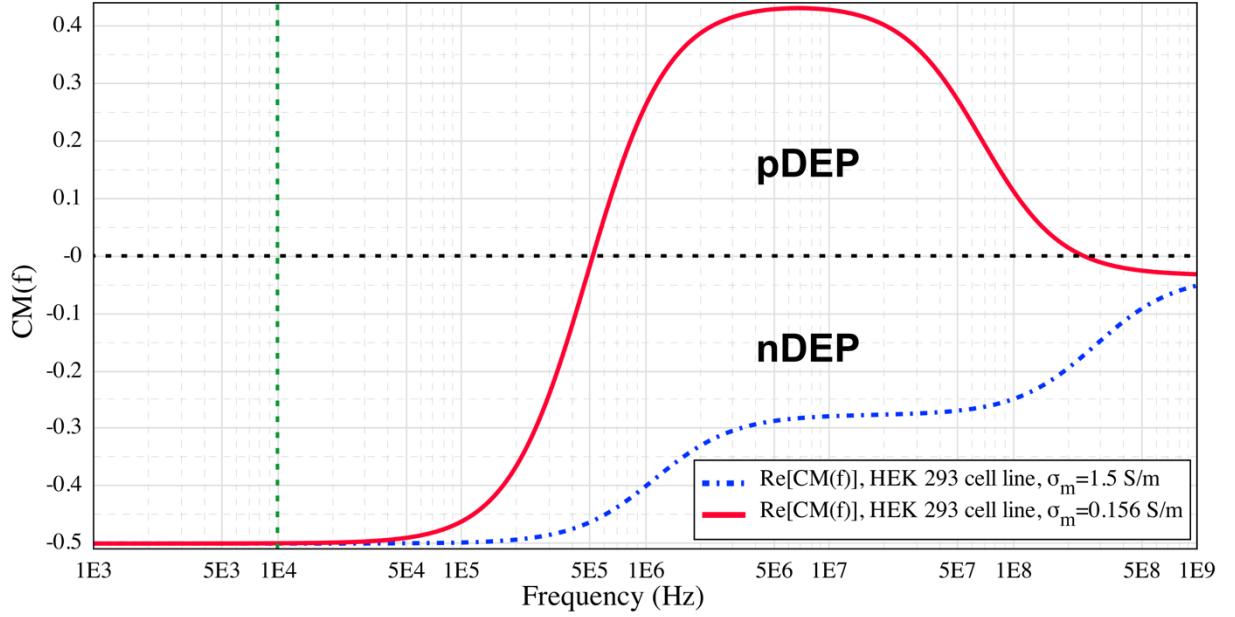


Figure 3:2 Real part of the Clausius-Mossotti factor for a HEK cell in two media with  $\sigma_m = 1.5$  S/m (blue dash dotted line) and  $\sigma_m = 0.156$  S/m (red line). The transition from nDEP to pDEP is represented by the black dotted line. At 10 kHz, HEK cells experience nDEP with the maximum amplitude in both media. Graph generated using MyDEP software (Cottet, et al. 2019a).

As it can be seen on the plots of  $Re[CM(f)]$  in Figure 3:1 and Figure 3:2, obtained using the MyDEP software (Cottet, et al. 2019a), the dielectrophoretic force stays maximal (nDEP) for frequencies lower than 10 kHz. Thus  $\sigma_m = 0.156$  S/m was selected as well as  $f_{DEP} = 10$  kHz.

### 3.1.4 Trapping design

This test design used to investigate the trapping of particles and cells is composed of 8 coplanar electrodes arranged in circle as presented in Figure 3:3. Each electrode is 100  $\mu\text{m}$  long and 50  $\mu\text{m}$  wide. The fluidic inlet and outlet are respectively located at electrodes 1 and 5. A recess of 50  $\mu\text{m}$  separates each electrode from the trapping chamber. This design offers a high flexibility to test different configurations of the electrodes to trap particles and cells with dielectrophoresis. Depending on the number of electrodes used and the operation mode (static or flow conditions), different configurations of the electrodes can be tested.

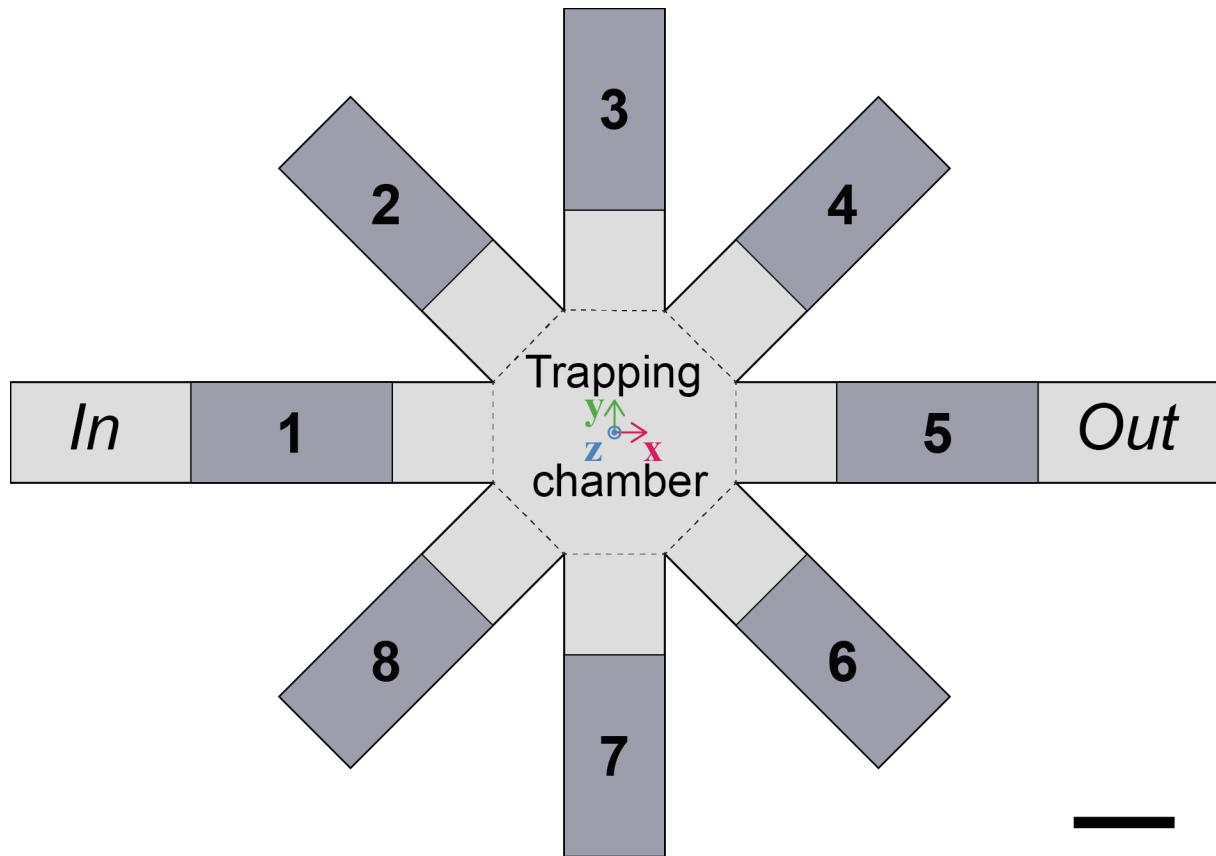


Figure 3:3 Trapping design composed of 8 electrodes arranged in circle (dark gray rectangles). The fluidic inlet and outlet are respectively located at electrodes 1 and 5. All electrodes are separated from the trapping chamber by a 50  $\mu\text{m}$  recess. Scalebar 50  $\mu\text{m}$ .

The electrodes are designed using the so-called “liquid electrodes” principle (Demierre, et al. 2007) as illustrated in Figure 3:4. In this configuration, coplanar electrodes are positioned at the bottom of dead-end chambers. This creates a homogeneous electric field over the channel height, as illustrated in Figure 3:4 E, if the distance of the electrodes to the channel is at least equal to the channel height (Demierre 2008).

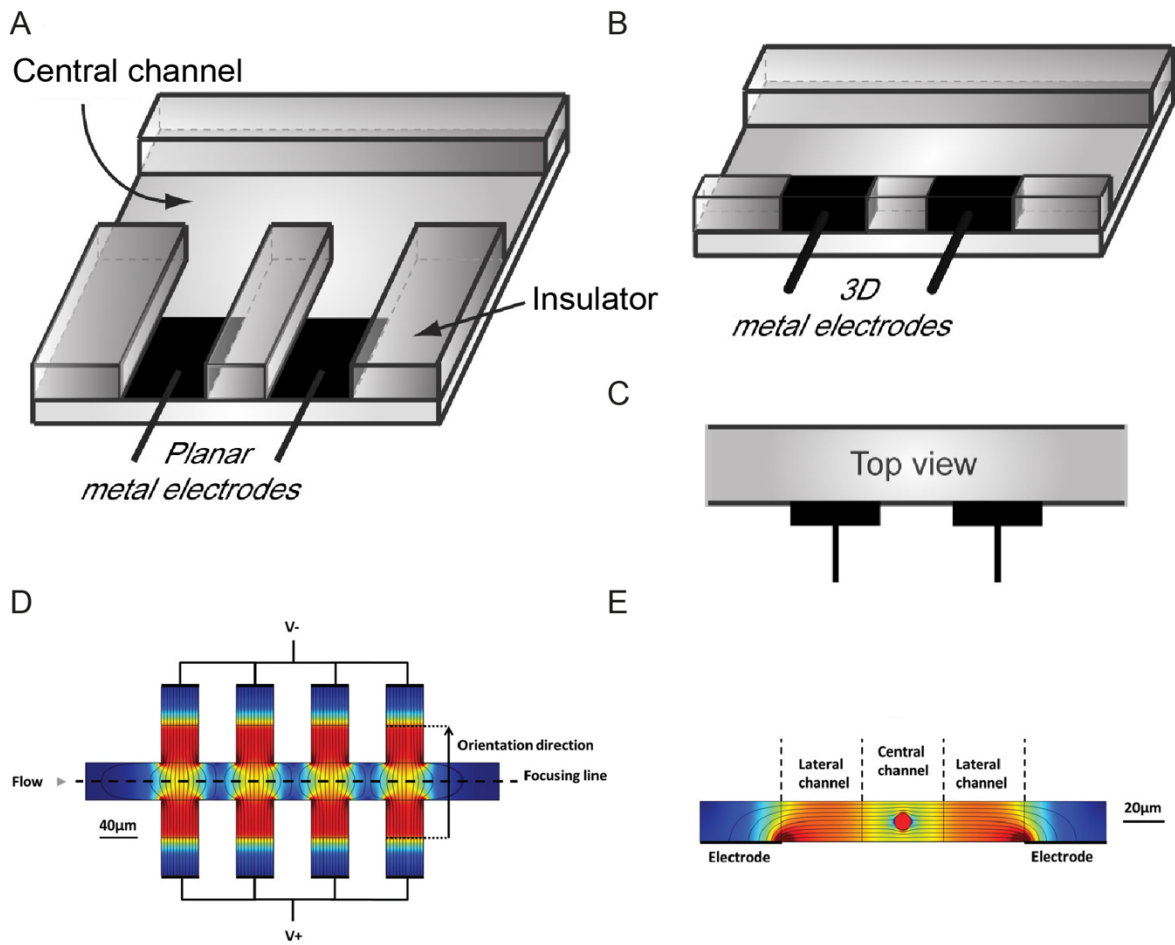


Figure 3:4 Design principle of liquid electrodes located on the same side of a microchannel A) Coplanar electrodes located on dead-end side chambers are equivalent to B) 3D electrodes located in the sidewall of the central channel. C) Top view of the simplified representation of the liquid electrodes. A) B) and C) are adapted from (Demierre 2008). D) Top and E) side view of the liquid electrodes located on both sides of the microchannel. D) and E) are adapted from (Shaker, et al. 2014).

In our design, the “3D equivalent” electrodes, presented in Figure 3:4 are used to trap particles and cells in the chamber. With such design the liquid can enter and exit the trapping chamber from electrodes 1 and 5, respectively.

As presented in Figure 3:3, a complex geometry was chosen for the trapping chamber, which prevents the use of an analytical model for the field calculation. The calculation of the electric field in such geometry requires the use of numerical method such as a finite element method. Since with the liquid electrodes the electric field is homogeneous vertically at a distance from the electrode equal to the channel height (Demierre 2008), 2D simulations can be used to get a first insight on the trapping capability of the design. 3D

simulations can then be performed afterwards to get the correct values of the voltages needed for trapping.

## 3.2 Finite element simulations

### 3.2.1 COMSOL Multiphysics simulations

The modeling of cell and particle trapping was performed using COMSOL Multiphysics 5.3 and the add-on AC/DC and Particle Tracing modules. Simulated particles were configured as single-shell particles (composed of a cytoplasm surrounded by a thin membrane as presented in Chapter 2 with HEK cell properties from the literature ( $r_{ext} = 7.5 \mu m$ ,  $\sigma_{cp} = 0.533 S/m$ ,  $\epsilon_{cp} = 71$ ,  $G_{cm} = 0 S/m^2$  and  $C_{cm} = 8.5 mF/m^2$ ) (Zimmermann, et al. 2008). The equation used to implement the single-shell model with  $G_{cm}$  and  $C_{cm}$  in COMSOL Multiphysics are presented in paragraph B.1 in Appendix B. The AC signal applied to each electrode was a sine wave of amplitude  $10 V_{p(peak)}$  and frequency 10 kHz.

### 3.2.2 Trapping simulation and test design

#### 3.2.2.1 Flow simulations

For this design the flow speed was set to  $500 \mu m/s$  and the particles were released from the inlet located on the left of each design. Since the channel height and width are both  $50 \mu m$ , such speed will correspond to a flow rate of  $1.25 \text{ nl/s}$  ( $4.5 \mu l/h$ ).

The fluid velocity profile in the chip is presented in Figure 3:5 A. The flow profile, originally set as constant at the microchannel inlet, will be parabolic and established after  $40 \mu m$  and in the trapping chamber as shown in Figure 3:5 B. The flow speed will be reduced in the trapping chamber, which will facilitate particle trapping.

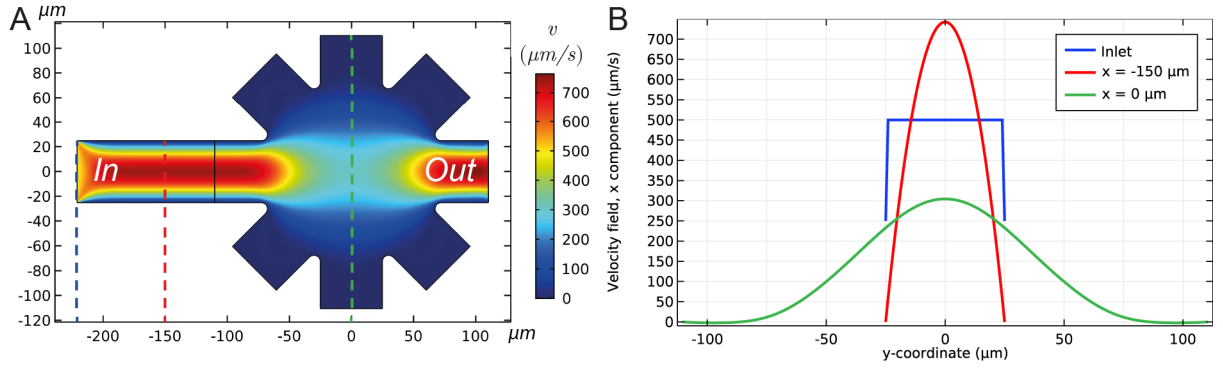


Figure 3:5 A) COMSOL Multiphysics 2D simulation of the fluid velocity profile along the x axis, in  $\mu\text{m/s}$ , in the chip with an inlet velocity of  $500 \mu\text{m/s}$ . B) Flow velocity profile along y at the inlet (in blue), at  $x = -150 \mu\text{m}$  (in red) and in the center of the trapping chamber (in green).

Reducing the flow rate enables to reduce the amplitude of the electric field but if this value is too low, particles will sediment in the microchannel and will not reach the trapping chamber. On the contrary, a high flow rate requires a high voltage on the electrode which may lead to overheating of the suspension medium.

If another force is exerted on the particle, then the fluid starts to exert a viscous drag force on the particle.

### 3.2.2.2 *Electric field and dielectrophoresis simulations*

To trap particles in the microchannel, the DEP force should compensate the viscous drag force. A sinusoidal trapping voltage  $V_{DEP} = 10 V_p (V_{peak})$  at 10 kHz was applied to the electrodes. Various combinations of those 8 electrodes were simulated in COMSOL Multiphysics with the particle tracing module. This first set of simulations offers the possibility to evaluate qualitatively the trapping and to compare the different trapping configurations. The results are presented in Table 1 and with more details in paragraph B.2 in Appendix B.



## Trapping design and simulations

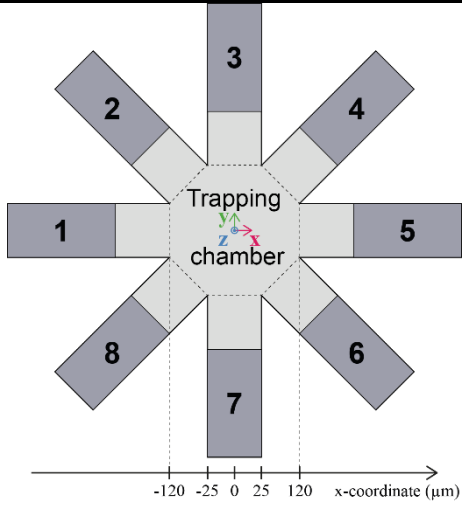
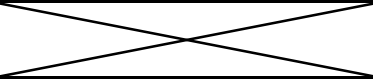
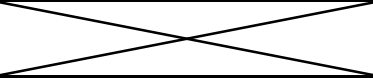
Number of active electrodes	Electrodes at		x trapping position	
	+V	-V	$\mu\text{m}$	
	2	4	6	
	3	5	4/6	24
		5	3/7	9
		5	2/8	On electrodes 4 and 6
	4	3/4	6/7	
	5	3/5/7	4/6	45
	7	4/5/6	2/3/7/8	-36

Table 1 Trapping result for each configuration of the electrodes tested in simulation. The trapping position is indicated with a number corresponding to the center of the particle of by a cross if the particle is not trapped.

Among the different configurations tested, 5 configurations enabled the trapping of 15  $\mu\text{m}$  cells with HEK properties in the simulation under flow conditions:

- With 3 active electrodes
  - a. Electrode 5 at +V and Electrodes 4/6 at -V
  - b. Electrode 5 at +V and Electrodes 3/7 at -V
  - c. Electrode 5 at +V and Electrodes 2/8 at -V
- With 5 active electrodes
  - a. Electrode 4/5/6 at +V and Electrodes 3/7 at -V
- With 7 active electrodes
  - a. Electrode 4/5/6 at +V and Electrodes 2/3/7/8 at -V

It is important to notice that trapping with 2 electrodes (4 at +V and 6 at -V) or 4 electrodes (3 and 4 at +V and 6 and 7 at -V) does not work for this voltage as shown in Table 1. The particles get centered in the trapping chamber and slow down but do not get trapped. Some configurations like 3(c) will trap the particles but will direct them in the recess of the unused electrodes 4 and 6.

### 3.2.3 All results

The best trapping configuration is the one that offers the highest DEP force on the particle to compensate the drag force. This configuration corresponds to the configuration 3(a) displayed in Figure 3:6 A). The evolution of  $|E^2|$  along the axis  $y=0$  is presented in Figure 3:6 B).

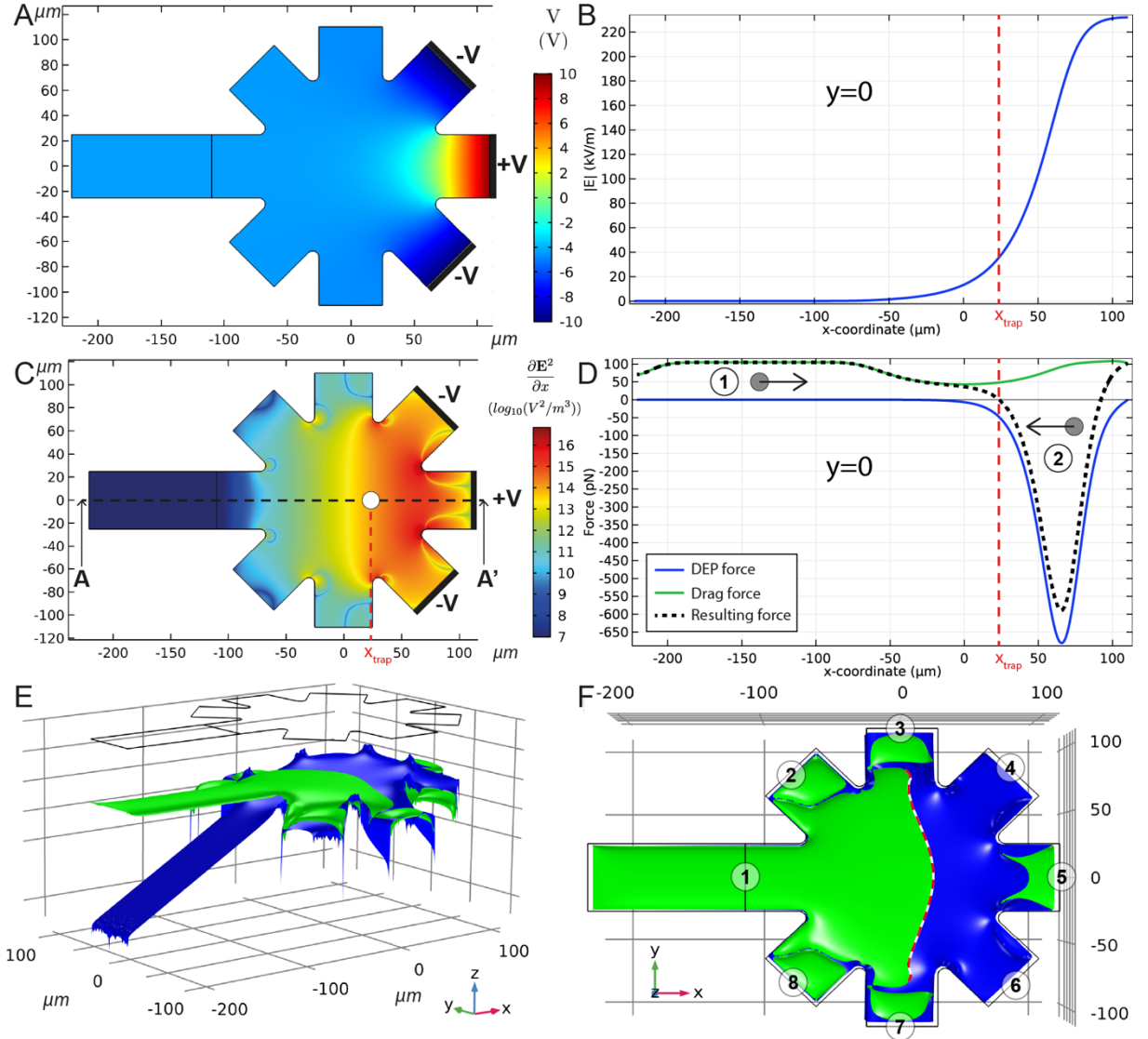


Figure 3:6 A) 2D simulation of the electric potential in the chip. B) Evolution of  $|E|$  along the x axis. C) 2D simulation of the trapping position of a cell using 3 electrodes (4, 5 and 6) supplied with  $V=10 V_p$  at 10 kHz. The surface represents  $\frac{\partial E^2}{\partial x}$ . The white dot indicates the trapping position of a HEK cell (diameter 15  $\mu m$ ). D) Evolution of the DEP and drag forces along the AA' cut. The resulting force is represented with the black dashed line and the red dashed vertical line indicates the position where the resulting force is equal to zero. The gray dot with the arrow indicates the direction of the force on the particle. E) Side and Top F) 3D representations of the amplitudes of the DEP (in blue) and drag (in green) forces along the x axis in the chip. The white/red dashed line in F) indicates where the x component of two forces are equal in the trapping chamber. The electrode numbers are indicated. A logarithmic scale is used for both representations.

## Trapping design and simulations

Since the DEP force is linked to  $\nabla E_{RMS}^2$ , the x component of the DEP force, proportional to  $\frac{\partial E^2}{\partial x}$ , represented by the surface in Figure 3:6 C), should overcome the drag force to allow cell trapping. In this case the particles should be stopped at approximately 24  $\mu\text{m}$  of the center of the chamber when the resulting force (black dashed line) is equal to zero as shown in Figure 3:6 D), marked by the red vertical dashed line  $x_{trap}$ . A 3D representation of the amplitudes of the DEP and drag force is provided in Figure 3:6 E) and F). The intersection between the two surfaces corresponds to a resulting force equal to zero. In the chip the particle will first reach the x trapping position indicated by the white/red dashed line in Figure 3:6 F).

Figure 3:7 presents the evolution of the y component of the DEP and drag forces for the chosen configuration of the electrodes.

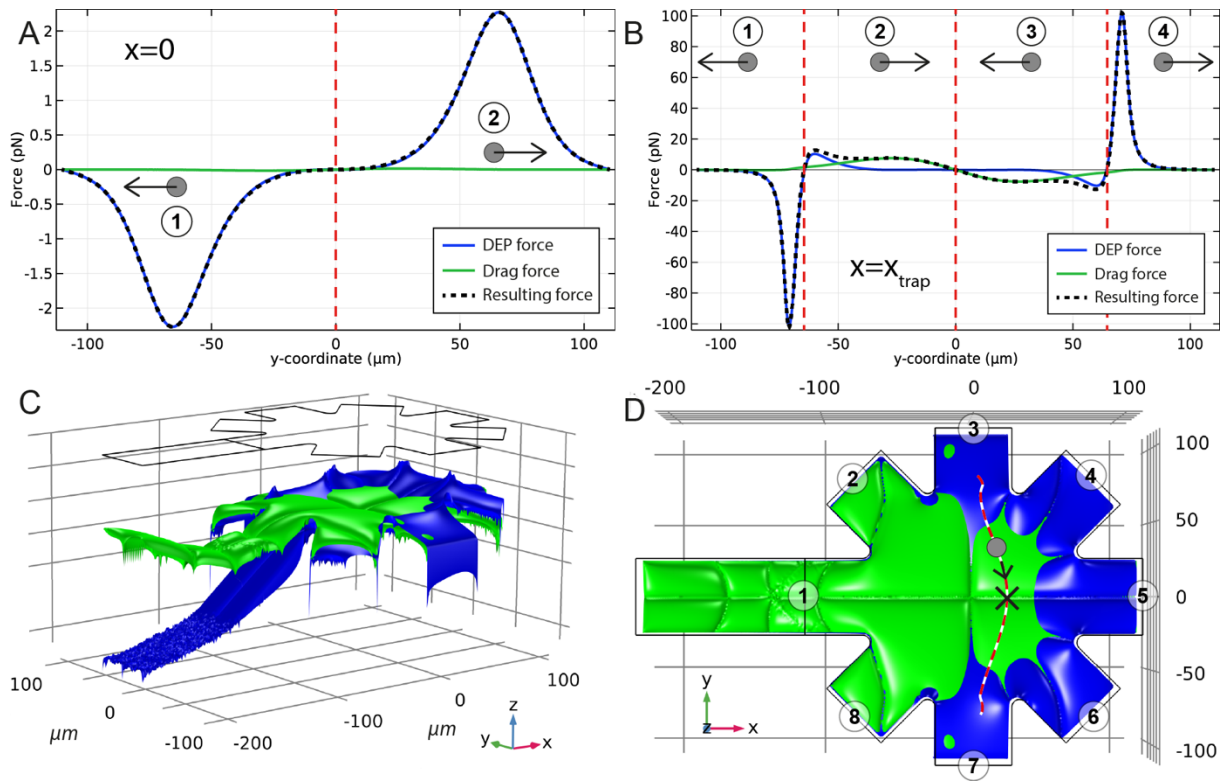


Figure 3:7 Evolution of the DEP and drag forces along the y axis at A)  $x=0$  and B)  $x=x_{trap}=24 \mu\text{m}$ . The resulting force is represented with the black dotted line and the red dotted line indicates the positions where the resulting force is equal to zero. The gray dot with the arrow indicates the direction of the force on the particle. C) Side and D) Top 3D representations of the amplitudes of the DEP (in blue) and drag (in green) forces along the y axis in the chip. The white/red dashed line in D) indicates where the x component of two forces are equal (from Figure 3:6 F) and the black cross the final position of the particle. The electrode numbers are indicated. A logarithmic scale is used for both representations.

At  $x=0$ , as displayed in Figure 3:7 A), the  $y$  component of the drag force is much smaller than the  $y$  component of the DEP force. In this case the particle would be exposed to a resulting force pushing it far from the center depending on its initial lateral position, either toward electrode 7 (zone 1) or electrode 3 (zone 2).

At the trapping position  $x=x_{\text{trap}}$  presented in Figure 3:7 B), both the DEP and drag forces push the particle towards the center of the microchannel in a stable trapping position (zones 2 and 3). Zones 2 and 3 are delimited by two other dashed lines which would correspond to two other equilibrium positions located at  $\pm 64 \mu\text{m}$ ). However, those two other equilibrium positions are unstable since a particle located farther than  $50 \mu\text{m}$  from the center will be pushed either towards electrode 7 (zone 1) or electrode 3 (zone 4). Figure 3:7 C) and D) present a 3D representation of the amplitude of the  $y$  component of the two forces.

The amplitude of the  $y$  component is two orders of magnitude smaller than the amplitude of the  $x$  component. In all cases, the particles will first reach the trapping position due to the  $x$  component of the force (white/red dashed line in Figure 3:7 D) and then get centered in the microchannel due to the  $y$  component as illustrated in Figure 3:7 D) with the grey particle and the arrow until it reaches the black cross.

The trapping positions are also called holding points (Voldman, et al. 2001) and correspond to the positions where both the  $x$  and  $y$  components of the resulting force are equal to zero. This equilibrium position should be stable as long as the flow rate is constant.

### 3.2.4 Limits of the 2D simulations

Cells simulated with COMSOL Multiphysics in the particle tracing module are considered as point particles. It calculates particle positions based on the forces at a specific point and displays the points as particles of specified diameter. Similarly, simulated particles do not disturb the flow leading to some inaccuracy in the simulations related to the laminar flow. Particles can interpenetrate each

other hence releasing many particles at the inlet will only lead to particles aggregating at one specific location with their center at this same point. A similar conclusion can be drawn for the wall penetration of particles. A possible improvement of the simulation to correct this effect would be to use particles defined as a material and calculate step by step their position. This would, however, require using a moving mesh for the particles and a lot of computing power. This computing power should be even bigger if several particles are simulated at the same time. Their interactions should also be modeled for increased accuracy.

### 3.2.5 3D simulations

3D simulations could be performed to understand how the vertical position of the particles would evolve during the trapping. However, those simulations require a lot of computing power and should be performed on the final design.

## 3.3 Conclusion

In this chapter the physics of the dielectrophoretic trapping was discussed as well as the effect of the electric field on cells.

The four important parameters for DEP trapping were discussed. MyDEP was used to select the electrical conductivity of the medium,  $\sigma_m = 0.156$  S/m, and trapping frequency,  $f_{DEP} = 10$  kHz to ensure nDEP trapping conditions. A flow speed  $v = 500$   $\mu\text{m}$  and a trapping voltage of  $V = 10$   $V_p$  ( $V_{peak}$ ) were used as a basis of comparison to select the best candidate for the trapping.

A design composed of 8 electrodes arranged in circle was proposed and COMSOL Multiphysics simulations were performed to obtain the drag and DEP forces applied on a particle in the microchannel. The best candidate for the trapping, involving 3 electrodes (1 in the outlet and two others located at  $45^\circ$  with the opposite voltage), was selected and analyzed in detail. The x and y components of the two forces were discussed to find the equilibrium position in the design.

The next chapter is dedicated to the fabrication of this design.

## Chapter 4 Chip fabrication

This chapter describes a reproducible method for  $\mu\text{m}$  precision alignment of PDMS microchannels with coplanar electrodes using a conventional mask aligner for lab-on-a-chip applications. It is based on the use of a silicon mold in combination with a PMMA sarcophagus for precise control of the parallelism between top and bottom surfaces of molded PDMS. The alignment of the fabricated PDMS slab with electrodes patterned on a glass chip is then performed using a conventional mask aligner with a custom-made steel chuck and magnets. This technique allows to bond and align chips with a resolution of less than  $2\ \mu\text{m}$ . The content of the chapter is based on the published article (Cottet, et al. 2017):

Cottet, J., Vaillier, C., Buret, F., Frenea-Robin, M. & Renaud, P. A reproducible method for  $\mu\text{m}$  precision alignment of PDMS microchannels with on-chip electrodes using a mask aligner. *Biomicrofluidics* 11, 064111, doi:10.1063/1.5001145 (2017).

## 4.1 Introduction

Polydimethylsiloxane (PDMS) is a polymer widely used in microfluidics. Its main advantages are that it is optically transparent, low-cost, chemically resistant to many solvents, easily bondable to itself and other materials and commercially available (Zhou, et al. 2010). This polymer enables 3D fabrication of nano or microscale structures by replica molding from a master that can be created in various materials like SU-8, Si or PMMA, or by using PDMS as a sensitive photoresist after the addition of various photoinitiators (Bhagat, et al. 2007, Lotters, et al. 1997). In the field of lab-on chip (LOC) systems, there are many situations in which a PDMS structure should be bonded to a patterned substrate after an air or oxygen plasma treatment. This operation may require precise alignment between the different layers, which can be quite challenging. Alignment may for instance be a concern in PDMS multilayer assembly, an approach widely used for the fabrication of 3D organ-on-a-chip platforms. For example, Huh et al. (Huh, et al. 2010) have designed a lung-on-a-chip system consisting of two side channels and a main channel divided by a porous membrane, obtained by stacking and bonding of three PDMS layers. Mechanical stretching of the membrane is ensured by applying vacuum to side chambers, in order to mimic the lung breathing movements. Here a misalignment between the different PDMS stacks would result in vacuum leakage and operational failure.

This issue is also particularly relevant for LOC applications implying integration of electrodes within a microfluidic chip, such as electrochemical sensors (Moreira, et al. 2009), cultured neuronal networks (Kim, et al. 2014), microfluidic sorters based on surface acoustic waves (Shi, et al. 2009) or dielectrophoresis (Doh and Cho 2005), capillary electrophoresis chips (Holcomb, et al. 2009), etc. To circumvent this technical difficulty, one approach consists in replacing the structured PDMS by a thick photoresist layer like SU-8 that can be patterned and aligned on top of electrodes using standard photolithography process, as proposed by Demierre et al. (Demierre, et al. 2008). The use of SU-8 enables to obtain microchannels with a high Young's modulus

that will not deform easily and allow precise alignment with structures already present at the wafer scale (Zhu, et al. 2016). However, SU-8 is less prevalent for prototyping in microfluidics compared to PDMS. This can be partially explained by challenges encountered by SU-8 users such as adhesion issues, a high sensitivity of the SU-8 polymerization to humidity as well as the question of microchannel sealing with other material such as PDMS with mechanical clamping or irreversible bonding (Ren, et al. 2015, Zhang, et al. 2011).

In some cases, there may also be a requirement for aligning PDMS stamps with electrodes, as described by Menad et al. (Menad, et al. 2014), who used bond-detach lithography to form selective openings in a thin PDMS layer covering an electrode array, thereby modifying the electric field pattern generated.

Another typical example where proper alignment is required is that of microfluidic chips dedicated to impedance spectroscopy. In such devices, the position of the sensing electrodes in the microchannel will, due to their shape, influence the detected signal and the distribution of the electric field, which may cause a wrong interpretation of the particle size and properties in case of misalignment (Adler 2002).

A necessary step prior to alignment is the PDMS shrinkage compensation. PDMS shrinkage occurs when it is cured and depends mostly on the cure temperature and time, the PDMS components ratio and the layer thickness. To overcome these problems, some authors proposed to avoid this shrinkage by either curing the PDMS at room temperature or to keep the soft PDMS always in bound with a stiff substrate (Badshah, et al. 2014, Choonee and Syms 2011). Curing at room temperature will decrease mechanical properties and will be very sensitive to small changes in temperature (Ye, et al. 2009). Using a stiff substrate always in contact with the PDMS requires to perform some alignment between layers when the PDMS is transferred on another patterned substrate (Moraes, et al. 2009). By precisely characterizing the shrinkage, Lee et al. (Lee and Lee 2008) proposed a scaling factor to be applied to the mold during fabrication. In this case the shrinkage has to be properly characterized for the specific conditions where the mold is used.



Another important requirement is to ensure that the parallelism between top and bottom surfaces of molded PDMS is effective as well as their flatness, as stated by Li (Li, et al. 2007), otherwise, the contact between the PDMS and the electrodes will not happen at exactly the same time on the surface and, thus, will lead to misalignment errors. Land et al. (Land, et al. 2011) proposed to use a PMMA assembly where the thickness of a PMMA part controls the thickness of the PDMS and the flatness and parallelism of the surfaces are ensured by a top PMMA part used as a smoothing jig. However, the closure may lead to the trapping of a thin PDMS layer between the PDMS parts which might reduce the control on the PDMS surface parallelism.

Different alignment methods were proposed in the literature, the simplest one being to carry out a manual alignment under a microscope, based on visible structures on the chip (Huh, et al. 2013) but it is rather limited both in terms of precision and reproducibility (Kim, et al. 2005). Another approach is to use mechanical jigs (Chen and Pan 2011) to improve the alignment but it requires additional structural features and the thickness variability of the different layers will limit the alignment precision. Most systems in the literature intend to reproduce the conventional mask aligner used in the cleanroom facilities, that allows both alignment between two different levels and a pressure control of the bonding. Kim et al. (Kim, et al. 2005) proposed a system based on a stereomicroscope and holding pins to hold the top PDMS slab, thereby, overcoming the problem of non-uniformity of the PDMS layer. Its effectiveness is, however, restricted to a small area because it is limited to the field of view of the stereomicroscope (less than 1 cm). An alternative approach, proposed by Sivakumarasamy et al. (Punniyakoti, et al. 2017, Sivakumarasamy, et al. 2014), is based on PDMS adhesion on an accessory placed on a microscope objective that allows precise and reliable alignment. However, the tool used limits the alignment to the central zone, which might complicate the correction of the tilt if alignment of distant patterns is required. Li et al. (Li, et al. 2015) proposed a custom-built desktop aligner capable of both local and global alignments. This instrument is based on two digital microscopes with a resolution of 20  $\mu\text{m}/\text{cm}$  to perform the alignment on structures up to 4 inches in size, but this requires

one to build a new machine and to calibrate it. More recently, an automatic multilayered integrated microfluidic device fabrication has been proposed by Kipper et al. (Kipper, et al. 2017) and relies on computerized control of the alignment between the different layers before contact to reach an average alignment resolution of 1  $\mu\text{m}/\text{cm}$ . However, those approaches require the construction and calibration of a dedicated machine.

Combining all the critical aspects together, from the control of the PDMS properties (the parallelism between the surfaces, surface flatness, shrinkage compensation and thickness) to the alignment of the PDMS slab with electrodes, is necessary to perform a reproducible alignment. Partial elements are presented in the literature but there remains a need for a systematic approach addressing all these issues at once.

In this chapter, we describe a full process for fabricating a PDMS slab with microfluidic features and a glass chip with patterned electrodes and aligning them with a conventional mask aligner with a resolution of more than 10  $\mu\text{m}/\text{cm}$  on structures up to 4 inches. This process has been used for the fabrication of the trapping and impedance sensing modules (presented in Chapter 6).

## 4.2 Methods

### 4.2.1 Fabrication

#### 4.2.1.1 *Process flow*

##### 4.2.1.1.1 Electrode fabrication

Electrodes are fabricated through a standard photolithography process. After a Piranha bath treatment, 20 nm of titanium and then 200 nm of platinum are sputtered on a 4 inches float glass wafer. A 1.5  $\mu\text{m}$  thick layer of positive photoresist AZ1512 is then deposited with an automatic wafer coater and developer, the ACS 200 (SUSS MicroTec – Garching, Germany), and subsequently structured by means of direct writing with a WaferWriter MLA150 (Heidelberg Instrument – Heidelberg, Germany) before being developed with the ACS 200. The wafer is then etched with Ion Beam Etching (IBE) up to the

## Chip fabrication

glass layer. Finally, the photoresist is stripped and the glass wafer with Ti/Pt electrodes is obtained. Afterwards, the wafer is diced to separate all the chips.

### 4.2.1.1.2 Microchannel fabrication

A PDMS mold is fabricated with a process based on silicon etching starting with either a silicon or a Silicon-On-Insulator (SOI) wafer. The use of a Si mold was first envisioned but was ruled out as explained in 4.2.1.2. We describe in Figure 4:1 the full process starting with a SOI wafer.

A SOI wafer (handle wafer Si (thickness 380  $\mu\text{m}$ ) – buried oxide (thickness 2  $\mu\text{m}$ )– device wafer Si (thickness 50  $\mu\text{m}$ )) is coated with 2  $\mu\text{m}$  of AZ1512 photoresist with the ACS 200 coater (Figure 4:1 A). The photoresist is later patterned with the MLA 150 (Figure 4:1 B) (with a design scaled of 1.015 to compensate the PDMS shrinkage) and further developed with the ACS 200 (Figure 4:1 C). The top silicon is etched with the Bosch process until the oxide layer is reached (with the Adixen AMS200 Deep Reactive Ion Etching (DRIE) etcher from Alcatel Micro Machining Systems, Annecy – France) (Figure 4:1 D). The resist is then stripped from the wafer (Figure 4:1 E), which is later silanized with Trichloro(1H,1H,2H,2H-perfluorooctyl)silane (PFOTS from Sigma Aldrich) (Figure 4:1 F). PDMS is later poured on the wafer (Figure 4:1 G), cured at 80°C for 2h before demolding, separating the PDMS slabs and punching the access holes (Figure 4:1 H).

The last step which needs to be performed is the alignment between the PDMS slab and the glass chip patterned with electrodes (Figure 4:1 I).

## Chip fabrication

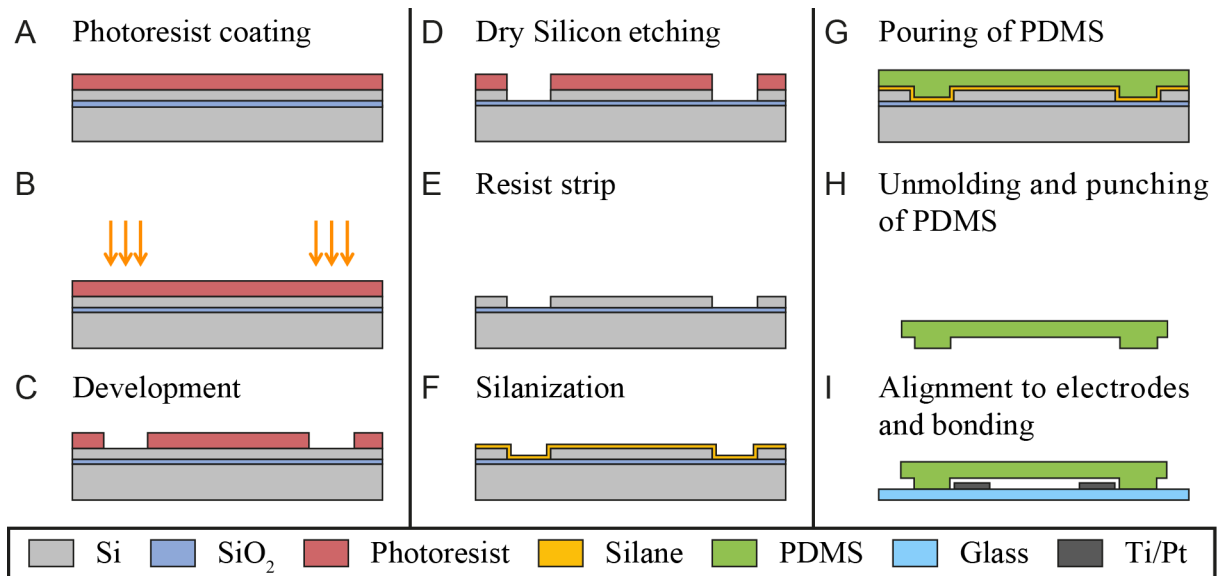


Figure 4:1 Process flow for the PDMS mold fabrication (A to F), PDMS molding (G and H) and alignment with the glass chip (I).

### 4.2.1.2 Mold fabrication

First trials of PDMS molding using an etched Si mold showed that PDMS walls did not bond completely up to the edge. This issue was further explained by Scanning Electron Microscope (SEM) pictures which showed that the edge of the Si mold structure had a different etched depth as presented in Figure 4:2 A). To overcome this issue, a SOI wafer was used so as to stop the etching as soon as the oxide would be reached, allowing to obtain a right angle in the mold structure as presented in Figure 4:2 B).

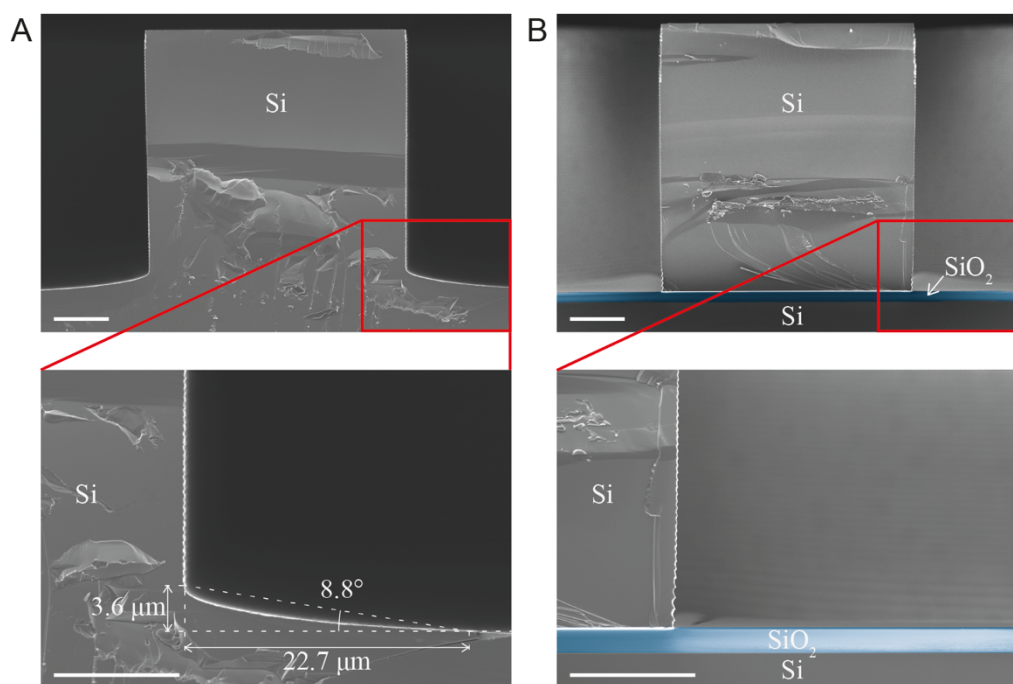


Figure 4:2 Scanning Electron Microscope (SEM) images of A) a Si mold and B) a SOI mold. For sake of clarity, the oxide layer is artificially colored in blue. Scalebar 10  $\mu\text{m}$ .

#### 4.2.1.3 PDMS molding in PMMA sarcophagus

To obtain a specific and reproducible thickness of PDMS and perfectly parallel surfaces, a PMMA sarcophagus mold was used as shown in Figure 4:3 A). This mold is composed of a 10-mm-thick aluminum part with threaded holes for the support (1). The wafer mold (3) is fixed with UV sensitive tape (2) to a PMMA part (4) defining the thickness of the PDMS. The PMMA cover (6) imposes the top surface of the PDMS to be flat and parallel and the combination with the closing PMMA part (8) enables a vertical pouring of the PDMS (Figure 4:3 B) as well as a horizontal position for PDMS curing (Figure 4:3 C). The gasket (5) located in a groove of the PMMA part (6) enables the sealing for both PDMS and air during degassing. The inox parts (7) and (9) are here to homogenize the stress distribution in the PMMA pieces (6) and (8).

A 10:1 mix ratio (base/curing agent) of PDMS (Sylgard 184 from Dow Corning) is poured in the sarcophagus mold and further degassed in a desiccator. The sarcophagus mold is then placed horizontally in the oven for 2h. Exposure of the UV sensitive tape to UV light after PDMS curing enables to retrieve the wafer mold after each molding. PDMS retrieval is described in paragraph C.1.5

in Appendix C. The different PDMS slabs are then separated and access holes are punched.

Here, the PDMS shrinkage (Sylgard 184 from Dow Corning) was characterized in the sarcophagus mold after curing at 80°C for 2 hours with a 10:1 mix ratio (base/curing agent). We obtained a scaling factor of 1.015 corresponding to the shrinkage of 1.5% measured on a 1 cm distance, which is in good agreement with previously reported values (Lee and Lee 2008, Marcus, et al. 2006).

A detail procedure of the sarcophagus mold assembly and final PDMS retrieval is provided in paragraph C.1 in Appendix C. All the CAD files and drawings are accessible in the supplementary of the article (Cottet, et al. 2017).

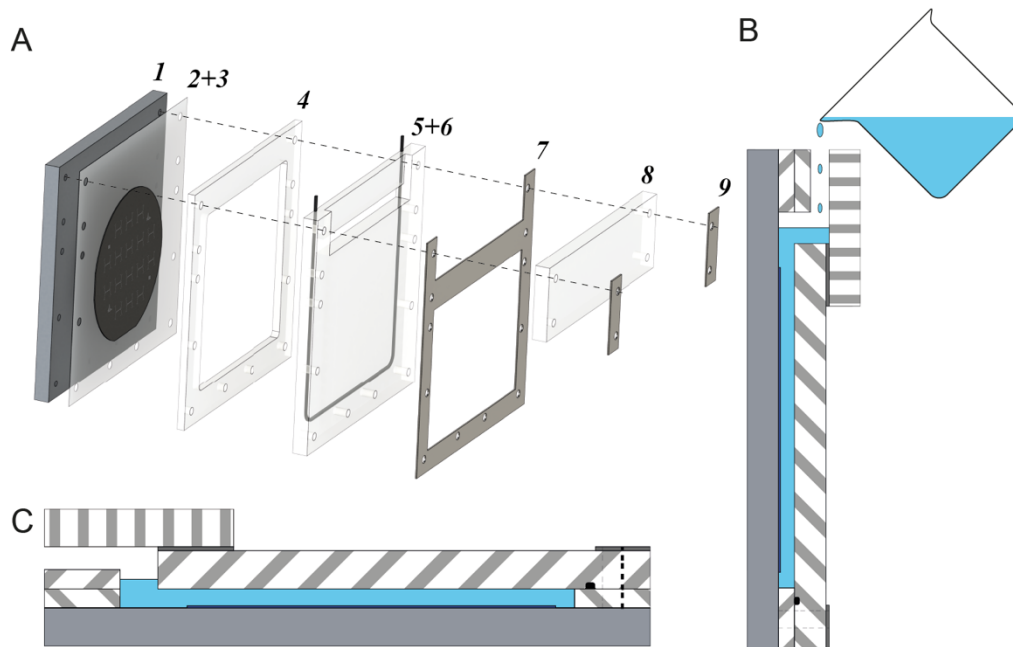


Figure 4:3 A) Exploded view of the sarcophagus for PDMS molding. B) Cross section of the sarcophagus during PDMS pouring. C) Cross section of the sarcophagus in curing position.

## 4.2.2 Alignment

### 4.2.2.1 Alignment with mask Aligner

The alignment is based on a conventional mask aligner MJB4 (SUSS MicroTec – Garching, Germany) (Figure 4:4 A). A custom-made steel chuck is used, covered with a 10  $\mu\text{m}$  layer of nickel deposited by chemical nickel plating to prevent rusting (see Figure S C:1 in Appendix C). The lateral positioning of the

glass chip is ensured by magnets, which means that any chip smaller than 4 inches can be positioned with the magnets and the vacuum is no longer required.

The PDMS slab is positioned on the glass mask, with the microfluidic features side facing the custom-made chuck for the pre-alignment. After plasma treatment, the PDMS slab is aligned with the glass chip using alignment marks (Figure 4:4 B). Once the rotation angle and the X and Y positions are corrected, the chuck is moved up until the contact. The chuck is then moved down leaving the bonded assembly PDMS-glass chip in contact with the glass mask (Figure 4:4 C). The bonded chip is carefully removed from the glass mask using tweezers and then placed in the oven at 80°C with a 40 g weight on top of it for 10 min.

A detail procedure of the alignment with the MJB4 mask aligner is provided in paragraph C.2 in Appendix C. All the CAD files and drawings are accessible in the supplementary of the article (Cottet, et al. 2017).

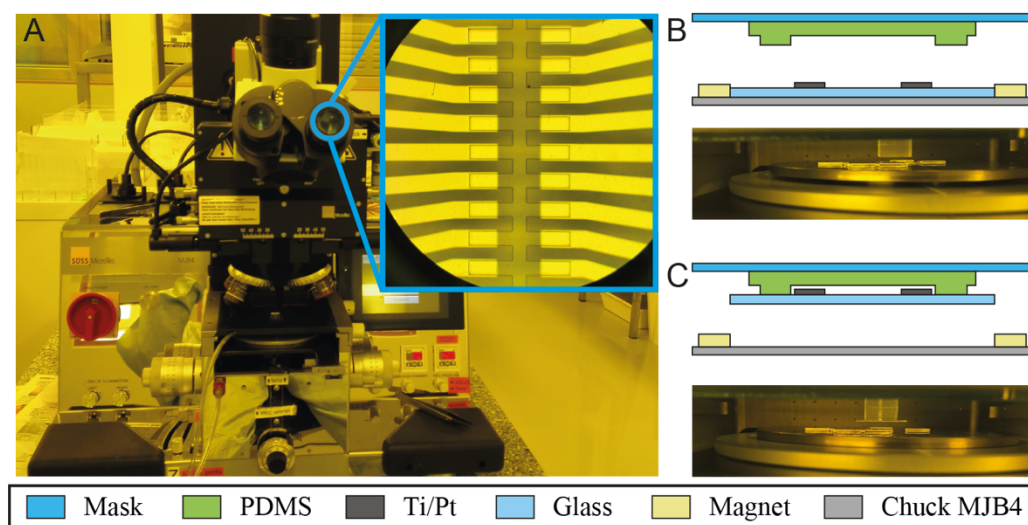


Figure 4:4 A) MJB4 mask aligner used in the alignment procedure and eyepiece view (insert). B) Scheme (cut view) and picture of the PDMS and chip before contact and C) after plasma bonding.

#### 4.2.2.2 Results and discussion

The aligned chip is displayed in Figure 4:5 A) and the alignment, illustrated in Figure 4:5 B) and C), is quantified using an image made by means of an optical microscope. The MJB4 mask aligner has a Top Side Alignment (TSA) accuracy of less than 0.5  $\mu\text{m}$ . The typical misalignment is less than 1  $\mu\text{m}$  over 3 mm distance which is mostly due to the shrinkage of PDMS corresponding to a

## Chip fabrication

resolution of more than 10  $\mu\text{m}/\text{cm}$ . The medium misalignment was found to be 0.4  $\mu\text{m}$  with a sample standard deviation of 0.2  $\mu\text{m}$ . The estimation error of the misalignment was in the order of 0.3  $\mu\text{m}$  (see paragraph C.3 in Appendix C for more details). To make the design more tolerant to misalignment, the microfluidic channels used are 50  $\mu\text{m}$  wide and the electrodes 60  $\mu\text{m}$  wide. Since the glass is 700  $\mu\text{m}$  thick, long distance objectives (x20 and x40) have been used but a more precise characterization is limited by the thickness of the glass. To reduce the misalignment, the shrinkage characterization can be more precise and performed on a larger area like the wafer scale.

The global thickness of the PDMS slab + glass chip should not exceed 6 mm to keep the vacuum clamping of the glass mask when the Wedge Error Compensation (WEC) knob is lowered down. If thicker PDMS should be used, then the mask (standard thickness 2.3 mm) or the chuck (custom-made chuck thickness 3 mm) should be thinner.

No leakage was notice on the chip neither locally as proved by Figure 4:5 B nor globally as shown by Figure S C:1 in Appendix C.



## Chip fabrication

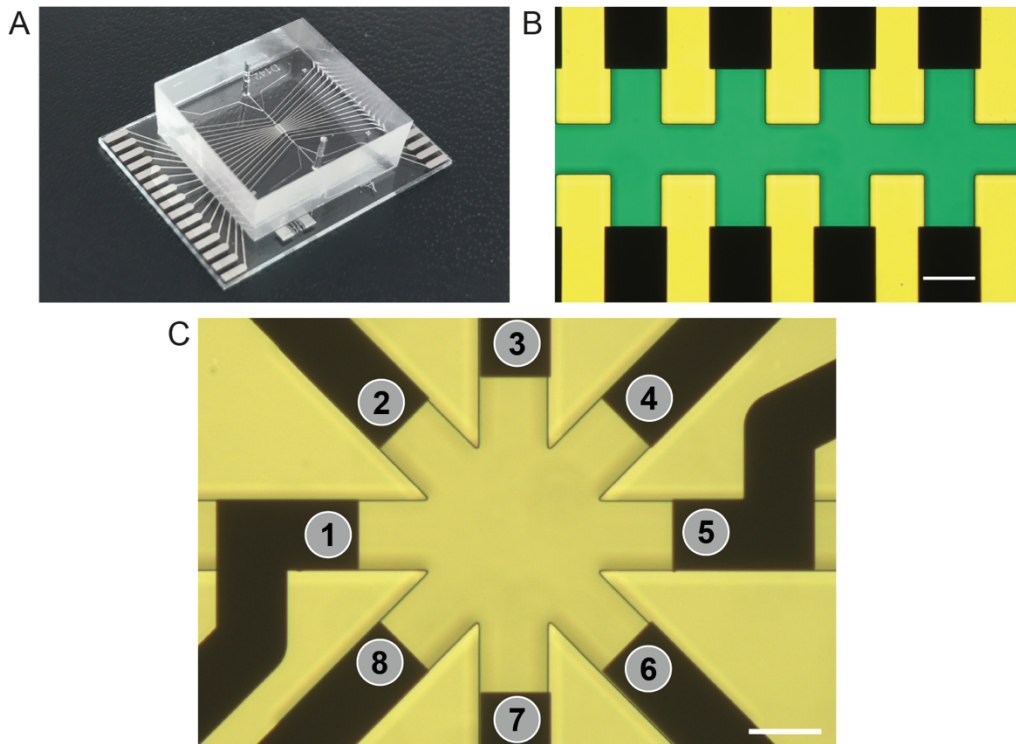


Figure 4:5 A) Fabricated chip with the PDMS slab bonded on the glass chip patterned with electrodes. B) Zoom in the DEP focusing region of the chip with an optical microscope. The channel was filled with a blue dye to make sure there was no leak. Scalebar 50  $\mu\text{m}$ . C) Trapping design fabricated Scalebar 50  $\mu\text{m}$ .

### 4.3 Conclusion

In this chapter, we have shown a reproducible method for  $\mu\text{m}$  precision alignment of PDMS microchannels with coplanar electrodes using a mask aligner, which is now routinely used to fabricate chips in the lab. This method relies on both PDMS molding with a PMMA sarcophagus for precise thickness and parallelism between the PDMS surfaces, and the use of a mask aligner with a custom-made chuck. This technique can also be used for PDMS-PDMS alignment, providing a high accuracy. The experimental testing of the fabricated microfluidic chips will be presented in the next chapter.

# Chapter 5 Experimental trapping results

This chapter presents the experimental results obtained for particles and cells. An improved version of the trapping design is proposed as well as a setup improvement based on automation with LabVIEW<sup>TM</sup>. The content of the chapter is partially published in the article (Cottet, et al. 2019b):

Cottet, J., Kehren, A., Lasli, S., van Lintel, H., Buret, F., Frénéa-Robin, M. & Renaud, P. Dielectrophoresis-assisted creation of cell aggregates under flow conditions using planar electrodes. *Electrophoresis* 40, 1498-1509, doi:10.1002/elps.201800435 (2019).

## 5.1 Introduction

Trapping particles and cells requires to understand how the different forces compensate each other to create equilibrium positions in a specific design. Such equilibrium positions have been discussed in Chapter 3 with a proposed design using 3 active electrodes. The proposed design has been successfully fabricated as presented in Chapter 4. To validate the trapping capability of the design, laboratory experiments need to be performed. Trapping cells can be challenging since those living objects have a dispersion of dielectric properties and size, as well as it is sensitive to the field and temperature. The first testing of the design is performed with polystyrene beads of known size and dielectric properties. Once the trapping of such objects is validated then cells can be trapped, considering that the medium might need to be adapted.

## 5.2 Materials and Methods

### 5.2.1 Beads preparation

Solutions of polystyrene beads of 8 and 15  $\mu\text{m}$  diameters were prepared from a bead stock solution of known concentration from Sigma Aldrich. The bead stock solution was first diluted ten times in Phosphate Buffer Saline (PBS) to reach a desired concentration of 1000 beads/ $\mu\text{l}$ . The PBS was then diluted ten times in Deionized Water (DIW) to reach an electrical conductivity of 0.156 S/m. This diluted solution had a final concentration of 100 beads/ $\mu\text{l}$ . Finally, 0.05% Tween was added to prevent beads to stick to PDMS.

### 5.2.2 Cell culture and preparation

Experiments were performed using the Human Embryonic Kidney (HEK) cell line from ATCC. Cells were cultured in a T75 flask using Dulbecco's Modified Eagle Medium (DMEM -  $\sigma_m = 1.5 \text{ S/m}$ ) with 1% Penicillin Streptomycin (PS) and 10% Fetal Bovine Serum (FBS). Cells were collected twice per week and re-suspended when a confluency of about 80% was reached.

Experimental medium consisted of DMEM diluted ten times in deionized water to reach  $\sigma_m = 0.156 \text{ S/m}$  in order to reduce thermal heating by Joule effect. The

## Experimental trapping results

osmolarity of the solution was corrected to reach the physiological value of 300 mOsm/L by addition of dextrose. Both the electrical conductivity and osmolarity were experimentally verified with a conductivity meter (InLab 710 from Mettler Toledo) and a micro-osmometer (Fiske Model 210).

### 5.2.3 BSA preparation

A 10% Bovine Serum Albumin (BSA) stock solution was prepared by dissolving 100 mg of BSA lyophilized powder (Sigma Aldrich) in 1 ml of deionized water and by gently rocking the capped tube until the BSA was fully dissolved.

### 5.2.4 Experimental setup

The microfluidic chip was placed on a PCB, which enabled the connection of DEP-trapping and DEP-centering electrodes to two arbitrary function generators (HMF2525 from Rohde & Schwarz), and also detection electrodes (design presented in Chapter 6). The PCB presented in Figure 5:1 A) was mounted on an inverted microscope (from DMIL Leica), and a uEye camera (UI-3060CP Rev. 2 from IDS Imaging Development Systems GmbH) enabled the real time visualization with the computer. Fluid was automatically injected in the chip using either a flow control pump (Nemesys Syringe Pump) or a pressure controller (Flow EZ from Fluigent). The flow control was used to validate the trapping at a specific flow rate and the pressure control to reduce the flow variation and the flow rate. An impedance counting unit, presented in Chapter 6, was placed before and after the trapping chamber. Two flow controllers Flow EZ from Fluigent were used temporarily one after the other: a 1000 mbar to fill the chip with liquid and a 25 mbar for precise flow control. Applied frequencies were  $f_{DEP} = 10$  kHz for DEP centering and trapping electrodes. The schematics of the experimental setup with pressure control is presented in Figure 5:1 B). The PDMS chip was first filled with deionized water at 100 mbar and then primed by injecting the BSA solution for 10 minutes at 10 mbar to prevent the adhesion of cells to the PDMS walls and to the glass. The cell suspension was then injected at 25 mbar before reducing the pressure to 2 mbar for the trapping.

## Experimental trapping results

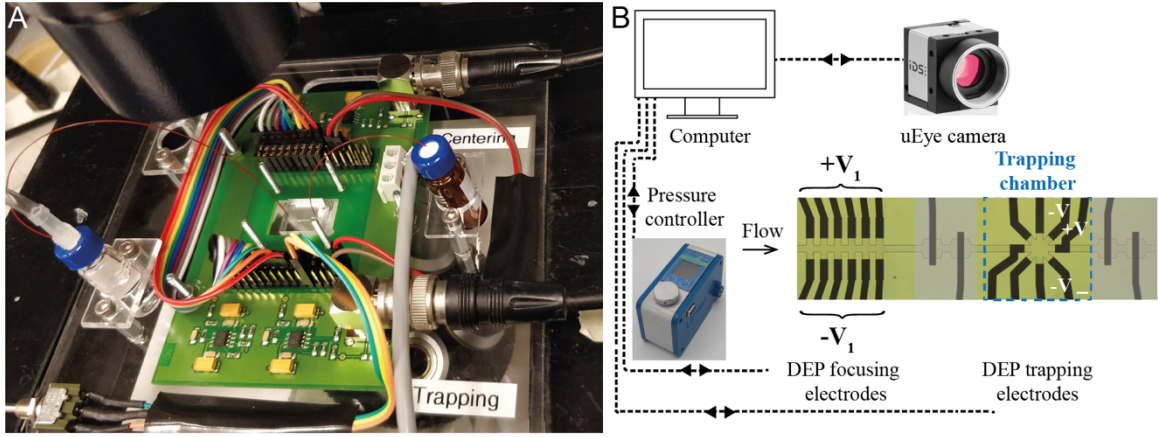


Figure 5:1 Experimental setup used for the trapping. A) PCB platform mounted on an inverted microscope (Leica) used to supply the chip with the centering and trapping voltages. B) Schematic representation of the system controlling by a computer with LabVIEW<sup>TM</sup> all the different instruments: the uEye camera for visualization, the pressure controller and two arbitrary function generators. DEP centering electrodes are used to center particles laterally and to provide a vertical lift. The grey areas corresponding to our impedance sensing unit are presented in the following chapter.

### 5.3 Experimental testing of the test design

First experiments were performed using 8  $\mu\text{m}$  diameter beads with a flow controller (syringe pump) with configuration 3(a) presented and discussed in Chapter 3 section 3.2.3 for  $V_{DEP} = 17.3 V_p$  ( $V_{peak}$ ) at  $f_{DEP} = 10 \text{ kHz}$  as illustrated in Figure 5:2 a). The medium conductivity and flow rate were set to  $\sigma_m = 0.156 \text{ S/m}$  and  $Q = 1 \mu\text{L/h}$ , respectively. Two other configurations of the electrodes with 5 electrodes and 7 electrodes were also tested and are respectively presented in Figure 5:2 b) and c).

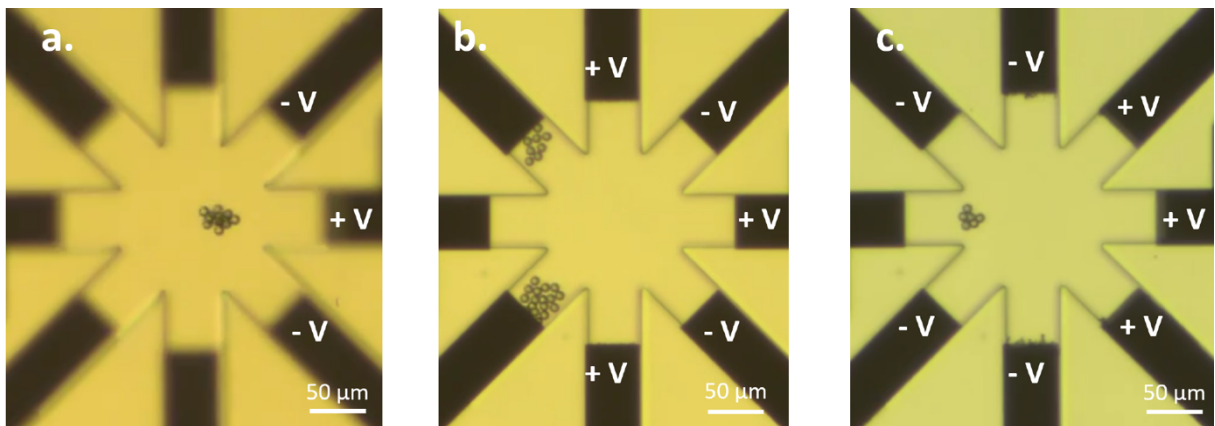


Figure 5:2 Illustration of the trapping of 8  $\mu\text{m}$  diameter polystyrene beads with 3 different configurations of the electrodes. Channel height 50  $\mu\text{m}$ , inlet and outlet width 50  $\mu\text{m}$ ,  $V = 22.5 V_p$  at  $f_{DEP} = 10 \text{ kHz}$ ,  $\sigma_m = 0.156 \text{ S/m}$  and  $Q = 1 \mu\text{L/h}$ .

## Experimental trapping results

Polystyrene beads were successfully trapped in the chamber with the 3-electrode configuration. In the 5-electrode configuration, the trapped beads were directed towards the dead-end volume of electrodes 2 and 7. In the 7-electrode configuration, beads were trapped but at the entrance of the trapping chamber.

For configuration 3(a), polystyrene beads were successfully trapped in the chamber and formed clusters that were moved towards the inlet as the size of the cluster increased as presented in Figure 5:3. The evolution of the cluster position followed the profile of the simulation-predicted position of a particle of increasing size presented in Figure 5:4). After stopping the DEP trapping voltage, the particles composing the cluster separated from each other.

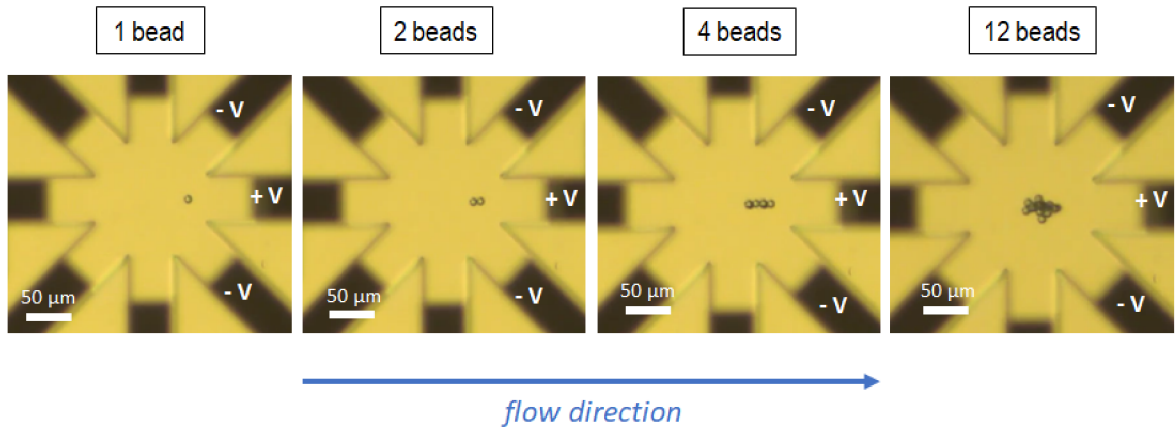


Figure 5:3 Evolution of the position of 8  $\mu\text{m}$  diameter polystyrene beads with the number of beads in the trapping chamber with 3 electrodes. The solution flows in the chip from left to right.  $V = 17.3 V_p$ ,  $f_{DEP} = 10 \text{ kHz}$ ,  $\sigma_m = 0.156 \text{ S/m}$  and  $Q = 1 \mu\text{L/h}$ .

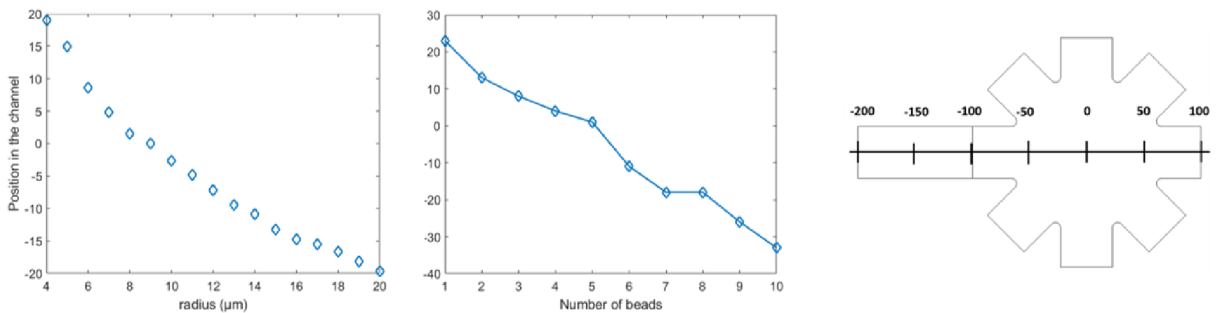


Figure 5:4: For configuration 3(a) Left: Simulated evolution of the position of a polystyrene bead with the diameter. Center: Experimental evolution of the position of the cluster with the increase of the number of beads.  $V = 17.3 V_p$ ,  $f_{DEP} = 10 \text{ kHz}$ ,  $\sigma_m = 0.156 \text{ S/m}$  and  $Q = 1 \mu\text{L/h}$ . Right: Sketch of the design with the axis origin and the scale in  $\mu\text{m}$ .

## Experimental trapping results

This approach was repeated successfully for HEK cells, switching from a flow controller to a pressure controller to enable to reduce the flow rate and to have a better control at small flow rates. Trapping was achieved for the lowest possible voltage of  $V_{DEP} = 22.5 V_p$  and a pressure  $P_{in} = 2 \text{ mbar}$  as presented in Figure 5:5. This time a group of cells could be formed in the chamber as more cells arrived in the chamber. The video showing the cell aggregate formation is available at (Cottet 2018b).

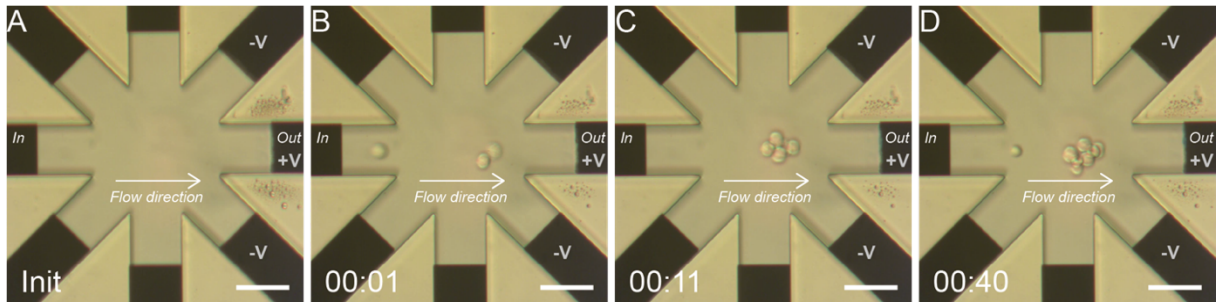


Figure 5:5 Example of HEK cell aggregation under flow conditions using 3 electrodes. The time stamps are in the mm:ss format. Scalebar 50  $\mu\text{m}$ . A) Chip with only fluid inside. B) Cells reaching the trapping zone are stopped when the DEP force compensates the drag force. C) and D) The aggregate increased in size as more cells were reaching the trapping zone with 5 cells (C) and 8 cells and 1 arriving (D). Channel height 50  $\mu\text{m}$ , Inlet and Outlet width 50  $\mu\text{m}$ ,  $V = 22.5 V_p$  at  $f_{DEP} = 10 \text{ kHz}$ ,  $\sigma_m = 0.156 \text{ S/m}$  and  $P_{in} = 2 \text{ mbar}$ .

### 5.3.1 Initial assessment of the cell viability

Cell integrity needs to be preserved during the aggregation process. An initial assessment was performed using Trypan blue. Trypan blue is a marker of the cell membrane permeability: living cells will look normal whereas permeable cells (for example dead cells) will be stained in blue. Cells were trapped and the resulting aggregates were let in the chamber for more than 5 minutes. Snapshots of this experiment are displayed on Figure 5:6. Cells located at the center of the chamber survived well, whereas those located in the periphery, close to the electrodes in high-field regions appeared in blue. As the number of cells increased with time, the aggregate became larger and tended to get closer to the electrodes, exposing cells located at the periphery to a larger field and temperature.

## Experimental trapping results

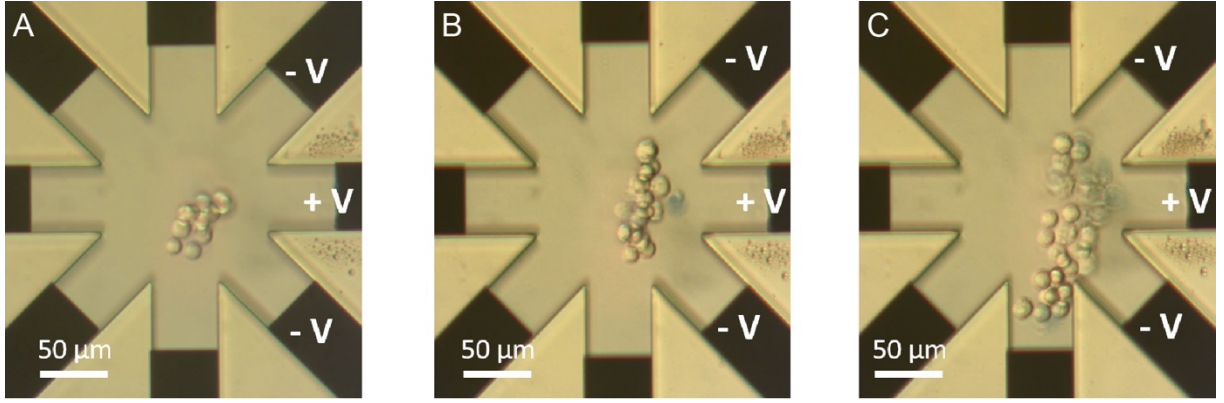


Figure 5:6 Evolution of an HEK aggregate for different number of trapped cells with a 3-electrode configuration.  $V = 22.5 V_p$  at  $f_{DEP} = 10 \text{ kHz}$ ,  $\sigma_m = 0.156 \text{ S/m}$ . The solution flows in the chip from left to right.

### 5.4 Discussion on the test design

Cells were successfully trapped in the chamber and were forming a small cell aggregate. Quantification of the time needed to observe adhesion between the cells requires to overcome certain inherent limitations of the design. Out of the 8 electrodes only 3 were used to perform the trapping. However, large aggregates were not stable due to the fact that the outlet of the chamber corresponds to a narrowing of the channel thus a re-acceleration zone for the fluid. In addition, the trapping zone is close to the electrodes, which due to the higher temperature, might lead to cell damage and aggregate disruption. Another limitation of the trapping with this configuration is that cells arrive continuously in the trapping chamber, increasing the size of the aggregate. Reducing the pressure to prevent the arrival of new cells requires to dynamically modify the trapping voltage in order to preserve the same position of the cells in the chamber.

### 5.5 Design and setup improvement

Improving the cell trapping requires to improve both the design layout and the experimental setup.

#### 5.5.1 Design improvements

##### 5.5.1.1 Design

In order to improve the stability of the trapping and to avoid instabilities such as reacceleration in the vicinity of the trapping area, the fluidic design can be



## Experimental trapping results

modified, based on the previous study, as displayed in Figure 5:7. Since only 3 electrodes out of 8 were used for trapping, the improved design should only have 3 (electrodes 2, 3 and 4 in Figure 5:7).

Doubling the electrodes recess i.e. the distance between the electrode and the chamber, will reduce the heat transfer to the trapping zone. Similarly, doubling the width of the trapping chamber will reduce the fluid velocity hence the particle velocity and drag force. Moving this widening (respectively narrowing of the channel) before the trapping chamber (respectively after) will improve the stability of the trapping since the drag force will be lower and constant in the center of the chamber.

To further reduce the fluid velocity in the chamber, additional outlets can be added to the side electrodes (electrodes 2 and 4 in Figure 5:7) while ensuring a high hydrodynamic resistance to prevent particles to go through the auxiliary outlets. This can be obtained by having relatively narrow and long microchannels.

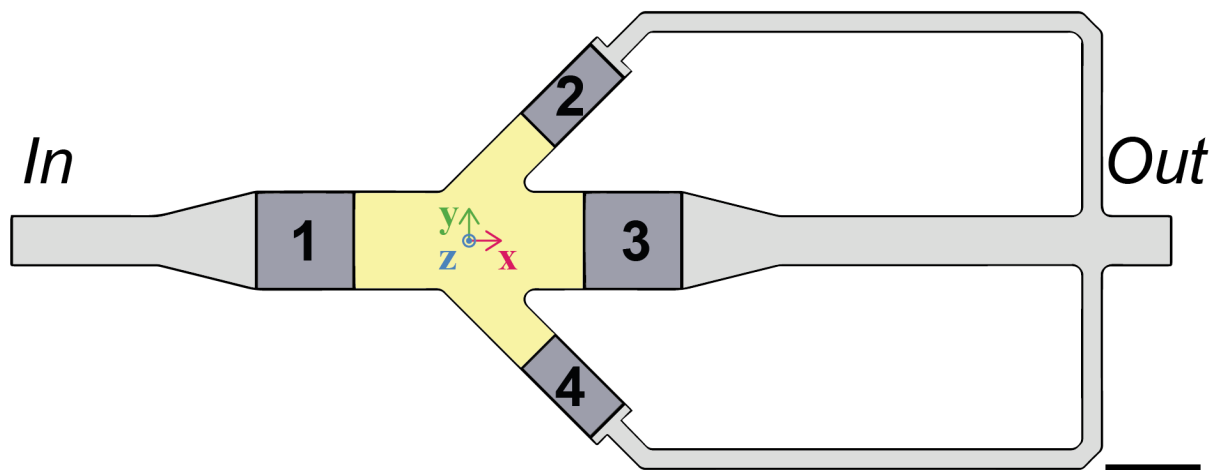


Figure 5:7 Improved trapping design composed of 4 electrodes (dark gray rectangles) with 1 inlet/3 outlets located at electrodes 1 and 2/3/4 respectively (Scalebar 50  $\mu\text{m}$ ). The trapping chamber is colored in yellow. Scalebar 100  $\mu\text{m}$ .

### 5.5.1.2 Fluidic simulations

Figure 5:8 A) presents the fluid velocity profile in the improved design. The flow profile, originally set with a constant flow speed of 500  $\mu\text{m}/\text{s}$  at the microchannel inlet, will be parabolic and established after 40  $\mu\text{m}$  and in the

## Experimental trapping results

trapping chamber as shown in Figure 5:8 B) (red line). The flow speed will be reduced in the entire trapping chamber, which will facilitate particle trapping. As predicted, the liquid speed in the central outlet (corresponding to electrode 3 and  $x = 400 \mu\text{m}$  with the black line in Figure 5:8 B) is reduced compared to the one at the trapping chamber inlet (red line) thanks to the use of the two auxiliary outlets (located at electrodes 2 and 4). By adjusting the ratio of the fluidic resistance between the auxiliary outlets and the central outlet, the flow can be reduced in the central channel without particles going in the auxiliary outlets.

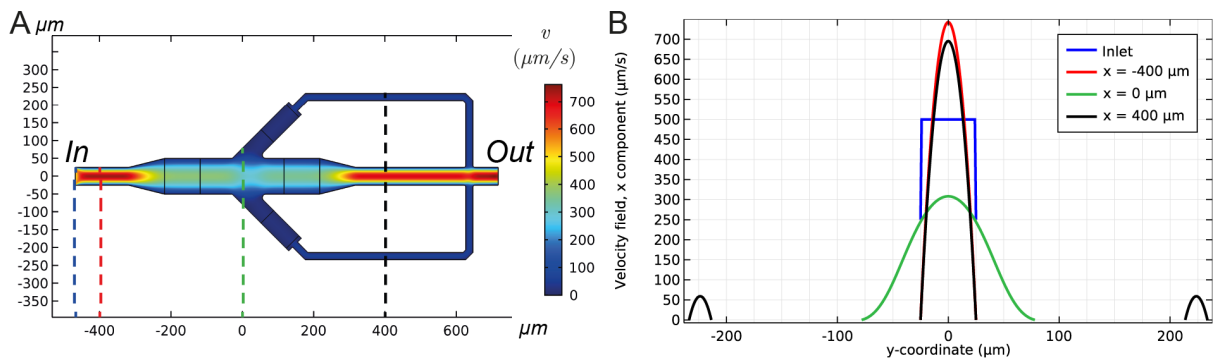


Figure 5:8 A) COMSOL Multiphysics 2D simulation of the fluid velocity profile, in  $\mu\text{m/s}$ , in the improved chip design with an inlet velocity of  $500 \mu\text{m/s}$ . B) Flow velocity profile along  $y$  at the inlet (in blue), at  $x = -400 \mu\text{m}$  (in red), in the center of the trapping chamber at  $x = 0$  (in green) and after the trapping chamber at  $x = 400 \mu\text{m}$  (in black).

### 5.5.1.3 Electric field and dielectrophoresis simulations

For comparison purpose, the improved design presented in Figure 5:7 was simulated with the same voltage, the same channel height and the same inlet flow speed as the test design presented in Figure 3:3. The field and trapping simulations are presented in Figure 5:9. The voltage distribution in the liquid is presented in Figure 5:9 A) while the evolution of  $|\mathbf{E}^2|$  along the axis  $y=0$  is presented in Figure 5:9 B). The field value is the same as the one presented for the test design. With this design, the particle should be trapped closer to the center of the trapping chamber (the center,  $x=0$ , corresponds to the geometrical center between electrodes 1 and 3) at  $x_{trap} = 17 \mu\text{m}$  as presented in Figure 5:9 C). Two equilibrium positions, where the resulting force is equal to zero, exist along the  $x$  axis as presented in Figure 5:9 D) but only the one located between zones 1 and 2, with the abscissa  $x_{trap} = 17 \mu\text{m}$ , is stable.

## Experimental trapping results

A 3D representation of the amplitudes of the DEP and drag force is presented in Figure 5:9 E) and F). The intersection between the two surfaces corresponds to a resulting force equal to zero. In the chip the particle will first reach the x trapping line materialized by the white/red dashed line in Figure 5:9 F) before moving along the line under the influence of the y component of the resulting force.

## Experimental trapping results

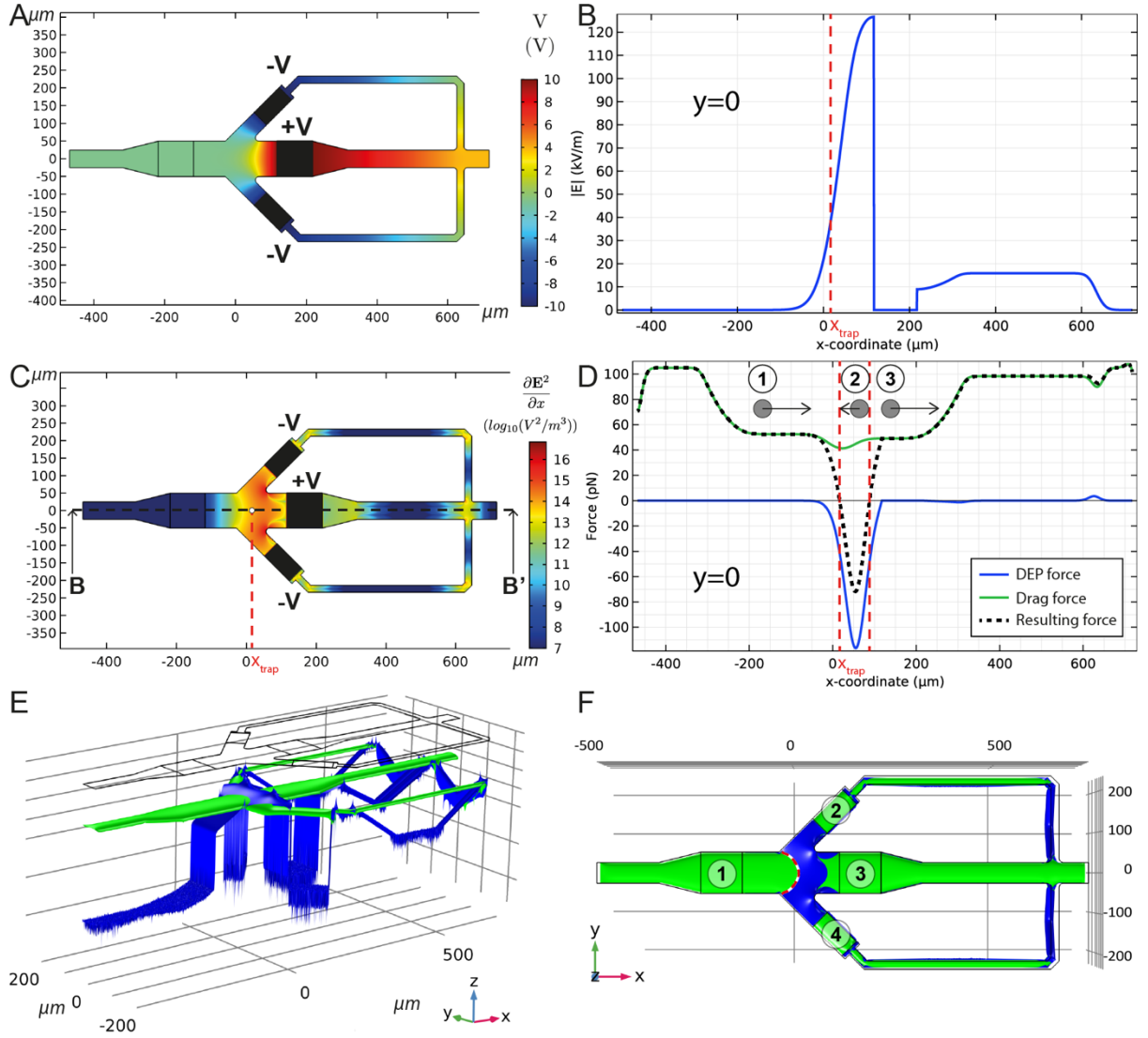


Figure 5:9 A) 2D simulation of the electric potential in the chip. B) Evolution of  $|E|$  along the x axis. C) 2D simulation of the trapping position of a cell using 3 electrodes supplied with  $V=10 V_p$  at 10 kHz. The surface represents  $\frac{\partial E^2}{\partial x}$ . The white dot indicates the trapping position,  $x_{trap}$ , of a HEK cell (diameter 15  $\mu m$ ). D) Evolution of the DEP and drag forces along the BB' cut. The resulting force is represented with the black dashed line and the red dashed vertical lines indicate the position where the resulting force is equal to zero. The gray dot with the arrow indicates the direction of the resulting force on the particle and the red dashed line between zones 1 and 2 the trapping position. E) Side and Top F) 3D representations of the amplitudes of the DEP (in blue) and drag (in green) forces along the y axis in the chip. The white/red dashed line in F) indicates where the x component of the two forces are equal in the trapping chamber. The electrode numbers are indicated. A logarithmic scale is used for both representations.

Figure 5:10 presents the evolution of the y component of the DEP and drag forces for the improved configuration of the design.

## Experimental trapping results

At  $x=0$  and  $x=x_{\text{trap}}$ , as displayed in Figure 5:10 A) and B), the  $y$  component of the drag force is smaller than the  $y$  component of the DEP force. In this case the particle would be exposed to a resulting force pushing it to the center ( $y=0$ ).

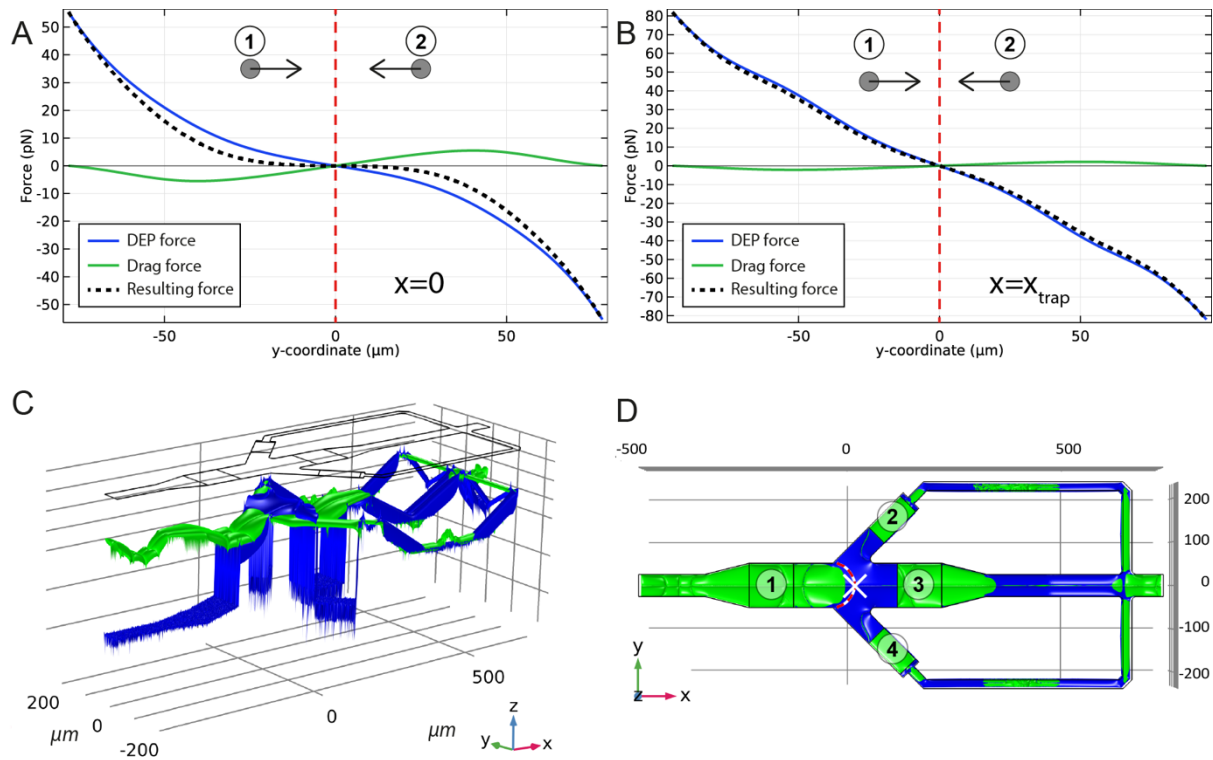


Figure 5:10 Evolution of the DEP and drag forces along the  $y$  axis at A)  $x=0$  and B)  $x=x_{\text{trap}}=17 \mu\text{m}$ . The resulting force is represented with the black dotted line and the red dotted line indicates the positions where the resulting force is equal to zero. The gray dot with the arrow indicates the direction of the force on the particle. C) Side and D) Top 3D representations of the amplitudes of the DEP (in blue) and drag (in green) forces along the  $y$  axis in the chip. The white/red dashed line in D) indicates where the  $x$  components of the two forces are equal (from Figure 5:9 F) and the white cross the final position of the particle. The electrode numbers are indicated. A logarithmic scale is used for both representations.

The amplitude of the  $y$  component is two orders of magnitude smaller than the  $x$  component. In all cases, the particles will first reach the trapping position due to the  $x$  component of the resulting force (white/red dashed line in Figure 5:10 D) and then get centered in the microchannel due to the  $y$  component of the resulting force as illustrated in Figure 5:10 D until it reaches the white cross.

This design, while improving the trapping, should, however, not concentrate particles at a specific point as predicted but in a wider area (making more of a chain) due to the wide zone of low fluid velocity. A 4<sup>th</sup> electrode (number 1 in Figure 5:7) was then added to enable to recenter the cell aggregate and prevent

## Experimental trapping results

new particles and cells to join the aggregate once the desired number of cells in the aggregate is reached.

### 5.5.2 Setup Improvements

To be able to prevent new cells from coming in the trapping chamber, the experimental setup was fully controlled with LabVIEW™ (National Instruments). This setup, presented in Figure 5:11, provides a control of all the instruments through a dedicated interface. When the required number of cells in the chamber is reached, the flow can be decreased together with the DEP trapping voltage. Once the arrival of new cells is stopped, electrode 1 from Figure 5:7 is supplied with the same voltage as electrode 3 using the manual switch from Figure 5:11 A), sealing the DEP cage and recentering the cell aggregate. Further increase of the voltage can improve the compaction of the aggregate.

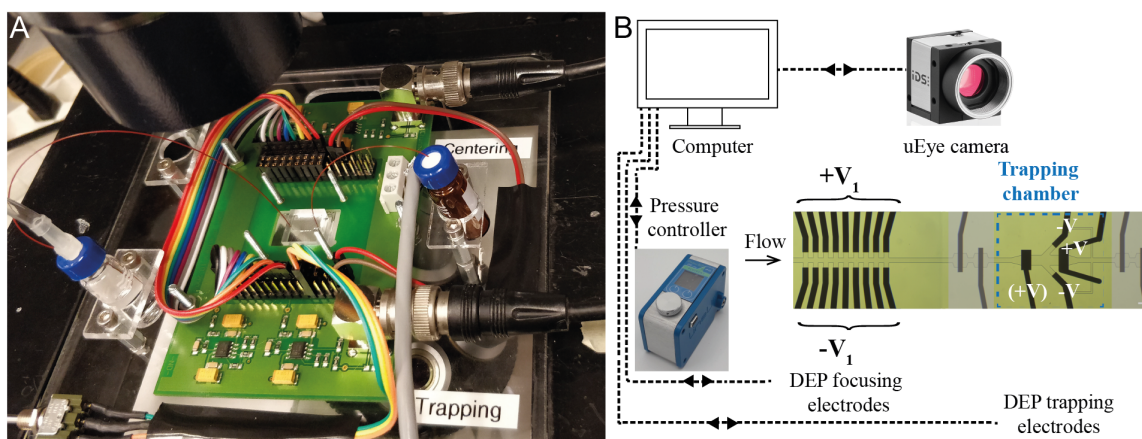


Figure 5:11 Experimental setup used for the trapping with the improved trapping design. A) PCB platform mounted on an inverted microscope (Leica) used to supply the chip with the centering and trapping voltages. A manual switch enables to activate a 4th electrode (number 1 in Figure 5:7) for compacting the aggregate. B) Schematic representation of the system with a computer controlling with LabVIEW™ all the different instruments as presented in Figure 5:1. The grey areas corresponding to our impedance sensing unit are presented in the following chapter.

### 5.5.3 Experiments and trapping with a fully automated setup

Experiments using the fully automated setup and the improved design are presented in Figure 5:12. The chip is first filled with deionized water and then primed with BSA as presented in Figure 5:12 A. The suspension of cells is injected and once the cells start to reach the trapping chamber, the pressure is

## Experimental trapping results

decreased to 2 mbar. Cells arrive slowly in the chamber (Figure 5:12 B) forming a cell line (Figure 5:12 C). Once the desired number of cells is reached (21 cells in Figure 5:12 D) both DEP trapping voltage and flow rate are reduced to prevent additional cells to reach the trapping zone. Electrode 1, located on the left, is activated leading to the centering of the cell aggregate (Figure 5:12 E). The DEP force is also increased to compact the aggregate. As displayed in Figure 5:12 F), the aggregate is more compact after 5 minutes. The DEP force is cancelled and the flow rate increased to help the formed aggregate to leave the trapping chamber as shown in Figure 5:12 G. The aggregate leaves the trapping chamber and no cell separation is observed, even in a narrower meander (width 40  $\mu\text{m}$ ) located after the trapping chamber as shown in Figure 5:12 H). The video showing the cell aggregate formation is available in (Cottet 2018a).

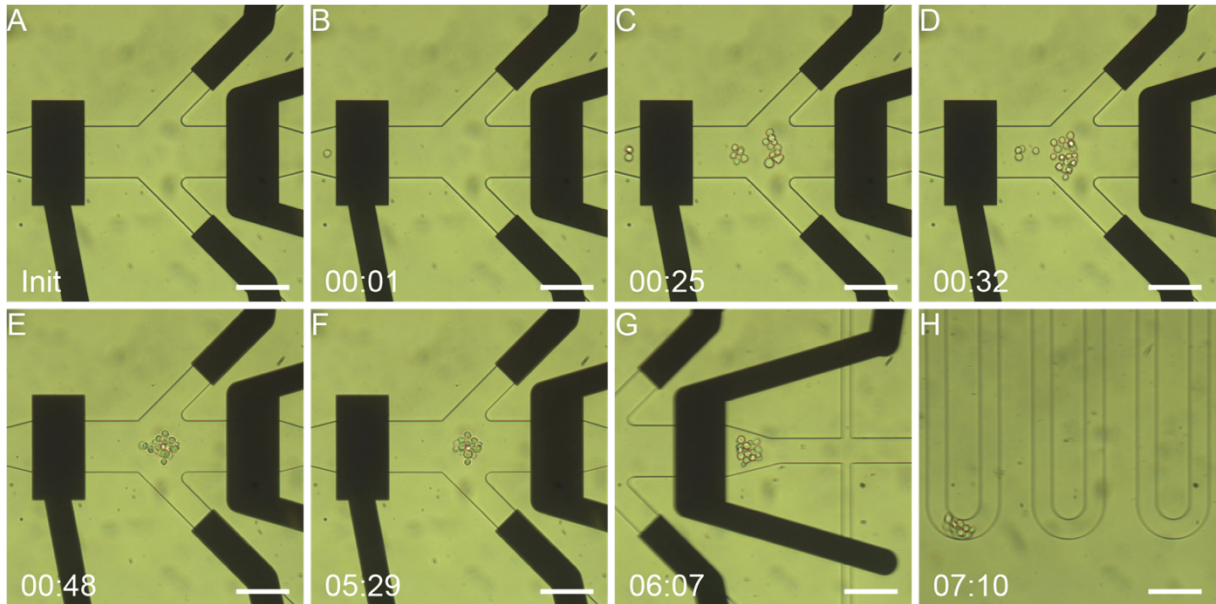


Figure 5:12 Example of HEK cell aggregation in flow using the 3 electrodes on the right. The time stamps are in the mm:ss format. Scalebar 100  $\mu\text{m}$ . A) Chip with only fluid inside. B) Arrival of the first cell in the trapping chamber. C) 10 cells are trapped under flow conditions, forming a line, while more cells arrive (4 then 3 cells arriving). D) DEP voltage and inlet pressure are reduced to  $V_f$  and  $P_f$  to prevent more cells to reach the 21 cells located in the trapping zone. E) The 4<sup>th</sup> electrode (located on the left) is activated leading to the centering of the cell aggregate. The DEP force is also increased back to  $V_{trap}$  to compact the aggregate. F) After 5 min, the aggregate is more compact. G) The DEP force is cancelled and the inlet pressure increased to  $P_{release}$  to help the formed aggregate to leave the trapping chamber. H) No cell separation is observed in a narrower meander (width 40  $\mu\text{m}$ ) located after the trapping chamber. Channel height 50  $\mu\text{m}$ ,  $V_{trap} = 15 V_p$  for the trapping and the compacting and  $V_f = 5 V_p$  when the flow is reduced (both at  $f = 10 \text{ kHz}$ ),  $\sigma_m = 0.156 \text{ S/m}$ ,  $P_{trap} = 2 \text{ mbar}$ ,  $P_f = 1 \text{ mbar}$  and  $P_{release} = 2 \text{ mbar}$ .

## 5.6 Conclusion

The proposed design offers a new way to create cell aggregates, on chip, with a controlled number of cells. It has been obtained with the help of simulations that required a few simplifications.

Simulations of the test design served as a basis for comparison between several electrode configurations in order to select the most promising one. The required voltage for trapping is higher than that expected from the simulations. These discrepancies can be explained by the fact that for the sake of simplifications, calculations were performed on a 2D model. In 2D simulations, electrodes are considered as equipotential lines located on the side of the microchannel. However, those equipotential lines, equivalent to “liquid electrodes” (Demierre, et al. 2007) are created by planar electrodes with a higher voltage in the 3D device. Furthermore, since the experiments are performed with pressure control, the flow speed depends on the design and tubing used. Simulating such system would require a 3D model implying lot of computing resources.

The best configuration has been tested experimentally and proved to be capable of trapping polystyrene beads as well as HEK cells under flow conditions. This test design was however not optimal for the trapping. An improved design was simulated, tested and proved to be capable of trapping the desired number of cells. However, creating a real “cell by cell aggregate” requires cells to be initially sufficiently separated, which is a point that still needs to be improved. As two impedance sensing stages, presented in (Cottet, et al. 2019c), have been added upstream and downstream the trapping area, it should also be possible to detect pre-aggregated cells and take them into account while evaluating the final aggregate size.

The absolute size limit of the cell assemblies is the size of the trapping chamber in both designs. Additionally, the size of the microchannel (50  $\mu\text{m}$  x 50  $\mu\text{m}$ ) can also be a limitation as cell aggregates with a larger cross-section might get stuck in the microchannel. Adding cells to the assembly will lead to two opposite and competitive effects. On the one hand, adding cells will create a larger assembly



## Experimental trapping results

which will behave as a larger particle which has been confirmed experimentally. On the other hand, adding cells will reduce the cross-section of the microchannel available for the fluid which will lead to a faster flow and thus decrease the trapping. Experimentally, the stability of the trapping has shown to be increased when the number of polystyrene beads forming a cluster increased. This effect can possibly be explained by the dependence of the force on the object size: the drag force is proportional to  $r_{\text{ext}}$  while the DEP force is proportional to  $r_{\text{ext}}^3$ .

All cells remained together as a permanent aggregate after 5 min of contact between trapped cells. While cell-cell interactions are favored thanks to dipole-dipole attraction forces between neighboring cells, the nature of the creation of permanent aggregates is not yet fully understood. Possibly cadherin-cadherin interactions take place as suggested by Menad et al. (Menad, et al. 2015). Cadherins are membrane proteins related to the physical linkages between cells. Mechanical forces such as compression enhance the protein-mediated adhesion as shown by Pontani et al. (Pontani, et al. 2012).

The number of cells composing the aggregate is controlled visually by means of a camera. This number could also be directly obtained using impedance flow cytometry. This point will be discussed in the next chapter. The created aggregate could be studied in a similar way.

The here presented set-up offers the possibility to further investigate interactions between different cell types by creating composite aggregates. Using different inlets for different cell types will offer the possibility to create composite aggregates with a known composition; using impedance flow cytometry the properties of each cell and of the created aggregates can be determined.

Aggregates created on-chip could also be part of a Lab-on-a-chip by adding the possibility to electroporate the created aggregates and observe their properties before and after electroporation. The next chapter is dedicated precisely to the implementation of an impedance sensing module on the chip.

# Chapter 6 Design proposition for impedance sensing of single cells and cell aggregates

This chapter is dedicated to the analysis of the influence of the geometry of a coplanar electrode layout for Electrical Impedance Flow Cytometry (EIFC) aimed to be used for the detection of single cells and small cell aggregates. The goal of this study is to (1) detect the particle with a signal as high as possible and (2) have a signal not sensitive to the particle position (lateral and vertical) in the microchannel. The content of the chapter is partially published in the article cottet (Cottet, et al. 2019c):

Cottet, J., Kehren, A., van Lintel, H., Buret, F., Frénéa-Robin, M. & Renaud, P. How to improve the sensitivity of coplanar electrodes and micro channel design in electrical impedance flow cytometry: a study. *Microfluidics and Nanofluidics* 23, doi:10.1007/s10404-018-2178-6 (2019).

## 6.1 Introduction

Electrical Impedance Flow Cytometry (EIFC) is a label-free technique for characterizing objects in suspension in a flowing liquid. The principle was described by Coulter in 1953 (Coulter 1953) and the devices became commonly known as Coulter counters. When a particle passes through a small aperture in a membrane connecting two reservoirs, the characteristics of the electrical path are modified and this modification is linked to the properties of the particle and the liquid. Originally used with direct current or low-frequency signals to assess the size, the principle was later extended by the use of multiple frequencies to enable the characterization of particle dielectric properties at higher frequencies (Coulter and Hogg 1970, Coulter and Rodriguez 1988).

In the late 1990's, the principle was translated in microsystems in which thick electrodes of the size of a microchannel were patterned for fluid analysis (Ayliffe, et al. 1999). Gawad et al (Gawad, et al. 2001) alternatively employed thin electrodes patterned in a microchannel for cell analysis and particle sizing and thereby pioneered the field of on-chip impedance flow cytometry as presented in Figure 6:1. Since then, a broad variety of cell types have been investigated by impedance spectroscopy, including blood cells (erythrocytes (Cheung, et al. 2005, Gawad, et al. 2001, Kuttel, et al. 2007), white blood cells (Han, et al. 2012, Holmes and Morgan 2010, Holmes, et al. 2009) and platelets (Evander, et al. 2013)), cancer cells (Spencer, et al. 2014, Zhao, et al. 2016a, Zhao, et al. 2014), microbes (yeast (Haandbaek, et al. 2014a, Haandbaek, et al. 2016, Shaker, et al. 2014), bacteria (Haandbaek, et al. 2014b), plankton (Benazzi, et al. 2007)), stem cells (Song, et al. 2016, Song, et al. 2013, Zhao, et al. 2016b), sperm (de Wagenaar, et al. 2016) etc. More detailed information can be found in the reviews of Morgan et al. (Morgan and Spencer 2015, Sun and Morgan 2010), Chen et al. (Chen, et al. 2015) and Petchakup et al. (Petchakup, et al. 2017).

Design proposition for impedance sensing of single cells and cell aggregates

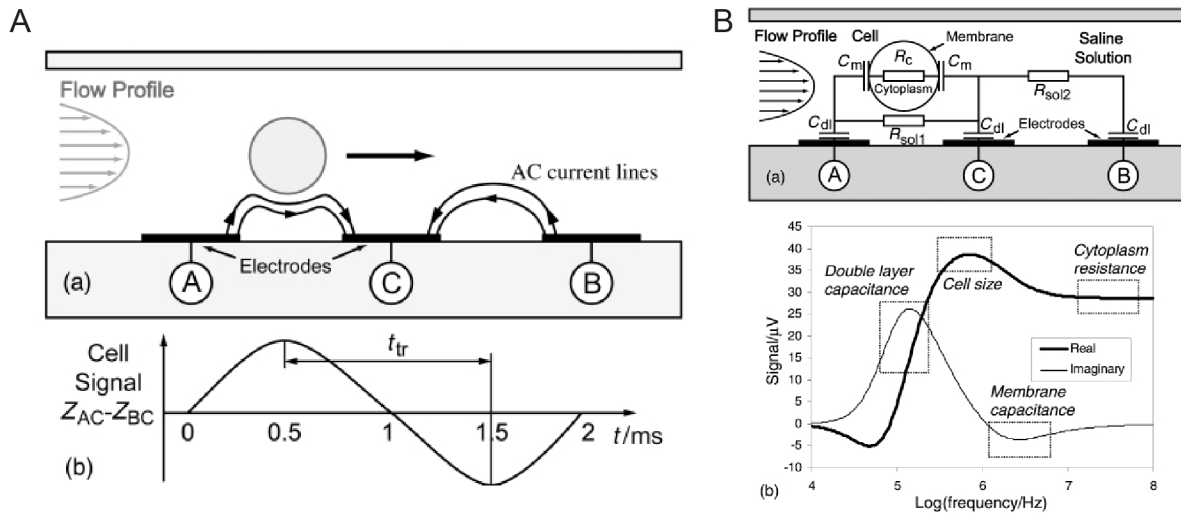


Figure 6:1 A a) Principle of differential impedance sensing with coplanar electrodes with b) the corresponding differential impedance signal. B a) Electrical equivalent circuit with b) the corresponding SPICE simulated complex impedance for a 10  $\mu\text{m}$  diameter cell. All schematics are adapted from (Gawad, et al. 2001).

Two main electrode configurations have been proposed: the coplanar and the parallel microelectrodes, also called “facing electrodes”. The coplanar design consists of two patterned electrodes located at the bottom of a microchannel. This design is sensitive to the height of the particle in the microchannel due to the electric field non-uniformity. Facing microelectrodes, presented in Figure 6:2, were proposed as an alternative by Cheung and Gawad (Cheung, et al. 2005) and allowed to have a more homogeneous current density around the cell under measurement. In this configuration, the electrodes are located at the top and the bottom of the microchannel, creating a more homogeneous electric field distribution in a smaller volume and thus improving the sensitivity. However, this design requires a more complex fabrication process and the signal is still dependent on the cell position in the detection volume (Spencer and Morgan 2011).

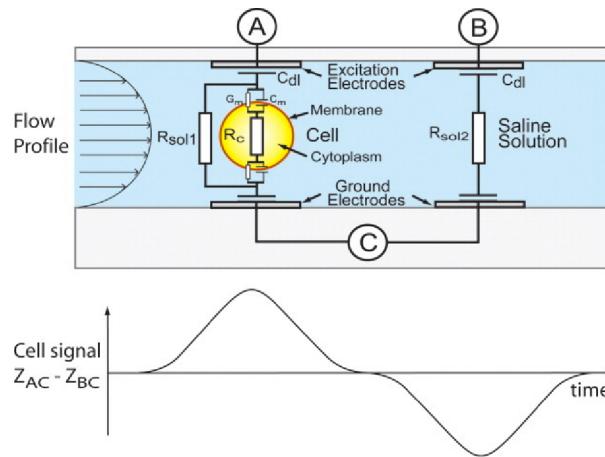


Figure 6:2 Principle of the facing electrode design. Adapted from (Cheung, et al. 2005).

The coplanar design has recently been reinvestigated because of its ease of fabrication. In order to improve this design, so-called “liquid electrodes”, presented in Chapter 3, were utilized to reduce the effect of the field non-uniformity (Demierre, et al. 2007). In this configuration, the electrodes are positioned at the bottom of dead-end chambers placed on each side of the main channel. This creates a homogeneous electric field over the channel height if the distance of the electrodes to the channel is at least equal to the channel height (Demierre 2008). However, the sensitivity is reduced due to a larger detection length and thus a larger detection volume.

More recently, a solution closer to a Coulter counter was proposed by Chen et al. (Chen, et al. 2011) who used a constriction channel with a cross-sectional area smaller than the investigated cell. In this case, the impedance amplitude value obtained is increased due to the fact that the deformed cell occupies most of the detection volume. On the other hand, the risk of clogging is higher and only a small range of cell sizes can be used for each design.

In order to mitigate the positional dependence of the particle in the coplanar design, Caselli et al. (Caselli and Bisegna 2017, De Ninno, et al. 2017) proposed to use multiple electrodes and to analyze the pulse shape to retrieve the position of the particle. The geometry was also reinvestigated by Clausen et al. (Clausen, et al. 2014), as presented in Figure 6:3, who showed that tuning the design of the microchannel could improve the sensitivity of Electrical Impedance Flow Cytometry measurements. In their study, they demonstrated that doubling the

Design proposition for impedance sensing of single cells and cell aggregates

electrode width allowed to increase the peak amplitude of more than 40 %. However, they only considered the effect of this parameter in their analysis.

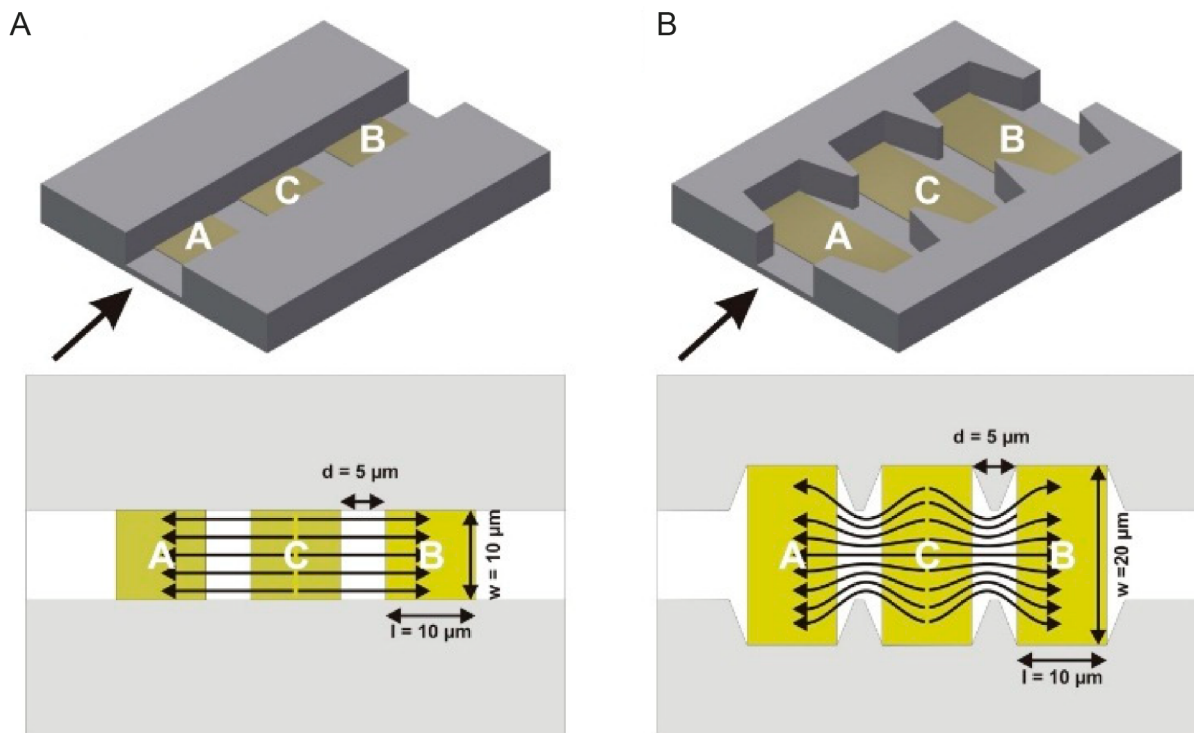


Figure 6:3 Comparison between two electrode layouts. A) Conventional layout composed of the 3 electrodes. B) Improved design proposed by Clausen. Adapted from (Clausen, et al. 2014).

The influence of the electrodes geometry on impedance was also studied for a design where electrodes had been fonctionnalized and trapped monocytes at their surface (Manczak, et al. 2016, Manczak 2016).

Most of the work described in the literature focuses on analyzing a specific size of cell, hence most of the sensors are suited for only a certain range of particles. A design capable of sizing and characterizing single cells and small cell aggregates is still missing. We are interested in creating cell aggregates of controllable size in flow, which requires the capability to analyze both single cells and cell aggregates.

In this chapter, we present a comprehensive study for the improvement of electrical impedance sensitivity of coplanar electrodes by investigating the influence of the microchannel design. The application is the characterization of single cells and small cell aggregates in a chip for dielectrophoresis-assisted

creation of cell aggregates under flow conditions. The impedance sensor presented in this chapter is a building block of the final chip where cells can be counted by impedance as single particles before entering in a DEP-trapping chamber where they aggregate and, after release of the DEP voltage used for trapping, can be characterized as cell aggregates.

The general configuration is composed of a 50  $\mu\text{m}$  square microchannel with a pair of 50  $\mu\text{m}$  long coplanar electrodes at its bottom, separated by 50 or 150  $\mu\text{m}$ . A detailed analysis of four designs is first performed through FEM (Finite Element Method) simulations with COMSOL Multiphysics and the results are confronted with experimental measurements carried out on 8  $\mu\text{m}$  diameter polystyrene beads. Frequently, in both facing and coplanar electrode layouts, a differential measurement is performed (Cheung, et al. 2005, Clausen, et al. 2014, Gawad, et al. 2001). In this chapter, the goal is to study the influence of the design of the impedance sensor on the signal. To assess such influence, only an absolute measurement scheme is needed without the need of a differential measurement since the baseline subtraction can be done numerically.

## 6.2 Simulations

### 6.2.1 Simulated designs

A conventional Electrical Impedance Flow Cytometry chip with a straight channel design further named “conventional” design is used as a reference design and presented in Figure 6:4 A). It consists of two coplanar electrodes located at the bottom of the microchannel. A voltage is applied between the two electrodes and the current is recorded. The current drops when a particle flows between the electrodes. The proposed analysis method consists in studying the variation of the current drop while changing several parameters as defined in Figure 6:4 B. The height,  $h$ , and width,  $w$ , of the microchannel are kept constant in the study ( $h = 50 \mu\text{m}$  and  $w = 50 \mu\text{m}$ ) as well as the length of the electrodes,  $l_{el}$ , while the other parameters are varying.

The influence of the following parameters on the sensitivity is tested:

## Design proposition for impedance sensing of single cells and cell aggregates

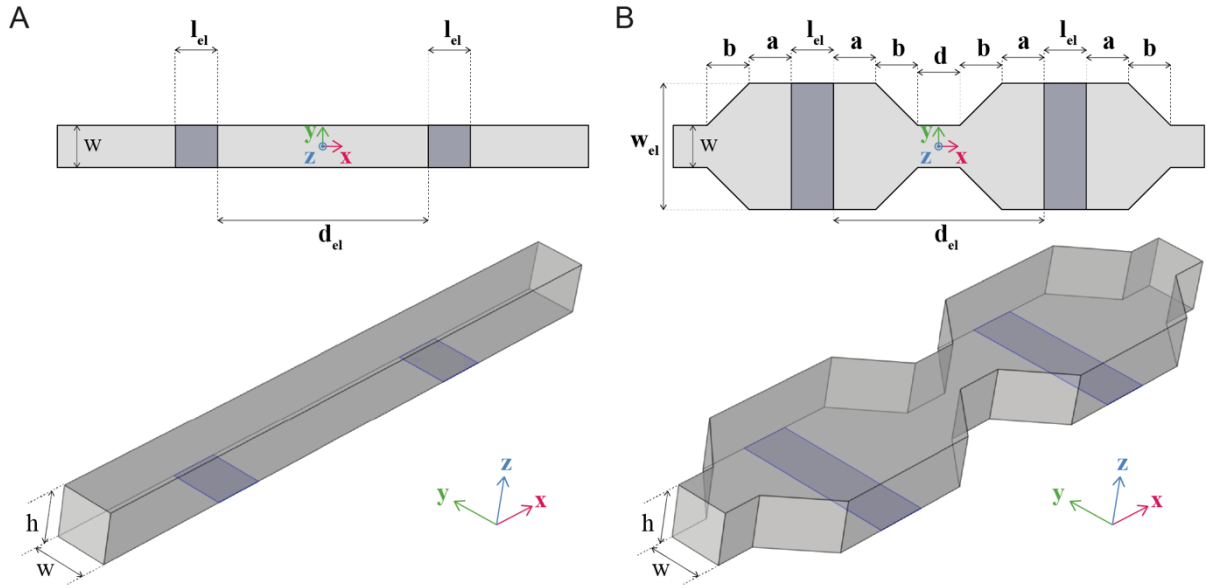


Figure 6:4 Top view and 3D view of A) the conventional design and B) the conceptual design.  $l_{el} = 50 \mu m$ ,  $h = 50 \mu m$  and  $w = 50 \mu m$  are kept constant.  $a$ ,  $b$ ,  $d$ ,  $d_{el}$  and  $w_{el}$  are the parameters to optimize. Electrodes are represented in blue.

- The inter-electrode distance,  $d_{el}$
- The width of the electrodes,  $w_{el}$
- The length of the maximum sensitivity area,  $d$
- The widening length,  $b$
- The widening to electrode distance,  $a$

The dimensions used in this design were selected to allow the sizing of  $8 \mu m$  diameter single cells as well as  $50 \mu m$  diameter cell aggregates. Increasing the length of the electrodes,  $l_{el}$ , can theoretically increase the current between the electrodes but would lead to an increase of the capacitance between the electrodes. Furthermore, most current lines added by a longer electrode would be confined to the top of the microchannel. Therefore,  $l_{el}$  was fixed to  $50 \mu m$  for the different designs to be equal to the height of the microchannel  $h$ .

### 6.2.2 Simulation specifications

The modeling of impedance variation was performed using COMSOL Multiphysics 5.3 and the AC/DC Module. COMSOL Multiphysics was used with MATLAB R2016a via LiveLink to extend the modeling with scripting



programming in the MATLAB environment. All the simulations performed aimed at studying the current variation due to an 8  $\mu\text{m}$  diameter polystyrene bead positioned at the center of the detection volume ( $x = 0 \mu\text{m}$ ,  $y = 0 \mu\text{m}$ ,  $z = h/2 = 25 \mu\text{m}$ ). The bead electrical conductivity and relative permittivity values were set to  $5 \times 10^{-6} \text{ S/m}$  and 2.5, respectively. The conductivity and relative permittivity of the liquid between the electrodes were set to 1.6 S/m (Phosphate Buffer Saline conductivity) and 80, respectively.

The relative current variation was considered with respect to the current between the electrodes without a particle. A spherical particle was defined as a change in material properties instead of a geometrical entity. The particle was moved along the channel by displacing its center using a parametric sweep. More details on this method are available in paragraph D.1 in Appendix D. An AC signal of amplitude  $0.8 V_{peak}$  ( $V_p$ ) at 500 kHz was applied between the two electrodes. In the numerical model, the electrode capacitance is not taken into account as the frequency used for the impedance measurements is 500 kHz.

The meshing as well as the corresponding mesh convergence study are described in paragraph D.2 in Appendix D, validating the choice of discretization.

### 6.2.3 Simulation results

#### 6.2.3.1 Influence of $d_{el}$

The first parameter examined was the inter-electrode distance,  $d_{el}$ , in a conventional design, with  $w = w_{el}$ . The evolution of the current variation with  $d_{el}$  is presented in Figure 6:5. As the distance between the electrodes increases from 40 to 180  $\mu\text{m}$ , both the absolute and relative current variations decrease. Two different distances were chosen for further study:  $d_{el} = 50 \mu\text{m}$ , corresponding to the height of the microchannel and the diameter of the targeted aggregate, and  $d_{el} = 150 \mu\text{m}$  corresponding to three times the height of the microchannel. For  $d_{el} = 50 \mu\text{m}$ , the electric field is not homogeneous along the  $z$  axis, leading to a strong height dependence of the current variation but the sensitivity to passing particles is significant at any height. For  $d_{el} = 150 \mu\text{m}$ , the electric field is homogeneous along the  $z$  axis in the central cube ( $50 \mu\text{m} \times$

50  $\mu\text{m}$  x 50  $\mu\text{m}$ ) offering a theoretically height-independent detection for both single particles and the entire aggregate. However, the overall sensitivity to single particles is reduced because of the smaller volume occupied by the particles compared to the inter-electrode volume. The designs with  $d_{el} = 50 \mu\text{m}$  and  $d_{el} = 150 \mu\text{m}$  will be referred to as “Short” and as “Long” respectively. The order of magnitude of the current variation induced by the passage of a bead, 0.1%, is in the same order of magnitude as the value reported by Spencer (Spencer and Morgan 2011).

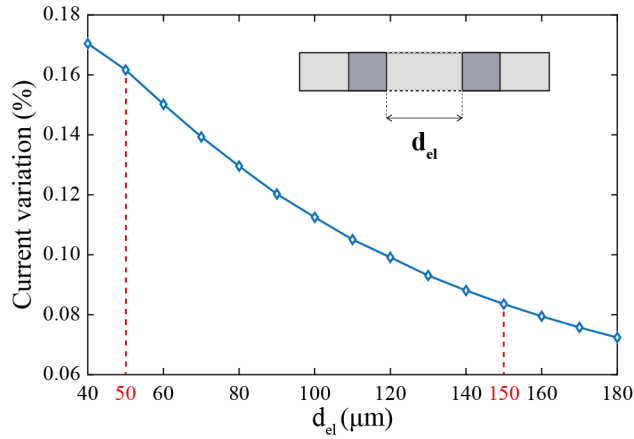


Figure 6:5 Simulation of the evolution of the current variation with the inter-electrode distance  $d_{el}$  due to an 8  $\mu\text{m}$  diameter polystyrene bead located at  $x = 0 \mu\text{m}$ ,  $y = 0 \mu\text{m}$  and  $z = h/2 = 25 \mu\text{m}$  for  $w = w_{el} = 50 \mu\text{m}$ .

### 6.2.3.2 Influence of $w_{el}$

Increasing the width of the electrodes  $w_{el}$  will lead to a larger current flowing between the electrodes. For the two designs (Short and Long), the evolution of the current variation with  $w_{el}$  is displayed in Figure 6:6 A) and B). In both cases the current variation increases with  $w_{el}$  until it reaches a final value. From the fluidic aspect  $w_{el}$  cannot be increased too drastically as it would lead to vorticity in the dead volumes. In both cases the increase was interpolated with an increasing exponential decay as displayed in Figure 6:6 A) and B).  $w_{el}$  was chosen as the time when approximately 95% of the final value was reached, as a compromise between the maximum sensitivity and fluidic considerations. This corresponds to  $w_{el} = 90 \mu\text{m}$  and  $w_{el} = 140 \mu\text{m}$  for  $d_{el} = 50 \mu\text{m}$  and  $150 \mu\text{m}$ , respectively. Details on the fitting parameters are given in paragraph D.6 in Appendix D.

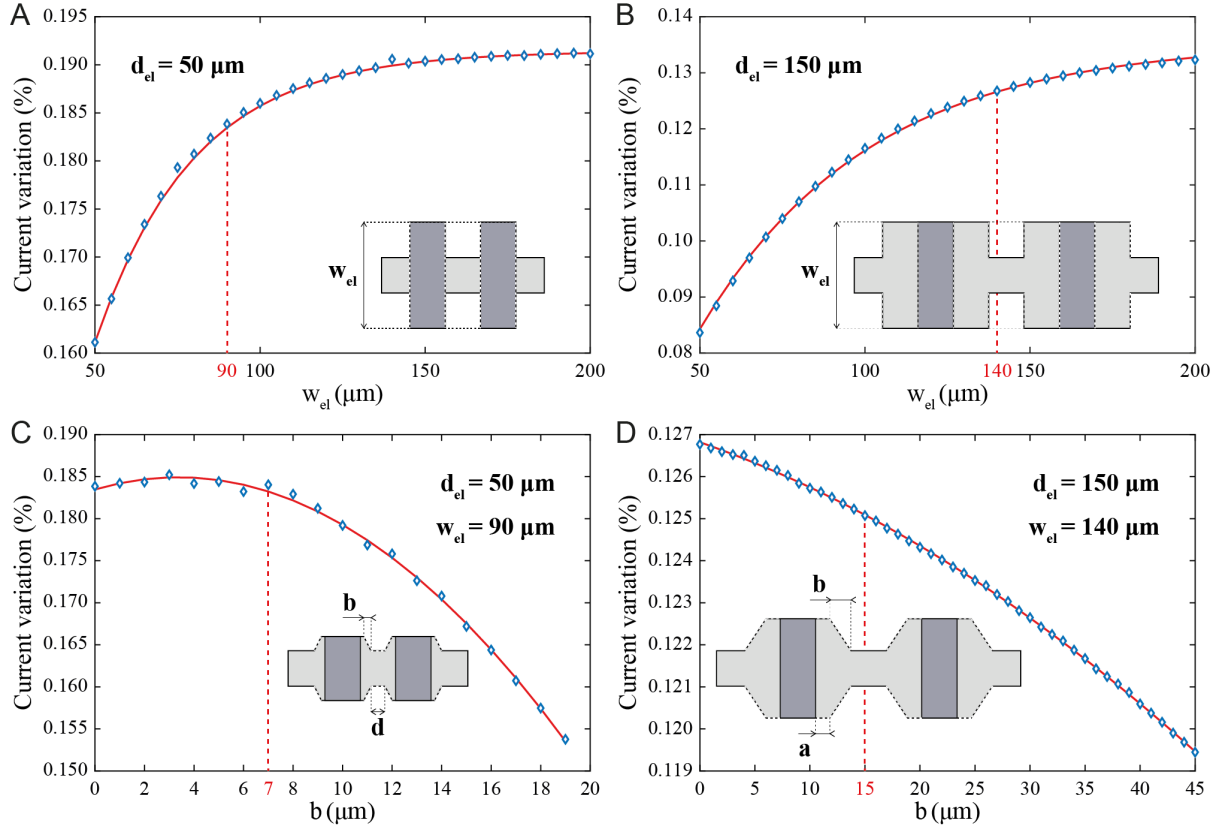


Figure 6:6 Simulation of the current variation due to an 8  $\mu\text{m}$  diameter polystyrene bead located at  $x = 0 \mu\text{m}$ ,  $y = 0 \mu\text{m}$ ,  $z = h/2 = 25 \mu\text{m}$ . Evolution with  $w_{el}$  for (a)  $d_{el} = d = 50 \mu\text{m}$  and (b)  $d_{el} = 150 \mu\text{m}$  with  $a = 50 \mu\text{m}$ ,  $b = 0 \mu\text{m}$ ,  $d = 50 \mu\text{m}$ . Evolution with  $b$  for (c)  $d_{el} = 50 \mu\text{m}$  for  $w_{el} = 90 \mu\text{m}$ ,  $a = 5 \mu\text{m}$ ,  $d = d_{el} - 2 * (a + b) = 40 - 2b$  and (d)  $d_{el} = 150 \mu\text{m}$  for  $w_{el} = 50 \mu\text{m}$ ,  $w_{el} = 140 \mu\text{m}$ ,  $d = 50 \mu\text{m}$ ,  $a = (d - d_{del})/2 - b = 50 - b$ . Fitted curves are displayed in red.

### 6.2.3.3 Influence of $b$

Increasing the widening length,  $b$ , should reduce the current variation as the confinement of the electric field lines will be reduced due to a smoother transition between the electrode side and the maximum sensitivity area,  $d$ . At the same time, a small  $b$  value will correspond to a geometry presenting corners. Figure 6:6 C) and D) shows the results for respectively a “Short” and a “Long” design.

In Figure 6:6 C),  $a$  is fixed to 5  $\mu\text{m}$  for fabrication considerations, 5  $\mu\text{m}$  being the minimum distance for which the electrodes will still be on each side of the constriction.  $b$  is optimized and  $d$  is deduced from the geometric relation  $d + 2 * (a + b) = d_{el}$ . The decrease was interpolated with a polynomial decay and  $b$  was taken as 99% of the maximum value of  $b$  as a compromise between the maximum

Design proposition for impedance sensing of single cells and cell aggregates

sensitivity and fluidic considerations. It corresponds to  $b = 7 \mu\text{m}$  and  $d = 26 \mu\text{m}$ . This design will be referred to as “Short Optimized” (SO) design and the original design with  $d_{el} = 50 \mu\text{m}$  as “Short Conventional” (SC) design. Details on the fitting parameters are given in paragraph D.6 in Appendix D.

In Figure 6:6 D),  $d$  is fixed to  $50 \mu\text{m}$ , to have the full central sensitive volume of the size of the aggregate,  $b$  is optimized and  $a$  is deduced from the geometric relation  $d + 2 * (a + b) = d_{el}$ . Following the same methodology, we obtained  $b = 15 \mu\text{m}$  and  $a = 35 \mu\text{m}$ . This design will be referred to as “Long Optimized” (LO) design and the original design with  $d_{el} = 150 \mu\text{m}$  as “Long Conventional” (LC) design.

#### 6.2.4 Proposed design for testing

All the geometrical parameters used for the four designs are summarized in Table 2. Figure 6:7 presents the current variation due to an  $8 \mu\text{m}$  diameter polystyrene bead located at  $y = 0 \mu\text{m}$  and  $z = h/2 = 25 \mu\text{m}$  for the four tested designs.

Design	h	l <sub>el</sub>	w	d <sub>el</sub> (*)	w <sub>el</sub>	b	d	a
	$\mu\text{m}$	$\mu\text{m}$	$\mu\text{m}$	$\mu\text{m}$	$\mu\text{m}$	$\mu\text{m}$	$\mu\text{m}$	$\mu\text{m}$
SC	50	50	50	50	50	0	50	0
SO	50	50	50	50	<b>90</b>	<b>7</b>	<b>26</b>	5
LC	50	50	50	150	50	0	50	0
LO	50	50	50	150	<b>140</b>	<b>15</b>	50	<b>35</b>

Table 2 Geometrical parameters used for each design, optimized parameters values are in bold. (\*) indicates that the value was chosen but not optimized.

In an optimized design, the peak amplitude for a centered particle is increased with both inter-electrode distances: +14.4% for the Short design and +50.1% for the Long design compared to the corresponding conventional designs. In both cases, the peaks are sharper for the optimized designs.

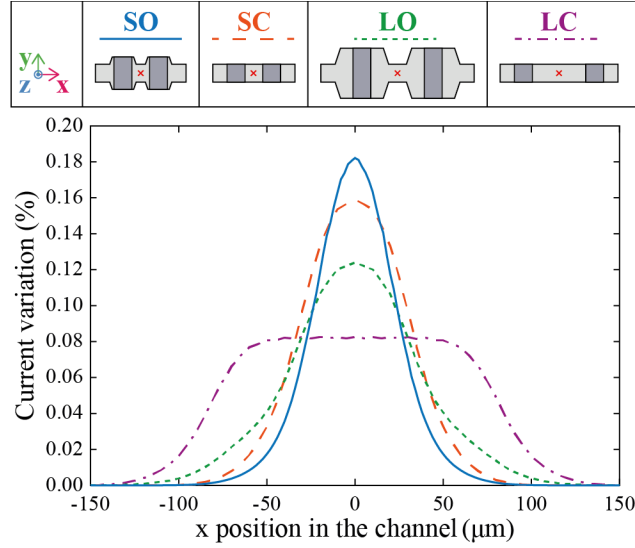


Figure 6:7 Simulation of the current variation due to an 8  $\mu\text{m}$  diameter polystyrene bead located at  $(y = 0 \mu\text{m}, z = h/2 = 25 \mu\text{m})$ . Evolution with the x position in the microchannel for the 4 designs: Short Optimized (SO), Short Conventional (SC), Long Optimized (LO) and Long Conventional (LC). The red cross indicates the point  $(x=0, y=0)$  on each design.

Figure 6:8 shows the evolution of the current variation for each design for an 8  $\mu\text{m}$  diameter polystyrene bead with A) the y position of the particle located at  $x = 0 \mu\text{m}$  and  $z = h/2 = 25 \mu\text{m}$  and with B) the z position of the particle located at  $x = 0 \mu\text{m}$  and  $y = 0 \mu\text{m}$ . In the case of the Short designs, the current variation is very dependent on both the lateral and vertical positions of the particle.

Concerning the lateral position, for the SO design, the variation of the current variation will be 32% greater near the wall in respect to the variation linked to a centered particle. For the SC design, it will be of 3.2%. For the Long design, those variations will be of 10.9% and 3.2% for the LO and LC designs respectively. Optimized designs are more sensitive to the y position hence requiring some lateral focusing.

Concerning the z position, the Short designs are more sensitive to the vertical position of the particle than the Long designs. The most sensitive design is the SC design with +70.5%/-26.9% of variation of the current variation compared to a z-centered particle ( $z = h/2 = 25 \mu\text{m}$ ), considering the lowest/highest z positions of the particle ( $z = 5 \mu\text{m}$  and  $z = 45 \mu\text{m}$ ). The SO design is a bit less sensitive with +48.7%/-18.5%. The Long designs are less sensitive to the z

position of the particle with +4%/-2.3% and +5.1%/-1.3% for the LO and LC designs respectively.

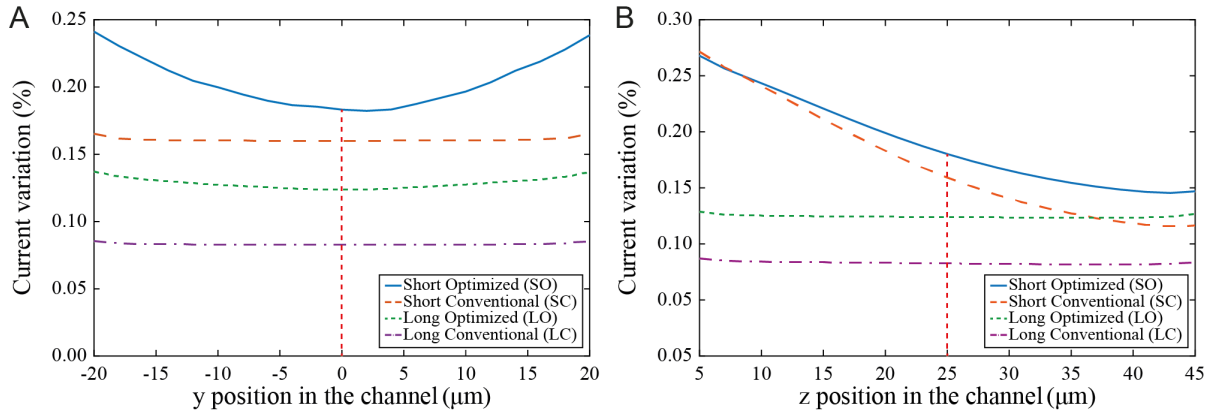


Figure 6:8 Simulation of the current variation due to an 8  $\mu\text{m}$  diameter polystyrene bead for the 4 designs. Evolution with (a) the y position in the microchannel (located at  $x = 0 \mu\text{m}$ ,  $z = h/2 = 25 \mu\text{m}$ ) and with (b) the z position in the microchannel (located at  $x = 0 \mu\text{m}$ ,  $y = 0 \mu\text{m}$ ). The red vertical dotted line represents the position of the particle in the center ( $x = 0 \mu\text{m}$ ,  $y = 0 \mu\text{m}$  and  $z = 25 \mu\text{m}$ ).

### 6.2.5 Vertical and longitudinal position sensitivity

As mentioned at the beginning of this chapter, the goal of this study is to (1) detect the particle with a signal as high as possible and (2) have a signal not sensitive to the particle position (lateral and vertical) in the microchannel. For each design, the evolution of the current variation with the x position in the channel at different heights is displayed in Figure 6:9. The Short designs are very sensitive to the height of the particle, as can be noticed both in the shape and in the amplitude compared to the Long designs.

The Long designs are sensitive to the height of the particle mostly in the shape but the amplitude of the current variation in the central zone ( $x = 0 \mu\text{m}$ ) varies little and hence will be mostly linked to the size of the particle.

For the conventional designs (SC and LC presented in Figure 6:9 A) and C) respectively), when the particle passes close to the electrodes (mostly  $z = 5 \mu\text{m}$ ), the shape of the peak is not just a drop but is strongly M-shaped. This is due to the fact that when the particle passes near the electrode (low heights) in the conventional design, the perturbation is higher than when the particle is in the middle of the detection area ( $x = 0 \mu\text{m}$ ). This particular peak form is also

## Design proposition for impedance sensing of single cells and cell aggregates

observed in the case of Coulter counters when the particle passes close to the wall of the aperture (Allen 1997). For the SO design, presented in Figure 6:9 B), the M shape is only present when the particle passes very close to the electrodes. In the case of the LO design in Figure 6:9 D), the M-shaped curve is also present but the maxima are only local maxima and the global maximum is in the central part of the channel ( $x = 0 \mu\text{m}$ ). In the optimized designs, as the electrode is wider, the passing of a particle close to the electrode induces less variation than in the conventional designs.

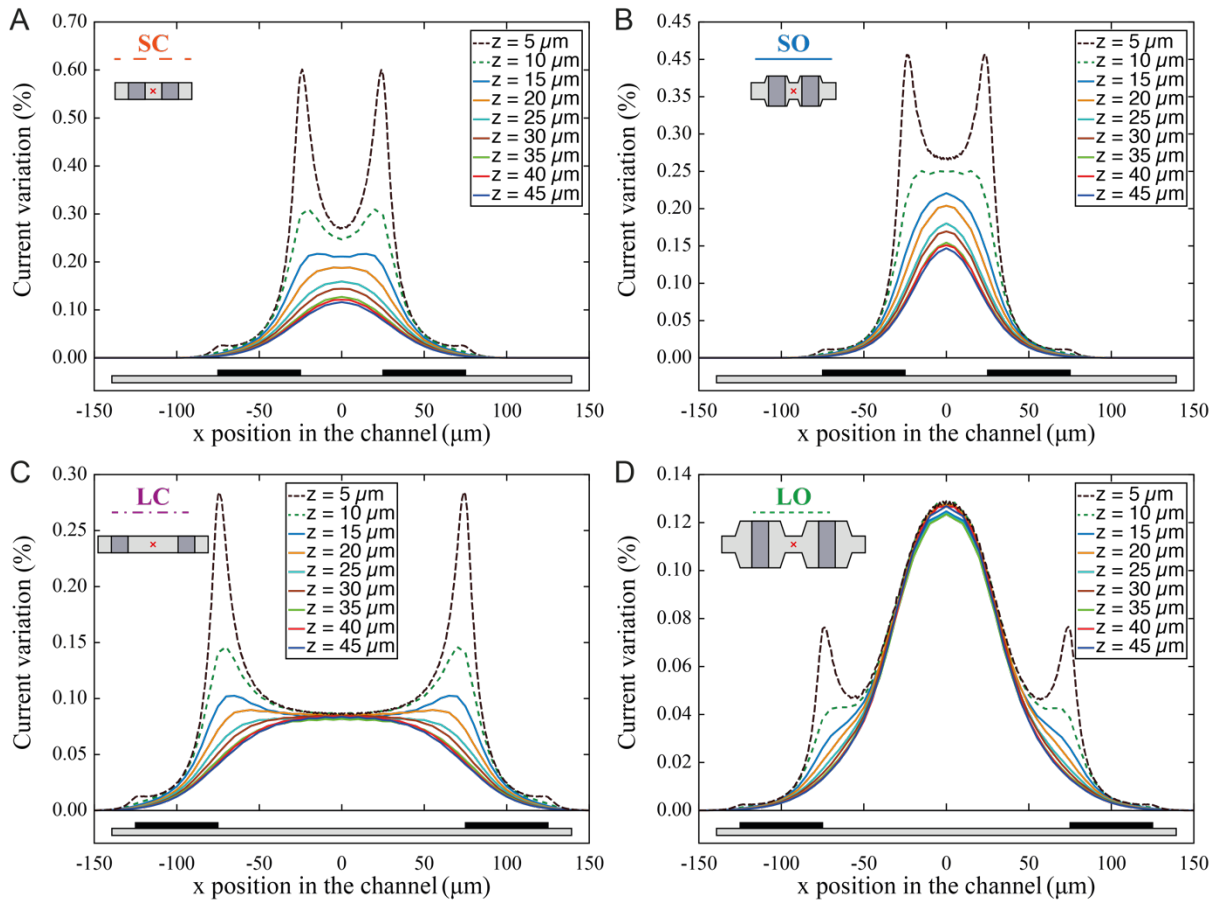


Figure 6:9 Simulation of the current variation due to an 8  $\mu\text{m}$  diameter polystyrene bead. Evolution with the x position in the microchannel (located at  $y = 0 \mu\text{m}$ ) at different heights for the 4 designs: (A) SC (B) SO (C) LC (D) LO. Electrode positions (in black) are indicated under each graph.

## 6.3 Laboratory experiments

### 6.3.1 Fabrication

The four designs were fabricated on two chips: each chip contains in the middle 9 electrodes used for DEP centering, and on both sides a combination of the 3 designs, symmetrically (SC, LC and either SO or LO). The process flow used for the fabrication is presented in Chapter 4 and in the article (Cottet, et al. 2017).

The different fabricated designs are presented in Figure 6:10.

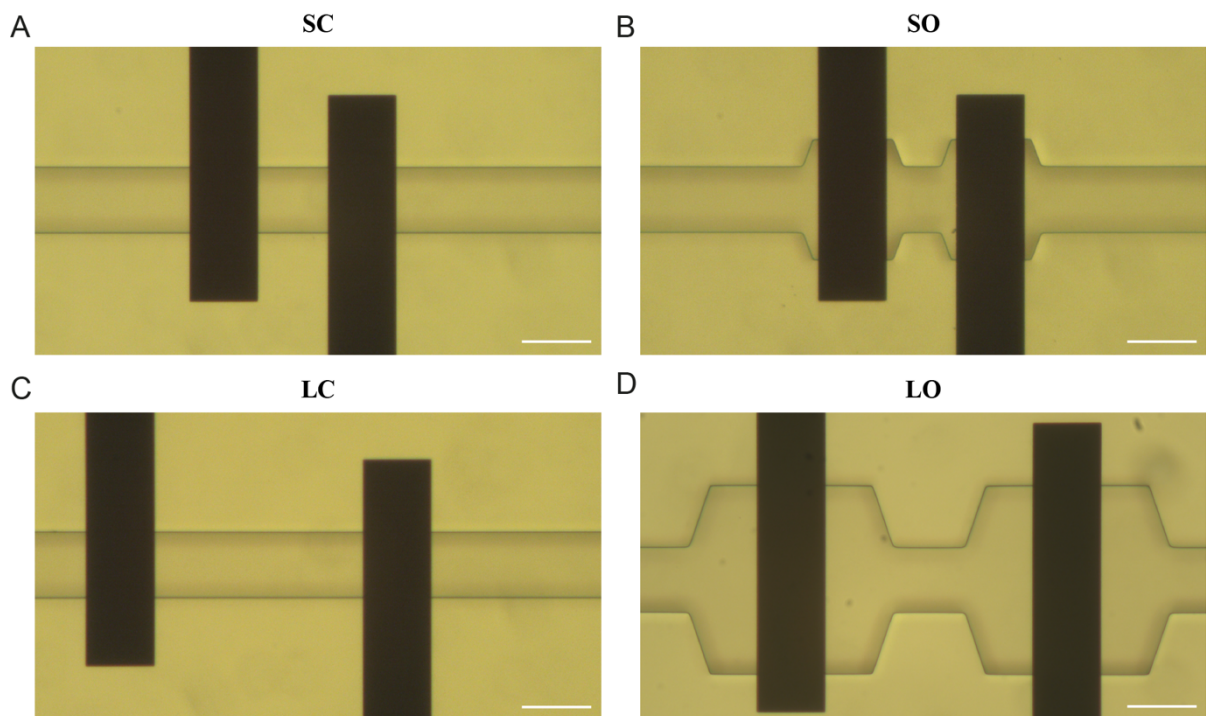


Figure 6:10 Photographs of the different designs (a) SC (b) SO (c) LC (d) LO. Scalebar 50  $\mu\text{m}$ . Ti/Pt Electrodes are visible as black stripes.

### 6.3.2 Experimental setup

Figure 6:11 presents the schematic representation of the experimental setup used.  $10 V_p$  at 100 kHz were applied on the DEP focusing electrodes to center the particles laterally (Braschler, et al. 2008, Demierre, et al. 2008) and to provide a vertical lifting (Shaker, et al. 2014).



Impedance measurements were performed by applying an AC signal of  $0.8 V_p$  at a frequency of 500 kHz on one electrode and amplifying the current change on the other electrode using an HF2TA current amplifier (Zurich Instruments, Zurich – Switzerland). The current was demodulated with an HF2LI Lock-In amplifier (Zurich Instruments, Zurich – Switzerland).

The channel was filled first with PBS (1.6 S/m) prior to the experiment using a Nemesis syringe pump. A suspension of 8  $\mu\text{m}$  diameter polystyrene beads (Sigma Aldrich, Buchs – Switzerland) in PBS at  $3.5 \times 10^5$  beads/ml was prepared and then perfused at 10  $\mu\text{l/h}$  during the experiment to provide a flow rate similar to the one that would be used for DEP trapping of cells in flow as presented in Chapter 5. Therefore, the DEP centering module enables to have a reproducible height of the particles at low flow rates. Experimental data were recorded and further processed with MATLAB.

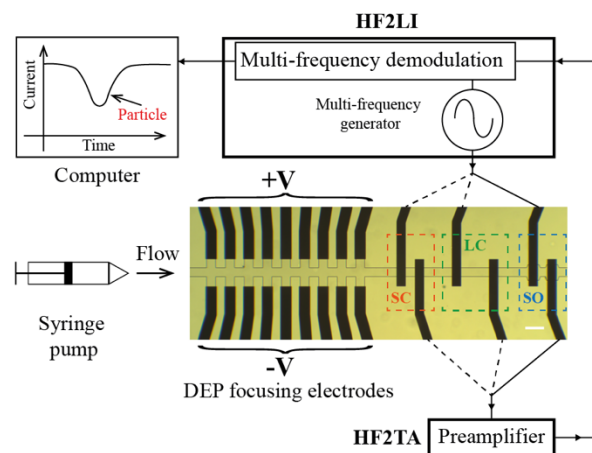


Figure 6:11 Schematic representation of the system with a photograph of the chip showing 3 designs. Scalebar 100  $\mu\text{m}$ .

## 6.4 Results and discussion

Figure 6:12 presents the experimental results obtained for the four different designs. In the SO and LO designs, the velocity of a particle passing through is not constant due to the widening of the microchannel. For this reason, the time scale in Figure 6:12 was not converted into a distance scale. The laboratory experiments are in good agreement with the simulations. The relative amplitudes of the curves at  $t = 0$  ms (particle at  $x = 0$ ) are similar to what was predicted by the simulations (cf Figure 6:7 and Figure 6:9). According to

observations with the microscope and to the standard dispersion observed in Figure 6:12, the shape of each curve corresponds to a particle centered laterally with DEP. The M-shape curves observed for the conventional designs (SC and LC) indicate that the particle is not centered vertically. According to the amplitude of the peak and the M-shape we can estimate the height of the center of the particles between 5 and 15  $\mu\text{m}$ . At this flow rate (10  $\mu\text{l/h}$ ) the DEP force overcome sedimentation but are insufficient to lift the particles up to the center of the channel.

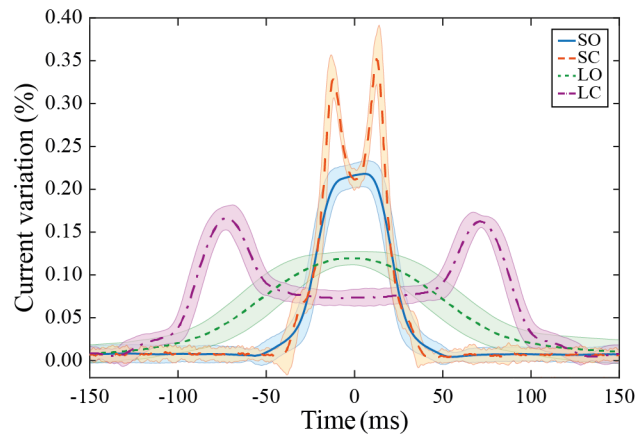


Figure 6:12 Experimental data showing the evolution with time of the average current variation for each design with  $\pm 2$  times the standard deviation ( $n \geq 8$ ) due to an 8  $\mu\text{m}$  diameter polystyrene bead in the microchannel for the 4 designs. Measurements were performed for the 4 designs at a flow rate of 10  $\mu\text{l/h}$  (particle speed in the order of 1000  $\mu\text{m/s}$ ).

Details on the data processing can be found in paragraph D.3 in Appendix D.

Both simulations and laboratory experiments provided insights on the performances of each design. The “Short” designs provide a higher signal when a particle is passing between the electrodes compared to the “Long” ones. The Short Conventional design (SC) provides a signal highly dependent both in shape and in amplitude on the height of the particle in the microchannel. The M shape obtained could be analyzed to determine the height of the particles. One of the challenges is to have enough points on the experimental curve to determine precisely the amplitude of the M. The signal could, however, be misinterpreted as two particles closely following each other. The model presented in this chapter is intended to be used with a small cell concentration. However, in case of doublets, the current variation is relatively higher than for

a single particle passing. Furthermore, the shape of the peak is modified. In case of separated particles passing through the detection area at the same time, a similar conclusion is still valid: higher variation of the current variation and/or two peaks close to each other depending of the distance between the particles.

The short optimized design (SO) provides a signal amplitude which is still dependent on the particle height but the experimentally observed shape is a single peak. The peak shape height dependency is less pronounced for this design: the M shape only occurs on very low heights and is not observed experimentally thanks to the DEP lifting. The long designs provide a broader signal because of a longer transition time between the electrodes. In the long conventional design (LC), the current variation at the center does not depend on the particle height. However, off-center, the current variation is higher and the related peak amplitude is height dependent. Finally, for the long optimized design (LO), there is only a single peak whose amplitude does not depend on the particle height. The current density at  $x = 0 \mu\text{m}$  for each design is displayed in paragraph D.4 in Appendix D.

The sensitivities to the longitudinal fabrication misalignment (along the x axis) of the optimized designs are presented in paragraph D.5 in Appendix D. For a misalignment of  $5 \mu\text{m}$ , this would result in a variation of the current variation of 0.5% for SO and 0.02% for LO compared to the respective references without longitudinal misalignment. Analysis of fabrication results presented in (Cottet, et al. 2017) showed that the maximum misalignment obtained was in all cases less than  $5 \mu\text{m}$  as can also be seen in Figure 6:10.

The best candidate for our application, characterization of particles at very low flow rate with a relative insensitivity to the particle height, is the long optimized design. Peak detection algorithms, after adjustment, will find central peaks in all cases (Brazey, et al. 2018). This design is also insensitive to longitudinal misalignment in the fabrication process. As  $8 \mu\text{m}$  polystyrene beads were used to perform all the optimization simulations, it was considered as the lower limit for the particle diameter. Different diameters were simulated for the long optimized (LO) design and the results show that the current variation

significantly increases when the particle diameter increases but does not depend on the electrical conductivities of the medium as illustrated in Table 3. The value of the electrical conductivity should be chosen according to the application: a high conductivity to obtain more signal for impedance sensing only and a lower conductivity if the sensor should be integrated in a chip with for example DEP trapping to reduce Joule heating.

Particle diameter (in $\mu\text{m}$ )	Current variation (in %)	
	$\sigma_m = 1.6 \text{ S/m}$	$\sigma_m = 0.16 \text{ S/m}$
8	0.1193	0.1193
10	0.2507	0.2495
12	0.4194	0.4178
14	0.6749	0.6732
16	1.0006	0.9995
18	1.4375	1.4341
20	1.9725	1.9638
22	2.6571	2.6494
24	3.4516	3.4434
26	4.4685	4.4558
28	5.5781	5.5657
30	6.9738	6.9619
32	8.5453	8.5241
34	10.4399	10.4135
36	12.5886	12.5617
38	15.1498	15.1200
40	18.0046	17.9733
42	21.5098	21.4709
44	25.4324	25.3903
46	30.3095	30.2645
48	36.0182	35.9647

Table 3 Comparison of the simulated influence of the different diameters of polystyrene beads (located at  $x = 0 \mu\text{m}$ ,  $y = 0 \mu\text{m}$ , and  $z = h/2 = 25 \mu\text{m}$ ) on the current variation for a Long Optimized (LO) design for two different electrical conductivities of the medium ( $\sigma_m = 1.6 \text{ S/m}$  and  $\sigma_m = 0.16 \text{ S/m}$ ).

The evolution of the current variation for a  $30 \mu\text{m}$  diameter particle in the LO design is displayed in Figure S D:8 in Appendix D.

## 6.5 Combining DEP Trapping with impedance measurement

A chip combining both the improved trapping design and the impedance sensing unit LO was designed and fabricated as presented in Figure 6:13.

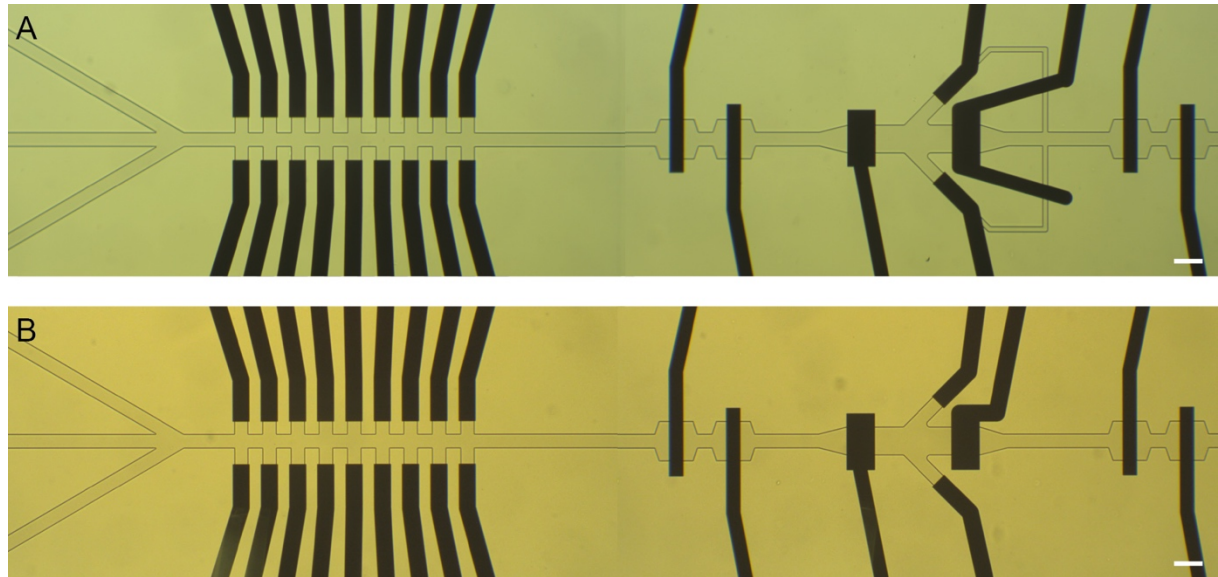


Figure 6:13 Full chip fabricated version with the DEP centering electrodes A) with and B) without the auxiliary outlets) and two LO designs located before and after the improved trapping chamber. Scalebar 100  $\mu\text{m}$ .

Preliminary tests were performed using the experimental setup presented in Figure 6:14 with the improved trapping design without the auxiliary outlets. The electrical conductivity used for the experiment was set to  $\sigma_m = 0.156 \text{ S/m}$  to limit the Joule heating and to be in a similar configuration to what was presented in Chapter 5 for the trapping. Reducing the electric conductivity will reduce the amplitude of the current drop but the relative current drop in percentage should remain the same as expected from Table 3. This reduction should also come with a lower noise level.

## Design proposition for impedance sensing of single cells and cell aggregates

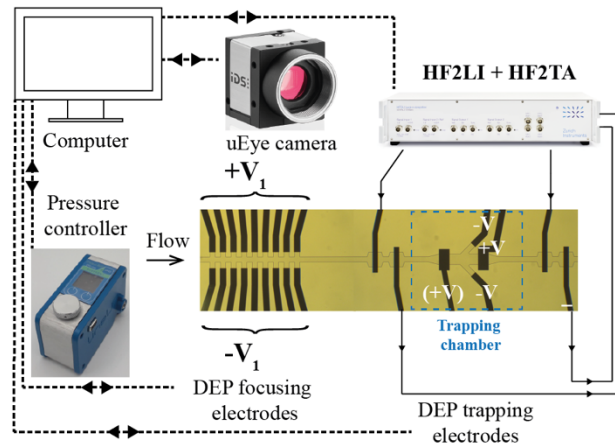


Figure 6:14 Schematic representation of the experimental setup with a computer controlling with LabVIEW™ all the different instruments: the uEye camera for visualization, the pressure controller, and HF2LI and HF2TA from Zurich Instruments and two arbitrary function generators. DEP centering electrodes are used to center particles laterally and to provide a vertical lift.

Preliminary experimental results are presented in Figure 6:15. In this experiment all the instruments were operated individually and the centering was inactive.

The relative current variations before and after the trapping chamber, respectively Signal IN and OUT, are measured during a trapping experiment. Groups of cells of various sizes entered the trapping chamber at different instant: at  $t = 40.4$  s, a group of 6 cells entering the trapping chamber was detected by the “IN” LO design in Figure 6:15 A). Groups of 3 and 2 cells were respectively detected at  $t = 57$  s and  $t = 67$  s by the “IN” LO design as presented in respectively Figure 6:15 B) and C). At  $t = 88$  s, DEP electrodes were switched off, letting the aggregate leave the trapping chamber to be detected by the “OUT” LO design at  $t = 91$  s as presented in Figure 6:15 D). At the same time another large group of cells was detected by the “IN” LO design. The amplitude of the different peaks of current variation measured was sufficient to be detected with the combination of the HF2LI + HF2TA. As displayed in all the graphs the amplitude of the signal was sensitive to the clusters and more specifically to its volume.

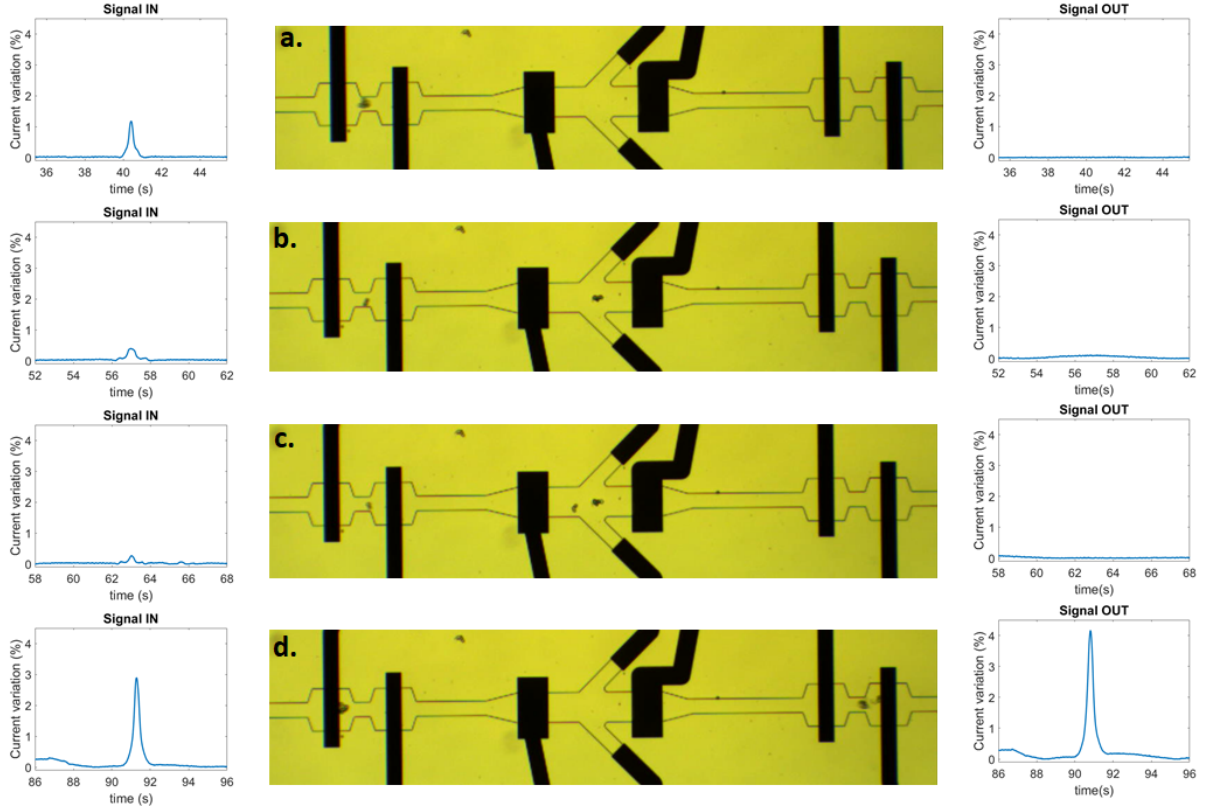


Figure 6:15 Snapshots of live HEK cells trapping with the improved trapping design without auxiliary outlets and detection with the LO design at (a)  $t = 40.4$  s (b)  $t = 57$  s (c)  $t = 63$  s and (d)  $t = 91$  s.  $V_{trap} = 22.5 V_p$  at  $f_{DEP} = 10$  kHz for the trapping and centering,  $V_{IS} = 0.8 V_p$  at  $f_{IS} = 500$  kHz for the impedance sensing with the LO design, no centering voltage was applied,  $\sigma_m = 0.156$  S/m and  $P = 2$  mbar.

This proves the feasibility of combining the trapping with dielectrophoresis with impedance sensing in the same microfluidic chip.

## 6.6 Conclusions

In this chapter, we describe a comprehensive methodology for improving the sensitivity of a coplanar electrode design by modifying the microchannel geometry. The results of the simulations were tested experimentally. The methodology described in this work can be applied for any size of channels. More importantly, two optimized designs were proposed and validated: depending on the specifications of the application (centering method, flow speed, acquisition setup, ...) one of the optimized designs would be preferred to the other. In particular, the short optimized design (SO) provides a maximum signal for centered particles (in all directions) and the long optimized (LO) is relatively

Design proposition for impedance sensing of single cells and cell aggregates

insensitive to the particle height while giving more signal than the conventional one. This conclusion would be applicable in general.

For our application, the Signal-to-Noise ratio (SNR) should be sufficient to detect single cells in a relatively large channel. For all designs the SNR was sufficient to enable good detection of 8  $\mu\text{m}$  diameter particles (Figure S D:4 in paragraph D.3 in Appendix D displays the signal obtained with the SO design).

The designs could be tested at higher flow rates to better overcome sedimentation. This should result in a smaller standard variation and better assessment of the size of the particle for all designs. However, the transition time of the particle between the electrodes will be shorter hence reducing the number of points measured. The variation of the current with the particle size could be validated experimentally.

Combining our optimized geometries (SO and LO) with more electrodes, as recently proposed by De Ninno et al. (De Ninno, et al. 2017), would enable a better characterization of the particles moving between the electrodes, even for the lateral position (Reale, et al. 2018). The designs are envisioned to be used for sizing and characterizing particles from single cells to cell aggregates as presented in paragraph 6.5. In the future, different sizes of particles will be used, as well as different cell types.



# Chapter 7 Conclusion and Outlook

This chapter describes the conclusions obtained from the work performed in this thesis and proposes an outlook of the use of cell aggregates created under flow conditions with dielectrophoresis.

### 7.1 Conclusion

The work described in this manuscript aimed at creating cell aggregates of controlled size and properties under flow conditions in a microsystem with dielectrophoresis.

The state of the art on cell trapping technologies and cell aggregate formation technologies showed that a method to create cell aggregates of controlled dielectric properties and size is still missing. For its label free capability to selectively move and trap cells, dielectrophoresis was selected as the method of choice. Most of the articles in the literature proposed either to trap single cells or to trap an unknown quantity of cells together with dielectrophoresis. A set of requirements to form cell aggregates of controlled size and properties under flow conditions in a microsystem with dielectrophoresis was proposed.

In this thesis, the work covers several fields:

- **Cell modeling:** A computational tool, MyDEP, was developed to study the dielectrophoretic behavior of particles and cells in a suspension medium. The software is also provided with a database where we compiled cell dielectric models available in the literature to be used by new DEP users as well as experts for their DEP simulations.
- **Fabrication:** A reproducible method for  $\mu\text{m}$  precision alignment of PDMS microchannels with coplanar electrodes using a conventional mask aligner was developed. It is based on the use of a silicon mold in combination with a PMMA sarcophagus for precise control of the parallelism between top and bottom surfaces of molded PDMS. This technique allows to bond and align chips with a resolution of less than  $2\ \mu\text{m}$ .
- **Trapping with DEP:** A trapping design based on coplanar electrodes was proposed, simulated and successfully tested experimentally on HEK cells with an automated setup. It proved its capability to create aggregates of a controlled number of cells with DEP. The cell

aggregates proved to be stable (no disruption) after only 5 minutes of contact.

- **Impedance sensing:** A comprehensive analysis of the influence of the geometry of a coplanar electrode layout for Electrical Impedance Flow Cytometry (EIFC) was performed. The goal of this study was to (1) detect the particle with a signal as high as possible and (2) have a signal not sensitive to the particle position (lateral and vertical) in the microchannel. Two optimized designs were proposed and validated. One design was combined with the trapping design to create a full Lab-On-a-Chip platform. This proves the feasibility of combining the trapping with dielectrophoresis with impedance sensing in the same microfluidic chip.

## 7.2 Outlook

The work performed in this thesis can be extended in several aspects:

### 7.2.1 Theory and MyDEP

In our computational tool MyDEP, the possibility to import and display datasets on each graph has been implemented. This option could be useful especially for electrorotation. Today the user can test different sets of values for the models and see if the simulated model and the experimental data superimpose. The next step is to implement a fitting algorithm to directly find the parameters<sup>2</sup>.

Another interesting feature to implement in MyDEP is the calculation of the volume fraction in a microsystem, which is necessary to be able to predict the variation of impedance generated by the passage of a particle between two electrodes. Formula can be found in the literature for the facing electrode

---

<sup>2</sup> Discussions with Kai Hoettges from the University of Liverpool suggest that algorithms such as the Levenberg–Marquardt algorithm (LMA or LM) also called the Damped Least-Square (DLS) might be the most suitable.

configuration (see (Morgan, et al. 2007) and (Gawad, et al. 2004)) but unfortunately not for the coplanar electrodes. Such analytical formula would allow to perform preliminary predictions of the impedance variation.

The created database combined at the time of the thesis writing 79 models from over 39 articles, each with the full references. Each user of MyDEP can submit a new model with all the related reference. We hope this will enable to enrich our database.

Cells DEP crossover frequencies are linked according to (Gascoyne and Shim 2014), to the cell membrane morphology. Cell membranes are most of the time not smooth and contain features such as microvilli, folds and ruffles that cause an underestimation of the cell surface membrane compared to an idealized spherical cell. Wang et al. (Wang, et al. 1994) introduced the concept of “membrane folding factor” as the ratio between the actual cell membrane area to the area of a perfectly smooth cell of similar volume. This factor could be added in the interface of MyDEP.

### 7.2.2 Simulations

2D FEM simulations were performed to simulate the trapping. In order to be able to consider the power dissipation in the chip, 3D simulations could be performed. On chip validation of the obtained values with a thermal camera for example would be challenging since measured temperature would be either above (PDMS) or under (glass) the microfluidic channel. Another possibility would be to use a temperature-dependent fluorescent dye such as rhodamine to assess the temperature (Ross, et al. 2001). Gravity could also be added in those 3D simulations.

As discussed in Chapter 3, particles simulated with the particle tracing module in COMSOL Multiphysics are considered as point particles and modify neither the flow lines nor the electric field distribution. They also can interpenetrate each other. 3D simulations with a moving mesh for each particle could be a way to overcome those limitations but would require a lot of computing power. The

dipole interaction between particles should also be considered for increased accuracy.

### 7.2.3 Fabrication

The fabrication technique developed in this thesis could be further improved by characterizing more deeply the shrinkage of PDMS with its curing temperature. This would allow to further reduce the mismatch between the PDMS microchannel and the electrodes which can occur when larger patterns need to be aligned. This would improve the diffusion of our published method, which is already used in other facilities.

### 7.2.4 Impedance

As mentioned in Chapter 6, the goal of the study was to (1) detect the particle with a signal as high as possible and (2) have a signal not sensitive to the particle position (lateral and vertical) in the microchannel. Only one frequency, 500 kHz was used for the measurements. Multiple frequencies could be used to improve the information that could be retrieve from the signal (size but also membrane and cytoplasm dielectric properties). Only the geometry of the sensor was discussed in this chapter. The treated signal, after removal of the baseline, still depends on the data processing used. To better improve the detection, a differential pair of sensors could be used as presented in (Gawad, et al. 2001) and (Clausen, et al. 2014) which would overcome this previous limitation. It would, however, require operating with a very low concentration of cells (real single cell suspension) to guarantee that only one cell at a time would pass in the sensor composed of three electrodes. Lastly to reduce the experimental noise, shielding could be integrated in the chip and in the PCB.

### 7.2.5 Design and experiments

The design of the trapping chamber was improved from the testing configuration to a 4-electrode configuration with a trapping chamber twice as large and auxiliary outlets. A similar study to what was done in the Chapter 6 on the impedance sensor could be performed to optimize the geometry of the chamber and the characteristics of the auxiliary outlets (width and length).

## Conclusion and Outlook

The proof of concept of impedance sensing together with DEP trapping was obtained. More experiments could be performed with a detailed analysis of the impedance signal obtained for the different sizes of the aggregates.

Preliminary assessment of the viability was performed with Trypan blue which only assesses the permeability of the cell. A deeper analysis would require studying the behavior of the cell aggregates after retrieving them, operation that was not initially designed for the chip and which could damage the aggregate. A larger chip with more integrated functions could be fabricated. In the actual version, all cells go through one path and it is not possible to discard only one cell coming between other cells. A possible solution would be to have parallel channels and to selectively decide which cell should penetrate the trapping chamber and to direct it there with DEP.

As stated by Gascoyne et al. (Gascoyne and Shim 2014), the modified medium used for DEP could alter cell function. In order to reduce this effect, cells could be transferred from a cell culture medium to a lower conductivity medium through a configuration such as an H-filter and inversely after aggregate formation as proposed in (Shim, et al. 2013).

All experiments were performed under a microscope without any control of the atmosphere. To reduce the impact of the experiments on cells, a controlled atmosphere (temperature, CO<sub>2</sub>) environment could be envisioned.

Parallelization of the creation of aggregates could also be envisioned but would require a more complex electronic and flow control which might limit the interest in the proposed design.

### 7.2.6 Applications

Many applications can be envisioned for the on-chip created aggregates. Composite aggregates made of different cell types could be one of the first step towards the use of DEP for organoid formation. More simply the fabricated chip offers a possibility to contact 2 cells together and to study their interaction as presented in Figure 7:1.

## Conclusion and Outlook

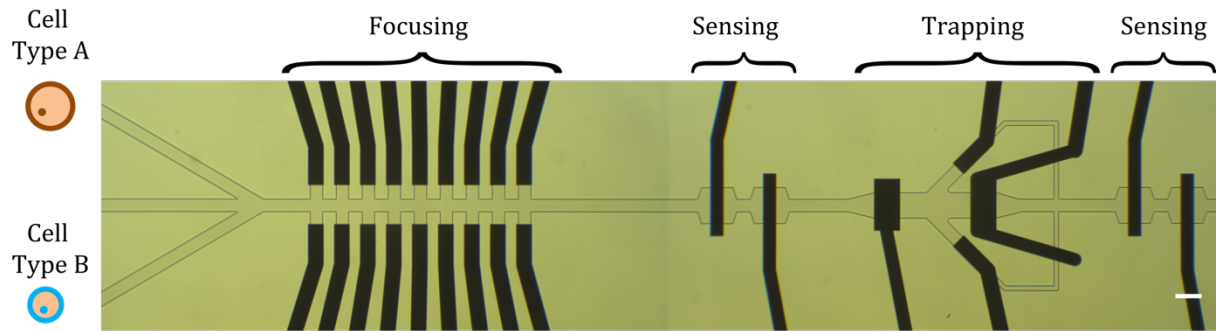


Figure 7:1 Proposal for creating composite aggregates. Scalebar 100  $\mu\text{m}$ .

The created aggregates could also be electroporated on chip and characterized before and after electroporation as presented in Figure 7:2.

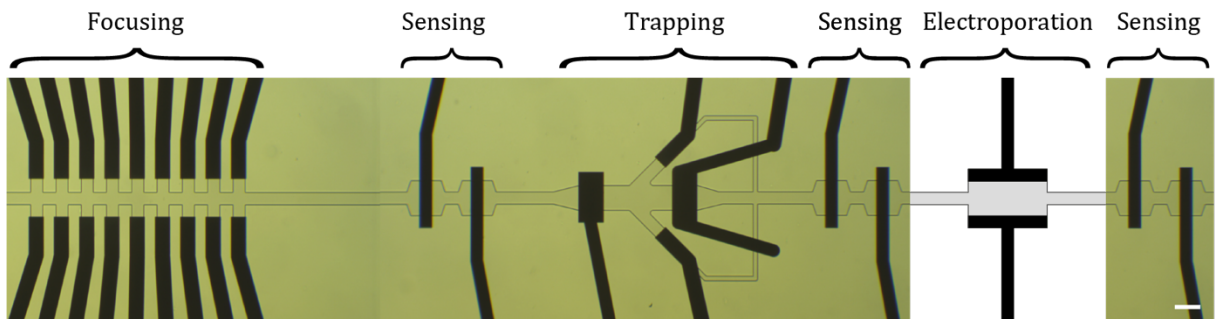


Figure 7:2 Design proposal of a chip combining cell centering, cell trapping and impedance sensing. Scalebar 100  $\mu\text{m}$ .

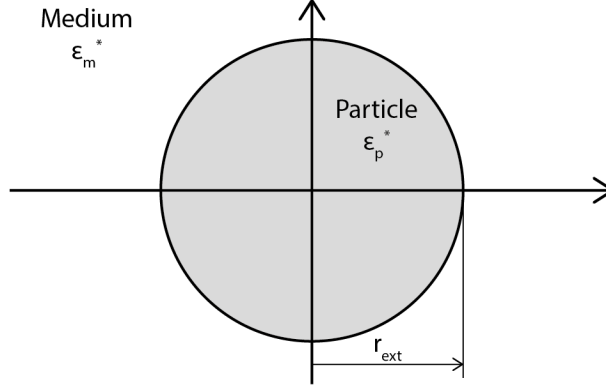
# Appendix A Dielectrophoresis theory and modeling with MyDEP

Theoretical calculations and formulas used in Chapter 2 are summarized hereafter. They also correspond to what was implemented in MyDEP software.



## A.1 Concentric shell models for a sphere

### A.1.1 Homogeneous particle



The DEP force acting on a homogeneous spherical particle in a medium is:

$$F_{DEP} = 2\pi r_{ext}^3 \epsilon_0 \epsilon_m \operatorname{Re}[CM(f)] \nabla E_{rms}^2$$

with  $CM(f)$  the Clausius-Mossotti factor:

$$CM(f) = \frac{\epsilon_p^* - \epsilon_m^*}{\epsilon_p^* + 2\epsilon_m^*}$$

$\epsilon^*$  is the complex permittivity defined as:

$$\epsilon_i^* = \epsilon_i \epsilon_0 - \frac{j\sigma_i}{\omega}$$

with  $\epsilon_0$  the vacuum permittivity,  $\epsilon_i$  the particle relative permittivity,  $\sigma_i$  the particle electrical conductivity and  $\omega = 2\pi f$  with  $f$  the frequency.

In this case:

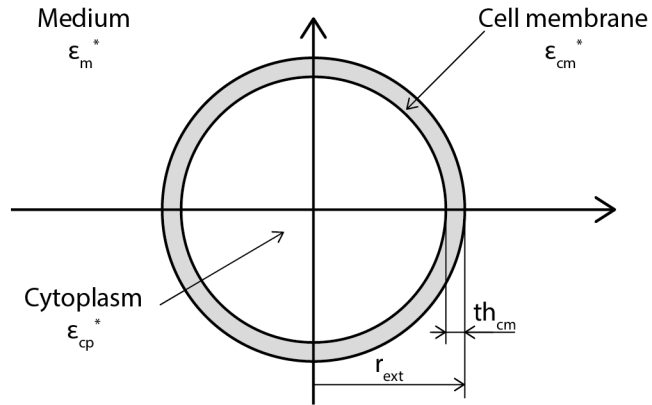
$$\text{Medium: } \epsilon_m^* = \epsilon_m \epsilon_0 - \frac{j\sigma_m}{\omega}$$

$$\text{Particle: } \epsilon_p^* = \epsilon_p \epsilon_0 - \frac{j\sigma_p}{\omega}$$

The torque on a homogeneous spherical particle in a medium due to an electric field is:

$$\Gamma_{DEP} = -4\pi r_{ext}^3 \epsilon_0 \epsilon_m \operatorname{Im}[CM(f)] |E^2|$$

### A.1.2 Single-shell

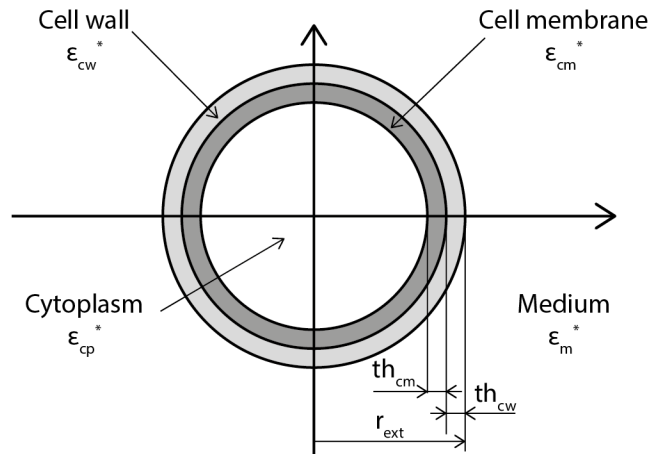


$$\text{Medium: } \epsilon_m^* = \epsilon_m \epsilon_0 - \frac{j\sigma_m}{\omega}$$

$$\text{Cell membrane: } \epsilon_{cm}^* = \epsilon_{cm} \epsilon_0 - \frac{j\sigma_{cm}}{\omega}$$

$$\text{Cytoplasm: } \epsilon_{cp}^* = \epsilon_{cp} \epsilon_0 - \frac{j\sigma_{cp}}{\omega}$$

### A.1.3 Two-shell



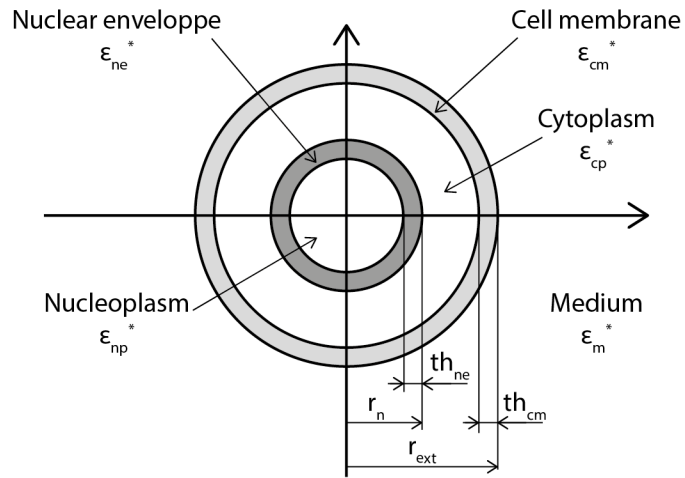
$$\text{Medium: } \epsilon_m^* = \epsilon_m \epsilon_0 - \frac{j\sigma_m}{\omega}$$

$$\text{Cell wall: } \epsilon_{cw}^* = \epsilon_{cw} \epsilon_0 - \frac{j\sigma_{cw}}{\omega}$$

$$\text{Cell membrane: } \epsilon_{cm}^* = \epsilon_{cm} \epsilon_0 - \frac{j\sigma_{cm}}{\omega}$$

$$\text{Cytoplasm: } \epsilon_{cp}^* = \epsilon_{cp} \epsilon_0 - \frac{j\sigma_{cp}}{\omega}$$

### A.1.4 Three-shell



$$\text{Medium: } \varepsilon_m^* = \varepsilon_m \varepsilon_0 - \frac{j\sigma_m}{\omega}$$

$$\text{Cell membrane: } \varepsilon_{cm}^* = \varepsilon_{cm} \varepsilon_0 - \frac{j\sigma_{cm}}{\omega}$$

$$\text{Cytoplasm: } \varepsilon_{cp}^* = \varepsilon_{cp} \varepsilon_0 - \frac{j\sigma_{cp}}{\omega}$$

$$\text{Nuclear envelope: } \varepsilon_{ne}^* = \varepsilon_{ne} \varepsilon_0 - \frac{j\sigma_{ne}}{\omega}$$

$$\text{Medium: } \varepsilon_{np}^* = \varepsilon_{np} \varepsilon_0 - \frac{j\sigma_{np}}{\omega}$$

**A.1.5 Four-shell**

A similar procedure can be used for a Four-shell sphere.

$$\text{Medium: } \varepsilon_m^* = \varepsilon_m \varepsilon_0 - \frac{j\sigma_m}{\omega}$$

$$\text{Cell wall: } \varepsilon_{cw}^* = \varepsilon_{cw} \varepsilon_0 - \frac{j\sigma_{cw}}{\omega}$$

$$\text{Cell membrane: } \varepsilon_{cm}^* = \varepsilon_{cm} \varepsilon_0 - \frac{j\sigma_{cm}}{\omega}$$

$$\text{Cytoplasm: } \varepsilon_{cp}^* = \varepsilon_{cp} \varepsilon_0 - \frac{j\sigma_{cp}}{\omega}$$

$$\text{Nuclear envelope: } \varepsilon_{ne}^* = \varepsilon_{ne} \varepsilon_0 - \frac{j\sigma_{ne}}{\omega}$$

$$\text{Nucleoplasm: } \varepsilon_{np}^* = \varepsilon_{np} \varepsilon_0 - \frac{j\sigma_{np}}{\omega}$$

## A.2 Concentric shell models for an ellipsoid

All calculation for single-shell, two-shell, three-shell, and four-shell ellipsoids are from (Kakutani, et al. 1993):

$$F_{DEP} = 2\pi a_{ext} b_{ext} c_{ext} \varepsilon_m \operatorname{Re}[CM(f)] \nabla E^2$$

$$\Gamma_{DEP} = -4\pi a_{ext} b_{ext} c_{ext} \varepsilon_0 \varepsilon_m \operatorname{Im}[CM(f)] |E^2|$$

if the particle is randomly oriented:

$$CM(f) = \frac{CM_x(f) + CM_y(f) + CM_z(f)}{3}$$

With a is the dimension along the x axis, b along y and c along z.

In this case the Clausius-Mossotti factor is:

$$CM_\alpha(f) = \frac{1}{3} \frac{\varepsilon_p^* - \varepsilon_m^*}{(\varepsilon_p^* - \varepsilon_m^*) A_\alpha + \varepsilon_m^*}$$

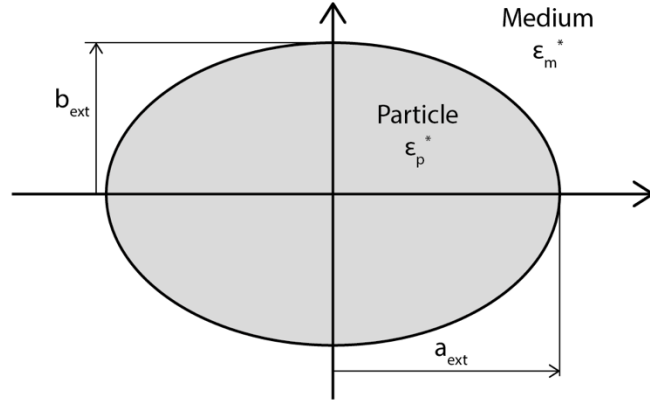
$\alpha$  represents either the  $x$ ,  $y$  or  $z$  axis and  $A_\alpha$  is the depolarization factor.

$$A_x = \frac{abc}{2} \int_0^\infty \frac{ds}{(s+a^2) \sqrt{(s+a^2) * (s+b^2) * (s+c^2)}}$$

$$A_y = \frac{abc}{2} \int_0^\infty \frac{ds}{(s+b^2) \sqrt{(s+a^2) * (s+b^2) * (s+c^2)}}$$

$$A_z = \frac{abc}{2} \int_0^\infty \frac{ds}{(s+c^2) \sqrt{(s+a^2) * (s+b^2) * (s+c^2)}}$$

## A.2.1 Homogeneous particle



$$a = a_{ext}, b = b_{ext} \text{ and } c = c_{ext}$$

$$A_{0x} = \frac{abc}{2} \int_0^\infty \frac{ds}{(s+a^2)\sqrt{(s+a^2)*(s+b^2)*(s+c^2)}}$$

$$A_{0y} = \frac{abc}{2} \int_0^\infty \frac{ds}{(s+b^2)\sqrt{(s+a^2)*(s+b^2)*(s+c^2)}}$$

$$A_{0z} = \frac{abc}{2} \int_0^\infty \frac{ds}{(s+c^2)\sqrt{(s+a^2)*(s+b^2)*(s+c^2)}}$$

$$\text{Medium: } \epsilon_m^* = \epsilon_m \epsilon_0 - \frac{j\sigma_m}{\omega}$$

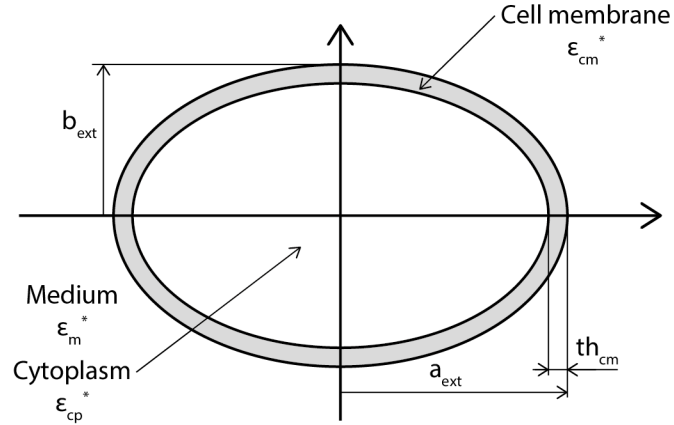
$$\text{Particle: } \epsilon_p^* = \epsilon_p \epsilon_0 - \frac{j\sigma_p}{\omega}$$

$$CM_\alpha = \frac{1}{3} \frac{\epsilon_p^* - \epsilon_m^*}{\epsilon_m^* + (\epsilon_p^* - \epsilon_m^*)A_{0\alpha}}$$

If the particle is randomly oriented:

$$CM(f) = \frac{CM_x(f) + CM_y(f) + CM_z(f)}{3}$$

### A.2.2 Single-shell



The dimensions involved in the calculation are:

$$a_0 = a_{ext}$$

$$a_1 = a_{ext} - th_{cm}$$

$b_i$  and  $c_i$  are defined in the same way.

$$\text{Medium: } \epsilon_m^* = \epsilon_m \epsilon_0 - \frac{j\sigma_m}{\omega}$$

$$\text{Cell membrane: } \epsilon_{cm}^* = \epsilon_{cm} \epsilon_0 - \frac{j\sigma_{cm}}{\omega}$$

$$\text{Cytoplasm: } \epsilon_{cp}^* = \epsilon_{cp} \epsilon_0 - \frac{j\sigma_{cp}}{\omega}$$

$$A_{1x} = \frac{a_1 b_1 c_1}{2} \int_0^{\infty} \frac{ds}{(s + a_1^2) \sqrt{(s + a_1^2) * (s + b_1^2) * (s + c_1^2)}}$$

$$A_{0x} = \frac{a_0 b_0 c_0}{2} \int_0^{\infty} \frac{ds}{(s + a_0^2) \sqrt{(s + a_0^2) * (s + b_0^2) * (s + c_0^2)}}$$

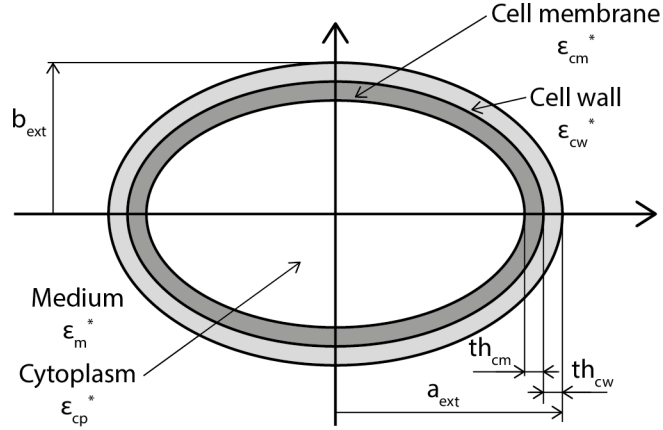
$$\epsilon_{1x}^* = \epsilon_{cm}^* \frac{\epsilon_{cm}^* + (\epsilon_{cp}^* - \epsilon_{cm}^*)(A_{1x} + l_1(1 - A_{0x}))}{\epsilon_{cm}^* + (\epsilon_{cp}^* - \epsilon_{cm}^*)(A_{1x} - l_1 A_{0x})}$$

$$CM_{\alpha} = \frac{1}{3} \frac{\epsilon_{1x}^* - \epsilon_m^*}{\epsilon_m^* + (\epsilon_{1x}^* - \epsilon_m^*) A_{0x}}$$



$$l_1 = \frac{a_1 b_1 c_1}{a_0 b_0 c_0}$$

### A.2.3 Two-shell



The dimensions involved in the calculation are:

$$a_0 = a_{ext}$$

$$a_1 = a_{ext} - th_{cw}$$

$$a_2 = a_{ext} - th_{cw} - th_{cm}$$

$b_i$  and  $c_i$  are defined in the same way.

The depolarizations factors are:

$$A_{2x} = \frac{a_2 b_2 c_2}{2} \int_0^\infty \frac{ds}{(s + a_2^2) \sqrt{(s + a_2^2) * (s + b_2^2) * (s + c_2^2)}}$$

$$A_{1x} = \frac{a_1 b_1 c_1}{2} \int_0^\infty \frac{ds}{(s + a_1^2) \sqrt{(s + a_1^2) * (s + b_1^2) * (s + c_1^2)}}$$

$$A_{0x} = \frac{a_0 b_0 c_0}{2} \int_0^\infty \frac{ds}{(s + a_0^2) \sqrt{(s + a_0^2) * (s + b_0^2) * (s + c_0^2)}}$$

Same procedure for  $A_{ix}$ ,  $A_{iy}$  and  $A_{iz}$  used with  $a_i$ ,  $b_i$  and  $c_i$ :

$$l_1 = \frac{a_1 b_1 c_1}{a_0 b_0 c_0}$$

$$l_2 = \frac{a_2 b_2 c_2}{a_1 b_1 c_1}$$

$$\text{Medium: } \epsilon_m^* = \epsilon_m \epsilon_0 - \frac{j\sigma_m}{\omega}$$

$$\text{Cell wall: } \epsilon_{cw}^* = \epsilon_{cw} \epsilon_0 - \frac{j\sigma_{cw}}{\omega}$$

$$\text{Cell membrane: } \epsilon_{cm}^* = \epsilon_{cm} \epsilon_0 - \frac{j\sigma_{cm}}{\omega}$$

$$\text{Cytoplasm: } \epsilon_{cp}^* = \epsilon_{cp} \epsilon_0 - \frac{j\sigma_{cp}}{\omega}$$

$$\epsilon_{2x}^* = \epsilon_{cm}^* \frac{\epsilon_{cm}^* + (\epsilon_{cp}^* - \epsilon_{cm}^*)(A_{2x} + l_2(1 - A_{1x}))}{\epsilon_{cm}^* + (\epsilon_{cp}^* - \epsilon_{cm}^*)(A_{2x} - l_2 A_{1x})}$$

$$\epsilon_{1x}^* = \epsilon_{cw}^* \frac{\epsilon_{cw}^* + (\epsilon_{2x}^* - \epsilon_{cw}^*)(A_{1x} + l_1(1 - A_{0x}))}{\epsilon_{cw}^* + (\epsilon_{2x}^* - \epsilon_{cw}^*)(A_{1x} - l_1 A_{0x})}$$

$$CM_x(f) = \frac{1}{3} \frac{\epsilon_{1x}^* - \epsilon_m^*}{(\epsilon_{1x}^* - \epsilon_m^*)A_{0x} + \epsilon_m^*}$$

Same procedure for the calculation of  $CM_y(f)$  and  $CM_z(f)$ .

If the particle is randomly oriented:

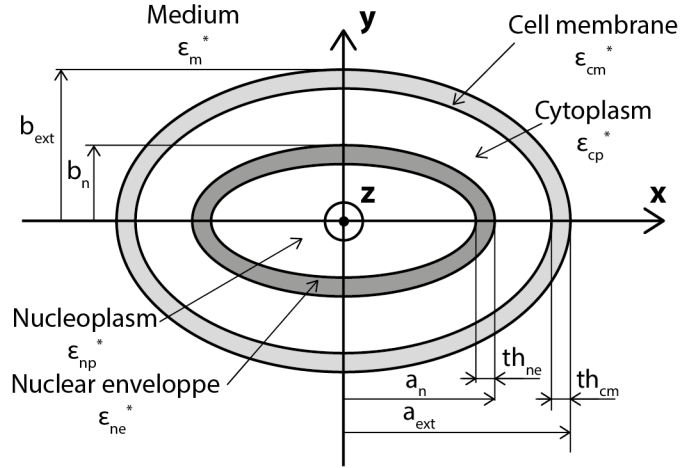
$$CM(f) = \frac{CM_x(f) + CM_y(f) + CM_z(f)}{3}$$

Then  $Re(CM(f))$  and  $Im(CM(f))$  can be used for the calculation for the calculation of respectively the DEP force and the torque.

If the particle is oriented in the x axis,  $\epsilon_{1x}^*$  is the permittivity of the particle.

If the particle is randomly oriented,  $\epsilon_{1_{eq}}^* = \frac{\epsilon_{1x}^* + \epsilon_{1y}^* + \epsilon_{1z}^*}{3}$  should be used.

### A.2.4 Three-shell



The dimensions involved in the calculation are

$$a_0 = a_{ext}$$

$$a_1 = a_{ext} - th_{cm}$$

$$a_2 = a_n$$

$$a_3 = a_n - th_{ne}$$

$b_i$  and  $c_i$  are defined in the same way.

The depolarizations factors are:

$$A_{3x} = \frac{a_3 b_3 c_3}{2} \int_0^{\infty} \frac{ds}{(s + a_3^2) \sqrt{(s + a_3^2) * (s + b_3^2) * (s + c_3^2)}}$$

$$A_{3y} = \frac{a_3 b_3 c_3}{2} \int_0^{\infty} \frac{ds}{(s + b_3^2) \sqrt{(s + a_3^2) * (s + b_3^2) * (s + c_3^2)}}$$

$$A_{3z} = \frac{a_3 b_3 c_3}{2} \int_0^{\infty} \frac{ds}{(s + c_3^2) \sqrt{(s + a_3^2) * (s + b_3^2) * (s + c_3^2)}}$$

Same procedure for  $A_{ix}$ ,  $A_{iy}$  and  $A_{iz}$  used with  $a_i$ ,  $b_i$  and  $c_i$

$$l_1 = \frac{a_1 b_1 c_1}{a_0 b_0 c_0}$$

$$l_2 = \frac{a_2 b_2 c_2}{a_1 b_1 c_1}$$

$$l_3 = \frac{a_3 b_3 c_3}{a_2 b_2 c_2}$$

$$\text{Medium: } \epsilon_m^* = \epsilon_m \epsilon_0 - \frac{j\sigma_m}{\omega}$$

$$\text{Cell membrane: } \epsilon_{cm}^* = \epsilon_{cm} \epsilon_0 - \frac{j\sigma_{cm}}{\omega}$$

$$\text{Cytoplasm: } \epsilon_{cp}^* = \epsilon_{cp} \epsilon_0 - \frac{j\sigma_{cp}}{\omega}$$

$$\text{Nuclear envelope: } \epsilon_{ne}^* = \epsilon_{ne} \epsilon_0 - \frac{j\sigma_{ne}}{\omega}$$

$$\text{Nucleoplasm: } \epsilon_{np}^* = \epsilon_{np} \epsilon_0 - \frac{j\sigma_{np}}{\omega}$$

$$\epsilon_{3x}^* = \epsilon_{ne}^* * \frac{\epsilon_{ne}^* + (\epsilon_{np}^* - \epsilon_{ne}^*)(A_{3x} + l_3(1 - A_{2x}))}{\epsilon_{ne}^* + (\epsilon_{np}^* - \epsilon_{ne}^*)(A_{3x} - l_3 A_{2x})}$$

$$\epsilon_{2x}^* = \epsilon_{cp}^* * \frac{\epsilon_{cp}^* + (\epsilon_{3x}^* - \epsilon_{cp}^*)(A_{2x} + l_2(1 - A_{1x}))}{\epsilon_{cp}^* + (\epsilon_{3x}^* - \epsilon_{cp}^*)(A_{2x} - l_2 A_{1x})}$$

$$\epsilon_{1x}^* = \epsilon_{cm}^* * \frac{\epsilon_{cm}^* + (\epsilon_{2x}^* - \epsilon_{cm}^*)(A_{1x} + l_1(1 - A_{0x}))}{\epsilon_{cm}^* + (\epsilon_{2x}^* - \epsilon_{cm}^*)(A_{1x} - l_1 A_{0x})}$$

$$CM_x(f) = \frac{1}{3} \frac{\epsilon_{1x}^* - \epsilon_m^*}{(\epsilon_{1x}^* - \epsilon_m^*)A_{0x} + \epsilon_m^*}$$

Same procedure for the calculation of  $CM_y(f)$  and  $CM_z(f)$ .

If the particle is randomly oriented:

$$CM(f) = \frac{CM_x(f) + CM_y(f) + CM_z(f)}{3}$$

Then  $Re(CM(f))$  and  $Im(CM(f))$  can be used for the calculation of the DEP force and the torque, respectively.

If the particle is oriented in the x axis,  $\epsilon_{1x}^*$  is the permittivity of the particle.

If the particle is randomly oriented,  $\epsilon_{1_{eq}}^* = \frac{\epsilon_{1x}^* + \epsilon_{1y}^* + \epsilon_{1z}^*}{3}$  should be used.

**A.2.5 Four-shell**

A similar procedure can be used for a Four-shell sphere.

$$\text{Medium: } \varepsilon_m^* = \varepsilon_m \varepsilon_0 - \frac{j\sigma_m}{\omega}$$

$$\text{Cell wall: } \varepsilon_{cw}^* = \varepsilon_{cw} \varepsilon_0 - \frac{j\sigma_{cw}}{\omega}$$

$$\text{Cell membrane: } \varepsilon_{cm}^* = \varepsilon_{cm} \varepsilon_0 - \frac{j\sigma_{cm}}{\omega}$$

$$\text{Cytoplasm: } \varepsilon_{cp}^* = \varepsilon_{cp} \varepsilon_0 - \frac{j\sigma_{cp}}{\omega}$$

$$\text{Nuclear envelope: } \varepsilon_{ne}^* = \varepsilon_{ne} \varepsilon_0 - \frac{j\sigma_{ne}}{\omega}$$

$$\text{Nucleoplasm: } \varepsilon_{np}^* = \varepsilon_{np} \varepsilon_0 - \frac{j\sigma_{np}}{\omega}$$

### A.3 Development of the equation of a single shell model using $C_{cm}$ and $G_{cm}$

For a cell modeled with the “single-shell” structure, which consists of a cytoplasm surrounded by a thin membrane, the equivalent complex permittivity is (Irimajiri, et al. 1979):

$$\epsilon_{eq}^* = \epsilon_{cm}^* \frac{\left(\frac{r_{ext}}{r_{ext} - th_{cm}}\right)^3 + 2\left(\frac{\epsilon_{cp}^* - \epsilon_{cm}^*}{\epsilon_{cp}^* + 2\epsilon_{cm}^*}\right)}{\left(\frac{r_{ext}}{r_{ext} - th_{cm}}\right)^3 - \left(\frac{\epsilon_{cp}^* - \epsilon_{cm}^*}{\epsilon_{cp}^* + 2\epsilon_{cm}^*}\right)}$$

where  $th_{cm}$  is the thickness of the cell membrane,  $\epsilon_{cm}^*$  and  $\epsilon_{cp}^*$  are respectively the complex permittivities of the cell membrane and of the cytoplasm. As for a cell  $th_{cm} \ll r_{ext}$ , we can rewrite this equation with:

$$\left(\frac{r_{ext}}{r_{ext} - th_{cm}}\right)^3 = (1 + x)^3$$

and

$$x = \frac{th_{cm}}{r_{ext} - th_{cm}}$$

$\epsilon_{eq}^*$  becomes:

$$\epsilon_{eq}^* = \epsilon_{cm}^* \frac{(1 + x)^3(\epsilon_{cp}^* + 2\epsilon_{cm}^*) + 2(\epsilon_{cp}^* - \epsilon_{cm}^*)}{(1 + x)^3(\epsilon_{cp}^* + 2\epsilon_{cm}^*) - (\epsilon_{cp}^* - \epsilon_{cm}^*)}$$

Using a limited development for  $x \ll 1$  to the first order:

$$(1 + x)^3 \simeq 1 + 3x$$

So

$$\epsilon_{eq}^* = \epsilon_{cm}^* \frac{(1 + 3x)(\epsilon_{cp}^* + 2\epsilon_{cm}^*) + 2(\epsilon_{cp}^* - \epsilon_{cm}^*)}{(1 + 3x)(\epsilon_{cp}^* + 2\epsilon_{cm}^*) - (\epsilon_{cp}^* - \epsilon_{cm}^*)}$$

Reordering the terms, we obtain



$$\epsilon_{eq}^* = \epsilon_{cm}^* \frac{\epsilon_{cp}^* ((1 + 3x) + 2) + \epsilon_{cm}^* (2(1 + 3x) - 2)}{\epsilon_{cp}^* ((1 + 3x) - 1) + \epsilon_{cm}^* (2(1 + 3x) + 1)}$$

So

$$\epsilon_{eq}^* = \epsilon_{cm}^* \frac{\epsilon_{cp}^* (3 + 3x) + \epsilon_{cm}^* (6x)}{\epsilon_{cp}^* (3x) + \epsilon_{cm}^* (3 + 6x)}$$

$$\epsilon_{eq}^* = \epsilon_{cm}^* \frac{3(1 + x)\epsilon_{cp}^* + 6x\epsilon_{cm}^*}{3x\epsilon_{cp}^* + 3(1 + 2x)\epsilon_{cm}^*}$$

As  $x \ll 1$ , equation  $\epsilon_{eq}^*$  simplifies as:

$$\epsilon_{eq}^* = \epsilon_{cm}^* \frac{3\epsilon_{cp}^* + 6x\epsilon_{cm}^*}{3x\epsilon_{cp}^* + 3\epsilon_{cm}^*} = \epsilon_{cm}^* \frac{\epsilon_{cp}^* + 2x\epsilon_{cm}^*}{x\epsilon_{cp}^* + \epsilon_{cm}^*}$$

With the hypothesis that  $2x\epsilon_{cm}^* \ll \epsilon_{cp}^*$ ,  $\epsilon_{eq}^*$  becomes:

$$\epsilon_{eq}^* = \epsilon_{cm}^* \frac{\epsilon_{cp}^*}{x\epsilon_{cp}^* + \epsilon_{cm}^*}$$

If we pose  $C_{cm}^*$  the complex capacitance:

$$C_{cm}^* = C_{cm} - j \frac{G_{cm}}{\omega}$$

where  $C_{cm} = \frac{\epsilon_{cm}\epsilon_0}{th_{cm}}$  and  $G_{cm} = \frac{\sigma_{cm}}{th_{cm}}$  are the membrane specific capacitance and conductance respectively. Then:

$$\epsilon_{cm}^* = th_{cm} C_{cm}^*$$

and, since  $x = \frac{th_{cm}}{r_{ext} - th_{cm}} \simeq \frac{th_{cm}}{r_{ext}}$ :

$$\epsilon_{eq}^* = th_{cm} C_{cm}^* \frac{\epsilon_{cp}^*}{\frac{th_{cm}}{r_{ext}} \epsilon_{cp}^* + th_{cm} C_{cm}^*} = C_{cm}^* \frac{r_{ext} \epsilon_{cp}^*}{\epsilon_{cp}^* + r_{ext} C_{cm}^*}$$

The final formula for  $\epsilon_{eq}^*$  can also be found in (Gascoyne, et al. 1995).

## A.4 Cell suspension

### A.4.1 For low volume fraction $\phi < 0.1$

Maxwell Garnett formula can be applied

From (Sihvola and Kong 1988), the two following equations are equivalent:

$$\frac{\epsilon_{mix}^* - \epsilon_m^*}{\epsilon_{mix}^* + 2\epsilon_m^*} = \phi \frac{\epsilon_p^* - \epsilon_m^*}{\epsilon_p^* + 2\epsilon_m^*}$$

$$\epsilon_{mix}^* = \epsilon_m^* \left( 1 + \frac{3\phi \frac{\epsilon_p^* - \epsilon_m^*}{\epsilon_p^* + 2\epsilon_m^*}}{1 - \phi \frac{\epsilon_p^* - \epsilon_m^*}{\epsilon_p^* + 2\epsilon_m^*}} \right)$$

Demonstration

$$\frac{\epsilon_{mix}^* - \epsilon_m^*}{\epsilon_{mix}^* + 2\epsilon_m^*} = \phi \frac{\epsilon_p^* - \epsilon_m^*}{\epsilon_p^* + 2\epsilon_m^*}$$

can be rewritten

$$(\epsilon_{mix}^* - \epsilon_m^*)(\epsilon_p^* + 2\epsilon_m^*) = \phi(\epsilon_p^* - \epsilon_m^*)(\epsilon_{mix}^* + 2\epsilon_m^*)$$

$$\epsilon_{mix}^* (\epsilon_p^* + 2\epsilon_m^* - \phi(\epsilon_p^* - \epsilon_m^*)) = \epsilon_m^* (\epsilon_p^* + 2\epsilon_m^*) + 2\epsilon_m^* \phi(\epsilon_p^* - \epsilon_m^*)$$

$$\epsilon_{mix}^* = \epsilon_m^* \frac{(\epsilon_p^* + 2\epsilon_m^*) + 2\phi(\epsilon_p^* - \epsilon_m^*)}{(\epsilon_p^* + 2\epsilon_m^* - \phi(\epsilon_p^* - \epsilon_m^*))}$$

$$\epsilon_{mix}^* = \epsilon_m^* \left( 1 + \frac{3\phi(\epsilon_p^* - \epsilon_m^*)}{(\epsilon_p^* + 2\epsilon_m^* - \phi(\epsilon_p^* - \epsilon_m^*))} \right)$$

$$\epsilon_{mix}^* = \epsilon_m^* \left( 1 + \frac{3\phi CM(f)}{1 - \phi CM(f)} \right)$$

with

$$CM(f) = \frac{\epsilon_p^* - \epsilon_m^*}{\epsilon_p^* + 2\epsilon_m^*}$$

#### A.4.2 For volume fraction $\phi < 0.8$

The Hanai equation (Hanai 1960) should be used:

$$\frac{\epsilon_{mix}^* - \epsilon_p^*}{\epsilon_m^* - \epsilon_p^*} * \left( \frac{\epsilon_m^*}{\epsilon_{mix}^*} \right)^{\frac{1}{3}} = 1 - \phi$$

Theoretically the equation should be used up to  $\phi = 0.74$ . However, it was experimentally confirmed that the dielectric behavior of some emulsions at volume fractions up to 0.8 was explained by the Hanai equation (Hanai 1968, Hanai, et al. 1982).

Unfortunately, there is no direct expression for the calculation of  $\epsilon_{mix}^*$ .

For calculation of  $\epsilon_{mix}^*$  with Hanai's equation we can use two methods:

- Method 1 is to solve the cubic equation derived from Hanai's equation
- Method 2 is to use numerical integration with the difference equation of Hanai's equation.

##### A.4.2.1 *Method 1: Analytical*

From (Asami 2002), (Hanai, et al. 1979) and (Irimajiri, et al. 1991): high volume fraction.

Both sides of Hanai's equation are cubed as:

$$\begin{aligned} (\epsilon_{mix}^* - \epsilon_p^*)^3 \epsilon_m^* &= (1 - \phi)^3 (\epsilon_m^* - \epsilon_p^*)^3 \epsilon_{mix}^* \\ (\epsilon_{mix}^*)^3 - 3(\epsilon_{mix}^*)^2 \epsilon_p^* + 3\epsilon_{mix}^* (\epsilon_p^*)^2 - (\epsilon_p^*)^3 &= \frac{(1 - \phi)^3 (\epsilon_m^* - \epsilon_p^*)^3 \epsilon_{mix}^*}{\epsilon_m^*} \\ (\epsilon_{mix}^*)^3 - 3(\epsilon_{mix}^*)^2 \epsilon_p^* + 3 \left[ (\epsilon_p^*)^2 + \frac{(\phi - 1)^3 (\epsilon_m^* - \epsilon_p^*)^3}{\epsilon_m^*} \right] \epsilon_{mix}^* - (\epsilon_p^*)^3 &= 0 \\ (\epsilon_{mix}^*)^3 - 3(\epsilon_{mix}^*)^2 \epsilon_p^* + 3[(\epsilon_p^*)^2 + B] \epsilon_{mix}^* - (\epsilon_p^*)^3 &= 0 \end{aligned}$$

with

$$B = \frac{(\phi - 1)^3 (\epsilon_m^* - \epsilon_p^*)^3}{\epsilon_m^*}$$

The cubic equation can be solved by Cardano's method as follows.

Substituting:

$$\epsilon_{mix}^* = X + \epsilon_p^*$$

$$(\epsilon_{mix}^*)^3 - 3(\epsilon_{mix}^*)^2\epsilon_p^* + 3[(\epsilon_p^*)^2 + B]\epsilon_{mix}^* - (\epsilon_p^*)^3 = 0$$

becomes

$$(X + \epsilon_p^*)^3 - 3(X + \epsilon_p^*)^2\epsilon_p^* + 3[(\epsilon_p^*)^2 + B](X + \epsilon_p^*) - (\epsilon_p^*)^3 = 0$$

$$[X^3 + 3X^2\epsilon_p^* + 3X(\epsilon_p^*)^2 + (\epsilon_p^*)^3] - 3X^2\epsilon_p^* + 6X(\epsilon_p^*)^2 + 3(\epsilon_p^*)^3 + 3[(\epsilon_p^*)^2 + B]X + 3[(\epsilon_p^*)^2 + B]\epsilon_p^* - (\epsilon_p^*)^3 = 0$$

$$X^3 + 3BX + 3B\epsilon_p^* = 0$$

Substituting

$$X = U - \frac{B}{U}$$

$$X^3 + 3BX + 3B\epsilon_p^* = 0$$

becomes

$$\left(U - \frac{B}{U}\right)^3 + 3B\left(U - \frac{B}{U}\right) + 3B\epsilon_p^* = 0$$

$$\left(U - \frac{B}{U}\right)^3 = U^3 - 3UB + \frac{3B^2}{U} - \frac{B^3}{U^3}$$

$$U^3 - 3UB + \frac{3B^2}{U} - \frac{B^3}{U^3} + 3B\left(U - \frac{B}{U}\right) + 3B\epsilon_p^* = 0$$

we multiply all the equation by  $U^3$

$$U^6 - 3U^4B + 3B^2U^2 - B^3 + 3BU^4 - 3B^2U^2 + 3BU^3\epsilon_p^* = 0$$

$$U^6 + 3BU^3\epsilon_p^* - B^3 = 0$$

which can be rewritten

$$(U^3)^2 + 3BU^3\epsilon_p^* - B^3 = 0$$

Substituting

$$Y = U^3$$

$$Y^2 + 3BY\epsilon_p^* - B^3 = 0$$

$$Y = -\frac{3B\epsilon_p^*}{2} \left[ 1 \pm \sqrt{1 + \frac{4B}{9(\epsilon_p^*)^2}} \right]$$

So

$$U^3 = -\frac{3B\epsilon_p^*}{2} \left[ 1 \pm \sqrt{1 + \frac{4B}{9(\epsilon_p^*)^2}} \right]$$

Either of the roots can be chosen because both roots provide the same result.

We then obtain 3 roots for  $U$ , if  $U_A$  is one of the roots then the other roots become

$$U_B = U_A e^{j\frac{2\pi}{3}} \text{ and } U_C = U_B e^{j\frac{2\pi}{3}}$$

Three values of  $\epsilon_{mix}^*$  are obtained from  $\epsilon_{mix}^* = X + \epsilon_p^* = U - \frac{B}{U} + \epsilon_p^*$

To select the true value of  $\epsilon_{mix}^*$ , the following function  $F$  derived from Hanai's equation is used:

$$F = (1 - \phi) \frac{\epsilon_m^* - \epsilon_p^*}{\epsilon_{mix}^* - \epsilon_p^*} \left( \frac{\epsilon_{mix}^*}{\epsilon_m^*} \right)^{\frac{1}{3}} = 1$$

Putting the value of  $\epsilon_{mix}^*$  obtained previously, the value of  $F$  becomes  $1$ ,  $-\frac{1}{2} + \frac{j\sqrt{3}}{2}$  or  $-\frac{1}{2} - \frac{j\sqrt{3}}{2}$ . The true value of  $\epsilon_{mix}^*$  is obtained when the conditions that  $F = 1$ ,  $Re(\epsilon_{mix}^*) > 0$  and  $Im(\epsilon_{mix}^*) > 0$  are satisfied.

#### **A.4.2.2 Method 2: Numerical**

Numerical implementation of Hanai's equation

$$\frac{\epsilon_{mix}^* - \epsilon_p^*}{\epsilon_m^* - \epsilon_p^*} * \left( \frac{\epsilon_m^*}{\epsilon_{mix}^*} \right)^{\frac{1}{3}} = 1 - \phi$$

logarithmic differential form obtained by applying ln

$$\ln \left( \frac{\epsilon_{mix}^* - \epsilon_p^*}{\epsilon_m^* - \epsilon_p^*} * \left( \frac{\epsilon_m^*}{\epsilon_{mix}^*} \right)^{\frac{1}{3}} \right) = \ln(1 - \phi)$$

so

$$\ln(\epsilon_{mix}^* - \epsilon_p^*) - \ln(\epsilon_m^* - \epsilon_p^*) + \frac{1}{3} \ln(\epsilon_m^*) - \frac{1}{3} \ln(\epsilon_{mix}^*) = \ln(1 - \phi)$$

differentiate (variable  $\epsilon_{mix}^*$  and  $\phi$ )

$$\frac{d\epsilon_{mix}^*}{\epsilon_{mix}^* - \epsilon_p^*} - \frac{d\epsilon_{mix}^*}{3\epsilon_{mix}^*} = \frac{-d\phi}{1 - \phi}$$

$$\left( \frac{2\epsilon_{mix}^* + \epsilon_p^*}{3\epsilon_{mix}^*(\epsilon_{mix}^* - \epsilon_p^*)} \right) d\epsilon_{mix}^* = \frac{-d\phi}{1 - \phi}$$

$$\left( \frac{2\epsilon_{mix}^* + \epsilon_p^*}{3\epsilon_{mix}^*(\epsilon_{mix}^* - \epsilon_p^*)} \right) d\epsilon_{mix}^* = \frac{-d\phi}{1 - \phi}$$

$$d\epsilon_{mix}^* = \frac{-d\phi}{1 - \phi} \frac{3\epsilon_{mix}^*(\epsilon_{mix}^* - \epsilon_p^*)}{2\epsilon_{mix}^* + \epsilon_p^*}$$

$$d\epsilon_{mix}^* = \frac{d\phi}{1 - \phi} \frac{3\epsilon_{mix}^*(\epsilon_p^* - \epsilon_{mix}^*)}{2\epsilon_{mix}^* + \epsilon_p^*}$$

For numerical integration with the previous equation we have:

$$d\epsilon_{mix}^* = \epsilon_{mix_{n+1}}^* - \epsilon_{mix_n}^*$$

For sake of clarity we will note  $\epsilon_{mix_{n+1}}^* = \epsilon_{n+1}^*$  and  $\epsilon_{mix_n}^* = \epsilon_n^*$

Hence, we use the following form:

$$\epsilon_{n+1}^* = \epsilon_n^* + \frac{h_\phi}{1 - \phi_n} \frac{3\epsilon_n^*(\epsilon_p^* - \epsilon_n^*)}{2\epsilon_n^* + \epsilon_p^*}$$

where subscript n refers to the n-th increment step and  $h_\phi$  is the increment of volume fraction.

The procedure is the following:

- (1) Calculate the value of  $\epsilon_p^*$  and  $\epsilon_m^*$  with  $\epsilon_m^* = \epsilon_m \epsilon_0 - \frac{j\sigma_m}{\omega}$  and  $\epsilon_p^* = \epsilon_p \epsilon_0 - \frac{j\sigma_p}{\omega}$ .
- (2) Set  $h_\phi$  as  $h_\phi = \frac{\phi}{m}$  with the final volume  $\phi$  and the number m of increments steps; Usually calculation with  $m \geq 100$  provides satisfactory results.
- (3) For  $n=0$ , the value of  $\epsilon_{n+1}^*$  is calculated with  $\phi_n = 0$  and  $\epsilon_n^* = \epsilon_m^*$ .
- (4) For  $n \geq 1$ ,  $\epsilon_{n+1}^*$  is calculated with  $\phi_n = nh_\phi$  and  $\epsilon_n^*$ .
- (5) After repeating Step (4) until  $n=m$ , the final value of  $\epsilon_{mix}^*$  at  $\phi$  is obtained.

# Appendix B Trapping design and simulations



## B.1 COMSOL Multiphysics model for a single shell using $C_{cm}$ and $G_{cm}$

To be able to use the single-shell model with  $C_{cm}$  and  $G_{cm}$  in COMSOL Multiphysics, the internal equation of the dielectrophoresis force was modified. More precisely, the equivalent complex relative permittivity of the particle was modified.

After enabling the *Equation View* in the *Model Builder*, the equations used to model dielectrophoresis can be modified in *Component* -> *Particle Tracing for Fluid Flow* -> *Dielectrophoresis Force 1* -> *Equation View* as illustrated in Figure S B:1.

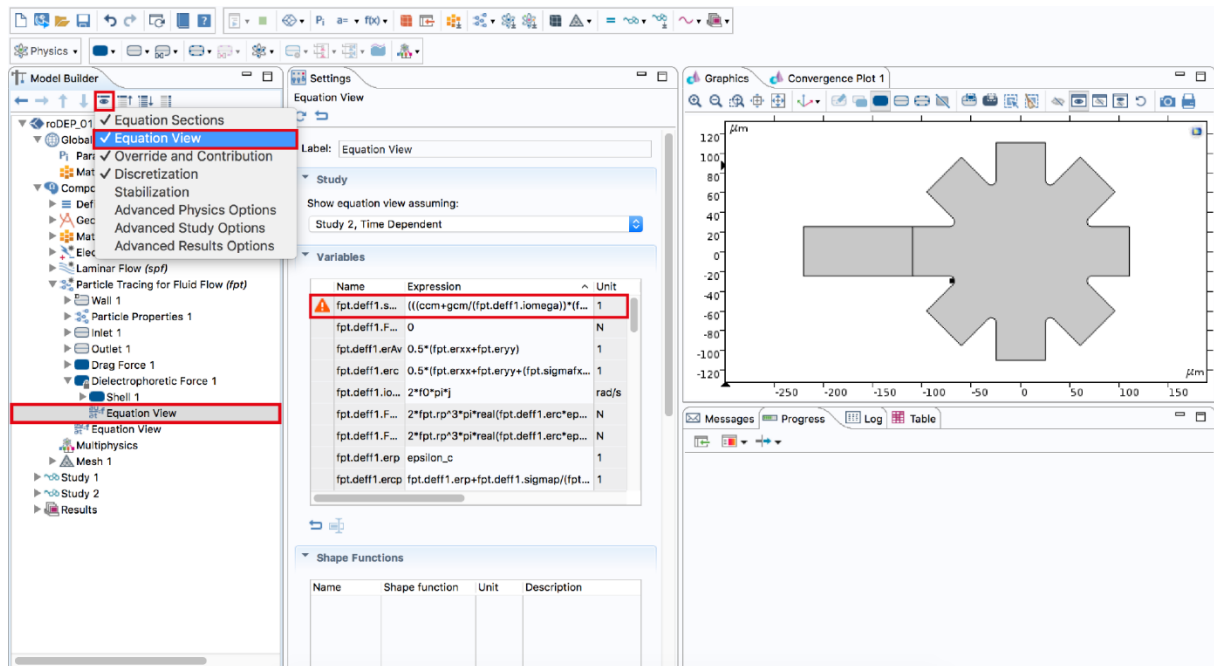


Figure S B:1 COMSOL Multiphysics location to change the equation used for dielectrophoresis to implement the single-shell model with  $C_{cm}$  and  $G_{cm}$

The equation `fpt.deff1.shl1.ereq` corresponding to the equivalent complex relative permittivity of the particle can be modified.

Originally:

`fpt.deff1.shl1.ereq =`

`fpt.deff1.shl1.ercs*((fpt.deff1.shl1.ro/fpt.deff1.shl1.ri)^3`

## Trapping design and simulations

$$\frac{+2*(fpt.deff1.ercp-fpt.deff1.shl1.ercs)/(fpt.deff1.ercp+2*fpt.deff1.shl1.ercs)}{((fpt.deff1.shl1.ro/fpt.deff1.shl1.ri)^3-(fpt.deff1.ercp-fpt.deff1.shl1.ercs)/(fpt.deff1.ercp+2*fpt.deff1.shl1.ercs))}$$

After:

$$\begin{aligned} fpt.deff1.shl1.ereq = & \\ & (((ccm+gcm/(fpt.deff1.iomega)) \\ & *(fpt.deff1.shl1.ro/(epsilon0_const)))*(fpt.deff1.ercp)) \\ & /(((ccm+gcm/(fpt.deff1.iomega))*fpt.deff1.shl1.ro/(epsilon0_const))+(fpt.deff1 \\ & .ercp)) \end{aligned}$$

where ccm and gcm are the membrane specific capacitance and conductance respectively.

## B.2 Tested configurations

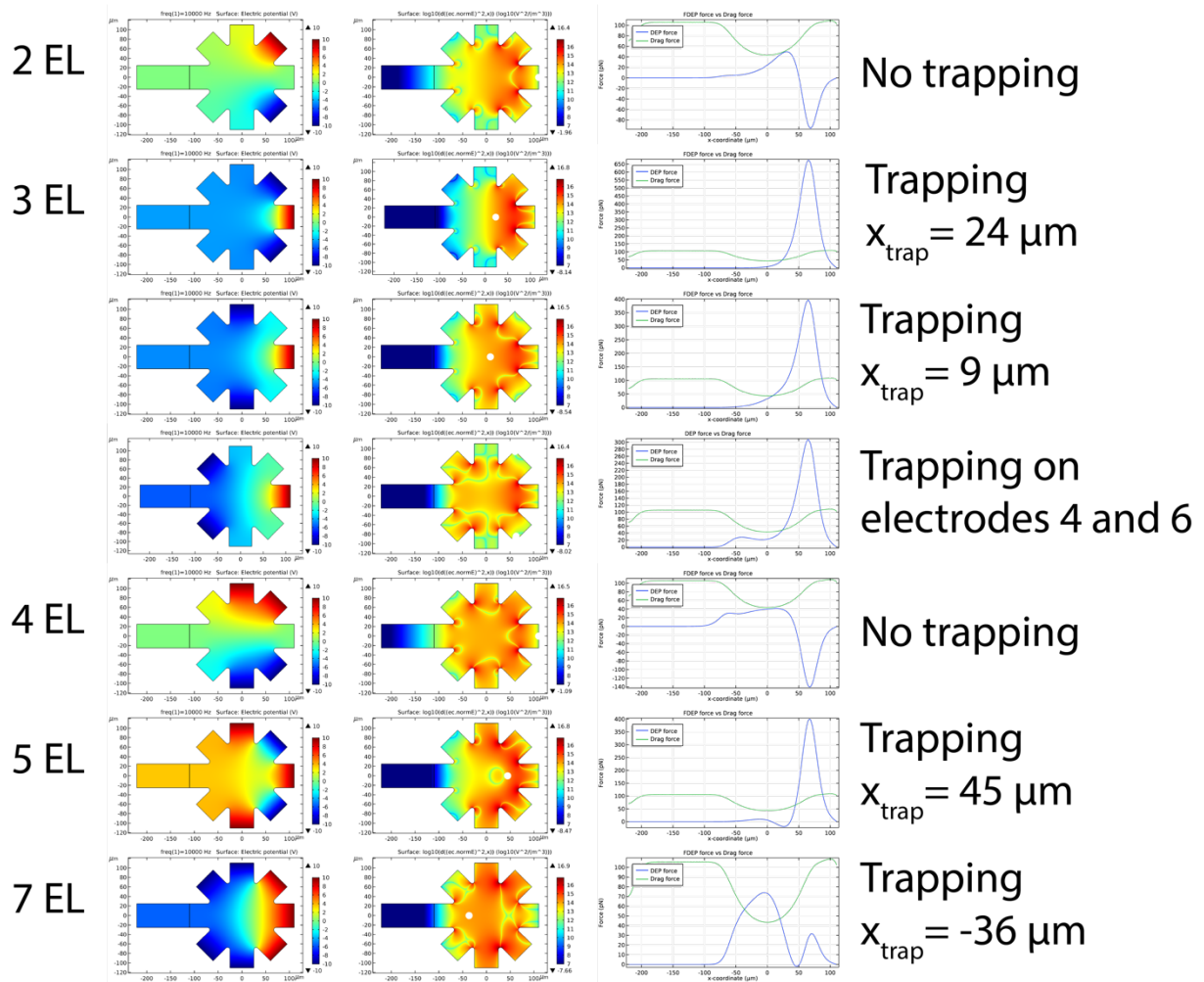


Figure S B:2 Graphs for all the tested trapping configurations

# Appendix C Chip fabrication

## C.1 Sarcophagus Molding Assembly

Equipment:

- Manual wafer mounter P-200 from Powatec (Hünenberg, Switzerland)
- Cutting mat
- UV curing machine U-200 from Powatec (Hünenberg, Switzerland)
- Thinky Mixer (optional) (from Thinky Co - Japan)

### C.1.1 Preparing the PMMA frame for wafer holding with manual wafer mounter P-200 from Powatec

- Place the PMMA frame (4) defining the height of the PDMS on the chuck of the P-200 (6 inches chuck).
- Pull the extremity of the UV tape until the full frame (4) is covered.
- Use the manual rolling pad to stick the tape (2) to the frame (4).
- Cut the tape loose from the roll (depending on the height of the frame the cutting system from the machine might be possible to use or not).
- Flip the tape+PMMA frame (2+4) on a cutting mat and cut the tape located at the outer periphery of the PMMA frame.
- Flip the tape+PMMA frame (2+4) and cut the tape located in each hole.
- ➔ At this step, the assembly PMMA frame + UV sensitive tape (4+2) is ready to hold the wafer.
- ➔ The UV sensitive (2) tape will:
  - Maintain the wafer in position while pouring the PDMS vertically.
  - Prevent PDMS from flowing under the wafer.
  - Be removed after each use -> wafer recovered after each use.
- ➔ The PMMA frame (4) will:
  - Help to control the height of the PDMS and make the PDMS height reproducible.
  - Help to hold the wafer in place (3).

### C.1.2 Positioning of the wafer

- Using tweezers, place the back-side of the wafer in contact with the sticking part of the tape at a small angle, the wafer should touch the tape only from the side.
- Release the wafer. The wafer should stick to the tape.
- Flip the ensemble (PMMA frame + UV sensitive tape + wafer) (4+2+3).
- Carefully remove the air from under the wafer by pressing with your hand from the exterior to the interior of the wafer.
- Carefully poke the air bubbles and then press the remaining tape with your hand. Repeat the procedure until all the big bubbles are gone.
- ➔ At this step, the ensemble PMMA frame + UV sensitive tape + wafer (4+2+3) is ready to be closed.

### C.1.3 Closing of the mold:

- Place the gasket (5) in the groove of the PMMA cover (6).
- Place on top of the ensemble (5+6) the flipped piece (4+2+3) and the aluminum back support (1).
- Flip the ensemble (1+2+3+4+5+6).
- Place the Inox part (7) on top of piece (6).
- Place on top of the Inox piece (7) the closing PMMA part (8).
- Place on top of the PMMA part (8) the two inox parts (9).
- Close everything with screws+washers: press enough to seal the assembly but not too much in order to avoid damaging the PMMA. The closing can be assessed by looking at the deformation of the gasket in the groove.
- ➔ At this step, the sarcophagus is complete and is ready for PDMS pouring!
- ➔ The aluminum support (1) has threaded holes (no nuts needed).
- ➔ The PMMA part (8) enables the sarcophagus to be placed vertically for PDMS pouring and desiccation.
- ➔ The ensemble (6+8) makes it possible to place the sarcophagus horizontally in the oven. for PDMS curing without modifying the height of the PDMS inside the sarcophagus.

- ➔ The inox parts (7) and (9) are here to homogenize the stress distribution in respectively the PMMA piece (6) and (9).

### C.1.4 Pouring of PDMS:

- Prepare the appropriate quantity of PDMS (10:1 ratio) (approximately 90 g -> two plastic cups of 45g if use of the Thinky Mixer) and degas it.
- Remove the bottom part of two other plastic cups, place them in the top opening of the sarcophagus: they will serve as funnels for PDMS pouring and as expansion zones for PDMS degassing.
- Stop pouring the PDMS once the PDMS reaches the middle of the slit of the PMMA part (6).
- Place the sarcophagus vertically in the desiccator for final degassing. If PDMS bubbles go too high in the funnels, vent the desiccator, explode the bubbles, and put everything under vacuum again. Repeat the procedure if necessary.
- ➔ If air bubbles are coming from the side part of the frame, it means that the sealing of the sarcophagus is insufficient and the related screws should be retightened.
- Once all the bubbles are gone, remove the plastics cups used as funnels and place the mold horizontally in the oven. To ensure that the PDMS height is kept constant it is advised to still keep a small angle of the sarcophagus with the horizontal

Place the sarcophagus in the oven at 80°C for at least two hours for PDMS curing.

### C.1.5 Unmolding of PDMS:

- Take the sarcophagus outside of the oven and wait until its temperature is back to room temperature.
- Take out the screws of the sarcophagus and remove the different parts. The PDMS should only be present within the frame (4) on top of the wafer (3) and UV sensitive tape (2)

### **C.1.6 Removal of the UV sensitive tape with the UV curing U-200 from Powatec**

- Unscrew the internal blue cover piece of the U-200 (because of the height of the frame (4 mm) and the PDMS part molded from the slit of the PMMA piece (6), the frame can not go under the internal blue cover piece).
- Place the frame such that the UV sensitive tape faces the LEDs (PDMS facing up).
- Close the lid and start the system pressing the green button.
- Wait for the frame to reach the right end part of the travel. If the tape is still sticking to the frame repeat the operation.
- Remove the UV tape from the frame and wafer
- Place the assembly PDMS+wafer on the cutting mat, wafer touching the mat (PDMS facing up)
- Peel off the PDMS from the wafer
- Separate the PDMS slabs with a razor blade and punch the necessary holes
- ➔ The size of the PDMS is important, it is recommended making marks in the wafer to help for PDMS chip dicing

## **C.2 Alignment Procedure**

The following procedure assumes the bonding of multiple chips.

Material and equipment used:

- Custom-made chuck in steel (CK45 steel covered with a 10- $\mu$ m layer of nickel deposited by chemical nickel plating to prevent rusting)
- Neodymium magnet (10 mm x 10 mm x 1 mm)
- MJB4 Mask Aligner from SUSS MicroTec (Garching, Germany)
- Transparent mask (2.3 mm thick or thinner)

### **C.2.1 Alignment of the 1<sup>st</sup> chip:**

- Pull the chuck holder
- Replace the standard chuck of the MJB4 by the custom-made chuck (Figure S C:1 A)



## Chip fabrication

- Place the glass chip patterned with electrodes in the center of the custom-made chuck (Figure S C:1 B).
- Place three magnets at the bottom left corner of the chip in order to make a L shape corner that will help to reposition the chip in the same position all the time. Add more magnets on the side of the L to improve the support as shown in (Figure S C:1 B).
- Place two magnets on the opposite corner to maintain the chip: the chip should now be completely held. (Figure S C:1 C)
- ➔ The magnets hold the chip in plane but allow the chip to be moved vertically after the bonding is performed.
- Push the chuck holder back in the machine.
- Place the PDMS slab on the transparent glass mask approximately in the center, feature side up, and mark the corners with a felt pen on the other side of the mask (Figure S C:1 D).
- ➔ In order to reduce the distance between the expected position of the PDMS slab on the mask and its actual position, the previous procedure can be done with an already bonded PDMS+electrodes chip until the previous step. In this case put the full chip (PDMS + electrodes) in contact with the mask by lifting the handle. Then mark corners with a felt pen on the other side of the mask and remove the full chip. Place the glass chip patterned with electrodes on the chuck (Figure S C:1 A, B and C) and the PDMS slab on the mask and repeat the procedure.
- Put the machine in contact position by lifting the handle on the MJB4 and adjusting the WEC so that glass chip and PDMS slab are about 1 mm apart
- ➔ Everything is ready for pre-alignment.
- ➔ This previous procedure will be performed only for the first chip

### C.2.2 Prealignment:

- Adjust the distance between the camera to fit the distance between the markers.
- Focus on the PDMS slab and find the top markers by moving the mask in X and Y direction, then adjust the rotation angle of cameras on microscope.

## Chip fabrication

The split field can be used to visualize both left and right markers at the same time.

- Correct the angle of the mask.
  - Move down the microscope as a whole and focus on glass chip.
  - Correct the angle of the chip and then align the X and Y position of the chip by finding both cross markers that are on the top right and left corners of the chip with the corresponding one of the PDMS slab.
- ➔ The machine is now ready for the final alignment.

### C.2.3 Plasma:

- Take the glass chip out of the chuck and the full mask with the PDMS slab.
  - Put everything in the plasma chamber at 29 W for 45 s at 530 mTor of O<sub>2</sub>
- ➔ Go quickly to the alignment after plasma treatment

### C.2.4 Alignment and Full contact:

- Replace the mask with the PDMS slab in the MJB4 and the glass chip in the custom-made chuck
  - Align the PDMS slab and glass chip again on MJB4, first on cross markers and then directly on the electrode patterns or zone of interest.
  - Move up the chuck until the glass chip is in contact with the PDMS.
- ➔ A front line will appear when the contact between the PDMS slab and the glass chip is occurring. Do not move neither the mask nor the chuck in X and Y after.
- Lower down the chuck by lifting down the handle of the MJB4. The glass chip should now be bonded to the PDMS and therefore should still be in contact with the PDMS.
  - Flip the mask holder and carefully remove the full chip by gently detaching the PDMS slab from the mask from the side with tweezers. (Figure S C:1 E). The operation is even more straightforward as the PDMS slab is thick, 4 mm in our case.
  - Put a 40-g weight on the chip and put it in the oven at 80°C for 10 min to enhance the bonding.
- ➔ Once all those steps are done a second chip can be bonded much faster.

## Chip fabrication

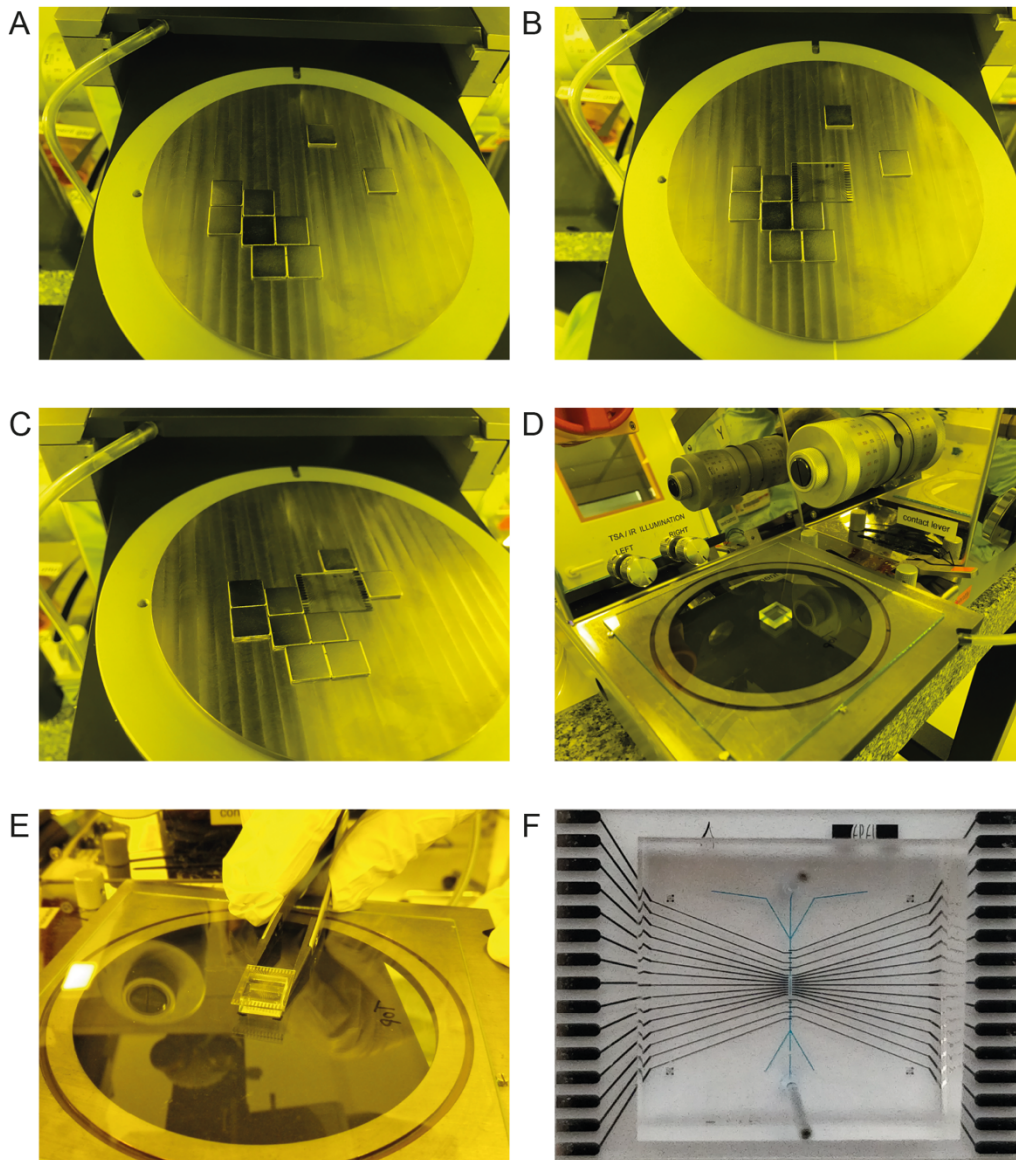


Figure S C:1 A) Custom-made steel chuck with magnets for positioning. B) Positioning of the glass chip at the center of the custom-made chuck. C) Positioning on the opposite corner of the chip of the two magnets. D) Positioning of the PDMS slab on the glass mask. E) Retrieval of the bonded chip with tweezers. F) Chip filled with blue ink: no leakage is visible.

### C.3 Characterization of the misalignment

The measurement of the misalignment was performed by looking at two symmetric patterns located 2.3 mm from each other. The misalignment of the center of each pattern was quantified. The procedure was repeated for 4 chips, leading to 8 measurement points. The medium misalignment was found to be 0.4  $\mu\text{m}$  (standard deviation 0.2  $\mu\text{m}$ ) with a maximum misalignment of 0.6  $\mu\text{m}$ . The error of estimation of the misalignment was in the order of 0.3  $\mu\text{m}$ . The measurements are presented in Table S C:1.

Chip	Point	Misalignment (Absolute)
		$\mu\text{m}$
1	A	0.575
	B	0.539
2	A	0.574
	B	0.190
3	A	0.573
	B	0.424
4	A	0.507
	B	0.079
	Mean	0.43
	Std	0.19

Table S C:1 Quantification of the misalignment



# Appendix D Design proposition for impedance sensing of single cells and cell aggregates

This appendix contains all the supplementary material for Chapter 6 about design proposition for impedance sensing of single cells and cell aggregates.

## D.1 Material definition

A spherical particle was defined as a change in material properties instead of a geometrical entity. The particle was moved along the channel by displacing its center (coordinate  $x_0$ ,  $y_0$  and  $z_0$ ) using a parametric sweep.

To do so a variable,  $rsq$ , is used to compute the distance from the center of a cavity and the points:

$$rsq = ((x-x_0)^2 + (y-y_0)^2 + (z-z_0)^2)$$

and the electrical properties of the material in the channel are defined as follow:

$$\sigma = \sigma_{par} + (\sigma_{sol} - \sigma_{par}) * (rsq > r_0^2)$$

$$\epsilon_r = \epsilon_{r,par} + (\epsilon_{r,sol} - \epsilon_{r,par}) * (rsq > r_0^2)$$

where  $\sigma_{par}$ ,  $\sigma_{sol}$ ,  $\epsilon_{r,par}$  and  $\epsilon_{r,sol}$  are respectively the electrical conductivity and the relative permittivity of the particle and the solution and  $r_0$  is the radius of the particle.

The expression  $(rsq > r_0^2)$  is a comparison, evaluating to 1 (for TRUE) outside the cavity and 0 (for FALSE) inside the cavity. The following settings give the particle properties inside the cavity (centered in  $(x_0, y_0, z_0)$  and with a radius of  $r_0$ ), and the properties of the solution outside of it.

The method was inspired by the tutorial “Electric Impedance Sensor” available on COMSOL Multiphysics website: <https://www.comsol.com/model/electric-impedance-sensor-7704>

## D.2 Meshing and Mesh convergence study

The domain was divided in the following way: a  $12\ \mu\text{m}$  wide slide (centered around the axis  $y = 0$ ) was discretized with a swept mesh of maximum element size  $2\ \mu\text{m}$  and the remaining region was meshed using free tetrahedral with a maximum element size of  $37.4\ \mu\text{m}$  as presented. For the optimization simulations (with a particle at a constant height  $z = 25\ \mu\text{m}$ ), the principle of the meshing was similar, with this time a swept mesh tube (maximum element size of  $2\ \mu\text{m}$ ) with a square cross section of  $12\ \mu\text{m} \times 12\ \mu\text{m}$  around the particle, and the rest of the geometry meshed with free tetrahedral as presented in Figure S D:1. The reason for this separation in two distinct meshing regions is that the region where the particle evolves must be finely meshed. Conversely, regions that do not contain the particle can afford a coarser meshing without impacting the result in a significant manner.

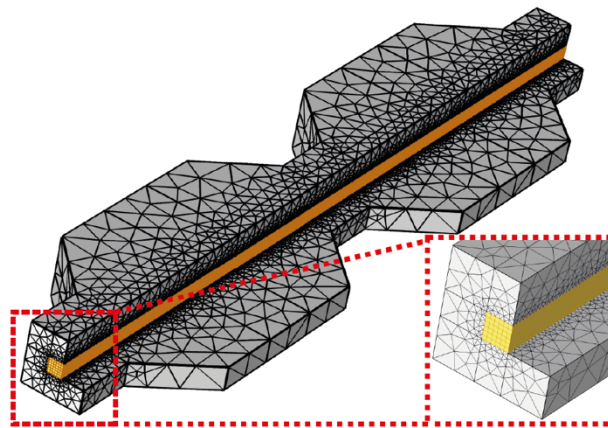


Figure S D:1 Mesh used for the optimization simulations in this study, presented on the conceptual design.

To determine the maximum Element Size to use in the Swept Mesh area, a mesh convergence study was performed using a Long Conventional (LC) design with an  $8\ \mu\text{m}$  diameter polystyrene bead located at  $x = 0\ \mu\text{m}$ ,  $y = 0\ \mu\text{m}$ , and  $z = h/2 = 25\ \mu\text{m}$ . The results of this study are presented in Figure S D:2 and show convergence of current value for mesh element size below  $3\ \mu\text{m}$ . Therefore, we selected a maximum element size for the central (fine) region of  $2\ \mu\text{m}$ .



## Design proposition for impedance sensing of single cells and cell aggregates

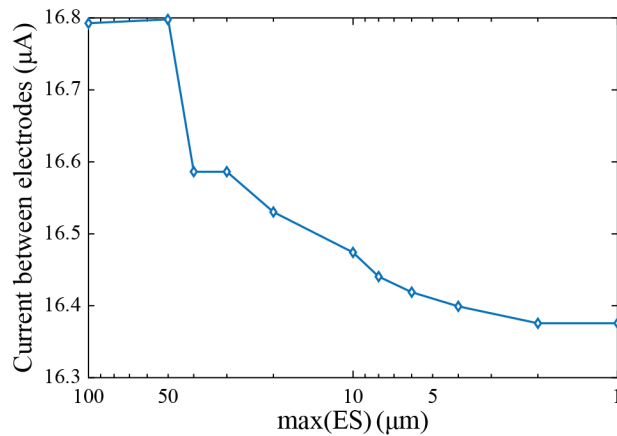


Figure S D:2 Mesh convergence study for a Long Conventional (LC) design with an 8  $\mu\text{m}$  diameter polystyrene bead located at  $x = 0 \mu\text{m}$ ,  $y = 0 \mu\text{m}$ , and  $z = h/2 = 25 \mu\text{m}$ . Evolution of the current between the two electrodes with the maximum size of the elements (ES) using a Swept Mesh on all the design.

The rest of the design was meshed with free tetrahedral elements, whose dimensions were also optimized by a convergence study. Figure S D:3 shows a strong stability of results across mesh subdivisions. We settled for of a maximum size of 37.4  $\mu\text{m}$  which provided similar results to what could have been obtained with finer values ( $<0.1\%$  error) and showed greater efficiency in terms of computation time.

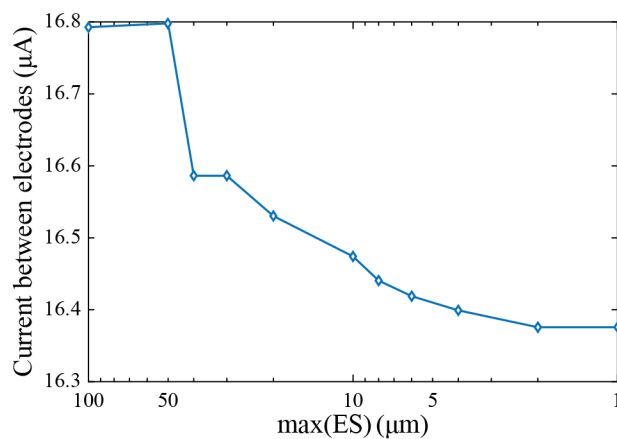


Figure S D:3 Mesh convergence study for a Long Conventional (LC) design with an 8  $\mu\text{m}$  diameter polystyrene bead located at  $x = 0 \mu\text{m}$ ,  $y = 0 \mu\text{m}$ , and  $z = h/2 = 25 \mu\text{m}$ . Evolution of the current between the two electrodes with the maximum size of the free tetrahedral elements (ES) (the central part of the design is meshed with the swept mesh with 2  $\mu\text{m}$  as the Maximum Element Size).

### D.3 Data processing

Experimental data were acquired at a sampling frequency of 1800 Hz. Baseline variations were removed using a moving-average filter with a sampling window of 5000 points. Local noise was attenuated by the mean of a third-order Savitzky-Golay filter with a frame length of 51 points. Experimental data were normalized in relation to the baseline current value (no particle flowing in the channel). An example of data acquisition is displayed on Figure S D:4 for the Short Optimized (SO) design.

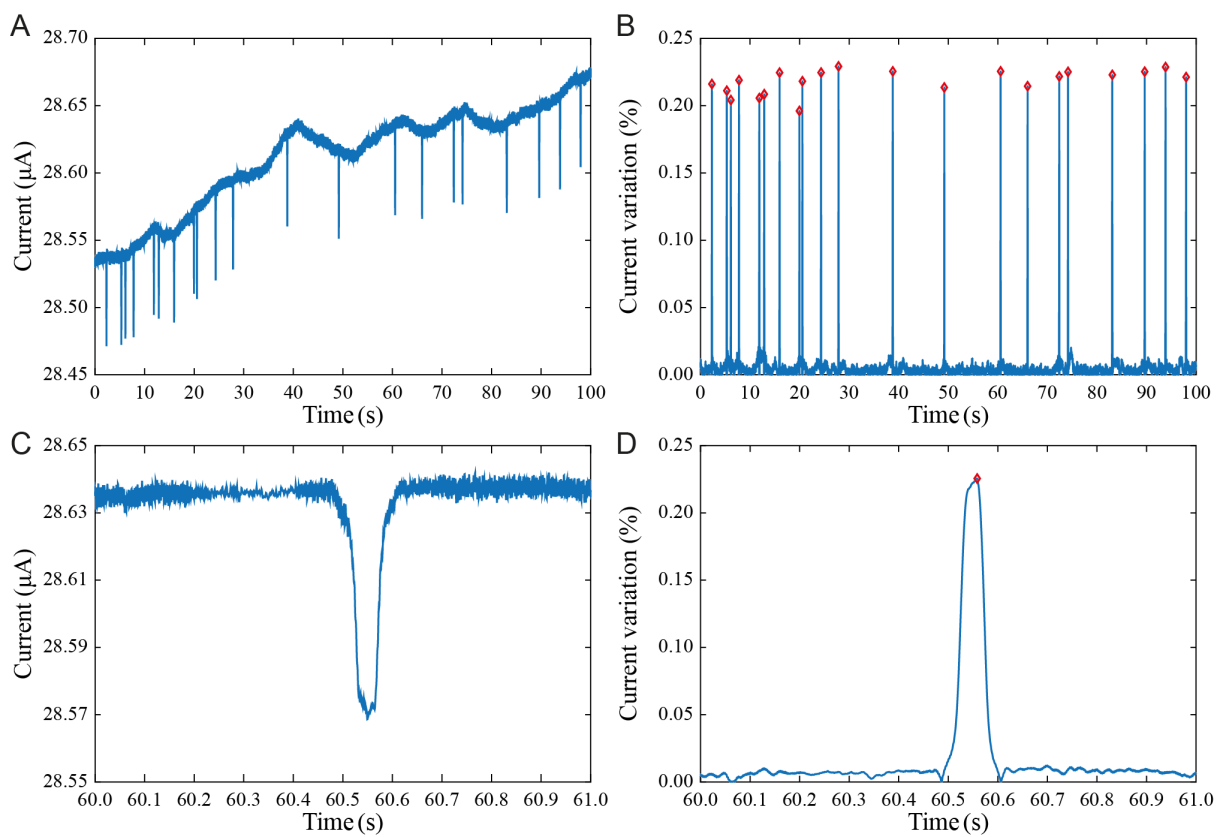


Figure S D:4 Evolution of the current with time for a SO design. (A) and (C) Raw data after acquisition (B) and (D) Processed signal after application of a moving average filter and a Savitzky-Golay filter and normalization of the value. Peaks are detected and marked with the red dots.

## D.4 Current density

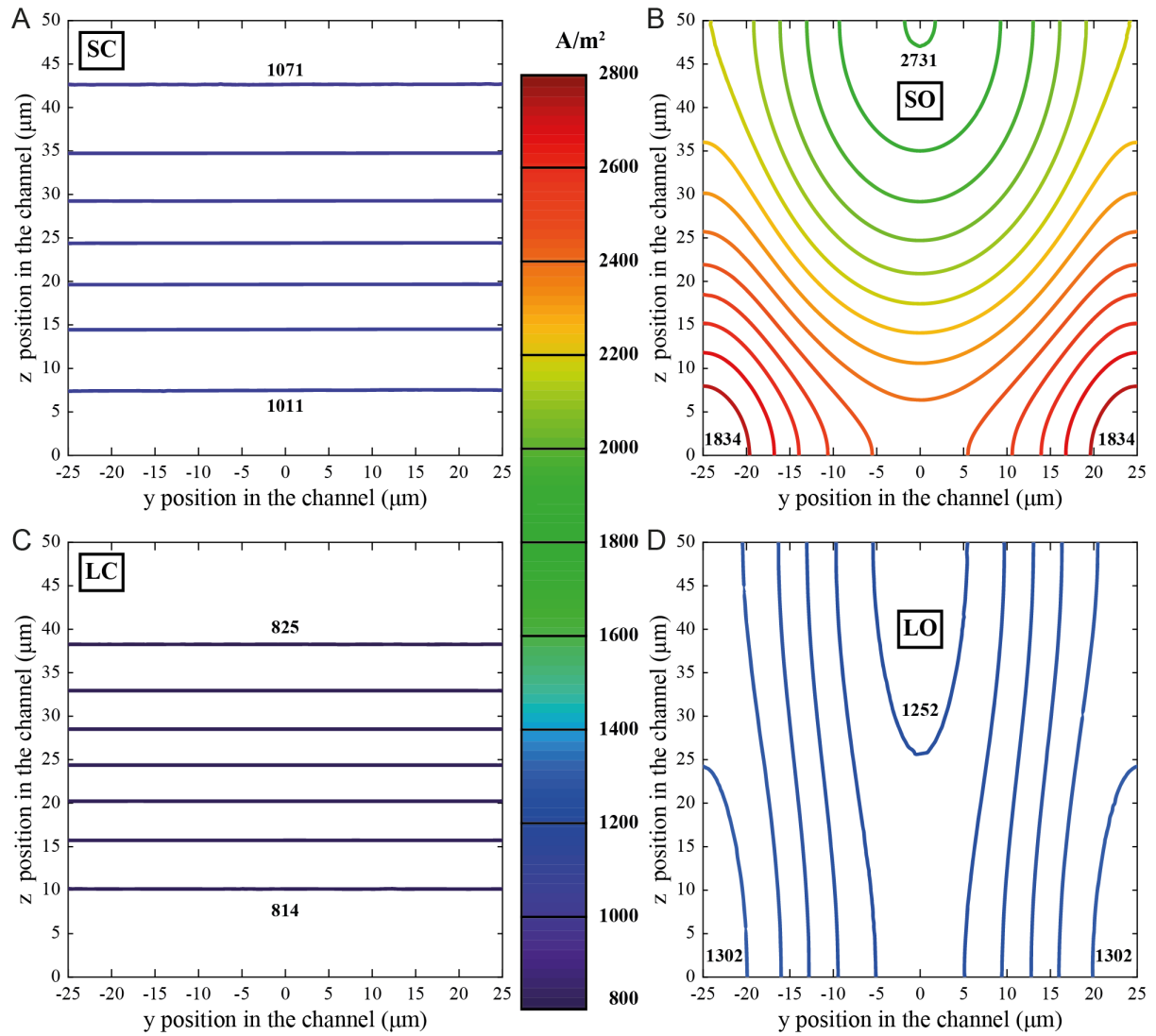


Figure S D:5 Figure S D:6 Current density line plot in the plane  $x = 0$  for the four designs (A) SC (B) SO (C) LC (D) LO

## D.5 Sensitivity to misalignment

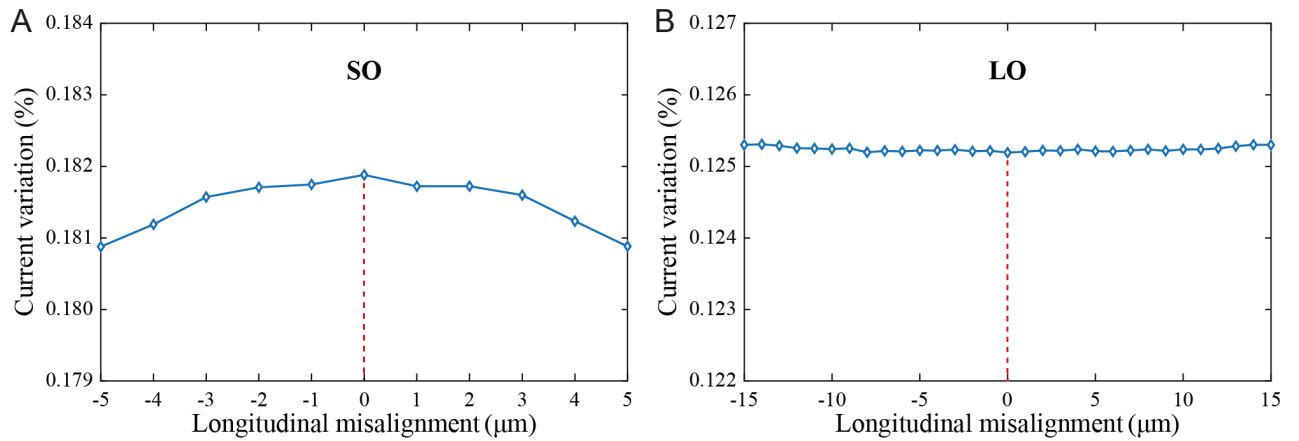


Figure S D:7 Evolution of the current variation with the longitudinal misalignment for (A) the SO and (B) LO designs.

## D.6 Fitting parameters

Parameter	Design	Fitting	Equation	R <sup>2</sup>	Coefficient		
					A	τ	
w <sub>el</sub>	Short	Exponential	A * [1-exp(τ * w <sub>el</sub> )]	0,9992	1,912 x 10 <sup>-3</sup>		
	Long				1,355 x 10 <sup>-3</sup>		
					p1	p2	p3
b	Short	Polynomial	p <sub>1</sub> * b <sup>2</sup> + p <sub>2</sub> * b + p <sub>3</sub>	0,9979	-1,285 x 10 <sup>-6</sup>	8,657 x 10 <sup>-6</sup>	1,835 x 10 <sup>-3</sup>
	Long				-1,607 x 10 <sup>-8</sup>	-9,120 x 10 <sup>-7</sup>	1,268 x 10 <sup>-3</sup>

Table S D:1 Parameters used for the fitting of the curves displayed in Figure 6:6

## D.7 Simulated current variation for a 30 $\mu\text{m}$ particle at different heights in the LO design

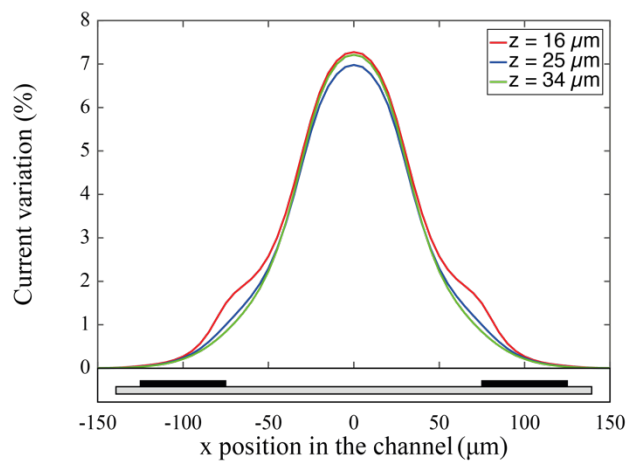


Figure S D:8 Simulation of the current variation due to a 30  $\mu\text{m}$  diameter polystyrene bead with the LO design. Evolution with the x position in the microchannel (located at  $y = 0 \mu\text{m}$ ) at 3 different heights ( $z = 16 \mu\text{m}$ ,  $z = 25 \mu\text{m}$  and  $z = 34 \mu\text{m}$ ). Electrode positions (in black) are indicated under the graph.

## Bibliography

- (Adler 2002) Adler, S. B. Reference Electrode Placement in Thin Solid Electrolytes. *Journal of the Electrochemical Society* **149**, E166-E172, doi:10.1149/1.1467368 (2002).
- (Akselrod, et al. 2006) Akselrod, G. M., Timp, W., Mirsaidov, U., Zhao, Q., Li, C., Timp, R., Timp, K., Matsudaira, P. & Timp, G. Laser-guided assembly of heterotypic three-dimensional living cell microarrays. *Biophysical Journal* **91**, 3465-3473, doi:10.1529/biophysj.106.084079 (2006).
- (Albrecht, et al. 2004) Albrecht, D. R., Sah, R. L. & Bhatia, S. N. Geometric and material determinants of patterning efficiency by dielectrophoresis. *Biophysical Journal* **87**, 2131-2147, doi:10.1529/biophysj.104.039511 (2004).
- (Albrecht, et al. 2006) Albrecht, D. R., Underhill, G. H., Wassermann, T. B., Sah, R. L. & Bhatia, S. N. Probing the role of multicellular organization in three-dimensional microenvironments. *Nature Methods* **3**, 369-375, doi:10.1038/Nmeth873 (2006).
- (Allen 1997) Allen, T. Volume 1: Powder sampling and particle size measurement. in *Particle Size Measurement* 335 (Springer Netherlands, 1997).
- (Altschuler and Wu 2010) Altschuler, S. J. & Wu, L. F. Cellular heterogeneity: do differences make a difference? *Cell* **141**, 559-563, doi:10.1016/j.cell.2010.04.033 (2010).
- (Arnold, et al. 1987) Arnold, W. M., Schwan, H. P. & Zimmermann, U. Surface Conductance and Other Properties of Latex-Particles Measured by Electrorotation. *Journal of Physical Chemistry* **91**, 5093-5098, doi:DOI 10.1021/j100303a043 (1987).
- (Arnold and Zimmermann 1988) Arnold, W. M. & Zimmermann, U. Electro-Rotation - Development of a Technique for Dielectric Measurements on Individual Cells and Particles. *Journal of Electrostatics* **21**, 151-191, doi:10.1016/0304-3886(88)90027-7 (1988).
- (Asami 2002) Asami, K. Characterization of heterogeneous systems by dielectric spectroscopy. *Progress in Polymer Science* **27**, 1617-1659, doi:10.1016/S0079-6700(02)00015-1 (2002).
- (Asami, et al. 1998) Asami, K., Gheorghiu, E. & Yonezawa, T. Dielectric behavior of budding yeast in cell separation. *Biochimica Et Biophysica Acta-General Subjects* **1381**, 234-240, doi:10.1016/S0304-4165(98)00033-6 (1998).
- (Asami, et al. 1999) Asami, K., Gheorghiu, E. & Yonezawa, T. Real-time monitoring of yeast cell division by dielectric spectroscopy. *Biophysical Journal* **76**, 3345-3348, doi:10.1016/S0006-3495(99)77487-4 (1999).
- (Asami, et al. 2000) Asami, K., Takahashi, K. & Shirahige, K. Progression of cell cycle monitored by dielectric spectroscopy and flow-cytometric analysis of DNA content. *Yeast* **16**, 1359-1363, doi:10.1002/1097-0061(200011)16:15<1359::Aid-yea631>3.0.Co;2-e (2000).

- (Ashkin, et al. 1986) Ashkin, A., Dziedzic, J. M., Bjorkholm, J. E. & Chu, S. Observation of a single-beam gradient force optical trap for dielectric particles. *Optics Letters* **11**, doi:10.1364/ol.11.000288 (1986).
- (Ashkin, et al. 1987) Ashkin, A., Dziedzic, J. M. & Yamane, T. Optical Trapping and Manipulation of Single Cells Using Infrared-Laser Beams. *Nature* **330**, 769-771, doi:10.1038/330769a0 (1987).
- (Ayliffe, et al. 1999) Ayliffe, H. E., Frazier, A. B. & Rabbitt, R. D. Electric impedance spectroscopy using microchannels with integrated metal electrodes. *Journal of Microelectromechanical Systems* **8**, 50-57, doi:10.1109/84.749402 (1999).
- (Badshah, et al. 2014) Badshah, M. A., Jang, H., Kim, Y. K., Kim, T. H. & Kim, S. M. Development of a rapid cure polydimethylsiloxane replication process with near-zero shrinkage. *Journal of Micro-Nanolithography Memes and Moems* **13**, doi:10.1117/1.Jmm.13.3.033006 (2014).
- (Benazzi, et al. 2007) Benazzi, G., Holmes, D., Sun, T., Mowlem, M. C. & Morgan, H. Discrimination and analysis of phytoplankton using a microfluidic cytometer. *Iet Nanobiotechnology* **1**, 94-101, doi:10.1049/iet-nbt:20070020 (2007).
- (Benya and Shaffer 1982) Benya, P. D. & Shaffer, J. D. Dedifferentiated Chondrocytes Reexpress the Differentiated Collagen Phenotype When Cultured in Agarose Gels. *Cell* **30**, 215-224, doi:10.1016/0092-8674(82)90027-7 (1982).
- (Berg 1993) Berg, H. C. *Random walks in biology*. Expanded ed., [1st Princeton Paperback printing] edn, (Princeton, N.J. : Princeton University Press, 1993).
- (Bhagat, et al. 2007) Bhagat, A. A. S., Jothimuthu, P. & Papautsky, I. in *TRANSDUCERS 2007 - 2007 International Solid-State Sensors, Actuators and Microsystems Conference*. 537-540 doi:10.1109/SENSOR.2007.4300186 (
- (Braschler, et al. 2008) Braschler, T., Demierre, N., Nascimento, E., Silva, T., Oliva, A. G. & Renaud, P. Continuous separation of cells by balanced dielectrophoretic forces at multiple frequencies. *Lab on a Chip* **8**, 280-286, doi:10.1039/b710303d (2008).
- (Brazey, et al. 2018) Brazey, B., Cottet, J., Bolopion, A., Van Lintel, H., Renaud, P. & Gauthier, M. Impedance-based real-time position sensor for lab-on-a-chip devices. *Lab on a Chip* **18**, 818-831, doi:10.1039/c7lc01344b (2018).
- (Breton and Mir 2012) Breton, M. & Mir, L. M. Microsecond and nanosecond electric pulses in cancer treatments. *Bioelectromagnetics* **33**, 106-123, doi:10.1002/bem.20692 (2012).
- (Brown, et al. 2018) Brown, D. W., Bahrami, A. J., Canton, D. A., Mukhopadhyay, A., Campbell, J. S., Pierce, R. H. & Connolly, R. J. Development of an adaptive electroporation system for intratumoral plasmid DNA delivery.

- Bioelectrochemistry* **122**, 191-198, doi:10.1016/j.bioelechem.2018.04.005 (2018).
- (Butler 2004) Butler, M. *Animal cell culture and technology*. (Taylor & Francis, 2004).
- (Calvet and Mir 2016) Calvet, C. Y. & Mir, L. M. The promising alliance of anti-cancer electrochemotherapy with immunotherapy. *Cancer Metastasis Rev* **35**, 165-177, doi:10.1007/s10555-016-9615-3 (2016).
- (Carlsson and Yuhás 1984) Carlsson, J. & Yuhás, J. M. Liquid-Overlay Culture of Cellular Spheroids. in *Spheroids in Cancer Research: Methods and Perspectives* (eds Helmut Acker, Jörgen Carlsson, Ralph Durand, & Robert M. Sutherland) 1-23 doi:10.1007/978-3-642-82340-4\_1 (Springer Berlin Heidelberg, 1984).
- (Caselli and Bisegna 2017) Caselli, F. & Bisegna, P. Simulation and performance analysis of a novel high-accuracy sheathless microfluidic impedance cytometer with coplanar electrode layout. *Medical Engineering & Physics* **48**, 81-89, doi:10.1016/j.medengphy.2017.04.005 (2017).
- (Castellanos 1998) Castellanos, A. *Electrohydrodynamics*. doi:10.1007/978-3-7091-2522-9 (1998).
- (Catterall 1995) Catterall, W. A. Structure and Function of Voltage-Gated Ion Channels. *Annual Review of Biochemistry* **64**, 493-531, doi:10.1146/annurev.bi.64.070195.002425 (1995).
- (Cervia and Yuan 2018) Cervia, L. D. & Yuan, F. Current Progress in Electrotransfection as a Nonviral Method for Gene Delivery. *Molecular Pharmaceutics* **15**, 3617-3624, doi:10.1021/acs.molpharmaceut.8b00207 (2018).
- (Chen and Pan 2011) Chen, A. & Pan, T. Three-dimensional fit-to-flow microfluidic assembly. *Biomicrofluidics* **5**, 46505-465059, doi:10.1063/1.3670368 (2011).
- (Chen, et al. 2015) Chen, J., Xue, C., Zhao, Y., Chen, D., Wu, M. H. & Wang, J. Microfluidic impedance flow cytometry enabling high-throughput single-cell electrical property characterization. *International Journal of Molecular Sciences* **16**, 9804-9830, doi:10.3390/ijms16059804 (2015).
- (Chen, et al. 2011) Chen, J., Zheng, Y., Tan, Q., Shojaei-Baghini, E., Zhang, Y. L., Li, J., Prasad, P., You, L., Wu, X. Y. & Sun, Y. Classification of cell types using a microfluidic device for mechanical and electrical measurement on single cells. *Lab on a Chip* **11**, 3174-3181, doi:10.1039/c1lc20473d (2011).
- (Cheung, et al. 2005) Cheung, K., Gawad, S. & Renaud, P. Impedance spectroscopy flow cytometry: on-chip label-free cell differentiation. *Cytometry Part A* **65**, 124-132, doi:10.1002/cyto.a.20141 (2005).
- (Choonee and Syms 2011) Choonee, K. & Syms, R. R. A. Hydraulically actuated micro-contact printing engines. *Journal of Micromechanics and Microengineering* **21**, doi:10.1088/0960-1317/21/8/085013 (2011).
- (Chopinnet, et al. 2012) Chopinnet, L., Wasungu, L. & Rols, M. P. First explanations for differences in electrotransfection efficiency in vitro and in vivo using



- spheroid model. *International Journal of Pharmacognosy* **423**, 7-15, doi:10.1016/j.ijpharm.2011.04.054 (2012).
- (Clausen, et al. 2014) Clausen, C., Skands, G., Bertelsen, C. & Svendsen, W. Coplanar Electrode Layout Optimized for Increased Sensitivity for Electrical Impedance Spectroscopy. *Micromachines* **6**, 110-120, doi:10.3390/mi6010110 (2014).
- (Cottet 2018a) Cottet, J. HEK cell aggregation in flow conditions using 3 electrodes in a 4 electrode configuration design. doi:10.5281/zenodo.1435006 (2018a).
- (Cottet 2018b) Cottet, J. HEK cell aggregation in flow conditions using 3 electrodes in a 8 electrode configuration design. doi:10.5281/zenodo.1434999 (2018b).
- (Cottet, et al. 2019a) Cottet, J., Fabregue, O., Berger, C., Buret, F., Renaud, P. & Frénéa-Robin, M. MyDEP: A New Computational Tool for Dielectric Modeling of Particles and Cells. *Biophysical Journal* **116**, 12-18, doi:10.1016/j.bpj.2018.11.021 (2019a).
- (Cottet, et al. 2018) Cottet, J., Fabregue, O., Berger, C., Buret, F., Renaud, P. & Frénéa-Robin, M. MyDEP: a new computational tool for dielectric modeling of particles and cells doi:10.5281/zenodo.1321928 (2018).
- (Cottet, et al. 2019b) Cottet, J., Kehren, A., Lasli, S., van Lintel, H., Buret, F., Frénéa-Robin, M. & Renaud, P. Dielectrophoresis-assisted creation of cell aggregates under flow conditions using planar electrodes. *Electrophoresis* **40**, 1498-1509, doi:10.1002/elps.201800435 (2019b).
- (Cottet, et al. 2019c) Cottet, J., Kehren, A., van Lintel, H., Buret, F., Frénéa-Robin, M. & Renaud, P. How to improve the sensitivity of coplanar electrodes and micro channel design in electrical impedance flow cytometry: a study. *Microfluidics and Nanofluidics* **23**, doi:10.1007/s10404-018-2178-6 (2019c).
- (Cottet, et al. 2017) Cottet, J., Vaillier, C., Buret, F., Frénéa-Robin, M. & Renaud, P. A reproducible method for  $\mu\text{m}$  precision alignment of PDMS microchannels with on-chip electrodes using a mask aligner. *Biomicrofluidics* **11**, 064111, doi:10.1063/1.5001145 (2017).
- (Coulter 1953) Coulter, W. H. Means for counting particles suspended in a fluid. US patent (1953).
- (Coulter and Hogg 1970) Coulter, W. H. & Hogg, W. R. Signal modulated apparatus for generating and detecting resistive and reactive changes in a modulated current path for particle classification and analysis. (1970).
- (Coulter and Rodriguez 1988) Coulter, W. H. & Rodriguez, C. M. Particle analyzer for measuring the resistance and reactance of a particle. (1988).
- (Cummings and Singh 2003) Cummings, E. B. & Singh, A. K. Dielectrophoresis in microchips containing arrays of insulating posts: Theoretical and experimental results. *Analytical Chemistry* **75**, 4724-4731, doi:10.1021/ac0340612 (2003).
- (Dababneh and Ozbolat 2014) Dababneh, A. B. & Ozbolat, I. T. Bioprinting Technology: A Current State-of-the-Art Review. *Journal of Manufacturing*

- Science and Engineering-Transactions of the Asme* **136**, doi:10.1115/1.4028512 (2014).
- (De Ninno, et al. 2017) De Ninno, A., Errico, V., Bertani, F. R., Businaro, L., Bisegna, P. & Caselli, F. Coplanar electrode microfluidic chip enabling accurate sheathless impedance cytometry. *Lab on a Chip* **17**, 1158-1166, doi:10.1039/C6LC01516F (2017).
- (de Wagenaar, et al. 2016) de Wagenaar, B., Dekker, S., de Boer, H. L., Bomer, J. G., Olthuis, W., van den Berg, A. & Segerink, L. I. Towards microfluidic sperm refinement: impedance-based analysis and sorting of sperm cells. *Lab on a Chip* **16**, 1514-1522, doi:10.1039/c6lc00256k (2016).
- (Demierre 2008) Demierre, N. *Continuous-flow separation of cells in a lab-on-a-chip using "liquid electrodes" and multiple-frequency dielectrophoresis*, EPFL, doi:10.5075/epfl-thesis-4099 (2008).
- (Demierre, et al. 2007) Demierre, N., Braschler, T., Linderholm, P., Seger, U., van Lintel, H. & Renaud, P. Characterization and optimization of liquid electrodes for lateral dielectrophoresis. *Lab on a Chip* **7**, 355-365, doi:10.1039/b612866a (2007).
- (Demierre, et al. 2008) Demierre, N., Braschler, T., Muller, R. & Renaud, P. Focusing and continuous separation of cells in a microfluidic device using lateral dielectrophoresis. *Sensors and Actuators B-Chemical* **132**, 388-396, doi:10.1016/j.snb.2007.09.078 (2008).
- (Doh and Cho 2005) Doh, I. & Cho, Y. H. A continuous cell separation chip using hydrodynamic dielectrophoresis (DEP) process. *Sensors and Actuators a-Physical* **121**, 59-65, doi:10.1016/j.sna.2005.01.030 (2005).
- (Dona, et al. 2003) Dona, M., Sandri, M., Rossini, K., Dell'Aica, I., Podhorska-Okolow, M. & Carraro, U. Functional in vivo gene transfer into the myofibers of adult skeletal muscle. *Biochemical and Biophysical Research Communications* **312**, 1132-1138, doi:10.1016/j.bbrc.2003.11.032 (2003).
- (Dontu, et al. 2003) Dontu, G., Abdallah, W. M., Foley, J. M., Jackson, K. W., Clarke, M. F., Kawamura, M. J. & Wicha, M. S. In vitro propagation and transcriptional profiling of human mammary stem/progenitor cells. *Genes & Development* **17**, 1253-1270, doi:10.1101/gad.1061803 (2003).
- (Erdem, et al. 2017) Erdem, N., Yıldızhan, Y. & Elitaş, M. A numerical approach for dielectrophoretic characterization and separation of human hematopoietic cells. *International Journal of Engineering Research & Technology (IJERT)* **6**, 1079-1082 (2017).
- (Escoffre and Rols 2012) Escoffre, J. M. & Rols, M. P. Electrochemotherapy: Progress and Prospects. *Current Pharmaceutical Design* **18**, 3406-3415, doi:10.2174/138161212801227087 (2012).
- (Evander, et al. 2013) Evander, M., Ricco, A. J., Morser, J., Kovacs, G. T. A., Leung, L. L. K. & Giovangrandi, L. Microfluidic impedance cytometer for platelet analysis. *Lab on a Chip* **13**, 722-729, doi:10.1039/c2lc40896a (2013).

- (Fennema, et al. 2013) Fennema, E., Rivron, N., Rouwkema, J., van Blitterswijk, C. & de Boer, J. Spheroid culture as a tool for creating 3D complex tissues. *Trends in Biotechnology* **31**, 108-115, doi:10.1016/j.tibtech.2012.12.003 (2013).
- (Ferrari, et al. 2005) Ferrari, E., Emiliani, V., Cojoc, D., Garbin, V., Zahid, M., Durieux, C., Coppey-Moisan, M. & Di Fabrizio, E. Biological samples micro-manipulation by means of optical tweezers. *Microelectronic Engineering* **78-79**, 575-581, doi:10.1016/j.mee.2005.01.017 (2005).
- (Fiedler, et al. 1998) Fiedler, S., Shirley, S. G., Schnelle, T. & Fuhr, G. Dielectrophoretic sorting of particles and cells in a microsystem. *Analytical Chemistry* **70**, 1909-1915, doi:10.1021/ac971063b (1998).
- (Foster and Schwan 1989) Foster, K. R. & Schwan, H. P. Dielectric properties of tissues and biological materials: a critical review. *Critical Reviews in Biomedical Engineering* **17**, 25-104 (1989).
- (Fox, et al. 2006) Fox, M. B., Esveld, D. C., Valero, A., Luttgge, R., Mastwijk, H. C., Bartels, P. V., Van Den Berg, A. & Boom, R. M. Electroporation of cells in microfluidic devices: A review. *Analytical and Bioanalytical Chemistry* **385**, 474-485, doi:10.1007/s00216-006-0327-3 (2006).
- (Frénéa, et al. 2003) Frénéa, M., Faure, S. P., Le Pioufle, B., Coquet, P. & Fujita, H. Positioning living cells on a high-density electrode array by negative dielectrophoresis. *Materials Science and Engineering: C* **23**, 597-603, doi:10.1016/s0928-4931(03)00055-9 (2003).
- (Fuhr, et al. 1992) Fuhr, G., Arnold, W. M., Hagedorn, R., Muller, T., Benecke, W., Wagner, B. & Zimmermann, U. Levitation, Holding, and Rotation of Cells within Traps Made by High-Frequency Fields. *Biochimica et Biophysica Acta* **1108**, 215-223, doi:10.1016/0005-2736(92)90028-K (1992).
- (Fuhr, et al. 1994) Fuhr, G., Glasser, H., Muller, T. & Schnelle, T. Cell manipulation and cultivation under a.c. electric field influence in highly conductive culture media. *Biochimica et Biophysica Acta (BBA) - Reviews on Cancer* **1201**, 353-360, doi:10.1016/0304-4165(94)90062-0 (1994).
- (Fuhr, et al. 1991) Fuhr, G., Hagedorn, R., Muller, T., Benecke, W., Wagner, B. & Gimsa, J. Asynchronous Traveling-Wave Induced Linear Motion of Living Cells. *Studia Biophysica* **140**, 79-102 (1991).
- (Gagnon 2011) Gagnon, Z. R. Cellular dielectrophoresis: applications to the characterization, manipulation, separation and patterning of cells. *Electrophoresis* **32**, 2466-2487, doi:10.1002/elps.201100060 (2011).
- (Gascoyne and Shim 2014) Gascoyne, P. R. & Shim, S. Isolation of circulating tumor cells by dielectrophoresis. *Cancers (Basel)* **6**, 545-579, doi:10.3390/cancers6010545 (2014).
- (Gascoyne, et al. 1995) Gascoyne, P. R. C., Becker, F. F. & Wang, X. B. Numerical-Analysis of the Influence of Experimental Conditions on the Accuracy of Dielectric Parameters Derived from Electrorotation Measurements.

- Bioelectrochemistry and Bioenergetics* **36**, 115-125, doi:10.1016/0302-4598(94)05015-M (1995).
- (Gascoyne, et al. 1992) Gascoyne, P. R. C., Huang, Y., Pethig, R., Vykoukal, J. & Becker, F. F. Dielectrophoretic Separation of Mammalian-Cells Studied by Computerized Image-Analysis. *Measurement Science and Technology* **3**, 439-445, doi:10.1088/0957-0233/3/5/001 (1992).
- (Gawad, et al. 2004) Gawad, S., Cheung, K., Seger, U., Bertsch, A. & Renaud, P. Dielectric spectroscopy in a micromachined flow cytometer: theoretical and practical considerations. *Lab on a Chip* **4**, 241-251, doi:10.1039/b313761a (2004).
- (Gawad, et al. 2001) Gawad, S., Schild, L. & Renaud, P. H. Micromachined impedance spectroscopy flow cytometer for cell analysis and particle sizing. *Lab on a Chip* **1**, 76-82, doi:10.1039/b103933b (2001).
- (Gersing 1998) Gersing, E. Impedance spectroscopy on living tissue for determination of the state of organs. *Bioelectrochemistry and Bioenergetics* **45**, 145-149, doi:10.1016/s0302-4598(98)00079-8 (1998).
- (Gil-Cardeza, et al. 2010) Gil-Cardeza, M. L., Villaverde, M. S., Fiszman, G. L., Altamirano, N. A., Cwirenbaum, R. A., Glikin, G. C. & Finocchiaro, L. M. E. Suicide gene therapy on spontaneous canine melanoma: correlations between in vivo tumors and their derived multicell spheroids in vitro. *Gene Therapy* **17**, 26-36, doi:10.1038/gt.2009.107 (2010).
- (Glasser and Fuhr 1998) Glasser, H. & Fuhr, G. Cultivation of cells under strong ac-electric field—differentiation between heating and trans-membrane potential effects. *Bioelectrochemistry and Bioenergetics* **47**, 301-310, doi:10.1016/s0302-4598(98)00146-9 (1998).
- (Golberg, et al. 2015) Golberg, A., Bruinsma, B. G., Uygun, B. E. & Yarmush, M. L. Tissue heterogeneity in structure and conductivity contribute to cell survival during irreversible electroporation ablation by "electric field sinks". *Scientific Reports* **5**, doi:10.1038/srep08485 (2015).
- (Gorges, et al. 2016) Gorges, T. M., Kuske, A., Rock, K., Mauermann, O., Muller, V., Peine, S., Verpoort, K., Novosadova, V., Kubista, M., Riethdorf, S. & Pantel, K. Accession of Tumor Heterogeneity by Multiplex Transcriptome Profiling of Single Circulating Tumor Cells. *Clinical Chemistry* **62**, 1504-1515, doi:10.1373/clinchem.2016.260299 (2016).
- (Gray, et al. 2008) Gray, D. S., Liu, W. F., Shen, C. J., Bhadriraju, K., Nelson, C. M. & Chen, C. S. Engineering amount of cell-cell contact demonstrates biphasic proliferative regulation through RhoA and the actin cytoskeleton. *Experimental Cell Research* **314**, 2846-2854, doi:10.1016/j.yexcr.2008.06.023 (2008).
- (Gray, et al. 2004a) Gray, D. S., Tan, J. L., Voldman, J. & Chen, C. S. Dielectrophoretic registration of living cells to a microelectrode array.

- Biosensors & Bioelectronics* **19**, 771-780, doi:10.1016/j.bios.2003.08.013 (2004a).
- (Gray, et al. 2004b) Gray, D. S., Tan, J. L., Voldman, J. & Chen, C. S. Dielectrophoretic registration of living cells to a microelectrode array (vol 19, pg 1765, 2004). *Biosensors & Bioelectronics* **19**, 1765-1774, doi:10.1016/j.bios.2004.03.016 (2004b).
- (Greco, et al. 2011) Greco, K. V., Iqbal, A. J., Rattazzi, L., Nalesso, G., Moradi-Bidhendi, N., Moore, A. R., Goldring, M. B., Dell'Accio, F. & Perretti, M. High density micromass cultures of a human chondrocyte cell line: A reliable assay system to reveal the modulatory functions of pharmacological agents. *Biochemical Pharmacology* **82**, 1919-1929, doi:10.1016/j.bcp.2011.09.009 (2011).
- (Grimnes and Martinsen 2014) Grimnes, S. & Martinsen, Ø. *Bioimpedance and bioelectricity basics*. (2014).
- (Guillemot, et al. 2010) Guillemot, F., Mironov, V. & Nakamura, M. Bioprinting is coming of age: Report from the International Conference on Bioprinting and Biofabrication in Bordeaux (3B'09). *Biofabrication* **2**, 010201, doi:10.1088/1758-5082/2/1/010201 (2010).
- (Guo, et al. 2016) Guo, F., Mao, Z. M., Chen, Y. C., Xie, Z. W., Lata, J. P., Li, P., Ren, L. Q., Liu, J. Y., Yang, J., Dao, M., Suresh, S. & Huang, T. J. Three-dimensional manipulation of single cells using surface acoustic waves. *Proceedings of the National Academy of Sciences of the United States of America* **113**, 1522-1527, doi:10.1073/pnas.1524813113 (2016).
- (Güven, et al. 2015) Güven, S., Chen, P., İnci, F., Tasoglu, S., Erkmen, B. & Demirci, U. Multiscale assembly for tissue engineering and regenerative medicine. *Trends in Biotechnology* **33**, 269-279, doi:10.1016/j.tibtech.2015.02.003 (2015).
- (Haandbaek, et al. 2014a) Haandbaek, N., Burgel, S. C., Heer, F. & Hierlemann, A. Characterization of subcellular morphology of single yeast cells using high frequency microfluidic impedance cytometer. *Lab on a Chip* **14**, 369-377, doi:10.1039/c3lc50866h (2014a).
- (Haandbaek, et al. 2016) Haandbaek, N., Burgel, S. C., Rudolf, F., Heer, F. & Hierlemann, A. Characterization of Single Yeast Cell Phenotypes Using Microfluidic Impedance Cytometry and Optical Imaging. *Acs Sensors* **1**, 1020-1027, doi:10.1021/acssensors.6b00286 (2016).
- (Haandbaek, et al. 2014b) Haandbaek, N., With, O., Burgel, S. C., Heer, F. & Hierlemann, A. Resonance-enhanced microfluidic impedance cytometer for detection of single bacteria. *Lab on a Chip* **14**, 3313-3324, doi:10.1039/c4lc00576g (2014b).
- (Haisler, et al. 2013) Haisler, W. L., Timm, D. M., Gage, J. A., Tseng, H., Killian, T. C. & Souza, G. R. Three-dimensional cell culturing by magnetic levitation. *Nature Protocols* **8**, 1940-1949, doi:10.1038/nprot.2013.125 (2013).

- (Han, et al. 2012) Han, X. J., van Berkel, C., Gwyer, J., Capretto, L. & Morgan, H. Microfluidic Lysis of Human Blood for Leukocyte Analysis Using Single Cell Impedance Cytometry. *Analytical Chemistry* **84**, 1070-1075, doi:10.1021/ac202700x (2012).
- (Hanai 1968) Hanai, T. Electrical properties of emulsions. in *Emulsion science* (ed Philipp Sherman) 353-478 (Academic Press, 1968).
- (Hanai 1960) Hanai, T. Theory of the dielectric dispersion due to the interfacial polarization and its application to emulsions. *Kolloid-Zeitschrift* **171**, 23-31, doi:10.1007/bf01520320 (1960).
- (Hanai, et al. 1979) Hanai, T., Asami, K. & Koizumi, N. Dielectric theory of concentrated suspension of shell-spheres in particular reference to the analysis of biological cell suspensions. *Bulletin of the Institute for Chemical Research, Kyoto University* **57**, 297-305 (1979).
- (Hanai, et al. 1982) Hanai, T., Imakita, T. & Koizumi, N. Analysis of Dielectric Relaxations of W/O Emulsions in the Light of Theories of Interfacial Polarization. *Colloid and Polymer Science* **260**, 1029-1034, doi:Doi 10.1007/Bf01451650 (1982).
- (Hatfield 1924) Hatfield, H. S. *Trans. Inst. Min. Metall.*, 335 (1924).
- (Hatschek and Thorne 1923) Hatschek, E. & Thorne, P. C. L. Metal sols in non-dissociating liquids. I. Nickel in toluene and benzene. *Proceedings of the Royal Society of London Series a-Containing Papers of a Mathematical and Physical Character* **103**, 276-284, doi:DOI 10.1098/rspa.1923.0056 (1923).
- (Heath, et al. 2016) Heath, J. R., Ribas, A. & Mischel, P. S. Single-cell analysis tools for drug discovery and development. *Nature Reviews Drug Discovery* **15**, 204-216, doi:10.1038/nrd.2015.16 (2016).
- (Heida, et al. 2001) Heida, T., Rutten, W. L. C. & Marani, E. Dielectrophoretic trapping of dissociated fetal cortical rat neurons. *IEEE Transactions on Biomedical Engineering* **48**, 921-930, doi:10.1109/10.936368 (2001).
- (Henslee, et al. 2011) Henslee, E. A., Sano, M. B., Rojas, A. D., Schmelz, E. M. & Davalos, R. V. Selective concentration of human cancer cells using contactless dielectrophoresis. *Electrophoresis* **32**, 2523-2529, doi:10.1002/elps.201100081 (2011).
- (Holcomb, et al. 2009) Holcomb, R. E., Kraly, J. R. & Henry, C. S. Electrode array detector for microchip capillary electrophoresis. *Analyst* **134**, 486-492, doi:10.1039/b816289a (2009).
- (Holmes and Morgan 2010) Holmes, D. & Morgan, H. Single Cell Impedance Cytometry for Identification and Counting of CD4 T-Cells in Human Blood Using Impedance Labels. *Analytical Chemistry* **82**, 1455-1461, doi:10.1021/ac902568p (2010).
- (Holmes, et al. 2009) Holmes, D., Pettigrew, D., Reccius, C. H., Gwyer, J. D., van Berkel, C., Holloway, J., Davies, D. E. & Morgan, H. Leukocyte analysis and

- differentiation using high speed microfluidic single cell impedance cytometry. *Lab on a Chip* **9**, 2881-2889, doi:10.1039/b910053a (2009).
- (Hooke 1665) Hooke, R. *Micrographia, or, Some physiological descriptions of minute bodies made by magnifying glasses :with observations and inquiries thereupon.* doi:10.5962/bhl.title.904 (1665).
- (Hsiao, et al. 2012) Hsiao, A. Y., Tung, Y. C., Kuo, C. H., Mosadegh, B., Bedenis, R., Pienta, K. J. & Takayama, S. Micro-ring structures stabilize microdroplets to enable long term spheroid culture in 384 hanging drop array plates. *Biomedical Microdevices* **14**, 313-323, doi:10.1007/s10544-011-9608-5 (2012).
- (Huang, et al. 1997) Huang, Y., Wang, X. B., Becker, F. F. & Gascoyne, P. R. C. Introducing dielectrophoresis as a new force field for field-flow fractionation. *Biophysical Journal* **73**, 1118-1129, doi:Doi 10.1016/S0006-3495(97)78144-X (1997).
- (Hughes 2016) Hughes, M. P. Fifty years of dielectrophoretic cell separation technology. *Biomicrofluidics* **10**, doi:10.1063/1.4954841 (2016).
- (Hughes 2002) Hughes, M. P. *Nanoelectromechanics in engineering and biology.* (CRC, 2002).
- (Huh, et al. 2013) Huh, D., Kim, H. J., Fraser, J. P., Shea, D. E., Khan, M., Bahinski, A., Hamilton, G. A. & Ingber, D. E. Microfabrication of human organs-on-chips. *Nature Protocols* **8**, 2135-2157, doi:10.1038/nprot.2013.137 (2013).
- (Huh, et al. 2010) Huh, D., Matthews, B. D., Mammoto, A., Montoya-Zavala, M., Hsin, H. Y. & Ingber, D. E. Reconstituting Organ-Level Lung Functions on a Chip. *Science* **328**, 1662-1668, doi:10.1126/science.1188302 (2010).
- (Ibrahim, et al. 2012) Ibrahim, S. N., Murray, L., Nock, V., Evans, J. J. & Alkaisi, M. M. The quadrupole microelectrode design on a multilayer biochip for dielectrophoretic trapping of single cells. *Microelectronic Engineering* **97**, 369-374, doi:10.1016/j.mee.2012.04.018 (2012).
- (Ingram, et al. 1997) Ingram, M., Tegy, G. B., Saroufeem, R., Yazan, O., Narayan, K. S., Goodwin, T. J. & Spaulding, G. F. Three-dimensional growth patterns of various human tumor cell lines in simulated microgravity of a NASA bioreactor. *In Vitro Cellular & Developmental Biology-Animal* **33**, 459-466 (1997).
- (Irimajiri, et al. 1996) Irimajiri, A., Ando, M., Matsuoka, R., Ichinowatari, T. & Takeuchi, S. Dielectric monitoring of rouleaux formation in human whole blood: a feasibility study. *Biochimica et Biophysica Acta (BBA) - Reviews on Cancer* **1290**, 207-209, doi:10.1016/0304-4165(96)00048-7 (1996).
- (Irimajiri, et al. 1979) Irimajiri, A., Hanai, T. & Inouye, A. A dielectric theory of "multi-stratified shell" model with its application to a lymphoma cell. *Journal of Theoretical Biology* **78**, 251-269, doi:10.1016/0022-5193(79)90268-6 (1979).

- (Irimajiri, et al. 1991) Irimajiri, A., Suzaki, T., Asami, K. & Hanai, T. Dielectric modeling of biological cells. Models and algorithm. *Bull. Inst. Chem. Res., Kyoto University* **69**, 421-438 (1991).
- (Jaeger, et al. 2008) Jaeger, M. S., Uhlig, K., Schnelle, T. & Mueller, T. Contact-free single-cell cultivation by negative dielectrophoresis. *Journal of Physics D-Applied Physics* **41**, 175502, doi:10.1088/0022-3727/41/17/175502 (2008).
- (Johnstone, et al. 1998) Johnstone, B., Hering, T. M., Caplan, A. I., Goldberg, V. M. & Yoo, J. U. In vitro chondrogenesis of bone marrow-derived mesenchymal progenitor cells. *Experimental Cell Research* **238**, 265-272, doi:10.1006/excr.1997.3858 (1998).
- (Jones 2003) Jones, T. B. Basic theory of dielectrophoresis and electrorotation. *IEEE Eng Med Biol Mag* **22**, 33-42 (2003).
- (Jones 1995) Jones, T. B. *Electromechanics of Particles*. doi:10.1017/cbo9780511574498 (Cambridge University Press, 1995).
- (Kakutani, et al. 1993) Kakutani, T., Shibatani, S. & Sugai, M. Electrorotation of non-spherical cells: Theory for ellipsoidal cells with an arbitrary number of shells. *Bioelectrochemistry and Bioenergetics* **31**, 131-145, doi:10.1016/0302-4598(93)80002-c (1993).
- (Kelm, et al. 2003) Kelm, J. M., Timmins, N. E., Brown, C. J., Fussenegger, M. & Nielsen, L. K. Method for generation of homogeneous multicellular tumor spheroids applicable to a wide variety of cell types. *Biotechnology and Bioengineering* **83**, 173-180, doi:10.1002/bit.10655 (2003).
- (Kilchenmann, et al. 2016) Kilchenmann, S. C., Rollo, E., Maoddi, P. & Guiducci, C. Metal-Coated SU-8 Structures for High-Density 3-D Microelectrode Arrays. *Journal of Microelectromechanical Systems* **25**, 425-431, doi:10.1109/Jmems.2016.2539000 (2016).
- (Kim, et al. 2005) Kim, J. Y., Baek, J. Y., Lee, K. A. & Lee, S. H. Automatic aligning and bonding system of PDMS layer for the fabrication of 3D microfluidic channels. *Sensors and Actuators a-Physical* **119**, 593-598, doi:10.1016/j.sna.2004.09.023 (2005).
- (Kim, et al. 2014) Kim, R., Joo, S., Jung, H., Hong, N. & Nam, Y. Recent trends in microelectrode array technology for in vitro neural interface platform. *Biomedical Engineering Letters* **4**, 129-141, doi:10.1007/s13534-014-0130-6 (2014).
- (Kipper, et al. 2017) Kipper, S., Frolov, L., Guy, O., Pellach, M., Glick, Y., Malichi, A., Knisbacher, B. A., Barbiro-, E., Avrahami, M. D., Yavets-Chen, Y., Levanon, E. Y. & Gerber, D. Control and automation of multilayered integrated microfluidic device fabrication. *Lab on a Chip* **17**, 557-566, doi:10.1039/c6lc01534d (2017).
- (Kuttel, et al. 2007) Kuttel, C., Nascimento, E., Demierre, N., Silva, T., Braschler, T., Renaud, P. & Oliva, A. G. Label-free detection of Babesia bovis infected red blood cells using impedance spectroscopy on a microfabricated flow



- cytometer. *Acta Tropica* **102**, 63-68, doi:10.1016/j.actatropica.2007.03.002 (2007).
- (Lancaster and Knoblich 2014) Lancaster, M. A. & Knoblich, J. A. Organogenesis in a dish: Modeling development and disease using organoid technologies. *Science* **345**, doi:10.1126/science.1247125 (2014).
- (Land, et al. 2011) Land, K. J., Mbanjwa, M. B., Govindasamy, K. & Korvink, J. G. Low cost fabrication and assembly process for re-usable 3D polydimethylsiloxane (PDMS) microfluidic networks. *Biomicrofluidics* **5**, 36502-365026, doi:10.1063/1.3641859 (2011).
- (Lapizco-Encinas, et al. 2004) Lapizco-Encinas, B. H., Simmons, B. A., Cummings, E. B. & Fintschenko, Y. Dielectrophoretic concentration and separation of live and dead bacteria in an array of insulators. *Analytical Chemistry* **76**, 1571-1579, doi:10.1021/ac034804j (2004).
- (Lee and Lee 2008) Lee, S. W. & Lee, S. S. Shrinkage ratio of PDMS and its alignment method for the wafer level process. *Microsystem Technologies-Micro-and Nanosystems-Information Storage and Processing Systems* **14**, 205-208, doi:10.1007/s00542-007-0417-y (2008).
- (Lei, et al. 2006) Lei, U., Yang, C. Y. & Wu, K. C. Viscous torque on a sphere under arbitrary rotation. *Applied Physics Letters* **89**, doi:10.1063/1.2372704 (2006).
- (Lenshof and Laurell 2010) Lenshof, A. & Laurell, T. Continuous separation of cells and particles in microfluidic systems. *Chemical Society Reviews* **39**, 1203-1217, doi:10.1039/b915999c (2010).
- (Levsky and Singer 2003) Levsky, J. M. & Singer, R. H. Gene expression and the myth of the average cell. *Trends in Cell Biology* **13**, 4-6, doi:10.1016/S0962-8924(02)00002-8 (2003).
- (Li, et al. 2007) Li, J., Le Gac, S. & Berg, P. d. i. A. v. d. in *Eleventh International Conference on Miniaturized Systems for Chemistry and Life Sciences - The proceedings of microTAS 2007 Conference*. (eds J. L. Viovy, P. Tabeling, S. Descroix, & L. Malaquin) 1756-1758 (Chemical and Biological Microsystems Society,
- (Li, et al. 2015) Li, X., Yu, Z. T., Geraldo, D., Weng, S., Alve, N., Dun, W., Kini, A., Patel, K., Shu, R., Zhang, F., Li, G., Jin, Q. & Fu, J. Desktop aligner for fabrication of multilayer microfluidic devices. *Review of Scientific Instruments* **86**, 075008, doi:10.1063/1.4927197 (2015).
- (Li and Kaler 2004) Li, Y. L. & Kaler, K. V. I. S. Dielectrophoretic fluidic cell fractionation system. *Analytica Chimica Acta* **507**, 151-161, doi:10.1016/j.aca.2003.08.071 (2004).
- (Llorens-Bobadilla, et al. 2015) Llorens-Bobadilla, E., Zhao, S., Baser, A., Saiz-Castro, G., Zwadlo, K. & Martin-Villalba, A. Single-Cell Transcriptomics Reveals a Population of Dormant Neural Stem Cells that Become Activated upon Brain Injury. *Cell Stem Cell* **17**, 329-340, doi:10.1016/j.stem.2015.07.002 (2015).

- (Lobjois, et al. 2009) Lobjois, V., Frongia, C., Jozan, S., Truchet, I. & Valette, A. Cell cycle and apoptotic effects of SAHA are regulated by the cellular microenvironment in HCT116 multicellular tumour spheroids. *European Journal of Cancer* **45**, 2402-2411, doi:10.1016/j.ejca.2009.05.026 (2009).
- (Lotters, et al. 1997) Lotters, J. C., Olthuis, W., Veltink, P. H. & Bergveld, P. The mechanical properties of the rubber elastic polymer polydimethylsiloxane for sensor applications. *Journal of Micromechanics and Microengineering* **7**, 145-147, doi:10.1088/0960-1317/7/3/017 (1997).
- (Madsen, et al. 2006) Madsen, S. J., Sun, C. H., Tromberg, B. J., Cristini, V., De Magalhaes, N. & Hirschberg, H. Multicell tumor spheroids in photodynamic therapy. *Lasers in Surgery and Medicine* **38**, 555-564, doi:10.1002/lsm.20350 (2006).
- (Manaresi, et al. 2002) Manaresi, N., Medoro, G., Tartagni, M., Altomare, L. & Guerrieri, R. in *Solid-State Circuits Conference, 2002. ESSCIRC 2002. Proceedings of the 28th European*. 37-42 (
- (Manczak, et al. 2016) Manczak, R., Fouet, M., Courson, R., Fabre, P.-L., Montrose, A., Sudor, J., Gué, A.-M. & Reybier, K. Improved on-chip impedimetric immuno-detection of subpopulations of cells toward single-cell resolution. *Sensors and Actuators B: Chemical* **230**, 825-831, doi:10.1016/j.snb.2016.02.070 (2016).
- (Manczak 2016) Manczak, R. m. *Microfluidic device for quantification of subpopulations of cells*, Université Paul Sabatier - Toulouse III (2016).
- (Marcus, et al. 2006) Marcus, J. S., Anderson, W. F. & Quake, S. R. Microfluidic single-cell mRNA isolation and analysis. *Analytical Chemistry* **78**, 3084-3089, doi:10.1021/ac0519460 (2006).
- (Markx, et al. 1997) Markx, G. H., Rousselet, J. & Pethig, R. DEP-FFF: Field-flow fractionation using non-uniform electric fields. *Journal of Liquid Chromatography & Related Technologies* **20**, 2857-2872, doi:Doi 10.1080/10826079708005597 (1997).
- (Markx, et al. 1994) Markx, G. H., Talary, M. S. & Pethig, R. Separation of viable and non-viable yeast using dielectrophoresis. *Journal of Biotechnology* **32**, 29-37, doi:10.1016/0168-1656(94)90117-1 (1994).
- (Martinez-Duarte, et al. 2011) Martinez-Duarte, R., Renaud, P. & Madou, M. J. A novel approach to dielectrophoresis using carbon electrodes. *Electrophoresis* **32**, 2385-2392, doi:10.1002/elps.201100059 (2011).
- (Marty, et al. 2006) Marty, M., Sersa, G., Garbay, J. R., Gehl, J., Collins, C. G., Snoj, M., Billard, V., Geertsen, P. F., Larkin, J. O., Miklavcic, D., Pavlovic, I., Paulin-Kosir, S. M., Cemazar, M., Morsli, N., Soden, D. M., Rudolf, Z., Robert, C., O'Sullivan, G. C. & Mir, L. M. Electrochemotherapy – An easy, highly effective and safe treatment of cutaneous and subcutaneous metastases: Results of ESOPE (European Standard Operating Procedures of

- Electrochemotherapy) study. *European Journal of Cancer Supplements* **4**, 3-13, doi:10.1016/j.ejcsup.2006.08.002 (2006).
- (Marx and Sandig 2006) Marx, U. & Sandig, V. *Drug Testing in vitro*. doi:10.1002/9783527609611 (2006).
- (Medoro 2000) Medoro, G. *Method and apparatus for the manipulation of particles by means of dielectrophoresis*. (Google Patents, 2000).
- (Medoro, et al. 2003) Medoro, G., Manaresi, N., Leonardi, A., Altomare, L., Tartagni, M. & Guerrieri, R. A lab-on-a-chip for cell detection and manipulation. *IEEE Sensors Journal* **3**, 317-325, doi:10.1109/Jsen.2003.814648 (2003).
- (Meissner 2013) Meissner, R. *Impedance spectroscopy for in vitro toxicology*, EPFL, doi:10.5075/epfl-thesis-5875 (2013).
- (Mellor, et al. 2006) Mellor, H. R., Davies, L. A., Caspar, H., Pringle, C. R., Hyde, S. C., Gill, D. R. & Callaghan, R. Optimising non-viral gene delivery in a tumour spheroid model. *Journal of Gene Medicine* **8**, 1160-1170, doi:10.1002/jgm.947 (2006).
- (Menad, et al. 2014) Menad, S., El-Gaddar, A., Haddour, N., Toru, S., Brun, M., Buret, F. & Frenea-Robin, M. From bipolar to quadrupolar electrode structures: an application of bond-detach lithography for dielectrophoretic particle assembly. *Langmuir* **30**, 5686-5693, doi:10.1021/la5005193 (2014).
- (Menad, et al. 2015) Menad, S., Franqueville, L., Haddour, N., Buret, F. & Frenea-Robin, M. nDEP-driven cell patterning and bottom-up construction of cell aggregates using a new bioelectronic chip. *Acta Biomaterialia* **17**, 107-114, doi:10.1016/j.actbio.2015.01.011 (2015).
- (Mir, et al. 2006) Mir, L. M., Gehl, J., Sersa, G., Collins, C. G., Garbay, J.-R., Billard, V., Geertsen, P. F., Rudolf, Z., O'Sullivan, G. C. & Marty, M. Standard operating procedures of the electrochemotherapy: Instructions for the use of bleomycin or cisplatin administered either systemically or locally and electric pulses delivered by the Cliniporator™ by means of invasive or non-invasive electrodes. *European Journal of Cancer Supplements* **4**, 14-25, doi:10.1016/j.ejcsup.2006.08.003 (2006).
- (Mironov, et al. 2003) Mironov, V., Boland, T., Trusk, T., Forgacs, G. & Markwald, R. R. Organ printing: computer-aided jet-based 3D tissue engineering. *Trends in Biotechnology* **21**, 157-161, doi:10.1016/s0167-7799(03)00033-7 (2003).
- (Mittal, et al. 2007) Mittal, N., Rosenthal, A. & Voldman, J. NDEP microwells for single-cell patterning in physiological media. *Lab on a Chip* **7**, 1146-1153, doi:10.1039/b706342c (2007).
- (Moraes, et al. 2009) Moraes, C., Sun, Y. & Simmons, C. A. Solving the shrinkage-induced PDMS alignment registration issue in multilayer soft lithography. *Journal of Micromechanics and Microengineering* **19**, doi:10.1088/0960-1317/19/6/065015 (2009).

- (Moreira, et al. 2009) Moreira, N. H., de Almeida, A. L., Piazzeta, M. H., de Jesus, D. P., Deblire, A., Gobbi, A. L. & da Silva, J. A. Fabrication of a multichannel PDMS/glass analytical microsystem with integrated electrodes for amperometric detection. *Lab on a Chip* **9**, 115-121, doi:10.1039/b807409g (2009).
- (Morgan and Green 2003) Morgan, H. & Green, N. G. *AC electrokinetics: colloids and nanoparticles*. (Research Studies Press, 2003).
- (Morgan and Spencer 2015) Morgan, H. & Spencer, D. Microfluidic Impedance Cytometry for Blood Cell Analysis. in *Microfluidics for Medical Applications* 213-241 doi:10.1039/9781849737593-00213 (The Royal Society of Chemistry, 2015).
- (Morgan, et al. 2007) Morgan, H., Sun, T., Holmes, D., Gawad, S. & Green, N. G. Single cell dielectric spectroscopy. *Journal of Physics D: Applied Physics* **40**, 61-70, doi:10.1088/0022-3727/40/1/s10 (2007).
- (Moroni, et al. 2008) Moroni, L., De Wijn, J. R. & Van Blitterswijk, C. A. Integrating novel technologies to fabricate smart scaffolds. *Journal of Biomaterials Science, Polymer Edition* **19**, 543-572, doi:10.1163/156856208784089571 (2008).
- (Nakamura, et al. 1999) Nakamura, K., Hanibuchi, M., Yano, S., Tanaka, Y., Fujino, I., Inoue, M., Takezawa, T., Shitara, K., Sone, S. & Hanai, N. Apoptosis induction of human lung cancer cell line in multicellular heterospheroids with humanized antiganglioside GM2 monoclonal antibody. *Cancer Research* **59**, 5323-5330 (1999).
- (Napolitano, et al. 2007a) Napolitano, A. P., Chai, P., Dean, D. M. & Morgan, J. R. Dynamics of the self-assembly of complex cellular aggregates on micromolded nonadhesive hydrogels. *Tissue Engineering* **13**, 2087-2094, doi:10.1089/ten.2006.0190 (2007a).
- (Napolitano, et al. 2007b) Napolitano, A. P., Dean, D. M., Man, A. J., Youssef, J., Ho, D. N., Rago, A. P., Lech, M. P. & Morgan, J. R. Scaffold-free three-dimensional cell culture utilizing micromolded nonadhesive hydrogels. *BioTechniques* **43**, 494, 496-500, doi:10.2144/000112591 (2007b).
- (Narayanamurthy, et al. 2017) Narayanamurthy, V., Nagarajan, S., Khan, A. Y. F., Samsuri, F. & Sridhar, T. M. Microfluidic hydrodynamic trapping for single cell analysis: mechanisms, methods and applications. *Analytical Methods* **9**, 3751-3772, doi:10.1039/c7ay00656j (2017).
- (Neumann, et al. 1982) Neumann, E., Schaeferriidder, M., Wang, Y. & Hofschneider, P. H. Gene-Transfer into Mouse Lyoma Cells by Electroporation in High Electric-Fields. *EMBO Journal* **1**, 841-845 (1982).
- (Nieminen, et al. 2007) Nieminen, T. A., Knoner, G., Heckenberg, N. R. & Rubinsztein-Dunlop, H. Physics of optical tweezers. *Laser Manipulation of Cells and Tissues* **82**, 207-236, doi:10.1016/S0091-679x(06)82006-6 (2007).

- (Pampaloni, et al. 2007) Pampaloni, F., Reynaud, E. G. & Stelzer, E. H. K. The third dimension bridges the gap between cell culture and live tissue. *Nature Reviews Molecular Cell Biology* **8**, 839-845, doi:10.1038/nrm2236 (2007).
- (Pesch 2018) Pesch, G. On the Dielectrophoretic Particle Retention in Porous Media. (2018).
- (Petchakup, et al. 2017) Petchakup, C., Li, K. H. H. & Hou, H. W. Advances in Single Cell Impedance Cytometry for Biomedical Applications. *Micromachines* **8**, doi:10.3390/mi8030087 (2017).
- (Pethig 2010) Pethig, R. Review article-dielectrophoresis: status of the theory, technology, and applications. *Biomicrofluidics* **4**, 022811, doi:10.1063/1.3456626 (2010).
- (Pethig 2017) Pethig, R. R. *Dielectrophoresis: Theory, methodology and biological applications*. doi:10.1002/9781118671443 (John Wiley & Sons, 2017).
- (Pohl 1978) Pohl, H. A. *Dielectrophoresis : the behavior of neutral matter in nonuniform electric fields*. (Cambridge University Press, 1978).
- (Pohl 1951) Pohl, H. A. The Motion and Precipitation of Suspensoids in Divergent Electric Fields. *Journal of Applied Physics* **22**, 869-871, doi:10.1063/1.1700065 (1951).
- (Pontani, et al. 2012) Pontani, L. L., Jorjadze, I., Viasnoff, V. & Brujic, J. Biomimetic emulsions reveal the effect of mechanical forces on cell-cell adhesion. *Proc Natl Acad Sci U S A* **109**, 9839-9844, doi:10.1073/pnas.1201499109 (2012).
- (Punniyakoti, et al. 2017) Punniyakoti, S., Sivakumarasamy, R., Vaurette, F., Joseph, P., Nishiguchi, K., Fujiwara, A. & Clement, N. Hydrogen Silsesquioxane-Based Nanofluidics. *Advanced Materials Interfaces* **4**, doi:10.1002/admi.201601155 (2017).
- (Puttaswamy, et al. 2010) Puttaswamy, S. V., Sivashankar, S., Chen, R. J., Chin, C. K., Chang, H. Y. & Liu, C. H. Enhanced cell viability and cell adhesion using low conductivity medium for negative dielectrophoretic cell patterning. *Biotechnol J* **5**, 1005-1015, doi:10.1002/biot.201000194 (2010).
- (Qian, et al. 2002) Qian, L., Scott, M., Kaler, K. V. I. S. & Paul, R. Integrated planar concentric ring dielectrophoretic (DEP) levitator. *Journal of Electrostatics* **55**, 65-79, doi:10.1016/S0304-3886(01)00184-X (2002).
- (Raicu and Feldman 2015) Raicu, V. & Feldman, Y. *Dielectric Relaxation in Biological Systems: Physical Principles, Methods, and Applications*. doi:10.1093/acprof:oso/9780199686513.001.0001 (Oxford University Press, 2015).
- (Raicu, et al. 1998) Raicu, V., Saibara, T., Enzan, H. & Irimajiri, A. Dielectric properties of rat liver in vivo: analysis by modeling hepatocytes in the tissue architecture. *Bioelectrochemistry and Bioenergetics* **47**, 333-342, doi:10.1016/S0302-4598(98)00172-X (1998).

- (Ramos, et al. 1998) Ramos, A., Morgan, H., Green, N. G. & Castellanos, A. Ac electrokinetics: a review of forces in microelectrode structures. *Journal of Physics D-Applied Physics* **31**, 2338-2353, doi:Doi 10.1088/0022-3727/31/18/021 (1998).
- (Reale, et al. 2018) Reale, R., De Ninno, A., Businaro, L., Bisegna, P. & Caselli, F. Electrical measurement of cross-sectional position of particles flowing through a microchannel. *Microfluidics and Nanofluidics* **22**, doi:10.1007/s10404-018-2055-3 (2018).
- (Reichle, et al. 1999) Reichle, C., Muller, T., Schnelle, T. & Fuhr, G. Electro-rotation in octopole micro cages. *Journal of Physics D-Applied Physics* **32**, 2128-2135, doi:10.1088/0022-3727/32/16/323 (1999).
- (Reichle, et al. 2000) Reichle, C., Schnelle, T., Muller, T., Leya, T. & Fuhr, G. A new microsystem for automated electrorotation measurements using laser tweezers. *Biochimica Et Biophysica Acta-Bioenergetics* **1459**, 218-229, doi:10.1016/S0005-2728(00)00150-X (2000).
- (Ren, et al. 2015) Ren, Y. F., Huang, S. H., Mosser, S., Heuschkel, M. O., Bertsch, A., Fraering, P. C., Chen, J. J. J. & Renaud, P. A Simple and Reliable PDMS and SU-8 Irreversible Bonding Method and Its Application on a Microfluidic-MEA Device for Neuroscience Research. *Micromachines* **6**, 1923-1934, doi:10.3390/mi6121465 (2015).
- (Rivron, et al. 2009) Rivron, N. C., Rouwkema, J., Truckenmüller, R., Karperien, M., De Boer, J. & Van Blitterswijk, C. A. Tissue assembly and organization: Developmental mechanisms in microfabricated tissues. *Biomaterials* **30**, 4851-4858, doi:10.1016/j.biomaterials.2009.06.037 (2009).
- (Rodriguez-Devora, et al. 2011) Rodriguez-Devora, J. I., Shi, Z. D. & Xu, T. Direct assembling methodologies for high-throughput bioscreening. *Biotechnol J* **6**, 1454-1465, doi:10.1002/biot.201100100 (2011).
- (Rols, et al. 1998) Rols, M. P., Delteil, C., Golzio, M., Dumond, P., Cros, S. & Teissie, J. In vivo electrically mediated protein and gene transfer in murine melanoma. *Nature Biotechnology* **16**, 168-171, doi:10.1038/nbt0298-168 (1998).
- (Ross, et al. 2001) Ross, D., Gaitan, M. & Locascio, L. E. Temperature Measurement in Microfluidic Systems Using a Temperature-Dependent Fluorescent Dye. *Analytical Chemistry* **73**, 4117-4123, doi:10.1021/ac010370l (2001).
- (Sale and Hamilton 1968) Sale, A. J. & Hamilton, W. A. Effects of high electric fields on micro-organisms. 3. Lysis of erythrocytes and protoplasts. *Biochimica et Biophysica Acta (BBA) - Reviews on Cancer* **163**, 37-43, doi:10.1016/0005-2736(68)90030-8 (1968).
- (Sambrook and Russell 2006) Sambrook, J. & Russell, D. W. DNA transfection by electroporation. *CSH Protoc* **2006**, doi:10.1101/pdb.prot3751 (2006).
- (Santini, et al. 2000) Santini, M. T., Rainaldi, G. & Indovina, P. L. Apoptosis, cell adhesion and the extracellular matrix in the three-dimensional growth of

- multicellular tumor spheroids. *Critical Reviews in Oncology Hematology* **36**, 75-87, doi:10.1016/S1040-8428(00)00078-0 (2000).
- (Schaefer, et al. 2002) Schaefer, M., Gross, W., Ackemann, J. & Gebhard, M. M. The complex dielectric spectrum of heart tissue during ischemia. *Bioelectrochemistry* **58**, 171-180, doi:10.1016/s1567-5394(02)00152-4 (2002).
- (Schwan 1957) Schwan, H. P. Electrical Properties of Tissue and Cell Suspensions. in *Advances in Biological and Medical Physics* Vol. 5 (eds John H. Lawrence & Cornelius A. Tobias) 147-209 doi:10.1016/b978-1-4832-3111-2.50008-0 (Elsevier, 1957).
- (Schwan 1994) Schwan, H. P. in *Proceedings of 16th Annual International Conference of the IEEE Engineering in Medicine and Biology Society*. A70-A71 vol.71 doi:10.1109/IEMBS.1994.412155 (
- (Sebastian, et al. 2006) Sebastian, A., Buckle, A. M. & Markx, G. H. Formation of multilayer aggregates of mammalian cells by dielectrophoresis. *Journal of Micromechanics and Microengineering* **16**, 1769-1777, doi:10.1088/0960-1317/16/9/003 (2006).
- (Sebastian, et al. 2007) Sebastian, A., Buckle, A. M. & Markx, G. H. Tissue engineering with electric fields: immobilization of mammalian cells in multilayer aggregates using dielectrophoresis. *Biotechnology and Bioengineering* **98**, 694-700, doi:10.1002/bit.21416 (2007).
- (Seger-Sauli, et al. 2005) Seger-Sauli, U., Panayiotou, M., Schnydrig, S., Jordan, M. & Renaud, P. Temperature measurements in microfluidic systems: heat dissipation of negative dielectrophoresis barriers. *Electrophoresis* **26**, 2239-2246, doi:10.1002/elps.200410358 (2005).
- (Shaker, et al. 2014) Shaker, M., Colella, L., Caselli, F., Bisegna, P. & Renaud, P. An impedance-based flow microcytometer for single cell morphology discrimination. *Lab on a Chip* **14**, 2548-2555, doi:10.1039/c4lc00221k (2014).
- (Shi, et al. 2009) Shi, J. J., Huang, H., Stratton, Z., Huang, Y. P. & Huang, T. J. Continuous particle separation in a microfluidic channel via standing surface acoustic waves (SSAW). *Lab on a Chip* **9**, 3354-3359, doi:10.1039/b915113c (2009).
- (Shim, et al. 2013) Shim, S., Stemke-Hale, K., Tsimberidou, A. M., Noshari, J., Anderson, T. E. & Gascoyne, P. R. Antibody-independent isolation of circulating tumor cells by continuous-flow dielectrophoresis. *Biomicrofluidics* **7**, 11807, doi:10.1063/1.4774304 (2013).
- (Sihvola and Kong 1988) Sihvola, A. H. & Kong, J. A. Effective permittivity of dielectric mixtures. *IEEE Transactions on Geoscience and Remote Sensing* **26**, 420-429, doi:10.1109/36.3045 (1988).
- (Sivakumarasamy, et al. 2014) Sivakumarasamy, R., Nishiguchi, K., Fujiwara, A., Vuillaume, D. & Clément, N. A simple and inexpensive technique for PDMS/silicon chip alignment with sub- $\mu$  m precision. *Anal. Methods* **6**, 97-101, doi:10.1039/c3ay41618f (2014).

- (Sivaraman, et al. 2005) Sivaraman, A., Leach, J. K., Townsend, S., Iida, T., Hogan, B. J., Stolz, D. B., Fry, R., Samson, L. D., Tannenbaum, S. R. & Griffith, L. G. A microscale in vitro physiological model of the liver: Predictive screens for drug metabolism and enzyme induction. *Current Drug Metabolism* **6**, 569-591, doi:10.2174/138920005774832632 (2005).
- (Slaughter, et al. 2009) Slaughter, B. V., Khurshid, S. S., Fisher, O. Z., Khademhosseini, A. & Peppas, N. A. Hydrogels in regenerative medicine. *Advanced Materials* **21**, 3307-3329, doi:10.1002/adma.200802106 (2009).
- (Song, et al. 2016) Song, H. J., Rosano, J. M., Wang, Y., Garson, C. J., Prabhakarbandian, B., Pant, K., Klarmann, G. J., Perantoni, A., Alvarez, L. M. & Lai, E. Identification of mesenchymal stem cell differentiation state using dual-micropore microfluidic impedance flow cytometry. *Analytical Methods* **8**, 7437-7444, doi:10.1039/c6ay01377e (2016).
- (Song, et al. 2013) Song, H. J., Wang, Y., Rosano, J. M., Prabhakarbandian, B., Garson, C., Pant, K. & Lai, E. A microfluidic impedance flow cytometer for identification of differentiation state of stem cells. *Lab on a Chip* **13**, 2300-2310, doi:10.1039/c3lc41321g (2013).
- (Souza, et al. 2010) Souza, G. R., Molina, J. R., Raphael, R. M., Ozawa, M. G., Stark, D. J., Levin, C. S., Bronk, L. F., Ananta, J. S., Mandelin, J., Georgescu, M. M., Bankson, J. A., Gelovani, J. G., Killian, T. C., Arap, W. & Pasqualini, R. Three-dimensional tissue culture based on magnetic cell levitation. *Nature Nanotechnology* **5**, 291-296, doi:10.1038/nnano.2010.23 (2010).
- (Spencer, et al. 2014) Spencer, D., Hollis, V. & Morgan, H. Microfluidic impedance cytometry of tumour cells in blood. *Biomicrofluidics* **8**, doi:10.1063/1.4904405 (2014).
- (Spencer and Morgan 2011) Spencer, D. & Morgan, H. Positional dependence of particles in microfluidic impedance cytometry. *Lab on a Chip* **11**, 1234-1239, doi:10.1039/c1lc20016j (2011).
- (Suehiro and Pethig 1998) Suehiro, J. & Pethig, R. The dielectrophoretic movement and positioning of a biological cell using a three-dimensional grid electrode system. *Journal of Physics D: Applied Physics* **31**, 3298-3305, doi:10.1088/0022-3727/31/22/019 (1998).
- (Sun and Morgan 2010) Sun, T. & Morgan, H. Single-cell microfluidic impedance cytometry: a review. *Microfluidics and Nanofluidics* **8**, 423-443, doi:10.1007/s10404-010-0580-9 (2010).
- (Sutherland 1988) Sutherland, R. M. Cell and Environment Interactions in Tumor Microregions - the Multicell Spheroid Model. *Science* **240**, 177-184, doi:10.1126/science.2451290 (1988).
- (Sutherland, et al. 1971) Sutherland, R. M., McCredie, J. A. & Inch, W. R. Growth of multicell spheroids in tissue culture as a model of nodular carcinomas. *Journal of the National Cancer Institute* **46**, 113-120 (1971).



- (Taff and Voldman 2005) Taff, B. M. & Voldman, J. A scalable addressable positive-dielectrophoretic cell-sorting array. *Analytical Chemistry* **77**, 7976-7983, doi:10.1021/ac0513616 (2005).
- (Talary, et al. 1996) Talary, M. S., Burt, J. P. H., Tame, J. A. & Pethig, R. Electromanipulation and separation of cells using travelling electric fields. *Journal of Physics D-Applied Physics* **29**, 2198-2203, doi:10.1088/0022-3727/29/8/021 (1996).
- (Tan, et al. 2003) Tan, J. L., Tien, J., Pirone, D. M., Gray, D. S., Bhadriraju, K. & Chen, C. S. Cells lying on a bed of microneedles: an approach to isolate mechanical force. *Proc Natl Acad Sci U S A* **100**, 1484-1489, doi:10.1073/pnas.0235407100 (2003).
- (Torisawa, et al. 2005) Torisawa, Y. S., Shiku, H., Yasukawa, T., Nishizawa, M. & Matsue, T. Multi-channel 3-D cell culture device integrated on a silicon chip for anticancer drug sensitivity test. *Biomaterials* **26**, 2165-2172, doi:10.1016/j.biomaterials.2004.05.028 (2005).
- (Trainito, et al. 2016) Trainito, C. I., Bayart, E., Subra, F., Francais, O. & Le Pioufle, B. The Electrorotation as a Tool to Monitor the Dielectric Properties of Spheroid During the Permeabilization. *Journal of Membrane Biology* **249**, 593-600, doi:10.1007/s00232-016-9880-7 (2016).
- (Tsong 1992) Tsong, T. Y. Molecular Recognition and Processing of Periodic Signals in Cells - Study of Activation of Membrane Atpases by Alternating Electric-Fields. *Biochimica et Biophysica Acta* **1113**, 53-70, doi:Doi 10.1016/0304-4157(92)90034-8 (1992).
- (Tung, et al. 2011) Tung, Y. C., Hsiao, A. Y., Allen, S. G., Torisawa, Y. S., Ho, M. & Takayama, S. High-throughput 3D spheroid culture and drug testing using a 384 hanging drop array. *Analyst* **136**, 473-478, doi:10.1039/c0an00609b (2011).
- (Valero, et al. 2008) Valero, A., Post, J. N., van Nieuwkasteele, J. W., Ter Braak, P. M., Kruijer, W. & van den Berg, A. Gene transfer and protein dynamics in stem cells using single cell electroporation in a microfluidic device. *Lab on a Chip* **8**, 62-67, doi:10.1039/b713420g (2008).
- (Voldman 2007) Voldman, J. Dielectrophoretic traps for cell manipulation. in *BioMEMS and Biomedical Nanotechnology* Vol. 4 159-186 doi:10.1007/978-0-387-25845-4\_8 (2007).
- (Voldman 2006) Voldman, J. Electrical forces for microscale cell manipulation. in *Annual Review of Biomedical Engineering* Vol. 8 425-454 doi:10.1146/annurev.bioeng.8.061505.095739 (2006).
- (Voldman, et al. 2001) Voldman, J., Braff, R. A., Toner, M., Gray, M. L. & Schmidt, M. A. Holding forces of single-particle dielectrophoretic traps. *Biophysical Journal* **80**, 531-541, doi:10.1016/S0006-3495(01)76035-3 (2001).

- (Voldman, et al. 2002) Voldman, J., Gray, M. L., Toner, M. & Schmidt, M. A. A Microfabrication-Based Dynamic Array Cytometer. *Analytical Chemistry* **74**, 3984-3990, doi:10.1021/ac0256235 (2002).
- (Wang and Bodovitz 2010) Wang, D. & Bodovitz, S. Single cell analysis: the new frontier in 'omics'. *Trends in Biotechnology* **28**, 281-290, doi:10.1016/j.tibtech.2010.03.002 (2010).
- (Wang, et al. 2007) Wang, L., Flanagan, L. A., Jeon, N. L., Monuki, E. & Lee, A. P. Dielectrophoresis switching with vertical sidewall electrodes for microfluidic flow cytometry. *Lab on a Chip* **7**, 1114-1120, doi:10.1039/b705386j (2007).
- (Wang, et al. 1994) Wang, X. B., Huang, Y., Gascoyne, P. R. C., Becker, F. F., Holzel, R. & Pethig, R. Changes in Friend Murine Erythroleukemia Cell-Membranes during Induced-Differentiation Determined by Electrorotation. *Biochimica Et Biophysica Acta-Biomembranes* **1193**, 330-344, doi:10.1016/0005-2736(94)90170-8 (1994).
- (Washizu 1990) Washizu, M. Electrostatic Manipulation of Biological Objects. *Journal of Electrostatics* **25**, 109-123, doi:Doi 10.1016/0304-3886(90)90040-3 (1990).
- (Weaver, et al. 1999) Weaver, J. C., Vaughan, T. E. & Martin, G. T. Biological Effects Due to Weak Electric and Magnetic Fields: The Temperature Variation Threshold. *Biophysical Journal* **76**, 3026-3030, doi:10.1016/s0006-3495(99)77455-2 (1999).
- (Ye, et al. 2009) Ye, X. D., Liu, H. Z., Ding, Y. C., Li, H. S. & Lu, B. H. Research on the cast molding process for high quality PDMS molds. *Microelectronic Engineering* **86**, 310-313, doi:10.1016/j.mee.2008.10.011 (2009).
- (Zanoni, et al. 2016) Zanoni, M., Piccinini, F., Arienti, C., Zamagni, A., Santi, S., Polico, R., Bevilacqua, A. & Tesei, A. 3D tumor spheroid models for in vitro therapeutic screening: a systematic approach to enhance the biological relevance of data obtained. *Sci Rep* **6**, 19103, doi:10.1038/srep19103 (2016).
- (Zhang, et al. 2011) Zhang, Z. Y., Zhao, P., Xiao, G. Z., Watts, B. R. & Xu, C. Q. Sealing SU-8 microfluidic channels using PDMS. *Biomicrofluidics* **5**, doi:10.1063/1.3659016 (2011).
- (Zhao, et al. 2016a) Zhao, Y., Jiang, M., Chen, D., Zhao, X., Xue, C., Hao, R., Yue, W., Wang, J. & Chen, J. Single-Cell Electrical Phenotyping Enabling the Classification of Mouse Tumor Samples. *Sci Rep* **6**, 19487, doi:10.1038/srep19487 (2016a).
- (Zhao, et al. 2016b) Zhao, Y., Liu, Q., Sun, H., Chen, D., Li, Z., Fan, B., George, J., Xue, C., Cui, Z., Wang, J. & Chen, J. Electrical property characterization of neural stem cells in differentiation. *PLoS ONE* **11**, doi:10.1371/journal.pone.0158044 (2016b).
- (Zhao, et al. 2014) Zhao, Y., Zhao, X. T., Chen, D. Y., Luo, Y. N., Jiang, M., Wei, C., Long, R., Yue, W. T., Wang, J. B. & Chen, J. Tumor cell characterization and classification based on cellular specific membrane capacitance and

cytoplasm conductivity. *Biosensors and Bioelectronics* **57**, 245-253, doi:10.1016/j.bios.2014.02.026 (2014).

(Zhong, et al. 2008) Zhong, J. F., Chen, Y., Marcus, J. S., Scherer, A., Quake, S. R., Taylor, C. R. & Weiner, L. P. A microfluidic processor for gene expression profiling of single human embryonic stem cells. *Lab on a Chip* **8**, 68-74, doi:10.1039/b712116d (2008).

(Zhou, et al. 2010) Zhou, J., Ellis, A. V. & Voelcker, N. H. Recent developments in PDMS surface modification for microfluidic devices. *Electrophoresis* **31**, 2-16, doi:10.1002/elps.200900475 (2010).

(Zhu, et al. 2016) Zhu, Z., Chen, P., Liu, K. G. & Escobedo, C. A Versatile Bonding Method for PDMS and SU-8 and Its Application towards a Multifunctional Microfluidic Device. *Micromachines* **7**, doi:10.3390/mi7120230 (2016).

(Zimmermann, et al. 2008) Zimmermann, D., Kiesel, M., Terpitz, U., Zhou, A., Reuss, R., Kraus, J., Schenk, W. A., Bamberg, E. & Sukhorukov, V. L. A combined patch-clamp and electrorotation study of the voltage- and frequency-dependent membrane capacitance caused by structurally dissimilar lipophilic anions. *Journal of Membrane Biology* **221**, 107-121, doi:10.1007/s00232-007-9090-4 (2008).



# List of publications

## Peer reviewed articles

**Cottet, J.**, Vaillier, C., Buret, F., Frenea-Robin, M. & Renaud, P. A reproducible method for  $\mu\text{m}$  precision alignment of PDMS microchannels with on-chip electrodes using a mask aligner. *Biomicrofluidics* **11**, 064111, doi:10.1063/1.5001145 (2017).

Brazey, B., **Cottet, J.**, Bolopion, A., Van Lintel, H., Renaud, P. & Gauthier, M. Impedance-based real-time position sensor for lab-on-a-chip devices. *Lab on a Chip* **18**, 818-831, doi:10.1039/c7lc01344b (2018).

**Cottet, J.**, Fabregue, O., Berger, C., Buret, F., Renaud, P. & Frénéa-Robin, M. MyDEP: A New Computational Tool for Dielectric Modeling of Particles and Cells. *Biophysical Journal* **116**, 12-18, doi:10.1016/j.bpj.2018.11.021 (2019).

**Cottet, J.**, Kehren, A., van Lintel, H., Buret, F., Frénéa-Robin, M. & Renaud, P. How to improve the sensitivity of coplanar electrodes and micro channel design in electrical impedance flow cytometry: a study. *Microfluidics and Nanofluidics* **23**, doi:10.1007/s10404-018-2178-6 (2019).

**Cottet, J.**, Kehren, A., Lasli, S., van Lintel, H., Buret, F., Frénéa-Robin, M. & Renaud, P. Dielectrophoresis-assisted creation of cell aggregates under flow conditions using planar electrodes. *Electrophoresis* **40**, 1498-1509, doi:10.1002/elps.201800435 (2019).

## Software

Cottet, J., Fabregue, O., Berger, C., Buret, F., Renaud, P. & Frénéa-Robin, M. MyDEP: a new computational tool for dielectric modeling of particles and cells doi:10.5281/zenodo.1321928 (2018)

## Conferences

Buret, F., **Cottet, J.**, Frénéa-Robin, M., Marchalot, J., Menad, S. & Renaud, P., Dielectrophoretic formation of cell aggregates mimicking tumors for in vitro study of

electrochemotherapy in 10th International Symposium on Electric and Magnetic Fields (EMF 2016) (Lyon, France, 2016, 12-14 avril) (Poster)

**Cottet, J.**, Frénéa-Robin, M., Buret, F. & Renaud, P., Microfluidic chip for the creation and characterization of cell aggregates with electrical engineering techniques in GDR Micro et Nanofluidique (IPGG, Paris, France, 2016, 23-24 Juin) (Poster)

**Cottet, J.**, Frénéa-Robin, M., Buret, F. & Renaud, P., Creation of cell aggregates by dielectrophoresis for the in vitro study of electrochemotherapy in Electroporation-Based Technologies and Treatments (Ljubljana, Slovenia, 2016, 13-19 Novembre) (Poster)

Seth, A., Voyer, D., **Cottet, J.**, Marchalot, J., Frénéa-Robin, M. & Scorretti, R., Modélisation de la dynamique de l'électroporation à l'échelle tissulaire in Modéliser le vivant, Journée scientifique de la Faculté des Sciences et Technologies, UCBL (Villeurbanne, France, 2017, 22 juin)

**Cottet, J.**, Kehren, A., Van Lintel, H., Buret, F., Frénéa-Robin, M. & Renaud, P., Improvement of the sensitivity of a coplanar electrode layout for Electrical Impedance Spectroscopy in NanoBioTech-Montreux (Montreux, Switzerland, 2017, 13-15 Novembre) (Poster)

**Cottet, J.**, Fabrègue, O., Marchalot, J., Scorretti, R., Buret, F., Frénéa-Robin, M. & Renaud, P., Bottom-up assembly of cells in flow with dielectrophoresis in GDR MicroNanoFluidique (MNF 2018) (Grenoble, France, 2018, 15-16 mars) (Poster)

**Cottet, J.**, Kehren, A., Van Lintel, H., Buret, F., Frénéa-Robin, M. & Renaud, P., Towards more sensitive coplanar electrode designs for analysis of single cells and small cell aggregates by Electrical Impedance Spectroscopy in 2nd International Conference of Microfluidics, Nanofluidics, and Lab-on-a-chip (ICMFLOC 2018) (Beijing, China, 2018, 8-10 Juin) (Oral)

**Cottet, J.**, Kehren, A., Van Lintel, H., Buret, F., Frénéa-Robin, M. & Renaud, P., Creation of cell aggregates under flow with dielectrophoresis using planar electrodes in Biosensors 2020 (Miami, United States, 2018, 12-15 Juin) (Oral)

**Cottet, J.**, Fabrègue, O., Marchalot, J., Scorretti, R., Buret, F., Frénéa-Robin, M. & Renaud, P., Développement de microsystèmes utilisant des champs électriques

pour la création et la caractérisation d'agrégats de cellules in Symposium de Génie Electrique (SGE 2018) (Nancy, France, 2018, 3-5 juillet) (Oral)

**Cottet, J.**, Fabrègue, O., berger, c., Buret, F., Renaud, P. & Frénéa-Robin, M., MyDEP, a software for dielectric modeling of particles and cells for simulation of dielectrophoretic response spectra in Dielectrophoresis 2018 (Surrey, United Kingdom, 2018, 23-25 Juillet) (Oral)

**Cottet, J.**, Kehren, A., Lasli, S., Van Lintel, H., Buret, F., Frénéa-Robin, M. & Renaud, P., Cell trapping and aggregation in flow with dielectrophoresis using planar electrodes in Dielectrophoresis 2018 (Surrey, United Kingdom, 2018, 23-25 Juillet) (Oral)

**Cottet, J.**, Kehren, A., Lasli, S., Van Lintel, H., Buret, F., Frénéa-Robin, M. & Renaud, P., A new planar electrode design for dielectrophoresis-assisted creation of cell aggregates under flow conditions in Nanobiotech (Montreux, Switzerland, 2018, 28-30 Novembre) (Poster)

### **Grant and Prizes**

International mobility grants from the PALSE (2017) and iMUST LABEX (2018)

Presentation prize “Early Career Researcher Award” obtained at the Dielectrophoresis 2018 conference.

Poster prize “Technology Poster Award” obtained at the Nanobiotech Montreux 2018 conference.





## **Titre de la thèse : Développement de microsystèmes pour la formation contrôlée d'agrégats de cellules par diélectrophorèse**

### **Résumé**

Les agrégats cellulaires constituent un modèle intermédiaire entre les cellules uniques et les tissus cellulaires et sont utilisés dans de nombreux domaines tels que l'ingénierie tissulaire et le criblage de médicaments in vitro. La création de tels agrégats cellulaires dont les propriétés et la taille seraient contrôlées nécessite cependant le développement de nouvelles approches ascendantes. Le travail présenté dans ce manuscrit vise à développer des microsystèmes pour la formation contrôlée d'agrégats de cellules sous flux via des champs électriques. Cette approche se base sur la diélectrophorèse (DEP), un phénomène induisant le déplacement des particules diélectriques lorsqu'elles sont placées dans un champ électrique non-uniforme. Un outil de calcul, MyDEP, a tout d'abord été développé afin d'être en mesure de prédire le comportement des cellules en suspension dans un certain milieu. Cet outil permet d'étudier la réponse diélectrique des particules et des cellules en fonction de la fréquence du champ. Il contient une base de données regroupant les propriétés diélectriques des cellules publiées dans la littérature afin d'aider tant les spécialistes que les utilisateurs néophytes à comprendre le comportement diélectrophoretique des particules et des cellules ainsi qu'à choisir les paramètres expérimentaux tels que la conductivité électrique du milieu et la fréquence du champ préalablement aux manipulations expérimentales en laboratoire. Différents designs pour le piégeage de cellules sont proposés avec les simulations, par la méthode des éléments finis en utilisant COMSOL Multiphysics, associées. Leur fabrication a nécessité le développement d'une méthode d'alignement reproductible, précise au micromètre, des microcanaux d'un polymère appelé le polydiméthylsiloxane (PDMS) avec des électrodes coplanaires en titane/platine déposées sur du verre via l'utilisation d'une aligneuse de masques conventionnelle. La méthode est basée sur l'utilisation d'un moule en silicium associé à un sarcophage en Poly(méthyl méthacrylate) (PMMA) afin de garantir le contrôle du parallélisme entre les parties supérieure et inférieure du PDMS moulé. Les puces contenant les différents designs de piégeage ainsi fabriquées ont été testées avec succès sur des cellules rénales embryonnaires humaines (HEK) à l'aide d'une installation expérimentale démontrant par là même la capacité des puces à créer des agrégats constitués d'un nombre contrôlé de cellules par diélectrophorèse. Les agrégats ainsi formés se sont avérés stables après 5 minutes de contact cellule à cellule sans qu'une séparation des cellules n'ait été observée. Le design d'un capteur par impédance a par ailleurs été proposé pour caractériser tant les cellules uniques que les agrégats cellulaires avant et après la chambre de piégeage. Celui-ci, associé au design de piégeage par DEP, a été testé expérimentalement avec succès pour détecter leur passage.

**Mots-Clés:** Diélectrophorèse, Piégeage de cellules, Agrégats cellulaires, Microfluidique, Approche ascendante, Alignement du PDMS, Modélisation diélectrique, Spectroscopie d'impédance.

### **Title in English: Development of microsystems for the controlled formation of cell aggregates by dielectrophoresis**

#### **Abstract:**

Cell aggregates are an intermediary model between single cells and cell tissues used in many applications such as tissue engineering and in vitro drug screening. The creation of cells aggregates of controlled size and properties requires the development of new bottom-up strategies. The work developed in this manuscript aims at presenting the development of microsystems for the electric force-driven controlled formation of cell aggregates under flow conditions. This approach is based on dielectrophoresis, a phenomenon that causes induced motion on dielectric particles placed in a non-uniform electric field. A computational tool, MyDEP, was first developed in order to predict the behavior of cells in a specific medium. It allows to study the dielectric response of particles and cells as a function of frequency. The software also includes a database gathering cell dielectric models available in the literature to help experienced users as well as neophytes to understand the dielectrophoretic behavior of particles and cells and to choose parameters such as electric conductivity of the medium and frequency before performing laboratory experiments. Different designs for cell trapping are proposed and simulated in 2D with FEM using COMSOL Multiphysics. Their fabrication implied the development of a reproducible method for  $\mu\text{m}$  precision alignment of microchannels in a polymer called polydimethylsiloxane (PDMS) with coplanar titanium/platinum electrodes deposited on glass, using a conventional mask aligner. It is based on the use of a silicon mold in combination with a Poly(methyl methacrylate) (PMMA) sarcophagus for precise control of the parallelism between top and bottom surfaces of molded PDMS. The trapping design based on coplanar electrodes was successfully tested experimentally on human embryonic kidney cells (HEK) with an automated setup. It proves its capability to create aggregates of a controlled number of cells with DEP. The cell aggregates proved to be stable (no disruption) after only 5 minutes of cell-cell contact. An impedance-based sensor design was proposed for characterizing single cells and cells aggregates before and after the trapping chamber. This sensor was successfully tested experimentally to detect particle passage in combination with the dielectrophoretic trapping design.

**Keywords:** Dielectrophoresis, Cell trapping, Cell aggregates, Microfluidics, Bottom-up assembly, PDMS Alignment, Dielectric modelling, Impedance spectroscopy